Large diameter dolphin piles

The effect of the inner soil on their local buckling resistance

J. Winkel

TU Delft Delft University of Technology

Challenge the future

Royal HaskoningDHV

Enhancing Society Together

Large diameter dolphin piles

The effect of the inner soil on their local buckling resistance

by

J. Winkel

to obtain the degree of Master of Science in Civil Engineering
at the Delft University of Technology,
to be defended publicly on Monday, 31 October 2016 at 3:30 p.m.

Faculty:	Civil Engineering and Geosciences	
Department:	Structural Engineering	
Programme:	Hydraulic Structures	
Thesis committee:	Prof. dr. ir. S. N. Jonkman,	TU Delft, Hydraulic Engineering
	Ir. D. J. Peters,	Royal HaskoningDHV;
		TU Delft, Hydraulic Engineering
	Dr. ir. S. H. J. van Es,	TU Delft, Structural Engineering
	Ing. H. J. Everts,	TU Delft, Geoscience and Engineering
Project duration:	11 January 2016 – 31 October 2016	

An electronic version of this thesis is available at `http://repository.tudelft.nl/`.

TU Delft

Royal HaskoningDHV

Abstract

Even though for most hydraulic and geotechnical structures clear guidelines are available, those for flexible dolphins are still missing. Consequently, whether a design is safe is usually subject of debate.

Economical dolphin piles are large diameter tubular piles, susceptible to local buckling. After installation the embedded part of these piles remains predominantly filled with soil. The aim of this research is to provide understanding of the effects concerning local buckling and therewith to contribute to the discussion whether a dolphin design is safe.

The main research question is:
Does the soil in dolphin piles contribute to the local buckling resistance and can this be used in the design of these piles?

Gresnigt [1] prescribes a strain based method to check a pile on local buckling. This method is incorporated in EN 1993-4-3 [2]. The resistance against local buckling depends on the slenderness ratio $D_e/t\varepsilon^2$. Also, ovalisation influences the resistance. The presence of a soil plug reduces the ovalisation, enhancing the local buckling resistance.

An analytical method is proposed in which beam theory is used to determine the dolphin pile deformation and loads on the pile. Literature provides equations to calculate the ovalisation that can be applied in three distinct parts: above the bed level, between the bed level and plug level and below the plug level. The provided equations however, show inconsistencies at the transitions. It is proposed to apply beam theory on the pile wall, modelled as a linear beam with springs providing resistance against ovalisation. Above the plug level, the resistance is provided by the ring behaviour of the shell. Below the plug level, the stiffness is increased with the stiffness of the soil plug. The model overcomes the inconsistencies in ovalisation. The method assumes the stiffness of the plug in the pile can be approximated. However, it is concluded that the suggested stiffness in CUR 211E [3] is not able to determine the plug stiffness for semi-filled piles.

Key parameters that affect the local buckling resistance are identified. These are the plug packing, plug level, slenderness ratio and the soil packing. The influence of these key parameters are studied with the finite element program Abaqus.

The parametric study proves that the soil in dolphin piles contributes to the local buckling resistance. A denser packing of the plug improves the capacities of the bending moment and lateral load. Most of all, the dolphin can dissipate more energy. The plug level influences the level at which local buckling is observed, as well as whether an inward or outward buckle occur. The contribution of the inner soil on the local buckling resistance can be compensated by designing a more slender dolphin pile. A more slender cross-section reduces the capacities of the pile. The packing of the outer soil also influences the buckling level and shape. Furthermore, a looser soil packing improves the energy capacity of the dolphin pile. To obtain a dolphin pile that optimises the improvements on the local buckling resistance by the inner and surrounding soil, an installation method is used that does not compact the soil and plug packing and after installation, the plug packing is compacted.

With the Abaqus analyses the stiffness of the soil plug is studied. It reveals that the plug is stiffer at deeper levels. For a pile with a diameter comparable to 914 mm, when the predicted ovalisation for that pile without a soil plug is less than 8 mm, a plug stiffness of 30,000 $\mathrm{kN/m^2}$ can be assumed in the proposed analytical method, regardless of the plug packing. The stiffness is independent of the slenderness ratio.

The Port of Rotterdam facilitated a full scale field test with eight piles. The Abaqus model shows reasonable comparison with the field test. The observed local buckling behaviour piles that were not modelled can well be explained with the results of the parametric study.

Preface

This report is my Master's thesis, the final product to obtain the degree of Master of Science in Civil Engineering at the Delft University of Technology. An end has come to an animated, enjoyable time that was educational and inspiring. Since six years, I am in Delft active to widely develop myself. Looking for new knowledge, skills and experiences.

I am inspired by Maslow's hierarchy of needs, that I encountered during the minor project management within the BSc degree program. In order to be happy, one requires the basic needs. It is my purpose to provide people safety. Hence, I choose to study Hydraulic Structures.

During my internship at the Maritime department of Royal HaskoningDHV, I was faced with the design of dolphin piles. It is not a lifesaving structure, yet the optimisation between strength and flexibility fascinates me. Dirk Jan Peters offered me this challenging master thesis project, that requires knowledge in structural engineering as well as soil mechanics.

In the course of this project, I learned a lot about soil structure interaction, thanks to Bert Everts. I am also grateful to Sjors van Es, for clarifying the differences between theory, codes and practice. Bas Jonkman showed me how a research project is set up and kept me focused towards the end, which I appreciate. Moreover, throughout this project I experienced that it can be more efficient to make assumptions and then to find out how to deal with the consequences, rather than first studying all the possible effects of an assumption. I consider these as valuable lessons.

Thanks to Royal HaskoningDHV for providing me the facilities I needed to be able to do this research. I am thankful to the colleagues that were willing to answer questions and think along. Special thanks to Dirk Jan Peters, for introducing me to this engineering world, with all its uncertainties. Yet, you showed me in person that with a wide knowledge there always is a way to cope with them.

Jort Winkel
Delft, October 2016

Nomenclature

Abbreviations

CPT	Cone penetration test
FEM	Finite element method
IFR	Incremental filling ratio
LA	Linear elastic shell analysis
LBA	Linear elastic bifurcation (eigenvalue) analysis
MNA	Materially nonlinear analysis
OCR	Overconsolidation ratio
PLR	Plug length ratio
SLS	Serviceability limit state
TEU	Twenty Foot Equivalent Unit
ULS	Ultimate limit state

Symbols

Roman upper case letters

D_e	External diameter: $D_m + t$	[m]
D_m	Diameter of the mid-line of the pile wall	[m]
D_{soil}	Diameter of the modelled outer soil in Abaqus	[m]
E	Young's modulus of elasticity	[kPa]
E_g	Young's modulus of elasticity of the soil	[kPa]
E_{plug}	Young's modulus of elasticity of the soil plug	[kPa]
E_{ref}	Young's modulus parameter of Plaxis	[kPa]
E_s	Young's modulus of elasticity of steel	[kPa]
E_{v}	Berthing energy	[kNm]
EI	Bending stiffness in beam theory	[kNm^2]
EI_p	Bending stiffness of the pile	[kNm^2]
EI_w	Bending stiffness of the pile wall per unit length	[kNm]
F_a	Active earth force	[kN]
F_p	Passive earth force	[kN]
F_{pt}	Ultimate lateral resistance	[kN]
F_{v}	Lateral load exerted by the vessel	[kN]
G	Shear modulus of elasticity	[kPa]
I_p	Second moment of inertia of the pile	[m^4]
I_w	Second moment of inertia of the pile wall per unit length	[m^3]
K	Lateral stress coefficient	[-]
K_0	Neutral earth pressure coefficient	[-]
K_0^{NC}	Neutral earth pressure coefficient for nonconsolidated soils	[-]
K_0^{OC}	Neutral earth pressure coefficient for over consolidated soils	[-]
K_a	Active earth pressure coefficient	[-]
K_p	Passive earth pressure coefficient	[-]
L_f	Length of the unembedded (free) part of the pile	[m]
L_{np}	Length of the embedded part of the pile without plug	[m]
L_p	Plug length	[m]
L_s	Length of the embedded part of the pile	[m]
M	Bending moment	[kNm]
M_p	Plastic moment capacity	[kNm]

M_y	Yield moment capacity	[kNm]
$Q_{f,i}$	Ultimate inner shaft friction	[kNm^{-1}]
Q_i	Support reaction in the form of indirectly transmitted earth pressure	[kNm^{-1}]
Q_p	Ultimate plug end bearing	[kNm^{-1}]
R_m	Radius of the of the mid-line of the pile wall: $D_m/2$	[m]
R_o	local radius of curvature of an ovalised cross section	[m]
U_0	Initial dimple parameter	[-]
U_1	Displacement in x-direction in Abaqus	[mm]
U_2	Displacement in y-direction in Abaqus	[mm]
U_3	Displacement in z-direction in Abaqus	[mm]
U_r	Out-of-roundness	[-]
V	Shear force	[kN]

Roman lower case letters

a	Ovalisation parameter	[m]
a_c	Ovalisation parameter due to bending	[m]
a_{empty}	Ovalisation parameter of an empty pile	[m]
a_q	Ovalisation parameter due to indirect earth pressure	[m]
$a_{\text{sand-filled}}$	Ovalisation parameter of a sand-filled cross section	[m]
c'	Cohesion	[kPa]
d	Internal diameter: $D_m - t$	[m]
f_b	Buckling capacity	[MPa]
f_{cr}	Critical stress	[MPa]
f_{ref}	Reference strength (235 MPa)	[MPa]
f_{rr}	Rerounding factor	[-]
f_y	Yield strength	[MPa]
k	Spring stiffness	[kPa]
k_θ	Circumferential buckling interaction parameter	[-]
k_τ	Shear buckling interaction parameter	[-]
k_i	Buckling interaction parameter	[-]
k_g	Stiffness of the soil	[kPa]
$k_{g,\text{applied}}$	Stiffness of the soil applied on a segment of the pile	[kPa]
$k_{g,b}$	Stiffness of the soil at the bottom of a segment of the pile	[kPa]
$k_{g,t}$	Stiffness of the soil at the top of a segment of the pile	[kPa]
k_{plug}	Stiffness of the sand plug	[kNm^{-2}]
k_{sys}	Stiffness of the berthing system	[kNm^{-1}]
k_x	Meridional buckling interaction parameter	[-]
k_{yi}	Deflection coefficient dependent on the loading pattern of the indirect soil load	[-]
k_{wall}	Stiffness of the pile wall	[kNm^{-2}]
l_g	Gauge length	[m]
m	Stress dependency power	[-]
p	Effective pressure: p_i+p_e	[kPa]
p_e	External pressure on the pile (positive when acting inward)	[kPa]
p_i	Internal pressure in the pile (positive outward)	[kPa]
p_{cr}	Theoretical value of the implosion pressure	[kNm^{-1}]
q	Distributed load	[kNm^{-1}]
q_c	Distributed load due to bending	[kNm^{-1}]
q_p	Back pressure from the plug	[kPa]
r	Internal diameter: $R_m - t/2$	[m]
r_{Rcr}	Elastic critical buckling resistance ratio	[-]
r_{Rpl}	Plastic reference resistance ratio	[-]
t	Pile wall thickness	[m]
y	Horizontal displacement	[m]
y_p	Horizontal displacement of the pile axis	[m]
y_{top}	Horizontal displacement of the dolphin at the fender height	[m]

y_w	Horizontal displacement of the pile wall	[m]
w	Radial pressure	[kPa]
z	Depth	[m]
z_{bed}	Depth of the bed level	[m]
z_{buckle}	Depth at which buckling is initiated	[m]
z_{Mmax}	Depth at which M_{max} occurs	[m]
z_{toe}	Depth of the toe of the dolphin	[m]

Greek letters

α	Angle of a retaining structure, from the vertical	[°]
β	Angle of the backslope behind a retaining structure	[°]
γ	Volumetric weight of soil	[kNm^{-3}]
γ_M	Partial factor for material strength	[-]
Δw_0	Depth of a dimple	[m]
δ	Angle of soil-wall friction	[°]
ε	Factor to determine the cross sectional class	[-]
ε	Strain	[-]
ε_{cr}	Critical strain	[-]
ε_{c}	Strain measured at the side of compression	[-]
ε_h	Strain in horizontal direction	[-]
ε_{t}	Strain measured at the side of tension	[-]
ε_{V}	Volumetric strain	[-]
θ	Circumferential coordinate around pile	[-]
κ	Curvature	[m^{-1}]
κ_a	Curvature of the pile wall due to ovalisation	[m^{-1}]
κ_{cr}	Critical curvature	[m^{-1}]
κ_e	Elastic curvature	[m^{-1}]
κ_y	Curvature of the pile due to its deformation	[m^{-1}]
λ	Characteristics of the system	[m^{-1}]
ν	Poisson's ratio	[-]
ρ	Radius of curvature	[m]
σ_θ	Circumferential buckling stress (positive when compression)	[kPa]
σ_x	Meridional buckling stress (positive when compression)	[kPa]
σ'_h	Effective horizontal soil stress	[kPa]
σ'_v	Effective vertical soil stress	[kPa]
$\tau_{x\theta}$	Buckling shear stress	[kPa]
φ'	Angle of internal friction	[°]
φ	Meridional slope: angle between axis of revolution and normal to the meridian of the shell	[°]
χ_θ	Circumferential buckling reduction factor	[-]
χ_τ	Shear buckling reduction factor	[-]
χ_x	Meridional buckling reduction factor	[-]

Subscripts

A	Position in x-y plane of pile cross section
B	Position in x-y plane of pile cross section
C	Position in x-y plane of pile cross section
E	Value of stress or displacement (arising from design actions)
R	Resistance
b	Value at the bottom of the beam element
d	Design value
k	Characteristic value
t	Value at the top of the beam element
max	Maximum value
min	Minimum value
nom	Nominal value

Contents

1 Introduction **1**
- 1.1 Dolphins . . . 1
- 1.2 Local Buckling . . . 4
- 1.3 Research objective . . . 12
- 1.4 Methodology and Outline . . . 13

2 Literature Study **15**
- 2.1 Loads . . . 15
  - 2.1.1 Bending . . . 15
  - 2.1.2 Lateral soil pressure . . . 17
- 2.2 Local buckling resistance . . . 21
- 2.3 Out-of-roundness . . . 24
  - 2.3.1 Initial out-of-roundness . . . 24
  - 2.3.2 Dimples . . . 25
  - 2.3.3 Ovalisation due to bending . . . 26
  - 2.3.4 Ovalisation due to soil pressure . . . 26
  - 2.3.5 Geometric non-linear effect . . . 29
  - 2.3.6 Rerounding effect . . . 29
- 2.4 Sand-filled piles . . . 29
- 2.5 Soil plug . . . 31
  - 2.5.1 Plug length . . . 33

3 Analytical model **35**
- 3.1 Beam Theory . . . 35
- 3.2 Pile Deformation . . . 36
- 3.3 Ovalisation . . . 38
  - 3.3.1 1^{st} part . . . 39
  - 3.3.2 2^{nd} part . . . 39
  - 3.3.3 3^{rd} part . . . 39
  - 3.3.4 Transitions . . . 40
  - 3.3.5 Continuous wall deformation . . . 40
- 3.4 Local Buckling . . . 41
- 3.5 Spring stiffness . . . 43
- 3.6 Discussion . . . 48
- 3.7 Key parameters . . . 48

4 Finite Element Model **51**
- 4.1 General . . . 51
- 4.2 Representative Pile . . . 51
- 4.3 Program . . . 52
- 4.4 Model . . . 54
  - 4.4.1 Part . . . 55
  - 4.4.2 Property . . . 58
  - 4.4.3 Interaction . . . 60
  - 4.4.4 Step . . . 60
  - 4.4.5 Boundary conditions . . . 62
  - 4.4.6 Load . . . 63
  - 4.4.7 Mesh . . . 63
- 4.5 Post-processing . . . 68
- 4.6 Imperfection . . . 70

5 Parametric Study **77**
5.1 Plug packing . . . 77
5.2 Plug level . . . 83
5.3 Slenderness ratio . . . 88
5.4 Soil packing . . . 92
5.5 Plug stiffness . . . 97
5.5.1 Plug packing . . . 100
5.5.2 Slenderness Ratio . . . 103

6 Validation with full scale tests **109**
6.1 Test set-up . . . 109
6.2 Evaluation methodology . . . 111
6.3 Test Results . . . 112
6.4 Pile 6 . . . 113
6.5 Validation - Pile 6 . . . 115
6.6 Piles 2, 3 and 8 . . . 119
6.6.1 Pile 2 . . . 119
6.6.2 Pile 3 . . . 121
6.6.3 Pile 8 . . . 122

7 Conclusions and recommendations **125**
7.1 Conclusions . . . 125
7.1.1 Analytical method . . . 125
7.1.2 FEM . . . 127
7.1.3 Full scale field tests . . . 134
7.2 Recommendations . . . 135
7.2.1 Analytical model . . . 135
7.2.2 FEM . . . 135
7.2.3 Field tests . . . 136

A Emperical equations for determination of K_0 **137**

B Influence of boundary conditions in a stress based calculation **139**

C Comparison stress based and strain based local buckling check **143**

D Finite Element Model Keywords Editing **145**

E Effect of plug packing on the ovalisation and plug stiffness **149**

Bibliography **153**

1 Introduction

In the Port of Rotterdam a lot of buoy berths and dolphin configurations will be replaced in the upcoming years [4]. Many new projects with flexible dolphins are therefore expected. The design of these dolphins has to be safe and the projects are preferably low-priced. In this chapter the flexible dolphin is introduced together with the limit states related to safety. Next, it is explained that the failure mode of local buckling plays an important role in order to make an economical design. Subsequently, the faced challenges are depicted and the objective of this research is declared. This introduction ends with the outline of the rest of this thesis, explaining how the main question is studied.

1.1. Dolphins

Breasting and mooring dolphins are relatively simple structures used for berthing or mooring a vessel. The structures have no functions other than slowing down vessels and keeping the vessel in position when it is moored. Typically, dolphins are placed in ports and next to jetties, bridges, locks or storm surge barriers.

Most of the 5,000 dolphins in the Port of Rotterdam are single thin-walled steel tubular vertical piles with external diameters D_e in the range of 1.2 m to 3.0 m. They are equipped with a proportionally small fender. Opposite to that, a comparatively large fender panel is assembled to the top of the pile. The largest part of the pile is either under water or embedded in the soil.

Figure 1.1: Typical flexible dolphin in the Port of Rotterdam. [5]

A breasting vessel hits the fender panel, resulting in deformation of the fender and a relatively large pile top displacement. Due to the displacement, the kinetic energy of the vessel will be dissipated. The setting with a breasting vessel in which a dolphin acts is schematised in figure 1.2. A moored vessel exerts a mooring force at the top of the dolphin. This lateral load F_v also causes deformation of the dolphin.

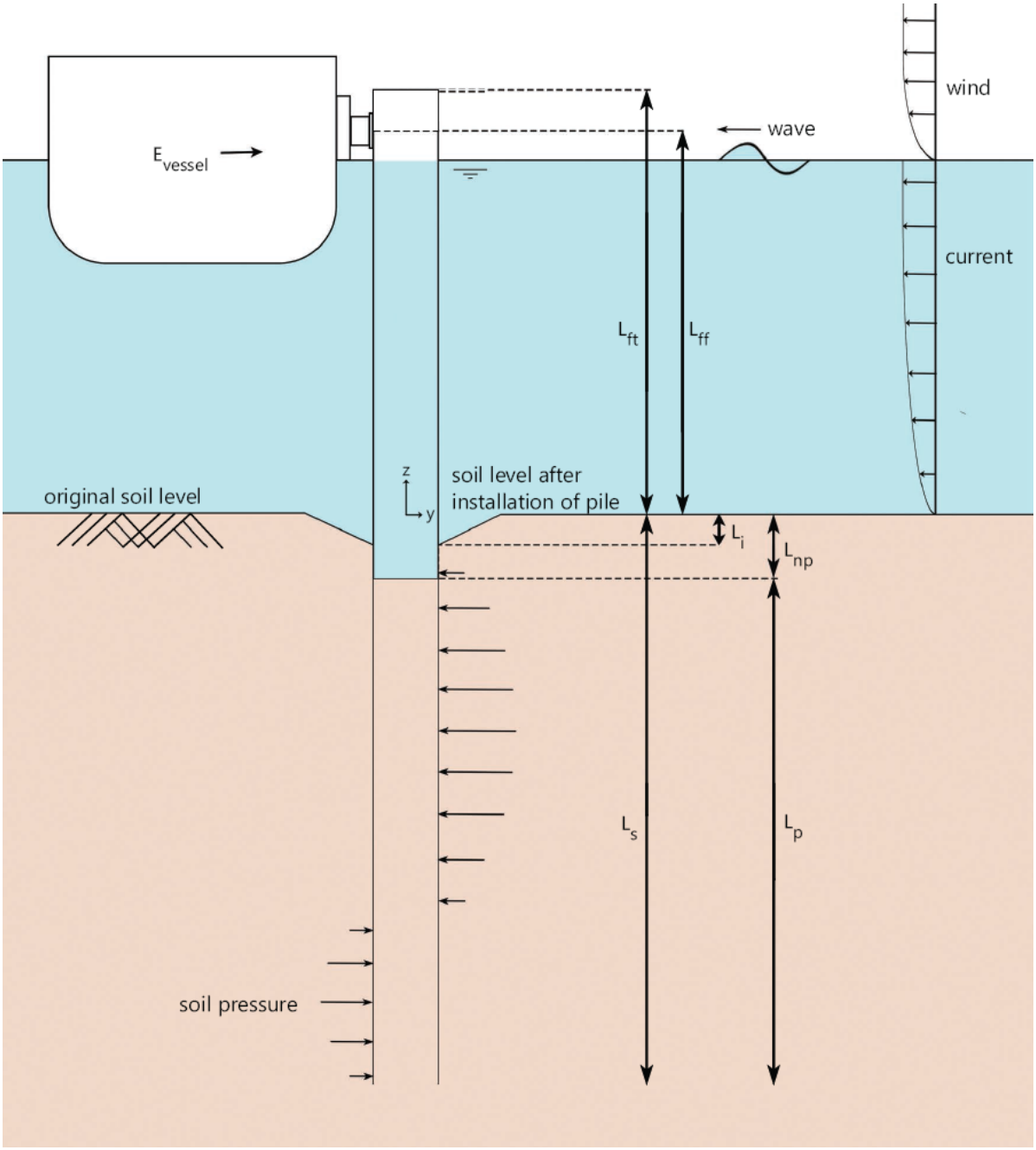

Figure 1.2: Dolphin setting scheme with a breasting vessel.

To stop a berthing vessel, the dolphin has to dissipate its berthing energy E_v. Part of the energy is dissipated by the deformation of the fender, E_fender. The remaining dissipated energy of the dolphin can be calculated as:

$$E_\mathrm{v} - E_\mathrm{fender} = \int_0^{y_f} F_\mathrm{v}(y)\mathrm{d}y \tag{1.1}$$

Where:

F_v	lateral load exerted by the vessel	[kN]
y_f	horizontal displacement of the dolphin at the fender height	[m]

The displacement of the pile triggers reaction forces in the soil to find equilibrium of horizontal forces. For the elastic loading model, the displacement y depends on the stiffness of the berthing system, k_{sys}, with the relation:

$$F_v = y_f \cdot k_{sys} \tag{1.2}$$

The piles are considered flexible dolphins because of the contribution of the pile deformation to the flexibility of the system. There are many methods to calculate the displacement y for a given lateral load F_v. Ruigrok [6] compared the most common methods and recommends to design laterally loaded piles with MSheet, P-y Curves or Plaxis. MSheet and P-y Curves are based on a spring model, whereas Plaxis is a Finite Element Method. In the spring model the soil is characterised by a series of springs (see figure 1.3). Winkler introduced this method with linear-elastic uncoupled springs in 1867 [7].

As gravity works on the structure, there is a normal force related to the steel weight. This is compensated by shaft resistance and point resistance. Besides the lateral load from the berthing or mooring vessel, also the water current, wind and possible waves exert lateral loads on the dolphin. These loads, as well as the gravitational load, are small compared to the lateral load of the vessel. Therefore, only the lateral load exerted by the vessel is considered in this thesis.

The total length of the pile is divided into an embedded part, L_s, and an unembedded (free) part, L_f. The first can again be divided into a part with soil in the pile, L_p, and a part without soil in the pile, L_{np}. Due to the friction between the shaft and the soil during installation of the dolphin, the surrounding soil level is lowered. This phenomenon is not studied in this thesis.

The setting can be modelled in the load diagram in figure 1.3. Typical displacement, bending moment, shear force and distributed load diagrams for laterally loaded dolphins are presented in figure 1.4.

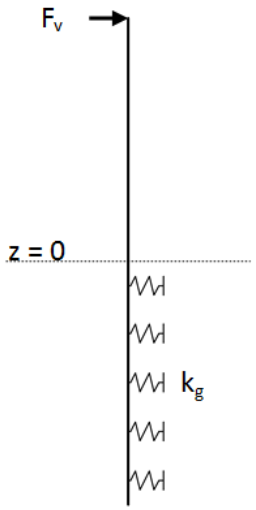

Figure 1.3: Load diagram.

During their intended service life, flexible dolphins need to be capable of absorbing many load repetitions, preferably with predictable and constant performance. Beyond the elastic range, this service requirement is no longer met and the serviceability limit state (SLS) is passed. Hence, the operational loading regime shall always be in the elastic range.

After an excessive loading the dolphin is no longer able to dissipate the amount of energy that it was designed for. In this thesis, this is seen as failure of the dolphin and referred to as the ultimate limit state (ULS).

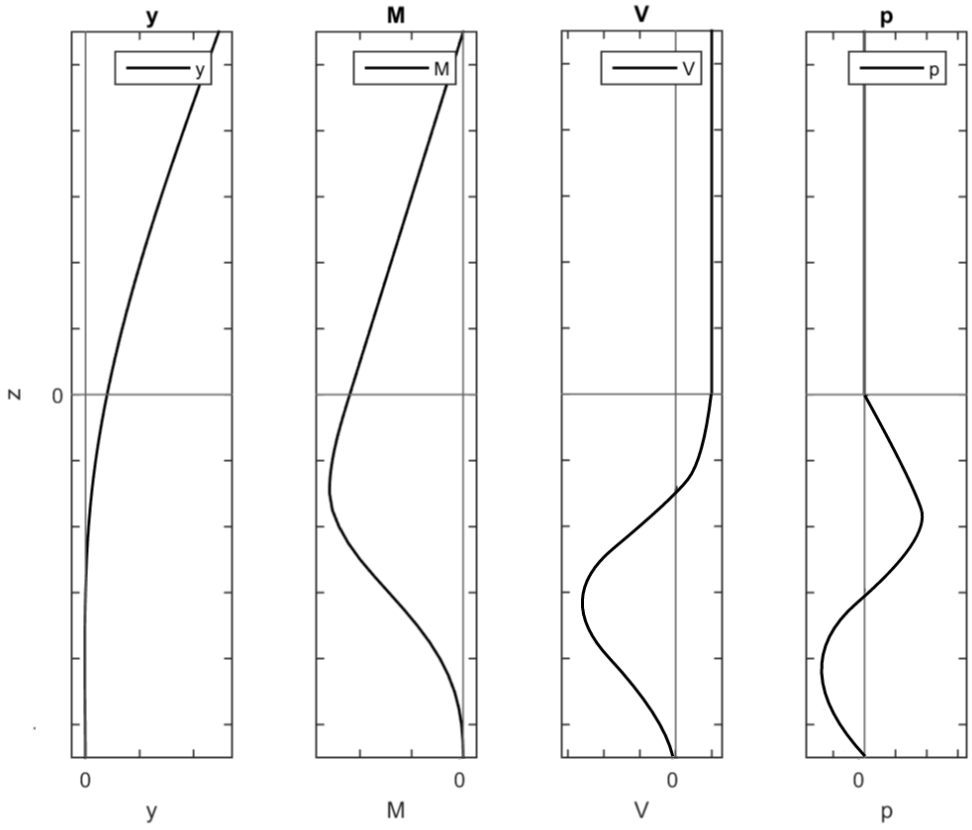

Figure 1.4: Typical displacement (y), bending moment (M), shear force (V) and distributed load (p) diagrams.

1.2. Local Buckling

Due to the fact that vessels have become bigger over the years (figure 1.5), breasting and mooring dolphins are to retain the associated increased berthing energy and larger mooring forces. One way to obtain dolphins capable of dissipating the increased energy, is to increase their diameter.

To keep their design economical, the tube walls remain thin. With an increased diameter, the cross-section becomes more slender. This makes the dolphin more susceptible to local buckling.

The loading on the dolphin results in axial compressive stresses in the wall. Buckling is the instability initialized by these compressive stresses. Instead of axial contraction, the compression stress causes bending. For small loads, the beam is compressed in the axial direction while keeping its linear shape (figure 1.6 b). Beyond a certain critical load however, it suddenly bends (figure 1.6 c). It buckles.

Steel members may experience two main modes of buckling failure: global buckling and local buckling. Global buckling is when the member as a whole bends under a compressive load. In local buckling, the strength of the cross-section is compromised by the buckling of a part of the cross-section, e.g. a web, a flange or a part of a thin shell.

Global buckling is not relevant as the compressive force on the dolphin is small. Local buckling on the other hand, can arise because of the compression in the wall caused by the bending moment.

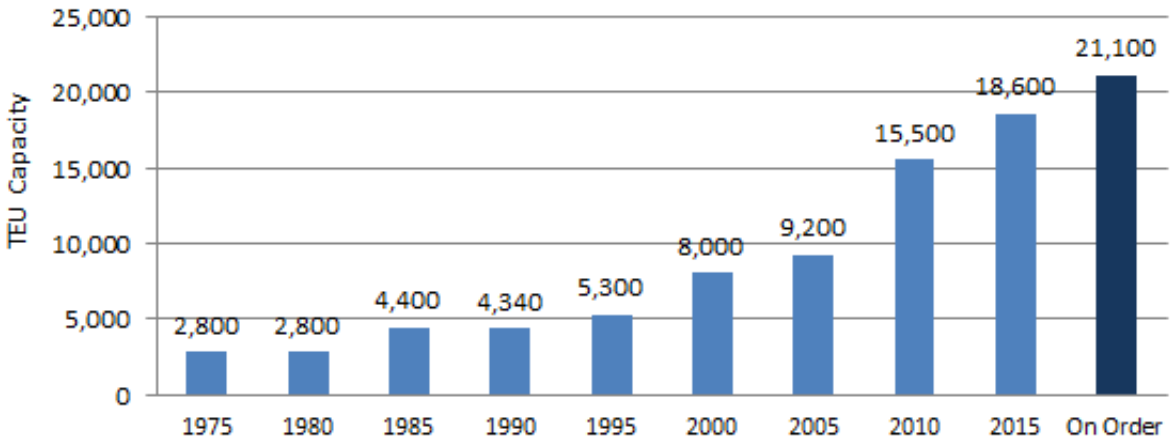

Figure 1.5: 40 years of container ship growth. [8]

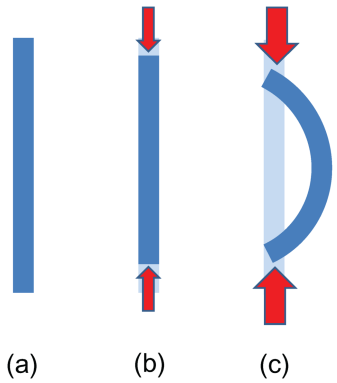

Figure 1.6: Schematic diagram of buckling of an elastic beam under axial compression: (a) pristine beam; (b) axial compression for a small load; (c) buckling observed beyond a critical load. [9]

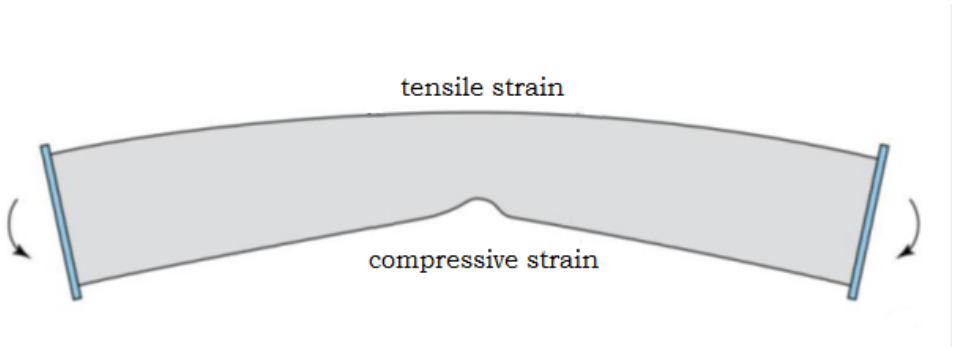

Figure 1.7: Buckling of the thin wall. Reprinted from [10].

Local buckling occurs due to the stresses within the zone of initial imperfections [11]. In a perfect geometry, with material isotropy and absence of residual stresses, local buckling cannot be initiated. However, experiments of Esslinger & Geier [12] show that even the utmost carefully produced circular cylinders, under as uniform axial compression as possible, are prone to local buckling.

The general rules on the design of steel structures in EN 1993-1-1 [13] classifies steel cross-sections in four different classes to make a distinction when local buckling is relevant and whether plastic or elastic calculations may be applied. In steel sections loaded in bending, different moment-rotation behaviour can be observed. The cross-sections are classified by the limit in rotation capacity as illustrated in figure 1.8. There are four classes for the different behaviour given:

1. Plastic cross-sections: They can develop their full plastic moment, M_p, and allow sufficient rotation at or above this moment. Redistribution of bending moments can take place in the structure until the complete failure mechanism is formed.

2. Compact cross-sections: They can develop their full-plastic moment, M_p. However, after the maximum the moment drops immediately, so that little moment-rotation capacity exists and redistribution of the bending moments is not possible.

3. Semi-compact cross-sections: They cannot develop a full-plastic moment, yet the capacity exceeds the yield moment capacity, M_y.

4. Slender cross-sections: They buckle before the capacity reaches the yield moment capacity, M_y. Yield in the extreme fibres cannot be attained in these cross-sections.

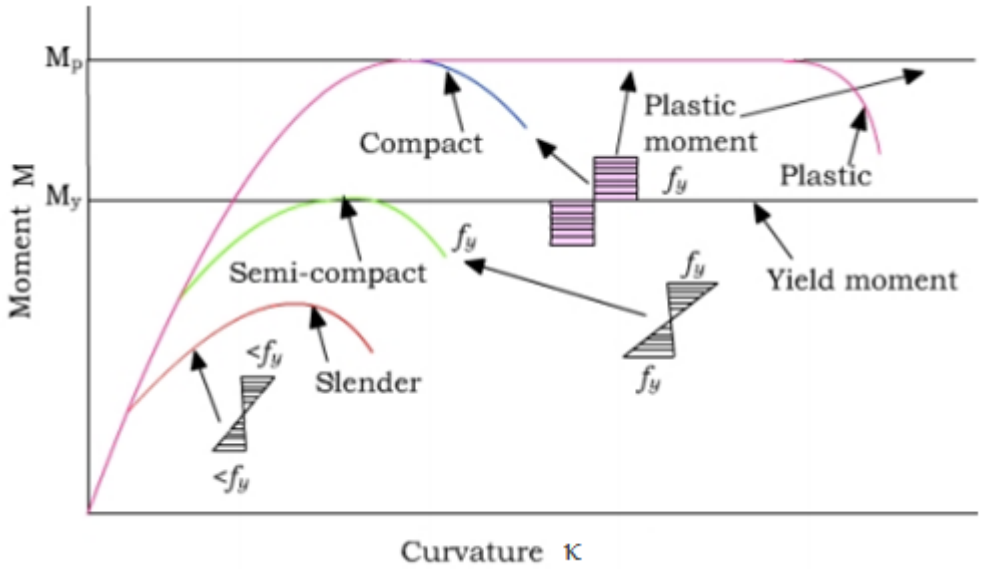

Figure 1.8: Cross-section classification based on moment-curvature characteristics. [14]

For the slender cross-sections in class 4, the maximum stress is determined by local buckling and the stress in the outer fibre is lower than the yield strength f_y. Dolphins with these slender cross-sections reach the ULS before they start yielding. Hence, their buckling behaviour is of interest to study.

Also other codes use this classification method. To which class a cross-section belongs is generally determined by the diameter-to-thickness ratio, D_e/t. In EN 1993-1-1 [13] this ratio is weighted with $\varepsilon^2 = f_{\text{ref}}/f_y$, in which f_{ref} is 235 MPa. Cross-sections with high values of $D_e/(t \cdot \varepsilon^2)$ are more susceptible to local buckling and are therefore in the lower classes. In table 1.1 the limit values of $D_e/(t \cdot \varepsilon^2)$ are given, in which the full plastic limit indicates the boundary between class 2 and class 3 and the first yield limit indicates the boundary between class 3 and class 4. It shows that there are significant differences in D_e/t limits recommended, especially in the American codes.

Local buckling will occur when the dolphin wall is loaded beyond its load capacity. Hence, in designing dolphins it is required to know what the load will be as well as the load that it is able to bear.

Table 1.1: Slenderness limits $D_e/(t \cdot \varepsilon^2)$ for the classification of cylindrical structural steel members.

Country	**Standard**	**Full Plastic Limit**	**First Yield Limit**
Australia	ASDR 87 164	77	129
Belgium	NBN B51-002 (08.88)	70	100
Canada	CAN/CSA S16.1-M89	77	97
Germany	DEN 18800 part 1	70	90
Japan	AIJ	80	100
Netherlands	NEN 6770	70	100
New Zealand	NZS 3404	54	180
United Kingdom	BS 5950	67	93
USA	AISC/LRFD	60	263
European Union	EN 1993-1-1	70	90

The compressive load on the dolphin wall is determined by the bending moment. At the location of the highest bending moment, the compressive load is the biggest. This makes it a risk location for local buckling to occur (figure 1.9).

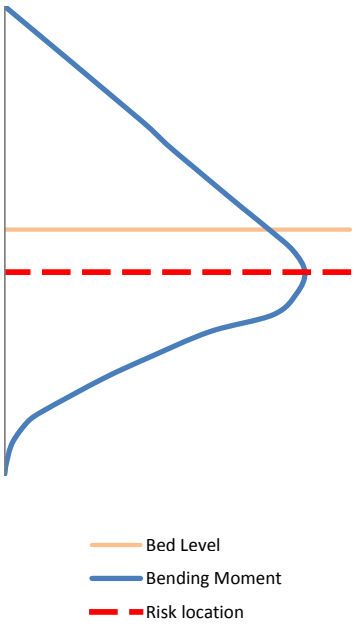

Figure 1.9: Risk location because of a high compressive load, caused by bending.

The resistance against local buckling is mainly determined by the slenderness ratio. Moreover, the load capacity is influenced by the presence of residual stresses, the stress-strain relation of the steel and effects of non-linear geometric behaviour [1]. The latter is affected by the forces it is exposed to. Loads working on the circular cross-section cause it to adopt an oval shape. In the y-direction the local diameter is decreased and also the dolphin wall is flatter (figure 1.10). Therefore, this ovalisation causes the cross-section to become more susceptible to local buckling.

The ovalisation is increased with a higher bending moment. Also a larger distributed load increases the ovalisation. The locations with the largest ovalisation, i.e. the locations with the largest loads, are risk locations. This is illustrated in figures 1.11 and 1.12.

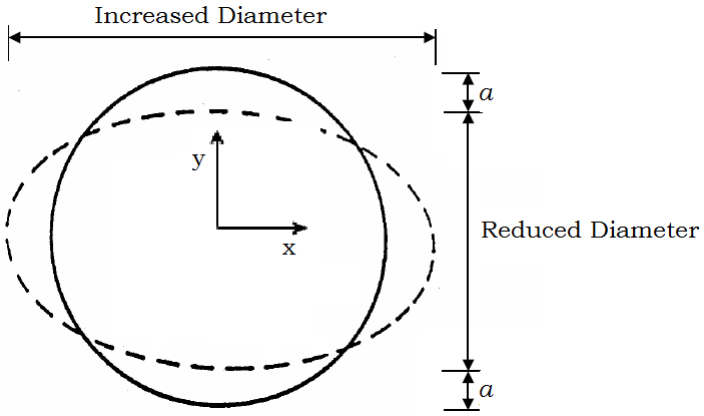

Figure 1.10: Ovalised cross-section.

The surrounding soil that exerts the distributed load on the dolphin also has a reducing effect on the ovalisation. In the x-direction the cross-section expands (figure 1.10). This triggers a local passive soil pressure as shown in figure 1.13b. The pressure provides resistance against the ovalisation, reducing the ovalisation (see figure 1.13c). Therefore from the surrounding soil also a positive effect on the local buckling resistance of the dolphin can be expected. Above the bed level this positive effect is not present. This makes the area around the bed level, with the transition from the area with surrounding soil to the area without soil, another risk location for local buckling as presented in figure 1.13.

An internal pressure from soil within the dolphin also has a reducing effect on the ovalisation [10, 15, 16]. Dolphins with a small diameter provide enough friction on the inside of the pile to push the soil down, resulting in a predominantly empty pile. Yet a bigger diameter means the soil plug reaches up to higher levels in the dolphin after installation [17]. Therefore the dolphin with increased diameter can be designed as a pile filled with sand up to a certain level. In reality the top of the sand-fill may be located 0.5 or 1 D_e under the bed level [18]. Due to the expected positive effect of a soil plug, the area around the plug level, with the transition from the area with soil plug to the area without soil plug, is again a risk location. This is illustrated in figure 1.14.

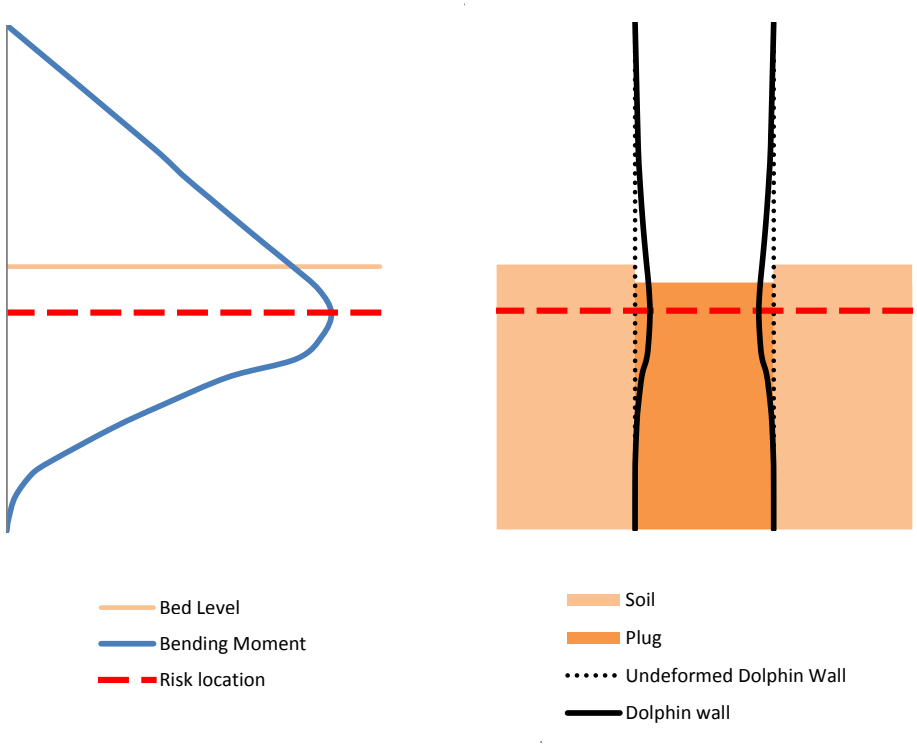

Figure 1.11: Risk location because of a reduced resistance, caused by ovalisation due to bending (not to scale).

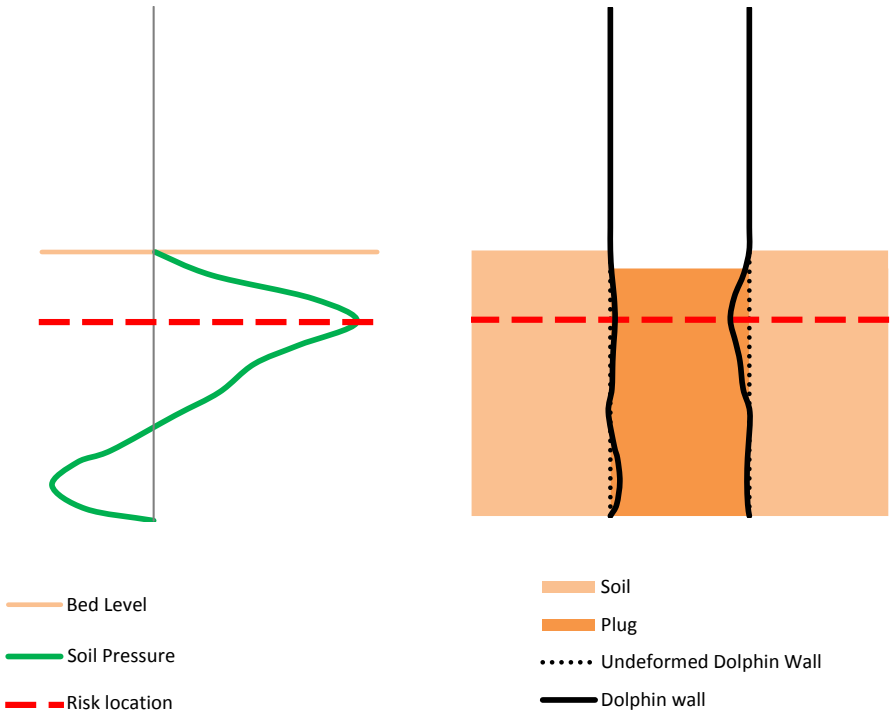

Figure 1.12: Risk location because of a reduced resistance, caused by ovalisation due to soil pressure (not to scale).

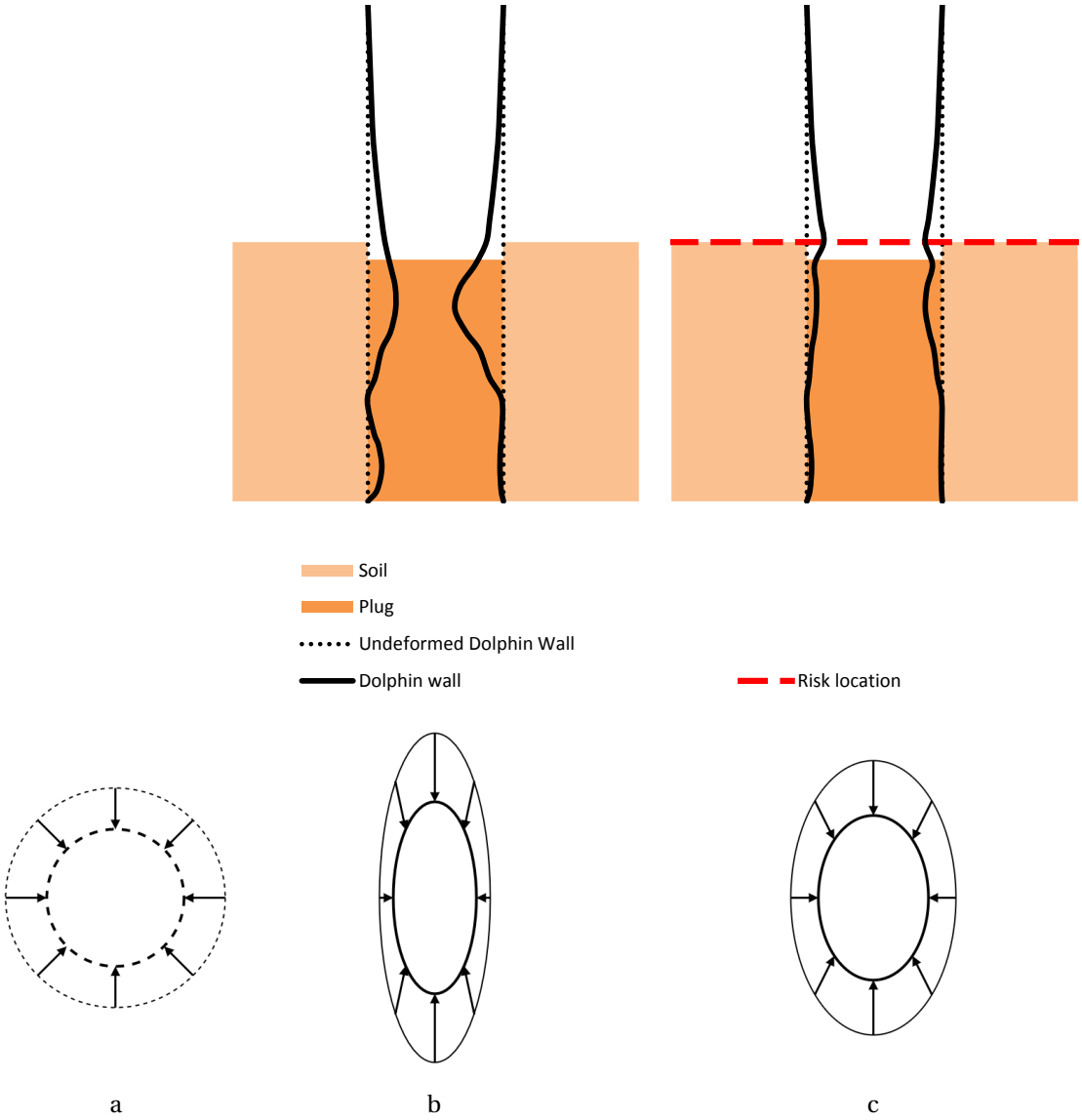

Figure 1.13: Risk location because of a reduced resistance, transposed to the bed level due to a rerounding effect of the surrounding soil (not to scale).

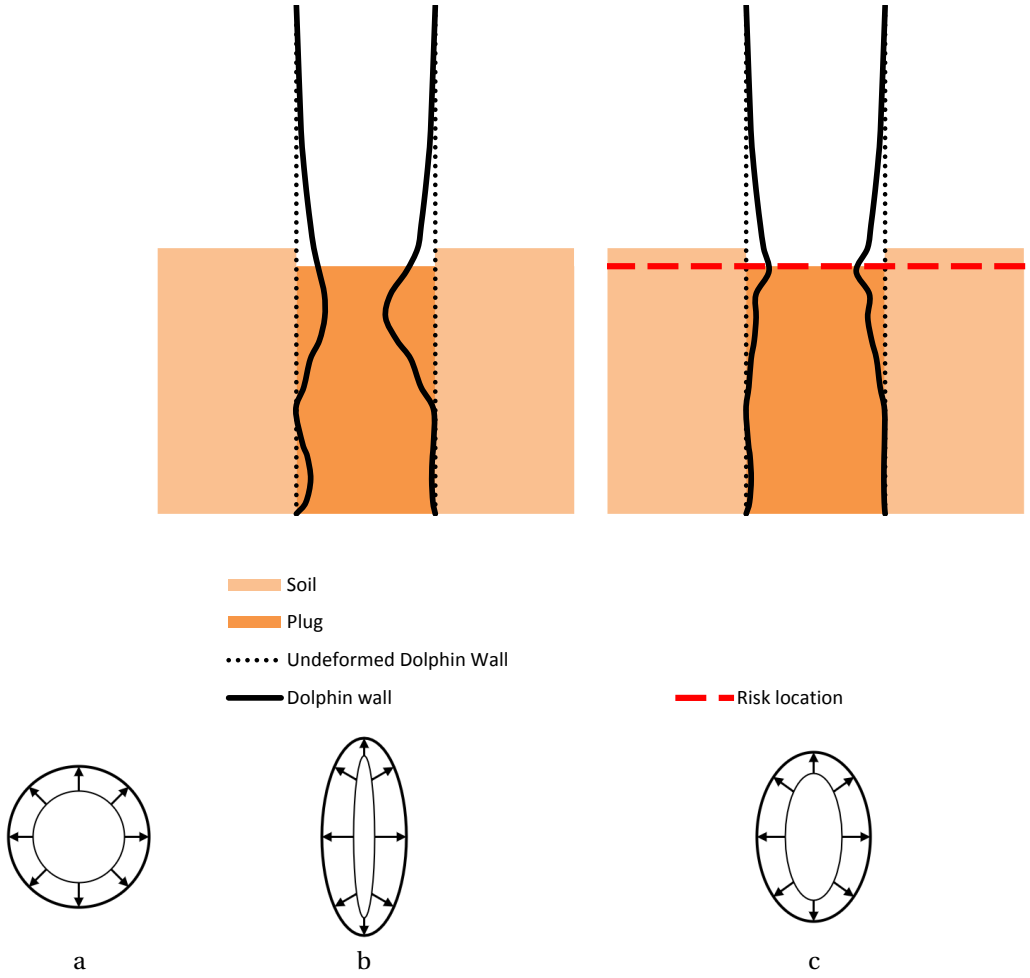

Figure 1.14: Risk location because of a reduced resistance, transposed to the plug level due to a rerounding effect of the plug (not to scale).

It is clear that there are four risk locations. These are the locations with the highest bending moment, the largest soil pressure, the bed level and the plug level. Local buckling is therefore expected in the area $5D_e$ below the bed level up to $2D_e$ above the bed level.

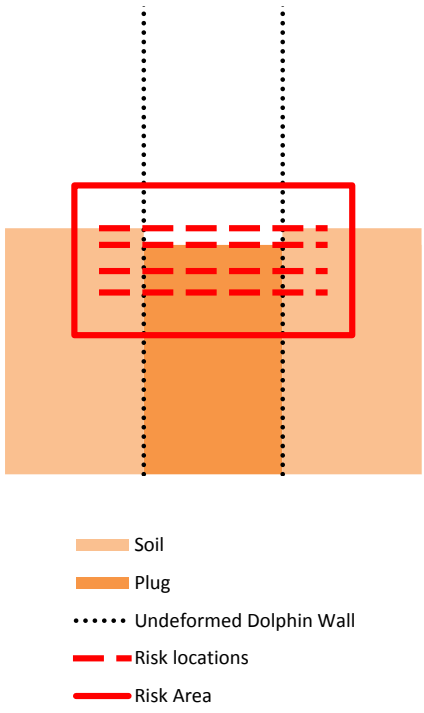

Figure 1.15: Risk area (not to scale).

1.3. Research objective

Even though for most hydraulic and geotechnical structures clear guidelines are available, those for flexible dolphins are still missing [18]. Consequently, whether a design is safe is usually subject of debate. The same applies to the procedure of determining loads caused by berthing ships, which is also not described in the Eurocodes.

Consulting engineers Royal HaskoningDHV and Witteveen+Bos set up a test programme to gain knowledge needed for optimal design of flexible dolphins. The research goals are to [19]:

a. Verify and quantify the effect of a bed slope on the stiffness and resistance of the system.

b. Measure the stiffness of the system when subjected to 'slow' dynamic loads.

c. Check whether a simple model of dynamic load and dynamic response shall be preferred over a traditional static model calculation.

d. Verify the stress level at which buckling occurs at the two risk locations: transition sand-filled vs empty and wall thickness transition.

e. Measure the effect of a full-length sand-fill on stiffness and on buckling risk.

This thesis origins from research question d. The focus will be on the transition between the sand-filled and the empty parts of the dolphin, in the risk area as described in paragraph 1.2.

The aim of this research is to provide understanding of the effects concerning local buckling and therewith to contribute to the discussion whether a dolphin design is safe. The new situation, in which the sand-fill is

present in the risk area, is assumed. The main research question focuses on the adaptations in the capacity calculations as a consequence of the addition of the plug. By this means, also for the situation without a plug as well, insight is gained in which aspects are of importance regarding the local buckling behaviour of dolphin piles. The main research question is:
Does the soil in dolphin piles contribute to the local buckling resistance and can this be used in the design of these piles?

1.4. Methodology and Outline

To be able to answer the main question, the research is divided in two linked parts (see figure 1.16).

First, a study of the available codes and general background is required. This provides an understanding of how a dolphin pile can be checked on local buckling with the existing knowledge. The available literature is studied in chapter 2.

In chapter 3 the knowledge is put together in an analytical model to determine whether local buckling of semi-filled piles can analytically be predicted. This shows how an engineer could test the design against local buckling with the previously acquired understandings. Uncertainties in designing a dolphin pile against local buckling are revealed. Moreover, with the knowledge from chapter 2 and 3 insight is gained in the parameters that affect local buckling in semi-filled piles.

In the second part, finite element method is used to study the influence of the identified key parameters on the local buckling behaviour. In chapter 4, a model is set up in a finite element programme. This programme has to be able to compute local buckling as well as the soil-structure interaction. In this thesis, Abaqus is used.

The actual study on the influence of the key parameters is performed in chapter 5. The analyses clarify how the inner soil affects the local buckling behaviour. From the results of the analyses it is also studied how an engineer can cope with uncertainties encountered in chapter 3.

The Port of Rotterdam facilitated a full scale field test to study the previously listed research questions of Royal HaskoningDHV and Witteveen+Bos. The piles were loaded until structural failure. These tests are used in chapter 6 to validate the finite element model. The field tests show how the insights from the research with the finite element model are noticed in reality.

From both parts conclusions are drawn that form an advice on how an engineer can make use of the key parameters in order to design a safe and economical dolphin. This advice, other conclusions that can be drawn and recommendations for further research are presented in chapter 7.

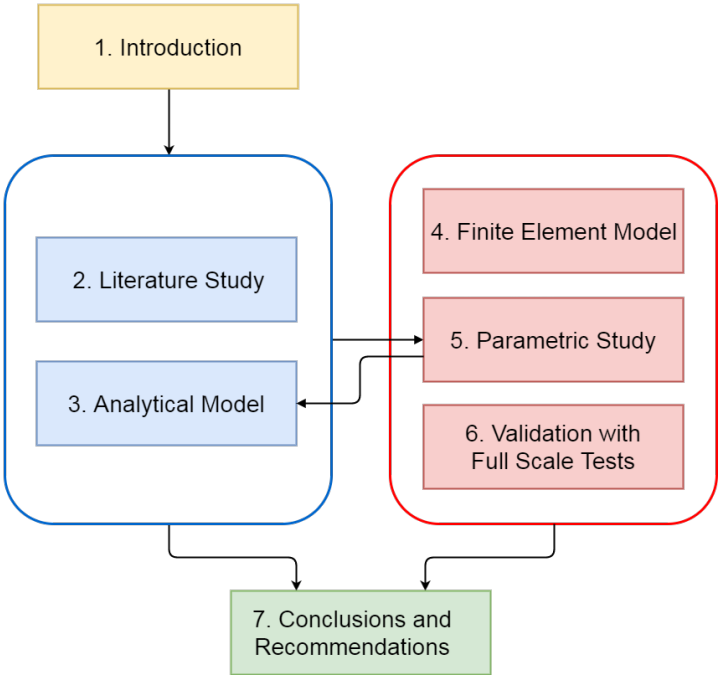

Figure 1.16: Outline.

2

Literature Study

In this chapter, literature related to local buckling of dolphin piles is studied. First, attention is paid to the loads on the system. Then, the resistance against local buckling is described. Next, the out-of-roundness is clarified. Furthermore, the relevance of sand in the dolphin is discussed. This chapter is closed with a background study on the existence of a soil plug and the soil plug level.

2.1. Loads

The dolphin is deformed by the applied force F_v. This force causes the dolphin pile to displace and to bend. The bending results in compression of the pile wall. A compressive load might cause local buckling. The displacement of the pile triggers reaction forces in the soil, to find equilibrium of the horizontal forces.

Also the lateral soil pressure and the bending cause the dolphin to ovalise. The oval shaped shell is more susceptible to local buckling.

2.1.1. Bending

Bending of a pile causes strains in the outer fibres. The fibres on the neutral surface (indicated by the dashed line in figure 2.1) do not change in length. Due to the bending, the fibres in the upper part of the beam are in tension, whereas those in the lower part are in compression.
The planes of cross-sections mn and pq of the deformed pile intersect in a line through the centre of curvature O'. The angle between the two planes is denoted by $\mathrm{d}\varphi$ and the distance between O' and the neutral axis is the radius of curvature ρ.

The initial distance $\mathrm{d}s$ between the two planes remains unchanged at the neutral surface. The length $\mathrm{d}s$ of a segment on the neutral axis can be related to the radius of curvature ρ:

$$\partial s = \rho \partial \varphi \tag{2.1}$$

From which follows:

$$\kappa = \frac{1}{\rho} = \frac{\partial \varphi}{\partial s} \tag{2.2}$$

The angle of rotation φ is related to the slope of the deflection curve by means of:

$$\frac{\partial y}{\partial z} = \tan\varphi \tag{2.3}$$

Here it is assumed $\partial s = \partial z$, since ∂z is infinitesimal. With very small rotations, $\tan\varphi \approx \varphi$. With equations 2.2 and 2.3 it is found:

$$\kappa = \frac{\partial^2 y}{\partial z^2} \tag{2.4}$$

A segment ef at distance y from the neutral axis is strained and its length is equal to:

$$\partial s_{ef} = (\rho - y)\partial \varphi \tag{2.5}$$

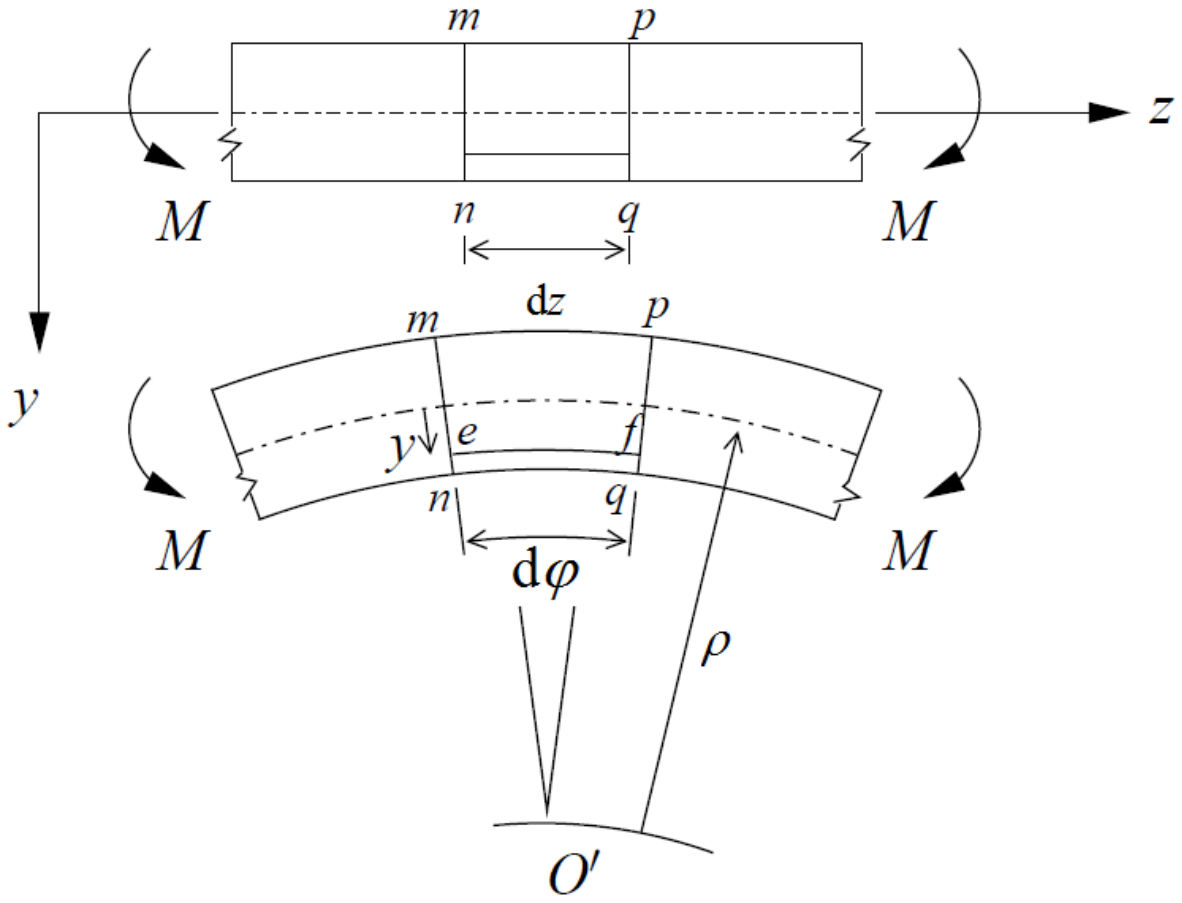

Figure 2.1: Strains from bending. [35]

Hence, the strain in the segment ef after bending is equal to:

$$\varepsilon_{zz}^{ef} = \frac{\partial s_{ef} - \partial z}{\partial z} = -\kappa y \tag{2.6}$$

The pile wall has a distance R_m from the neutral axis. Together with equation 2.4 the compressive strain in the pile wall ε_{zz} is found:

$$\varepsilon_{zz} = -\frac{\partial^2 y}{\partial z^2} r \tag{2.7}$$

Due to the strains, loads exist towards the neutral axis of the pile, causing the pile to ovalise. In HERON 31(4) [1], Gresnigt derives this load on the wall. The starting points used are presented in figure 2.2.
The uniformly distributed load due to bending q_c shown in figure 2.3 is equal to:

$$q_c = \frac{R_m t E_s}{\rho^2} = R_m t E_s \kappa^2 \tag{2.8}$$

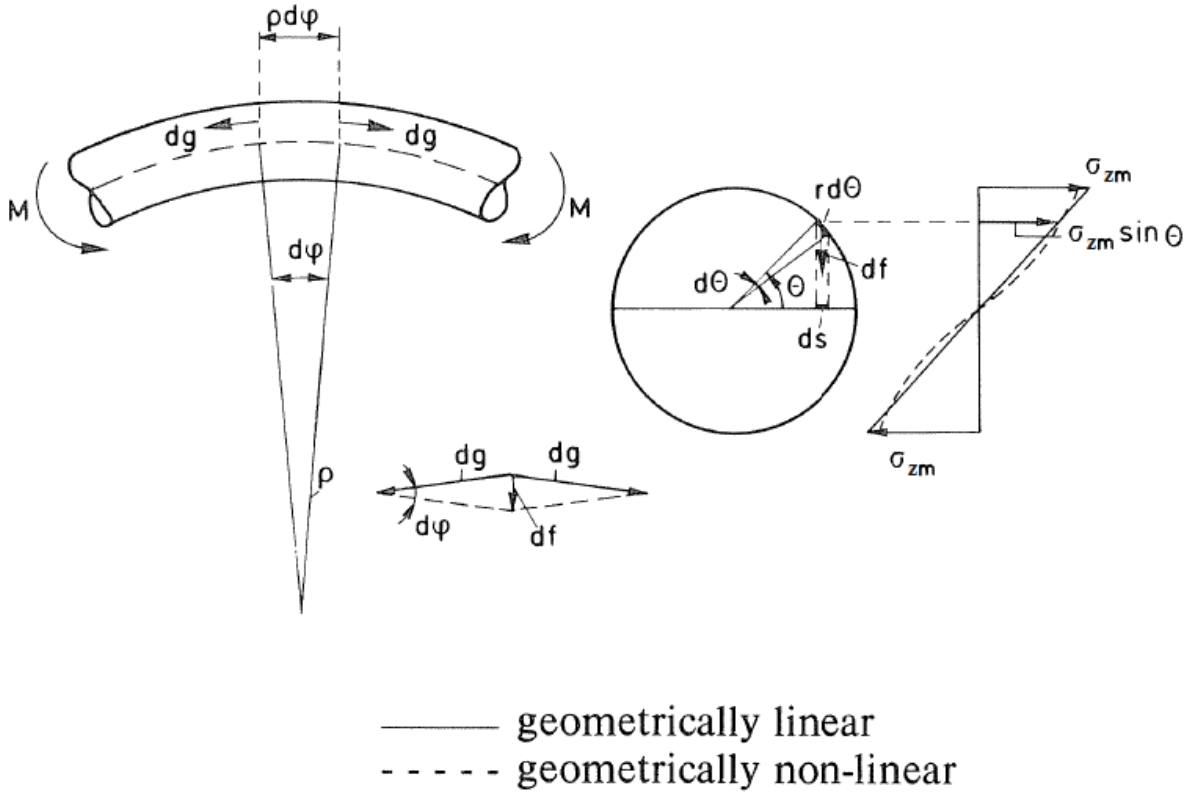

Figure 2.2: Calculation of ovalisation forces due to bending. Reprinted from [1].

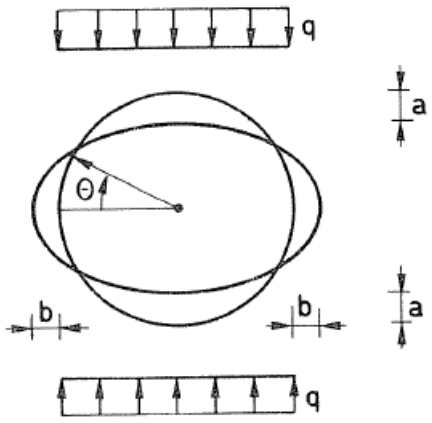

Figure 2.3: Equivalent load q_c due to the ovalisation forces. Reprinted from [1].

2.1.2. Lateral soil pressure

The lateral load triggers reaction forces in the soil. For soils, vertical stresses can be easily determined, while horizontal stresses are much more difficult to establish. Lateral soil pressure is determined by the ratio of the horizontal stress to the vertical by means of the lateral stress coefficient K.

$$\sigma'_h = K \cdot \sigma'_v \tag{2.9}$$

Where:

σ'_h	effective horizontal soil stress	[kPa]
σ'_v	effective vertical soil stress	[kPa]
K	lateral stress coefficient	[-]

The value of the pressure coefficient depends on the relative density, stress history, overconsolidation ratio (OCR), plasticity index, and other soil properties. An overconsolidated soil is a normal soil which was subjected to a greater load in the past.

Under the assumption that the soil is an elastic material, it can be found that:

$$K = \frac{\nu}{1-\nu} \tag{2.10}$$

$$\sigma'_h = \frac{\nu}{1-\nu}\sigma'_v - \frac{E_g}{1-\nu}\varepsilon_h \tag{2.11}$$

Where:

E_g	Young's modulus of elasticity of the soil	[kPa]
ε_h	strain in horizontal direction	[-]

If there is no horizontal strain, the lateral stress coefficient is denoted as the neutral earth pressure coefficient K_0. With a positive horizontal strain, with lateral extension of the soil, a smaller value of the lateral stress coefficient is found. In this case we speak of active soil pressure and the related coefficient is K_a. Passive soil pressure results in a negative strain and a higher coefficient, K_p.

Neutral soil pressure

In an elastic material the neutral earth pressure coefficient K_0 would be $\nu/(1-\nu)$. However this is not a very good estimate, as soil is not an elastic material and the history of the development of stresses in the soil may be more important than the condition of zero lateral deformation. K_0 is therefore determined by field or laboratory tests. The coefficient of earth pressure at rest decreases in the reloading stage, especially in loose sands. However in very dense sands K_0 values remain almost constant in the loading and reloading stages. Some of the most widely used relationships for non-consolidated soils are provided in appendix A. Widely accepted formulas to determine the neutral earth pressure coefficient for over consolidated soils K_0^{OC} are also given in appendix A. They can be found for known values of the neutral earth pressure coefficient for nonconsolidated soils K_0^{NC} and the OCR. In this thesis the equation of Jaky [27] is used:

$$K_0 = 1 - \sin\varphi' \tag{2.12}$$

Active and passive soil pressure

With active soil pressure, the soil actively applies a pressure on a structure, pushing it away. With passive soil pressure, the soil is compressed by the displacement of the structure requiring a reaction from the soil. The latter results in much higher pressures, one of the characteristics of soil material. This also causes the non-uniform stress as was shown in figure 2.12. Rankine [28] and Coulomb [29] produced two widely used theories for active and passive lateral soil pressure.

The Rankine Theory assumes:

- There is no adhesion or friction between the wall and soil;
- Lateral pressure is limited to vertical walls;
- Failure (in the backfill) occurs as a sliding wedge along an assumed failure plane, defined by the angle of internal friction φ';
- Lateral pressure varies linearly with depth and the resultant pressure is located one-third of the height above the base of the wall;

- The resultant force is parallel to the backfill surface.

The Rankine active and passive lateral earth pressure coefficients, for a horizontal backfill surface are given by:

$$K_a = \frac{1-\sin(\varphi')}{1+\sin(\varphi')} \tag{2.13}$$

$$K_p = \frac{1+\sin(\varphi')}{1-\sin(\varphi')} \tag{2.14}$$

The Coulomb theory is similar to Rankine, except that:

- There is friction between the wall and soil and takes this into account by using a soil-wall friction angle of δ (δ is assumed to be between $\frac{\varphi'}{2}$ to $\frac{2\varphi'}{3}$, $\delta = \frac{2\varphi'}{3}$ is commonly used);
- Lateral pressure is not limited to vertical walls;
- The resultant force is not necessarily parallel to the backfill surface, because of the soil-wall friction value δ.

The Coulomb active and passive lateral earth pressure coefficients are given by:

$$K_a = \frac{\cos^2(\varphi'-\alpha)}{\cos^2(\alpha)\cos(\delta+\alpha)\left(1+\sqrt{\frac{\sin(\delta+\varphi')\sin(\varphi'-\beta)}{\cos(\delta+\alpha)\cos(\beta-\alpha)}}\right)^2} \tag{2.15}$$

$$K_p = \frac{\cos^2(\varphi'+\alpha)}{\cos^2(\alpha)\cos(\delta-\alpha)\left(1-\sqrt{\frac{\sin(\delta+\varphi')\sin(\varphi'+\beta)}{\cos(\delta-\alpha)\cos(\beta-\alpha)}}\right)^2} \tag{2.16}$$

Where:

α	angle of a retaining structure, from the vertical	[°]
β	angle of the backslope behind a retaining structure	[°]

For a vertical pile ($\alpha = 0$) and horizontal backfill ($\beta = 0$) eqs. 2.15 and 2.16 reduce to:

$$K_a = \frac{\cos^2(\varphi')}{\cos(\delta)\left(1+\sqrt{\frac{\sin(\delta+\varphi')\sin(\varphi')}{\cos(\delta)}}\right)^2} \tag{2.17}$$

$$K_p = \frac{\cos^2(\varphi')}{\cos(\delta)\left(1-\sqrt{\frac{\sin(\delta+\varphi')\sin(\varphi')}{\cos(\delta)}}\right)^2} \tag{2.18}$$

Assuming a homogeneous soil, the effective active and passive lateral soil pressure as found with the Mohr-Coulomb criterion are:

$$\sigma'_h = K_a \gamma z - 2c\sqrt{K_a} \tag{2.19}$$

$$\sigma'_h = K_p \gamma z + 2c\sqrt{K_p} \tag{2.20}$$

Where:

γ	volumetric weight of soil	[kN/m^3]
z	depth	[m]
c	cohesion	[kPa]

The total horizontal pressures are found by adding the effective soil pressure and the water pressure.

It should be noted that the coefficients are the extreme values. The true lateral earth pressure coefficient is between these values. As the range between the values is large, the lateral pressure is yet undetermined to a high degree. Furthermore both theories are focused on a continuous wall and the pressures are per metre length. In case of a pile the soil beside it also effects the total soil pressure (see also figures 2.4 and 2.5). These 3D effects have to be taken into account. There are methods to approximate the true lateral soil pressure, for example with p-y curves [6].

P-y curves

The function of the soil pressure is a nonlinear function depending among others on the soil depth. For small deformations, the soil reacts stiffer than for larger deformations. The maximum soil resistance and stiffness increase nonlinearly with depth. McClelland and Focht [30] as well as Reese and Matlock [31] suggest the basic principles in the p-y curve method. The p-y curve presents the relation between the soil pressure Q_i and the deformation y at a specific depth.

Tests on fully instrumented test piles in sand installed at Mustang Island were carried out in 1966 and reported by Cox et al. in 1974 [32]. A semi-empirical p-y curve expression for sand is derived based on the Mustang Island test [33]. For different soil types, different p-y curves exist. The API RP2A [34] provides recommendations which curves to use.

The p-y curves are supported by the theoretical ultimate lateral resistance. The total ultimate lateral resistance, F_{pt}, is equal to the passive force, F_p, minus the active force, F_a, on the pile. At shallow depths a wedge will form in front of the pile assuming that the Mohr-Coulomb failure theory is valid. Reese et al. [33] uses the wedge shown in figure 2.4 to analytically calculate the passive ultimate resistance at shallow depths. By using this failure mode a smooth pile is assumed and therefore no tangential forces occur at the pile surface. The active force is also computed from Rankine's failure mode, using the minimum coefficient of active earth pressure.

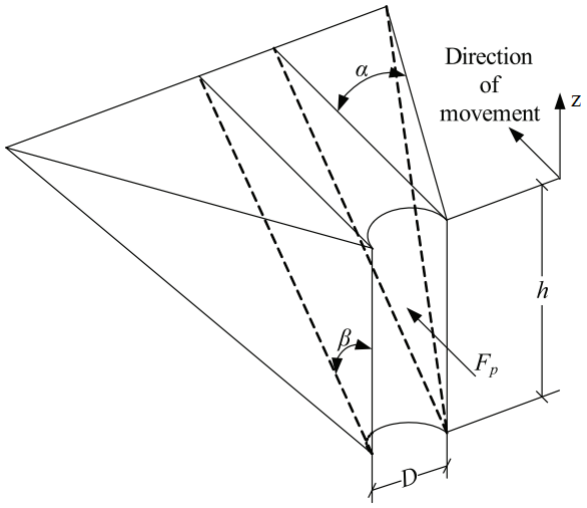

Figure 2.4: Failure mode for shallow depths. Reprinted from [33].

At deep depths the sand will, in contrast to shallow depths, flow around the pile and a statical failure mode as sketched in figure 2.5 is used to calculate the ultimate resistance.
The values found with the p-y curves consider a fully mobilised passive lateral soil pressure. Therefore they still result in upper boundaries for the real soil pressure.

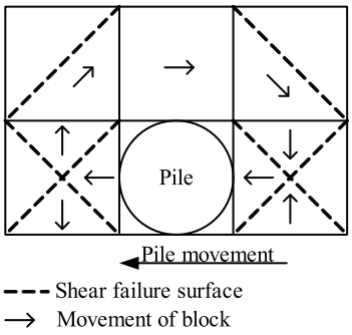

Figure 2.5: Failure mode for deep depths. [33]

2.2. Local buckling resistance

From the previous chapter it is known what loads are obtained in the dolphin system. To determine whether the loads might cause local buckling, the resistance to this phenomenon is studied. Eurocodes 1993-1-6 [21] and 1993-4-3 [2] provide two methods: a stress based method and a strain based method. To understand what parameters have an effect on the local buckling resistance, both methods are studied.

Stress based

Eurocodes 1993-1-6 [21] describes the stress based method. The verification of the buckling strength is a check whether the design value of the stress arose from the loading is below the design buckling stress resistance. If more than one of the three buckling-relevant membrane stress components are present, also the combined membrane stress state should be checked.

$$\begin{aligned} \sigma_{x,Ed} &\leq \sigma_{x,Rd} \\ \sigma_{\theta,Ed} &\leq \sigma_{\theta,Rd} \\ \tau_{x\theta,Ed} &\leq \tau_{x\theta,Rd} \end{aligned} \tag{2.21}$$

$$\left(\frac{\sigma_{x,Ed}}{\sigma_{x,Rd}}\right)^{k_x} - k_i\left(\frac{\sigma_{x,Ed}}{\sigma_{x,Rd}}\right)\left(\frac{\sigma_{\theta,Ed}}{\sigma_{\theta,Rd}}\right) + \left(\frac{\sigma_{\theta,Ed}}{\sigma_{\theta,Rd}}\right)^{k_\theta} + \left(\frac{\tau_{x\theta,Ed}}{\tau_{x\theta,Rd}}\right)^{k_\tau} \leq 1 \tag{2.22}$$

Where:

σ_x	meridional buckling stress (positive when compression)	[kPa]
σ_θ	circumferential buckling stress (positive when compression)	[kPa]
$\tau_{x\theta}$	buckling shear stress	[kPa]
k_x, k_θ, k_τ, k_i	buckling interaction parameters	[-]

In the American AISC [20], the critical stress for slender circular hollow sections f_{cr} is given by:

$$f_{\text{cr}} = 0.33 \cdot \frac{E_s}{D_e/t} \tag{2.23}$$

In which the Young's modulus of elasticity of steel E_s is 200 GPa.
According to EN 1993-1-6 [21], the characteristic buckling stresses are obtained by multiplying the characteristic yield strength $f_{y,\text{k}}$ by the buckling reduction factors χ:

$$\begin{aligned} \sigma_{x,\text{Rk}} &= \chi_x f_{y,\text{k}} \\ \sigma_{\theta,\text{Rk}} &= \chi_\theta f_{y,\text{k}} \\ \tau_{x\theta,\text{Rk}} &= \chi_\tau f_{y,\text{k}}/\sqrt{3} \end{aligned} \tag{2.24}$$

Dividing the characteristic values by the partial safety factor γ_M, results in the design values.

χ is the ratio of the design buckling capacity $f_{b,\mathrm{Rd}}$ to the plastic capacity $f_{y,\mathrm{d}}$.

$$\chi = f_{b,\mathrm{Rd}} / f_{y,\mathrm{d}} \tag{2.25}$$

For shells with clamped or pinned boundary conditions at both edges, the buckling reduction factors χ_x, χ_θ and χ_τ can be determined with expressions given in EN 1993-1-6 sections 8.5 and Annex D [21]. In this case however, there are free edges. Therefore there are no appropriate expressions given. Nevertheless, as the piles in this case are longer than twenty times their diameter, the boundary conditions do not influence the outcome of the unity checks. This is shown in appendix B. Therefore the expressions can still be used.

Also mentioned in EN 1993-1-6 [21] is another possibility to determine the elastic critical buckling stresses. They may be extracted from a numerical linear elastic bifurcation analysis (LBA) of the shell. This analysis should determine the elastic critical buckling resistance ratio r_{Rcr}. The critical buckling resistance is the smallest bifurcation or limit load determined assuming the idealised conditions of elastic material behaviour, perfect geometry, perfect load application, perfect support, material isotropy and absence of residual stresses. Therefore the elastic critical buckling resistance ratio r_{Rcr} is the lowest bifurcation load factor. See figure 2.6.

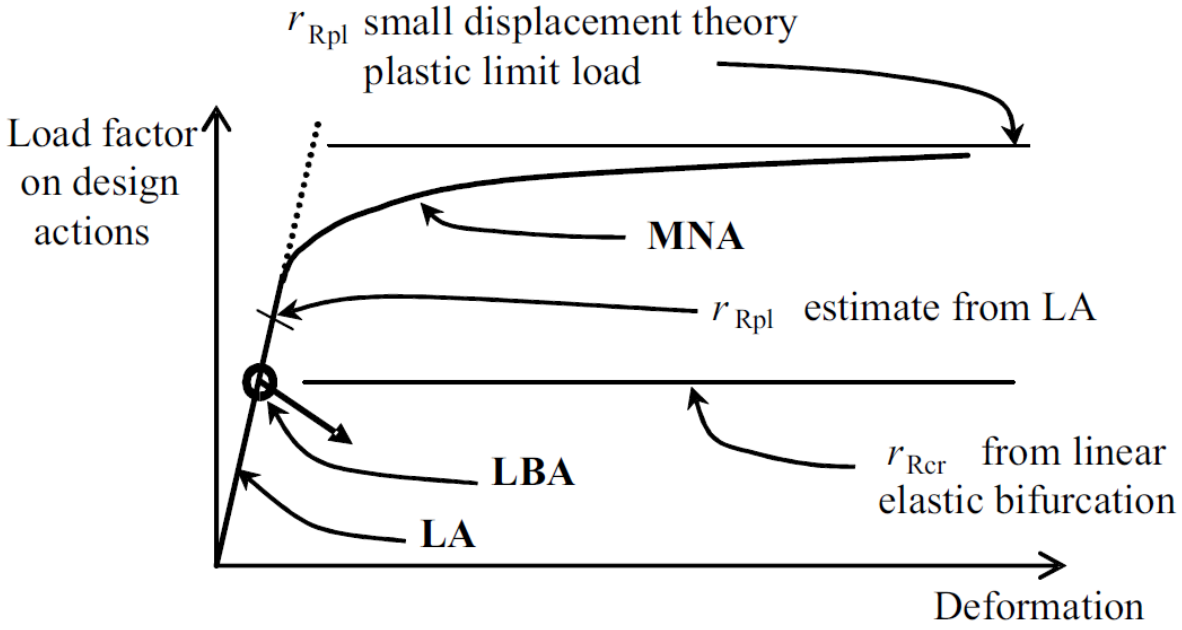

Figure 2.6: Definition of plastic reference resistance ratio r_{Rpl} and critical buckling resistance ratio r_{Rcr} derived from global MNA and LBA analyses. [21]

Strain based

Eurocode 1993-4-3 [2] describes a method based on the critical strain. This method is proposed by Gresnigt for buried steel pipelines [1]. In many projects and codes the strain based method is used, which may result in more economical designs. The comparison between the two methods is made in Appendix C.

Other than the stress based method, in the strain based method it has to be verified whether the strain is below its critical value, instead of the stress. The strain based method is described in EN 1993-4-3[2], which provides principles and application rules for the structural design of cylindrical steel pipelines for the transport of liquids or gases or mixtures of these two at ambient temperatures.

In the EN 1993-4-3 [2] the compressive strain is obtained from Gresnigt [1].

$$\begin{aligned} \varepsilon_{\mathrm{cr}} &= 0.25\frac{t}{R_o} - 0.0025 + 3000\left(\frac{pR_o}{E_s t}\right)^2 \frac{|p|}{p} \quad \text{for } \frac{r_o}{t} \leq 60 \\ &= 0.10\frac{t}{R_o} + 3000\left(\frac{pR_o}{E_s t}\right)^2 \frac{|p|}{p} \quad \text{for } \frac{R_o}{t} \geq 60 \end{aligned} \tag{2.26}$$

Where:

R_o	local radius of curvature of an ovalised cross-section (figure 2.7)	[m]
p	effective pressure, the difference in pressure between inside (p_i) and outside of the pile (p_e)	[kPa]
E_s	Young's modulus of elasticity of steel	[kPa]

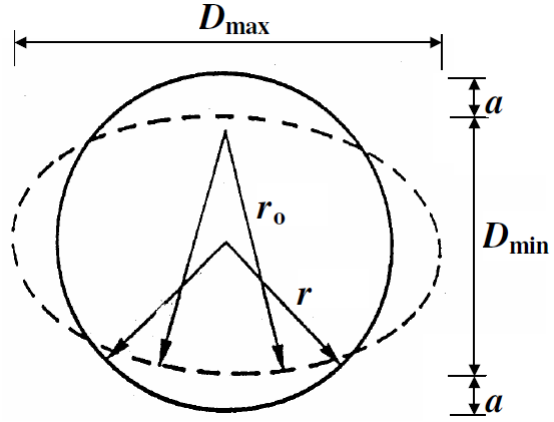

Figure 2.7: Radius R_o in an ovalised cross-section. [2]

In two reports of TNO [22][23] the critical strain from Gresnigt [1] is compared to other formulas with test results. For this comparison it was assumed there was no pressure and the Gresnigt criterium was rewritten as:

$$\begin{aligned} \varepsilon_{\text{cr}} &= 0.5 \cdot \left(\frac{t}{D_e - t} \right) - 0.0025 \quad \text{for } \frac{D_e - t}{t} \leq 120 \\ &= 0.2 \cdot \left(\frac{t}{D_e - t} \right) \quad \text{for } \frac{D_e - t}{t} \geq 120 \end{aligned} \tag{2.27}$$

The results from [22] are applicable to D_e/t ratios between 15 and 50, far below the ratios of interest in this thesis. Nevertheless, the report recommends the expression for the critical strain of Murphey Langner, compared to which Gresnigt [1] gives only slightly more conservative results (see table 2.1).

Table 2.1: Critical strain formulas compared in TNO-report 96-CON-R0500 [22].

Source	**Critical strain formula**
BS8010	$\varepsilon_{\text{cr}} = 15 \cdot \left(\frac{t}{D_e} \right)^2$
Gresnigt	$\varepsilon_{\text{cr}} = 0.5 \cdot \left(\frac{t}{D_e - t} \right) - 0.0025$
Igland	$\varepsilon_{\text{cr}} = 0.005 + 13 \cdot \left(\frac{t}{D_e} \right)^2$
Murphey & Langner	$\varepsilon_{\text{cr}} = 0.5 \cdot \left(\frac{t}{D_e - t} \right)$
PRCI	$\varepsilon_{\text{cr}} = \frac{t}{D_e} - 0.01$

Gresnigt [23] compares his expression with the expressions of Batterman and Timoshenko & Gere (see table 2.2), using test results of Bouwkamp, Kato, Kimura, Korol, Murphy, Reddy and Sherman, going up to D_e/t ratios of 120. The expression of Gresnigt (equation 2.27) is considered a safe criterium (with estimated 5% probability of a lower value) [23].

It can be noted that $D_e - t$ is equal to the diameter of the mid-line of pipe wall D_m. Yet for a clear comparison the same notation was used in the tables above.

Table 2.2: Critical strain formulas compared in IBBC-TNO Report 85(343) [23].

Source	**Critical strain formula**
Batterman	$\varepsilon_{cr} = \frac{4}{9} \cdot \left(\frac{t}{0.5D_e}\right)^2 \frac{E_t}{f_y} \quad E_t = \frac{E_s}{40}; f_y = 460$ MPa
Gresnigt	$\varepsilon_{cr} = 0.5 \cdot \left(\frac{t}{D_e - t}\right) - 0.0025$
Timoshenko & Gere	$\varepsilon_{cr} = 1.21 \cdot \frac{t}{D_e}$

The rules for local buckling in EN 1993-4-3 [2] are in line with those in other pipeline standards. The design critical curvatures according to EN 1993-4-3 [2] are larger than those that can be deduced from EN 1993-1-6 [21]. An example is presented in appendix C. The main reasons are that the loading in buried pipelines is mainly deformation controlled and the consequences of local buckling are less severe than in structures where the loading is mainly load controlled. Due to the expectation that the strain based method leads to more economical designs, this method is used in this thesis to check the local buckling resistance.

2.3. Out-of-roundness

The critical strain is influenced by the local radius of curvature of an ovalised cross-section R_o (equation 2.26). Brazier showed already in 1927, that due to radial loads, because of the bending and non-uniform radial soil, the circular cross-section of the pile deforms in an oval shape. This can be amplified because of initial deformations. An internal pressure reduces ovalisation, which is also known as the 'rerounding effect'. Out-of-roundness results in a smaller diameter on the y-axis and inherently a higher compressive stress. Therefore the pile becomes more susceptible to local buckling according to the stress method. To account for the reduced curvature, because of the ovalisation, in the critical strain equation, the radius of the mid-line of the pile wallR_m has to be adapted by:

$$R_o = \frac{R_m}{1 - \frac{3a}{R_m}} \tag{2.28}$$

In which a is the decrease of the radius, see figure 2.7.

2.3.1. Initial out-of-roundness

In reality tubular piles are never perfectly circular, even in the initial state. In En 1993-1-6 [21] the deviation from circularity is indicated by the out-of-roundness U_r.

$$U_r = \frac{d_{\max} - d_{\min}}{d_{\text{nom}}} \tag{2.29}$$

Where:

$d_{\max}$	maximum measured internal diameter	[m]
$d_{\min}$	minimum measured internal diameter	[m]
d_{nom}	nominal measured internal diameter	[m]

In EN 1993-4-3 [2] the ovalisation a is calculated with:

$$a = \frac{1}{4} \cdot U_r \cdot D_m \tag{2.30}$$

In the Eurocode EN 1993-1-6 [21], the initial out-of-roundness is categorized with the fabrication tolerance quality classes A (Excellent), B (High) and C (Normal).

Table 2.3: Recommended values for out-of-roundness tolerance parameter $U_{r,\max}$. [21]

	Diameter range	d [m] ≤ 0.50m	0.50m < d [m] < 1.25m	1.25m ≤ d [m]
Fabrication tolerance quality class	Description	Recommended value of $U_{r,\max}$		
Class A	Excellent	0.014	0.007 + 0.0093(1.25-d)	0.007
Class B	High	0.020	0.010 + 0.0133(1.25-d)	0.010
Class C	Normal	0.030	0.015 + 0.0200(1.25-d)	0.015

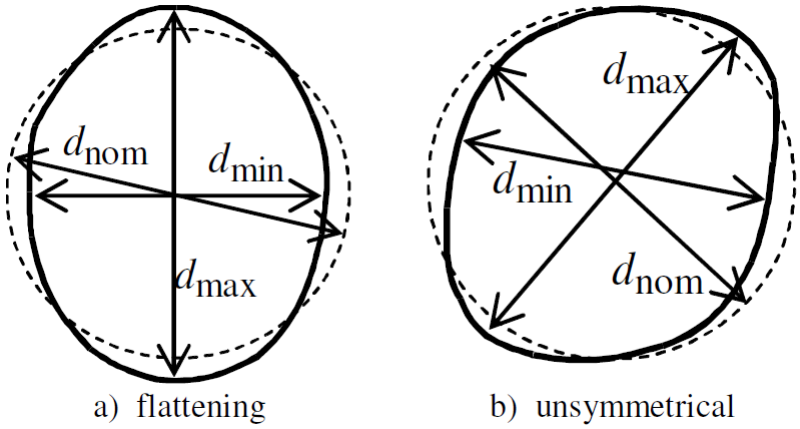

Figure 2.8: Measurement of diameters for assessment of out-of-roundness. [21]

2.3.2. Dimples

A dimple is a local normal deviation from the middle shell surface. It also reduces the radius. The depth of a dimple is denoted as Δw_0. Initial dimples can be measured by a gauge.

In EN 1993-1-6 [13] dimple tolerances are given for three fabrication tolerance quality classes. The depth of initial dimples should be assessed in terms of a dimple parameter U_0, which is the depth of the dimple Δw_0 divided by the gauge length l_g:

$$U_0 = \frac{\Delta w_0}{l_g} \tag{2.31}$$

Dimples should be measured in both the meridional and circumferential direction. The gauge length should be long enough to capture the initial buckles. These can have a length of $3.5\sqrt{R_m t}$ [24]. EN 1993-1-6 [21] prescribes a gauge length of $4\sqrt{R_m t}$.

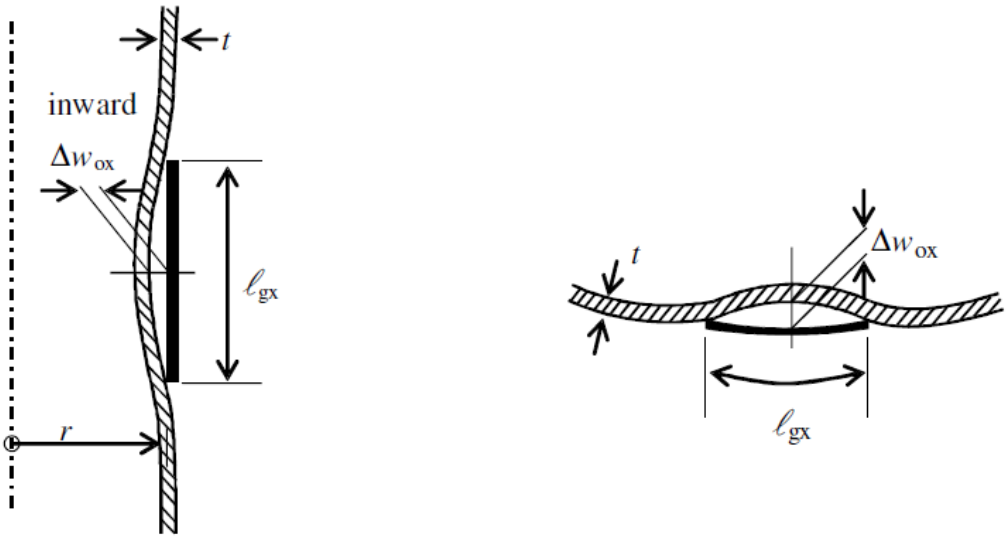

Figure 2.9: Depth of a dimple Δw_0 and the gauge length l_g. [21]

Table 2.5: Recommended values for dimple tolerance parameter $U_{0,\max}$. [21]

Fabrication tolerance quality class	**Description**	**Recommended value of $U_{0,\max}$**
Class A	Excellent	0.006
Class B	High	0.010
Class C	Normal	0.016

2.3.3. Ovalisation due to bending

The curvature from the bending of the pile causes pressure towards the inside of the pile. This pressure causes ovalisation a_c. In the elastic region Gresnigt [1] found:

$$a_c = q_c \frac{R_m^4}{12EI_w} \tag{2.32}$$

With:

$$q_c = r\,t E_s \kappa^2 \tag{2.33}$$

$$\kappa = \frac{M}{E_s I_p} = \frac{M}{E_s \pi R_m^3 t} \tag{2.34}$$

$$EI_w = \frac{E_s t^3}{12(1-\nu^2)} \tag{2.35}$$

Where:

a_c	ovalisation due to bending	[m]
q_c	uniformly distributed load due to bending (see chapter 2.1.1)	[kPa]
EI_w	bending stiffness of the pile wall per unit length	[$\mathrm{kNm^2/m}$]
κ	curvature	[$\mathrm{m^{-1}}$]
M	bending moment	[kNm]
I_p	second moment of inertia of the pile	[$\mathrm{m^4}$]
ν	Poisson's ratio	[-]

Equation 2.32 can be rewritten with equations 2.33, 2.34 and 2.35 to:

$$a_c = \kappa^2 \frac{R_m^5}{t^2} \tag{2.36}$$

2.3.4. Ovalisation due to soil pressure

The ovalisation caused by indirect soil pressure as a reaction on the lateral load a_q is in EN 1993-4-3 [2] calculated by:

$$a_q = 0.5 \cdot k_{yi} \frac{Q_i R_m^3}{EI_w} \tag{2.37}$$

Where:

Q_i	support reaction in the form of indirectly transmitted soil pressure (figure 2.10)	[$\mathrm{kN/m}$]
k_{yi}	deflection coefficient dependent on the loading pattern of the indirect soil load	[-]

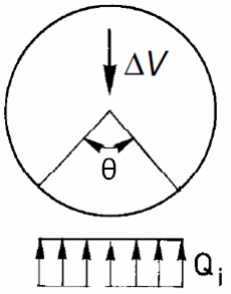

Figure 2.10: Earth load Q_i acting on the pipe-line cross-section. [2]

As the pile is loaded over the full diameter, θ is 180° and the value of k_{yi} in EN 1993-4-3 [2] is 0.042. Considering Q_i to be equal to $p_e \cdot 2r$:

$$a_q = \frac{1}{12}\frac{p_e R_m^4}{EI_w} \tag{2.38}$$

This is the same change in diameter prescribed by CUR 211E [3]. However the CUR 211E distinguishes the ovalisation on the side where the soil pressure is applied (A) and the opposite side (B). The proportion of the ovalisation in A compared to B is $\left(\frac{3}{8}-\frac{2}{3\pi}\right)/\left(\frac{2}{3\pi}-\frac{1}{8}\right)$. So approximately 65% of the change in diameter is due to ovalisation in A and the ovalisation in B contributes 35% of the total change in diameter. The ovalisation due

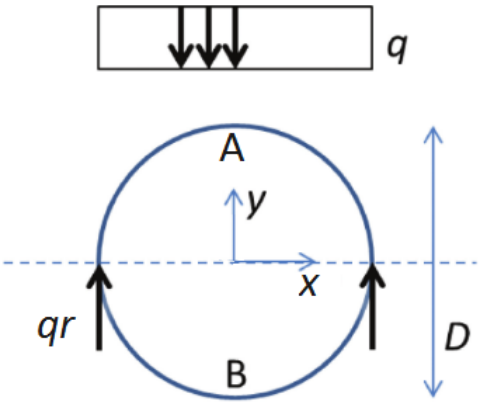

Figure 2.11: Ovalisation case with soil pressure from one side. Reprinted from [3].

to soil pressure as prescribed in the EN 1993-4-3 [2] and CUR 211E [3] are from simplified pressure models, shown in figures 2.10 and 2.11. Laterally loaded piles, in reality, have a different pressure field, presented in figure 2.12. In ROARK'S Formulas for Stress & Strain [25] analytical formulas to find the ovalisation for circular rings are given (equation 2.39). The stress field for lateral loaded piles can be seen as a combination of uniform stress normal to the pile with $\theta = \pi$ and a radial pressure that varies linearly from 0 to w as shown in figure 2.13. The cross-section does not ovalise due to the uniform pressure, $a = 0$. Therefore the ovalisation is found purely from the linearly varying pressure. The corresponding equations are presented below. The sum of the uniform and linear varying pressures around the cross-section has to be equal to the distributed load of the soil Q_i found from the p-y curves. In this way the value of w can be calculated.

$$a_q = \frac{wR_m^4}{2EI_w\pi(\pi-\theta)}\left\{k_1\left(\frac{\pi^2\cos\theta}{2}-2\cos\theta+2\pi-2-\theta sin\theta\right)-k_2\pi\left(2(\pi-\theta)-1+\cos\theta-\frac{\pi^2}{4}+\frac{\theta^2}{2}\right)-\right.$$
$$\left. k_2^2\left(2+2\cos\theta-(\pi-\theta)^2\right)\right\} \quad \text{for } \theta \le \frac{\pi}{2}$$

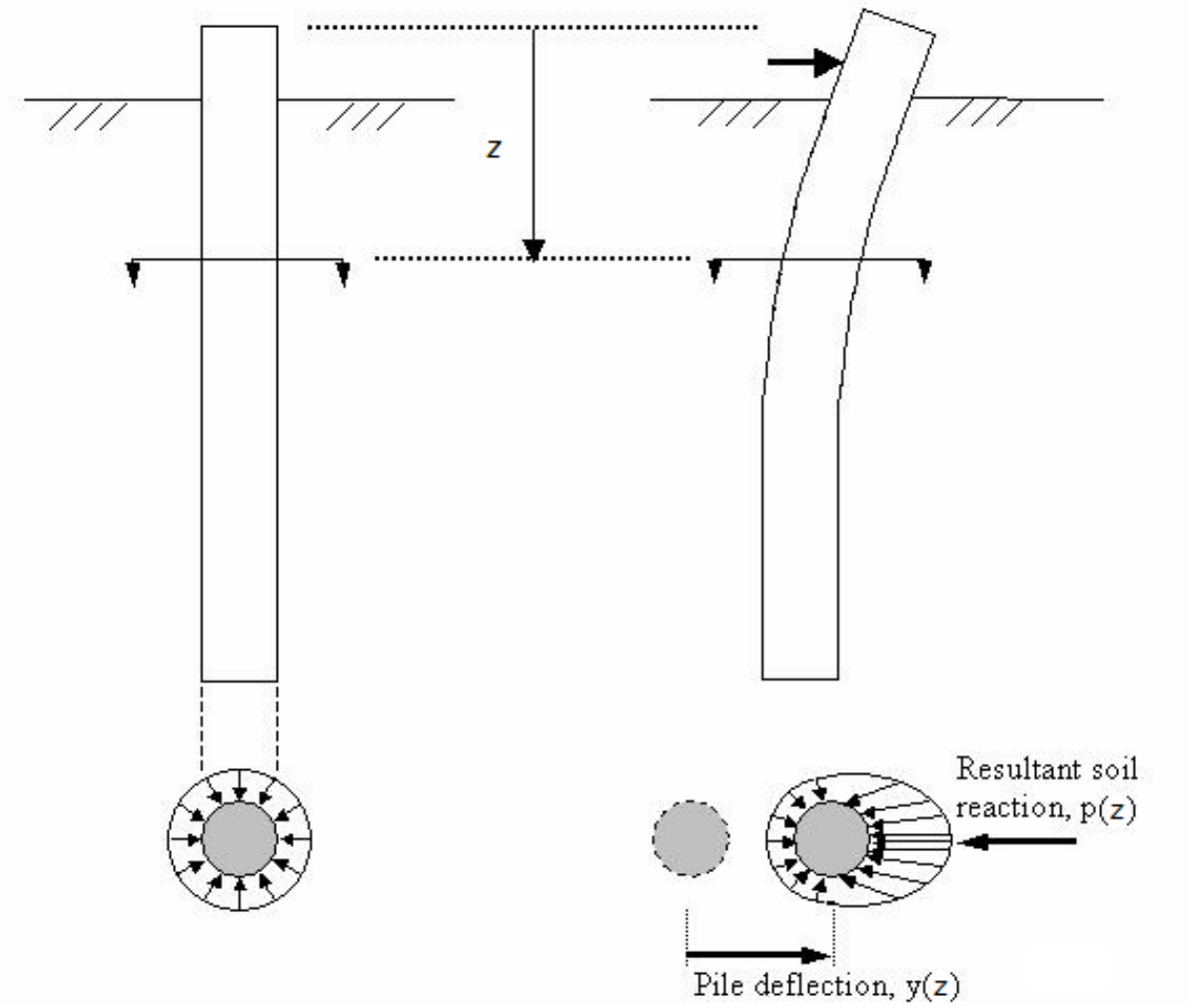

a) After installation
Stress acting on a horizontal plane are predominantly normal to pile and uniform

b) After lateral deflection
Stresses acting on a horizontal plane have normal and tangential components and are non-uniform

Figure 2.12: Resultant soil reaction. Reprinted from [26].

$$a_q = \frac{wR_m^4}{2EI_w\pi(\pi-\theta)}\left\{k_1\left(\pi\cos\theta(\pi-\theta)+2\pi\sin\theta-2\cos\theta-2-\theta sin\theta\right)-\right.$$
$$\left.k_2\pi\left(2(\pi-\theta)+1+\cos\theta-2\sin\theta-\frac{(\pi-\theta)^2}{2}\right)-k_2^2\left(2+2\cos\theta-(\pi-\theta)^2\right)\right\} \quad \text{for } \theta \geq \frac{\pi}{2} \tag{2.39}$$

With:

$$k_1 = 1-\frac{I_p}{AR_m^2}+\frac{2EI_p}{GAR_m^2}$$
$$k_2 = 1-\frac{I_p}{AR_m^2} \tag{2.40}$$

Where:

A	cross-sectional area	[m^2]
G	shear modulus of elasticity	[kPa]

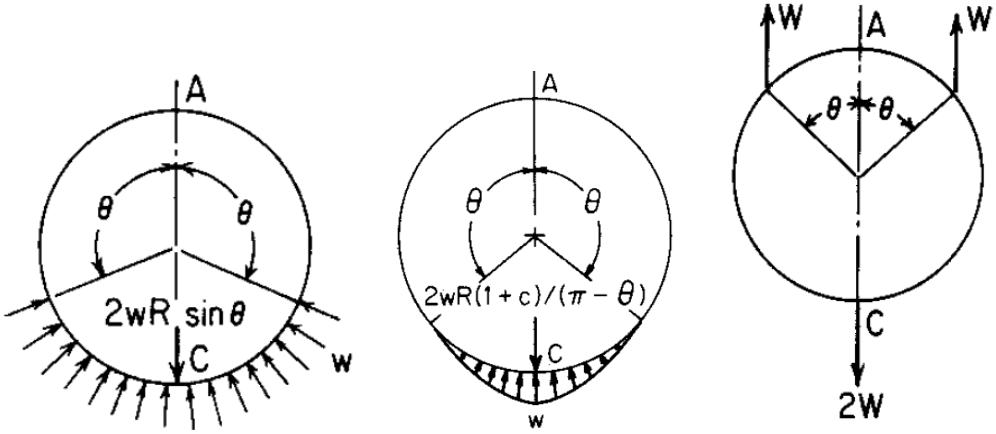

a) Uniform pressure b) Linear varying pressure c) Ring response

Figure 2.13: Loading schemes in ROARK'S Formulas for Stress and Strain [25] that combine to the pressure field for laterally loaded piles.

2.3.5. Geometric non-linear effect

The ovalisation is calculated with general equation 2.37. The influence of geometric non-linear behaviour is taken into account according to Gresnigt [1] with a factor $\left(1+\frac{a}{R_m}\right)^3$. After all, due to the ovalisation, the span R_m increases with a factor $1+\frac{a}{R_m}$. Here it is assumed that the ovalisation is symmetric, forming an oval with two axes of symmetry. The extension of one of these axes by an amount $2a$ is equal to the shortening of the other axis ($b = a$ in figure 2.3). As $\frac{a}{R_m}$ is small compared to the unity the increasing factor can be rewritten as $\left(1+3\frac{a}{R_m}\right)$. This factor is also prescribed in EN 1993-4-3 [2]. It should be noted that with a nonsymmetric load-distribution, the assumed oval shape is not correct. The soil pressure around dolphins is nonsymmetric. Furthermore, the load Q_i depends on the width of the dolphin. The ovalisation therefore effects the load. It may be questioned if the increasing factor should be $\left(1+\frac{a}{R_m}\right)^4$ instead.

2.3.6. Rerounding effect

An internal pressure gives resistance and reduces the ovalisation. This effect is known as rerounding. Therefore the ovalisation due to bending or soil pressure should be multiplied by a rerounding factor f_{rr}.

$$f_{rr} = \frac{p_{\text{cr}}}{p_{\text{cr}} + p} \tag{2.41}$$

In which p_{cr} is the theoretical value of the implosion pressure:

$$p_{\text{cr}} = \frac{3EI_w}{R_m^3} \tag{2.42}$$

Without any pressure in the pile, the rerounding factor f_{rr} is equal to 1.

2.4. Sand-filled piles

Dolphins are open tubular piles. Therefore when installed, it is possible that the dolphin is partly filled with sand.

Piles filled with sand tend to have more resistance regarding local buckling [16]. This is explained by the prevention of ovalisation of the sand-fill within the pile. In general the plastic buckled mode of over-stretched sand-filled piles has an outward shape.

Figure 2.14: Typical buckling shape of sand-filled pile. [16]

For an unchanged perimeter of the cross-section, its area is reduced under the effect of ovalisation. The sand is compressed and a reaction force from the soil is generated. This decreases the bending moments along the tube wall and therefore the ovalisation calculated by Gresnigt [1] will be less. Tests [15][16] show that the sand-fill provides extra resistance against ovalisation.

The sand plug provides an extra stiffness, k_{plug}. Assuming a 'vertical sand strut', as described in CUR 211E [3], the back pressure from the plug when it's squeezed by the ovalising pile, q_p, is found as:

$$q_p = \varepsilon_h E_{\text{plug}} = \frac{\Delta d}{d \cdot E_{\text{plug}}} \tag{2.43}$$

So when the ovalisation is symmetric:

$$k_{\text{plug}} = \frac{E_{\text{plug}}}{R_m - \frac{1}{2}t} \tag{2.44}$$

The external load remains the same for an empty pile and a sand-filled pile: $q_{\text{empty}} = q_{\text{sand-filled}} = q$. Therefore the ovalisation of a filled pile can be estimated from the ovalisation of an empty pile by:

$$a_{\text{sand-filled}} = a_{\text{empty}} \frac{k_{\text{wall}}}{k_{\text{wall}} + k_{\text{plug}}} \tag{2.45}$$

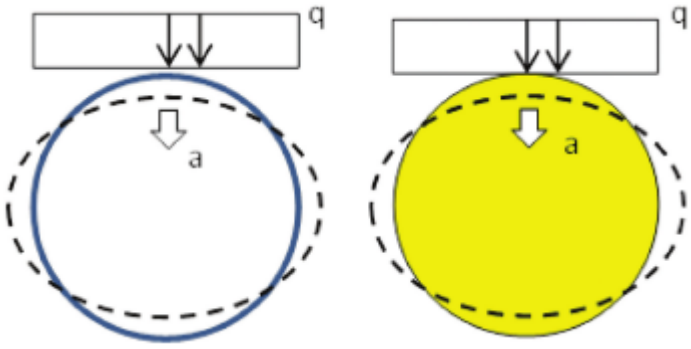

Figure 2.15: Stiffness of a steel tube and a sand volume. [3]

In which the stiffness k_{wall} is defined as:

$$k_{\text{wall}} = \frac{q}{a_{\text{empty}}} \tag{2.46}$$

Yet it is hard to determine the reaction force from the soil, because the vertical sand strut may collapse when the ovalisation increases above a certain critical value. The sand can move sideways.

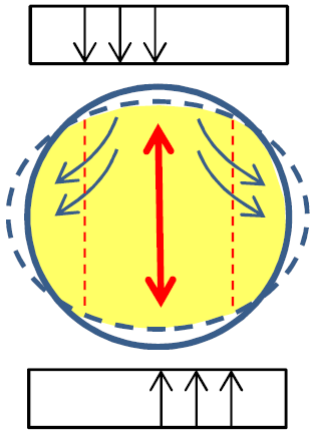

Figure 2.16: Cross-section with sand strut model. [36]

The reduced ovalisation, means a smaller radius. Which can be calculated in the same way as for empty piles. Equivalently the critical strain is higher. Kostis [10] did research on the contribution of the sand-fill. The ovalisation, moment capacity and the critical curvature of empty tubes were compared with their values for sand-filled tubes. Four tubes with slenderness ratios of 128, 133, 149 and 253 were used. The sand-fill shows a significant reduction in the ovalisation results, which causes failure to occur for larger curvature values. The reduction of the ovalisation of the sand-filled tubes compared to the empty ones, ranges between 30% to 65%. The reduction has most effect on the more slender tubes, with higher slender ratios. Compared to an empty tube the critical curvature and critical strain can increase with 10% for the low slenderness tubes and 50% for the more slender ones.

In the CUR 211E [3] it is stated that, optionally, the formula for the critical strain for sand-filled piles can be adapted to equation 2.47. This equation gives values 10% to 25% higher than the critical strains provided by Gresnigt [1].

$$\varepsilon_{\text{cr}} = 7\left(\frac{t}{R_o}\right)^2 \quad \text{for } 70 \leq \frac{D_e}{t} \leq 120 \tag{2.47}$$

2.5. Soil plug

As the sand-fill in a pile gives it more resistance to local buckling, it is relevant to know if there will be a soil plug in the dolphin and if so, what the soil plug level will be.

With the installation of the pile, a soil plug is entering into the pile tube. Initially the length of the soil plug is equal to the penetration depth and the pile is in an unplugged condition (figure 2.17a). Due to the friction between the pile's inner shaft and the soil, the length of the soil plug becomes less than the penetration and the pile is partially plugged (figure 2.17b). Eventually, the pile penetrates into the soil, but the soil plug length does not change. This creates a fully plugged condition (figure 2.17c).

Table 2.7: Incremental filling ratio (IFR) and plug length ratio (PLR).

	unplugged	partially plugged	fully plugged
IFR	$L_{p0}/L_{s0} = 1$	$(L_{p1} - L_{p0})/\Delta L_{s1}$	$(L_{p2} - L_{p1})/\Delta L_{s2} = 0$
PLR	$L_{p0}/L_{s0} = 1$	L_{p1}/L_{s1}	L_{p2}/L_{s2}

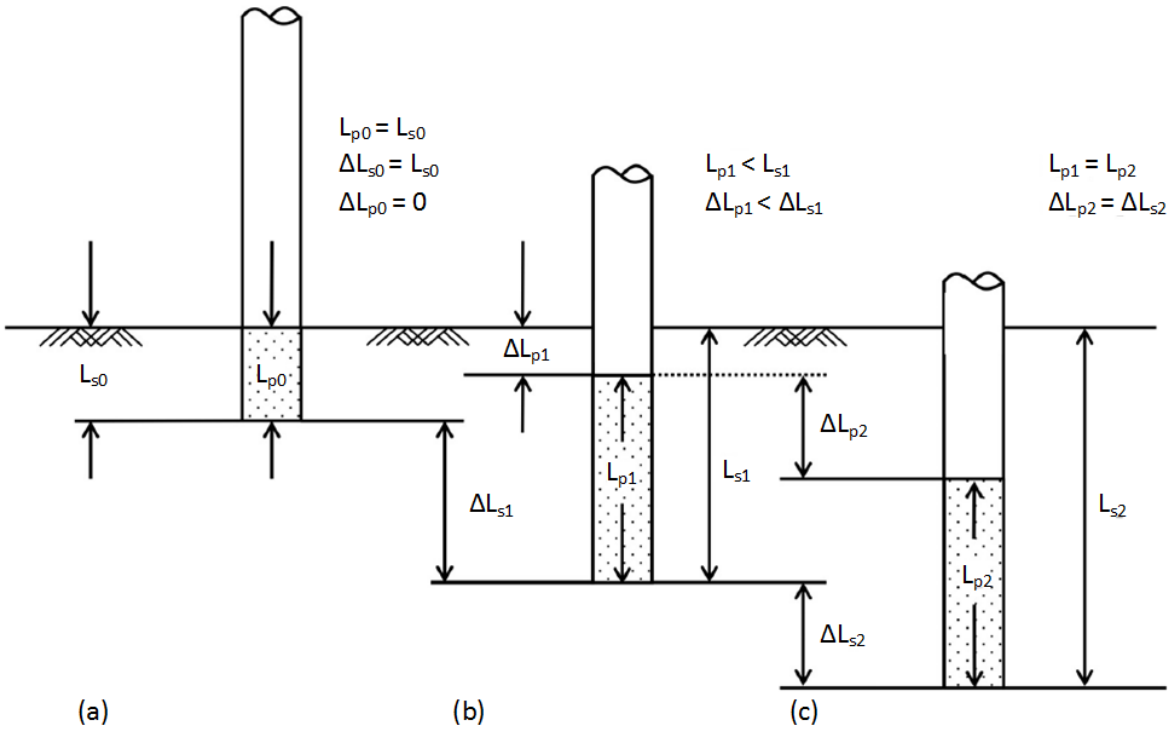

Figure 2.17: Conditions of plugging effect: (a) unplugged; (b) partially plugged; (c) fully plugged. Reprinted from [37].

In theory a pile gets plugged when the inner shaft friction $Q_{f,i}$ is bigger than the cone resistance of the plug Q_p, see figure 2.18. The same approach is used in the NEN-EN 9997-1 [38] and the international (offshore) standard API RP2A [34]: the pile is fully plugged when the inner shaft friction is big enough, so there is hardly any difference between the vertical displacement of the pile and the displacement of the soil on the inside of the pile.
A soil plug is able to mobilize an additional toe resistance and therefore the plugging effect is of importance for end bearing calculations. CUR 2001-8 [39] provides a design method to determine the bearing capacity of open steel tubular piles, however it does not answer whether soil plugging will occur. It states: "The mechanism of plugging is not yet well known". Nevertheless it is said that plugging will occur when the penetration is more than four to eight times the diameter of the pile.

The formulas in CUR 2001-8 [39] are based on a relatively small database of piles and soil conditions from several tests, in particular the Euripides project (1995) [40]. Therefore they are only valid for piles with $D_e/t <$ 60, a diameter range of 0.25 m and 3.00 m and a relative pile length of 5 to 80 L/D_m. Also only piles that are installed by soil displacement techniques (mainly driven piles) are taken into consideration.

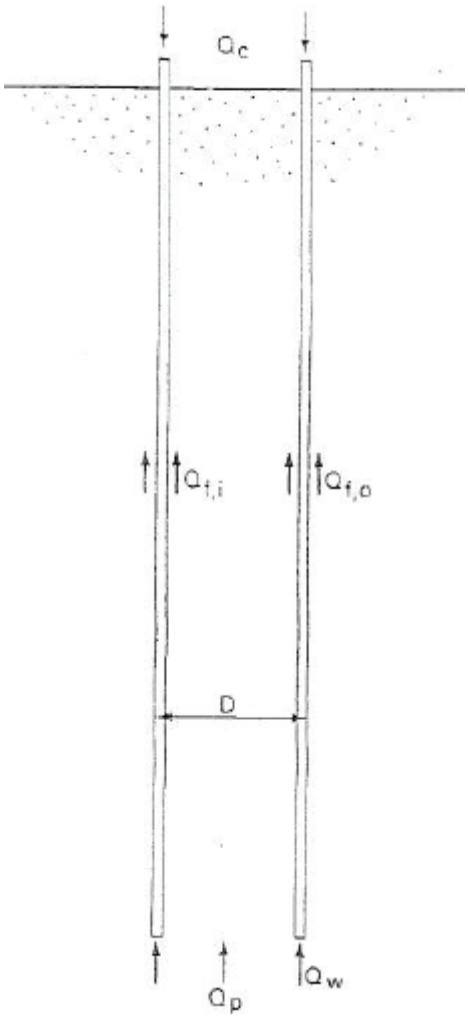

Figure 2.18: Plugging if $Q_{f,i} > Q_p$. [39]

2.5.1. Plug length

The height of the soil plug tends to increase until a limiting equilibrium is achieved and a fully plugged mode is formed. The degree of plugging is measured by the incremental filling ratio (IFR) of the soil plug ratio between the increment of soil plug length and the increment of pile penetration depth [41][37] (see table 2.7). The length of the plug L_p is found by:

$$L_p = \int_0^{L_s} \text{IFR}\, \mathrm{d}z \tag{2.48}$$

Alternatively the length of the soil plug can be described by the plug length ratio (PLR) (table 2.7). Among others, the soil plug length depends on the relative density of the sand near the pile base, the pile inner diameter and the pile embedment [42][43][44]. The major effects of these factors can be summarized as follows:

1. Piles installed in dense sand tend to plug more than those in loose sand;
2. Larger inner diameters generally lead to larger soil plug lengths;
3. Longer pipe piles are more likely to be fully plugged.

In reality it is not easy to determine the IFR, which involves continuously measuring the soil plug length during pile installation and also recording the penetration depth of the pile. Also it is not easy to measure

even PLR for routine piling work. For this reason, Lehane et al. [45] proposed a formula for estimating IFR_{avg}, averaged over twenty pile diameters of penetration, as a function of the pile internal diameter as follows:

$$IFR_{avg} = PLR = \min\left\{1, \left(\frac{d}{1.5}\right)^{0.2}\right\} \tag{2.49}$$

It should be noted that the average of the IFR measured with the same penetration increments over the entire pile length is equal to the PLR.

Yu and Yang [17] determined that the ratio of unit end bearing of soil plug to tip resistance from the cone penetrometer tests (CPT) depends on the PLR. They collected PLR data from literature and suggested the following equation to estimate PLR from the internal pile diameter:

$$PLR = \min\left\{1, d^{0.15}\right\} \tag{2.50}$$

Gudavalli, Safaqah and Seo [46] measured the plug lengths of a total of 1,355 hammered piles. The pile penetration depths ranged between about 10 m and 30 m. Based on these observations, they proposed the following equation, valid for pile inner diameter between 0.387 m and 0.876 m:

$$PLR = \left(\frac{d}{1.4}\right)^{0.19} \tag{2.51}$$

The three estimators were compared by Gudavalli et al. [46]. The predicted PLR values from Lehane et al. [45] show good agreement with mean PLR values measured by Gudavalli et al. [46], especially for large-diameter piles. Perhaps this is because Lehane et al. [45] derived their equation based on pile driving data of large-diameter off-shore piles. The equation proposed by Yu and Yang [17] appears to form the envelope for upper bound values.

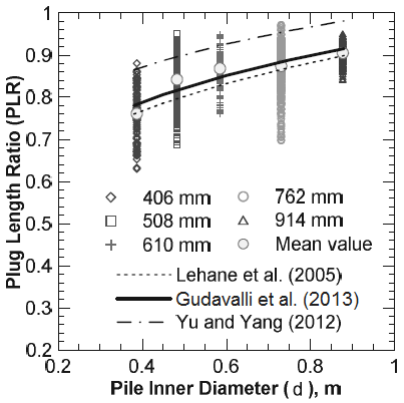

Figure 2.19: Pile inner diameter d versus measured PLR. Reprinted from [46].

Differently from the previous mentioned methods to indicate the soil plug level, Peters & Roubos [18] suggest soil plug levels measured from the original bed level (L_{np}). Based on a test with eleven vibrated piles, driven between 10.6 and 12.8 times the diameter, their suggestion is to assume the soil plug level at one diameter under the original bed level, for diameters up to 1.0 m. For diameters beyond 3.0 m the soil plug level can be assumed at $^1/_2 D_e$ below the bed level. Between D_e = 1.0 and 3.0 m Peters & Roubos recommend linear interpolation.

Even though the estimators are based on different installation methods, for pile diameters between 0.75 and 1.1 m the PLR ranges between 0.87 and 1. This provides an estimation of the soil plug level in this thesis.

3

Analytical model

With the available literature, it is presented how the local buckling resistance can be approached for the given new situation with a semi-filled dolphin pile. In order to check whether local buckling will occur, the strains in the dolphin wall have to be determined. Local buckling is expected at the critical point where the compressive strain exceeds the critical strain. For the critical strain, the strain proposed by Gresnigt [1] is assumed. Because Gresnigt's critical strain is influenced by the ovalisation, it is shown how the ovalisation can be obtained. The resulting analytical model provides a quantitative insight in the local buckling behaviour of flexible dolphins. Herewith key parameters that influence the local buckling behaviour are identified.

3.1. Beam Theory

Beam theory is used to obtain pile deformations and therewith the strains in the dolphin wall. Considering the dolphin pile as an Euler-Bernoulli beam in bending, the relationship between load, shear force V and bending moment M is derived by expressing the equilibrium of an infinitesimal element ∂z of a beam in bending with a distributed load of intensity q and soil pressure of intensity Q_i. The latter is equal to spring stiffness k multiplied by the deformation y. The positive directions are defined in figure 3.1.

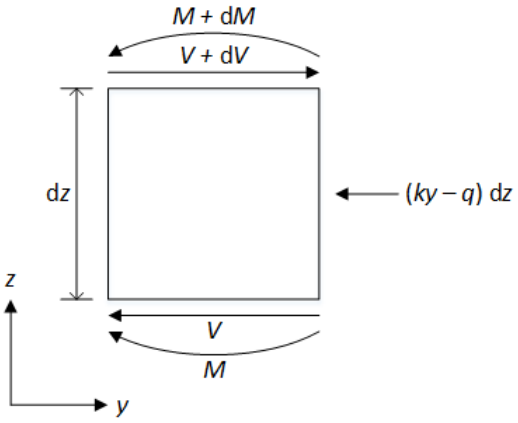

Figure 3.1: Element ∂z of a beam.

With reference to Hetényi [47], the following partial differential equation that describes the displacement of this system can be derived:

$$EI\frac{\partial^4 y}{\partial z^4} + ky = q \tag{3.1}$$

Where:

EI	Bending stiffness of the beam	[kNm^2]

There is no distributed load q applied on the dolphin pile. Furthermore, there are no springs above the soil, so the spring stiffness can be set to 0 kN/m^2 , reducing the equation to:

$$EI\frac{\partial^4 y}{\partial z^4} = 0 \quad \text{for } 0 \leq z \leq L_f \tag{3.2}$$

The general solution to this problem can be found in the form:

$$y(z) = A_0 + A_1 \cdot z + A_2 \cdot z^2 + A_3 \cdot z^3 \tag{3.3}$$

Here A_0 - A_3 are constants.

Below the bed level the springs have a stiffness k_g [kN/m^2] and the equation yields:

$$EI\frac{\partial^4 y}{\partial z^4} + k_g y = 0 \quad \text{for } L_s \leq z \leq 0 \tag{3.4}$$

Its general solution is:

$$y(z) = e^{\lambda z}(B_1 \cos(\lambda z) + B_2 \sin(\lambda z)) + e^{-\lambda z}(B_3 \cos(\lambda z) + B_4 \sin(\lambda z)) \tag{3.5}$$

With:

$$\lambda = \sqrt[4]{\frac{k_g}{4EI}} \tag{3.6}$$

Where:

λ	Characteristic of the system	[1/m]
B_1-B_4	Constants	[-]

In this derivation the soil stiffness is assumed independent of the deformation.

3.2. Pile Deformation

To determine the pile deformation, the soil stiffness should be known. These are related with the corresponding soil pressure:

$$k_g = \frac{Q_i}{y} \tag{3.7}$$

The interaction between pile deformation and soil pressure is described with the p-y curves (paragraph 2.1.2). To analytically find the deformation, iteration is required. First an estimation for k_g has to be made. Next, equations 3.3 and 3.5 provide a first estimation of the deformation. Now at any depth, the corresponding earth pressure can be obtained using the p-y curves. With equation 3.7, a new estimation of the secant soil stiffness can be made (figure 3.2). At different depths, different values for the soil stiffness are obtained. The general solution in beam theory requires a constant stiffness. Therefore, the pile is divided in elements over which the spring stiffness is taken the constant average value, calculated as the value at the top of the element ($k_{g,t}$) plus the value at the bottom of the element ($k_{g,b}$), divided by two. Figure 3.3 illustrates how the applied soil stiffness is derived.

$$k_{g,\text{applied}} = \frac{k_{g,t} + k_{g,b}}{2} \tag{3.8}$$

The new deformation has to be calculated with the new obtained soil stiffness estimates. Next, the spring constants k_g are re-estimated. This iteration process can be repeated until the new obtained values are approximately the same as the previous obtained values. This results in a prediction of the deformation of the

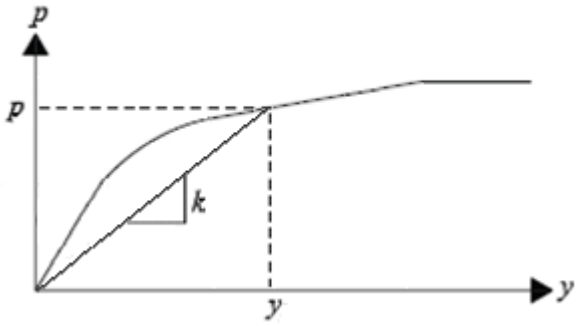

Figure 3.2: Determination of the secant stiffness of the soil.

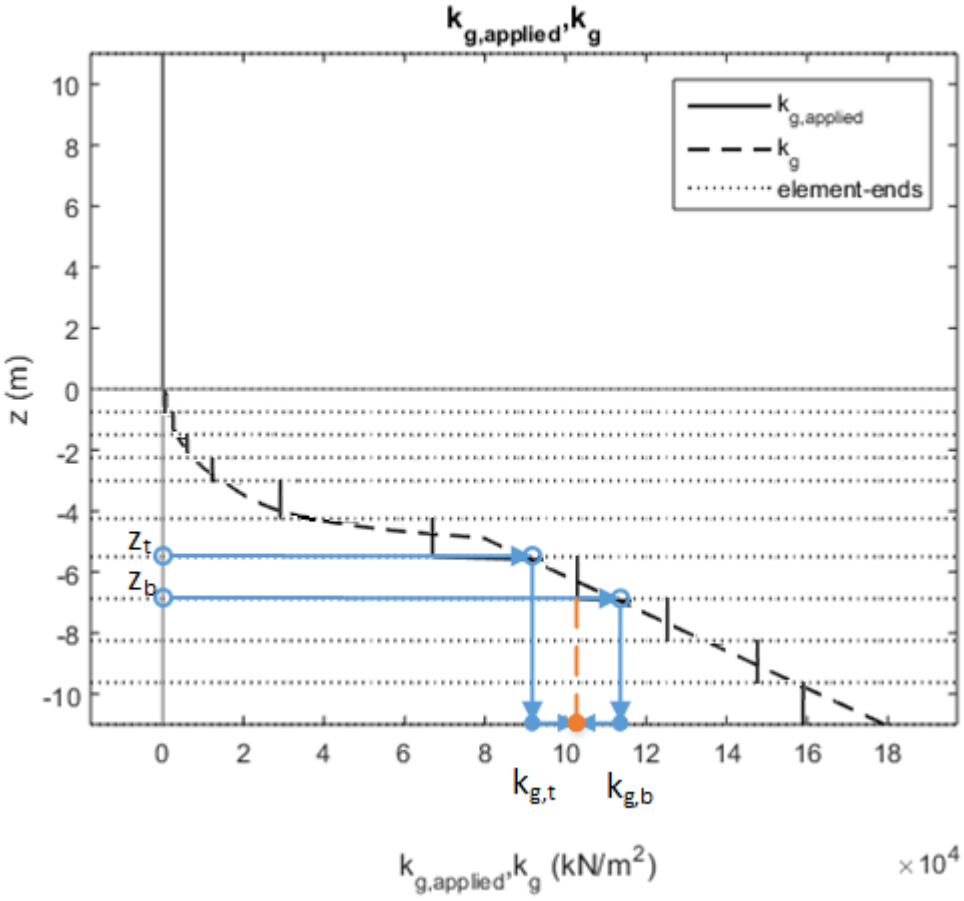

Figure 3.3: Applied soil stiffness.

pile and the corresponding pressure in the soil. From the deformation, the occurring strains in the dolphin wall can be derived (paragraph 2.1.1).
In figure 3.4 the results for the displacement y, bending moment M, shear force V and earth pressure Q_i are illustrated as an example. For the calculation a pile with a length of 22 m, embedded for 11m, is used. It has a diameter of 1 m and the wall thickness is 40 mm. The applied lateral force at the top of the pile is 1,000 kN. The p-y curves from Cox et al. [32] are used. The initial estimate for the soil stiffness is 10,000 kPa. Below the bed level, 10 beam elements are used.

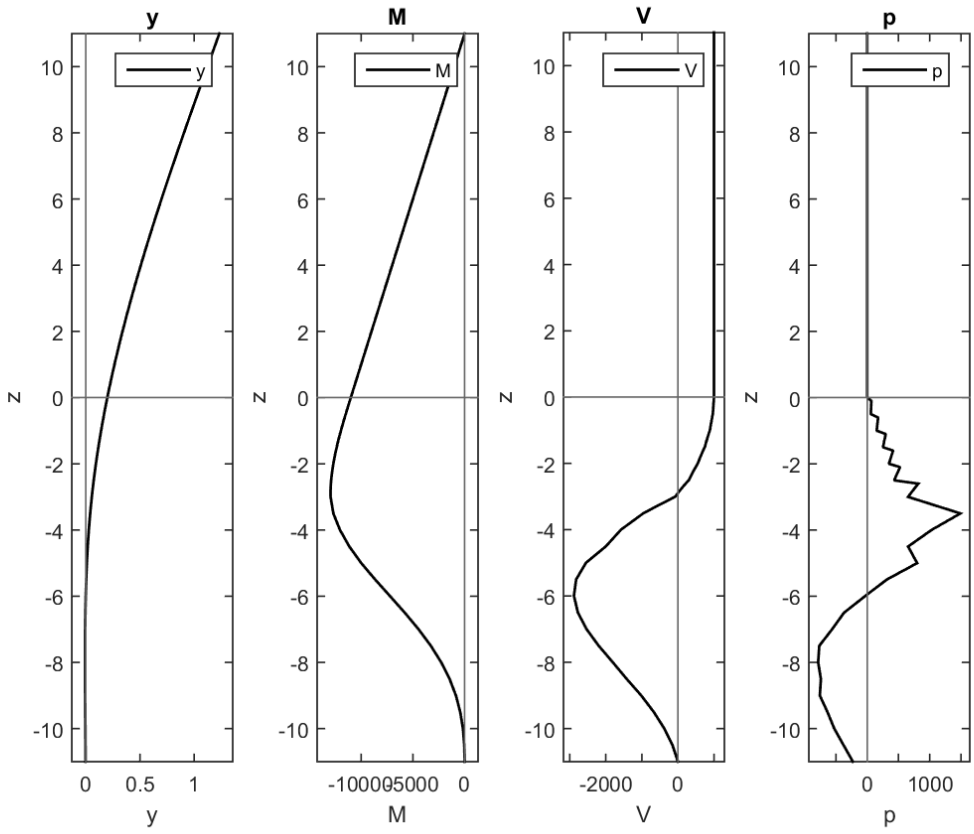

Figure 3.4: Analytical displacement for $F = 1,000$kN.

3.3. Ovalisation

To determine the critical strain with equations 2.26 and 2.28, besides the radius R_m and thickness t, the ovalisation a is required. The ovalisation is caused by bending and underneath the bed level also by soil pressure. Where the pile is filled with sand, the ovalisation is reduced. This means the pile can be divided in three parts (figure 3.5). For each of the parts the theoretical ovalisation is clarified. Also it is explained how to deal with the ovalisation at the transitions.

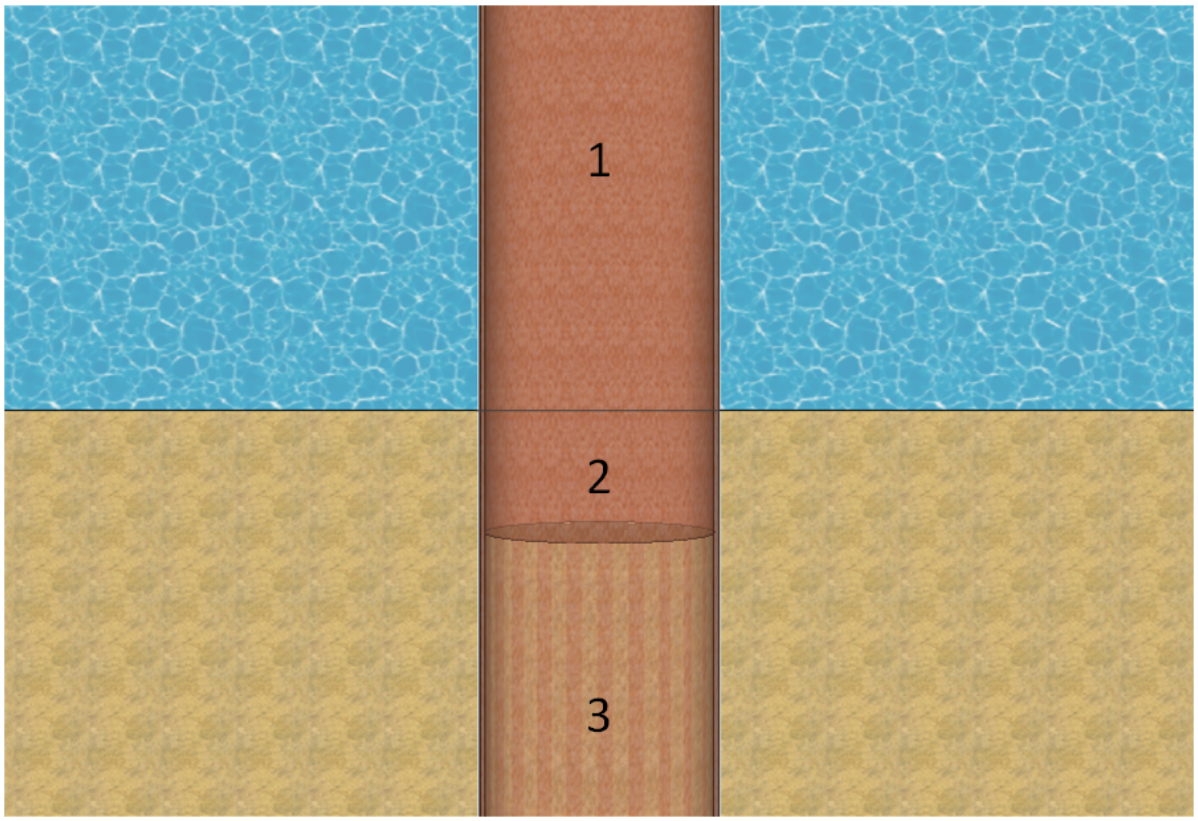

Figure 3.5: Pile devision.

3.3.1. 1st part

The first part is above the bed level. Ovalisation is merely due to bending. Following EN 1993-4-3 [2] it is calculated with equation 2.32. Taking the geometric non-linear effects in account the total ovalisation becomes:

$$\begin{aligned} a_{\text{empty},1} &= a_c \cdot \left(1 + 3\frac{a_c}{R_m}\right) \\ &= q_c \frac{R_m^4}{12EI_w} \cdot \left(1 + q_c \frac{R_m^3}{4EI_w}\right) \end{aligned} \tag{3.9}$$

3.3.2. 2nd part

The second part is the zone between the bed level and the soil plug level. It is the combination of bending and soil pressure causing the pile to ovalise (equations 2.32 and 2.38). The total ovalisation, including geometric non-linear effects, is therefore calculated with:

$$\begin{aligned} a_{\text{empty},2} &= (a_c + a_q) \cdot \left(1 + 3\frac{a_c + a_q}{R_m}\right) \\ &= \left((q_c + Q_i)\frac{R_m^4}{12EI_w}\right) \cdot \left(1 + (q_c + Q_i)\frac{R_m^3}{4EI_w}\right) \end{aligned} \tag{3.10}$$

3.3.3. 3rd part

Below the soil plug level, is part three. In this part, the ovalisation due to bending and soil pressure is reduced according to CUR 211E [3] with equation 2.45. In this equation a_{empty} results from equation 3.10. Assuming symmetric ovalisation, the extra stiffness provided by the sand in the pile is found with equation 2.44. The spring stiffness of the steel wall is defined in chapter 2.4 (eq. 2.46), in which the applied combined load q is equal to:

$$q = q_c + Q_i \tag{3.11}$$

Therefore:

$$
\begin{aligned}
k_{\text{wall}} &= \frac{q}{a_{\text{empty,2}}} \\
&= \frac{q_c + Q_i}{\left(\left(q_c + Q_i\right)\frac{R_m^4}{12EI_w}\right)\cdot\left(1 + \left(q_c + Q_i\right)\frac{R_m^3}{4EI_w}\right)} \\
&= \frac{1}{\frac{R_m^4}{12EI_w}\cdot\left(1 + \left(q_c + Q_i\right)\frac{R_m^3}{4EI_w}\right)}
\end{aligned}
\tag{3.12}
$$

3.3.4. Transitions

Applying the ovalisation equations in their corresponding parts, for the example pile in paragraph 3.2, results in the ovalisation as visualised in figure 3.6. At the transition between the parts, inconsistencies exist.

This is clearest in the transition between part two and three. At the soil plug level, the ovalisation in part three is less than the ovalisation in part two. In reality this gap does not exist. Furthermore, the reduction leads to a difference in gradient of the ovalisation.

Another inconsistency exists at the transition between part one and part two. At the bed level, the values for the ovalisation a are equal. This is because at this level, the earth pressure Q_i is still 0, reducing equation 3.10 to equation 3.9. Yet there is an inequality in the gradient of the ovalisation.

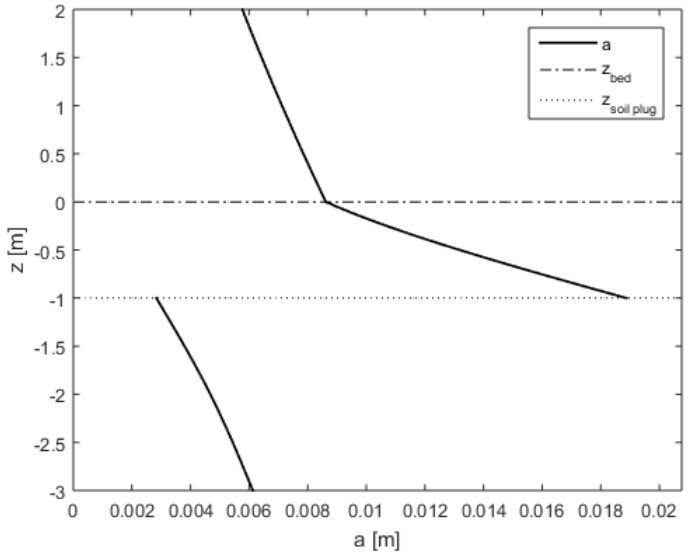

Figure 3.6: Ovalisation at transitions.

3.3.5. Continuous wall deformation

In order to overcome the inconsistencies at the transitions, beam theory is applied on the pile wall.

The wall is modelled as a linear beam, the vertical cross-section of the shell in point A (figure 2.11). Its deformation is resisted by the ring behaviour of the wall, which is modelled as springs with stiffness k_{wall} (eq. 3.12). The sand in the pile increases the resistance against ovalisation. Therefore the stiffness of the springs are increased with k_{plug}. This analytical model of the pile wall is visualized in figure 3.7. In part one the distributed load due to bending q_c is applied (eq. 2.33). Parts two and three are loaded by the combined load q (eq. 3.11). The result of this model is the continuous ovalisation of the pile, without inconsistencies at the transitions (figure 3.8).

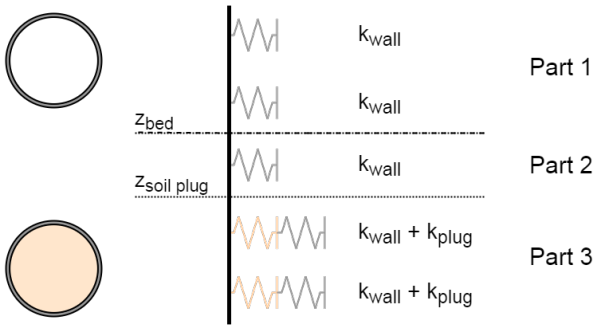

Figure 3.7: Model of pile wall.

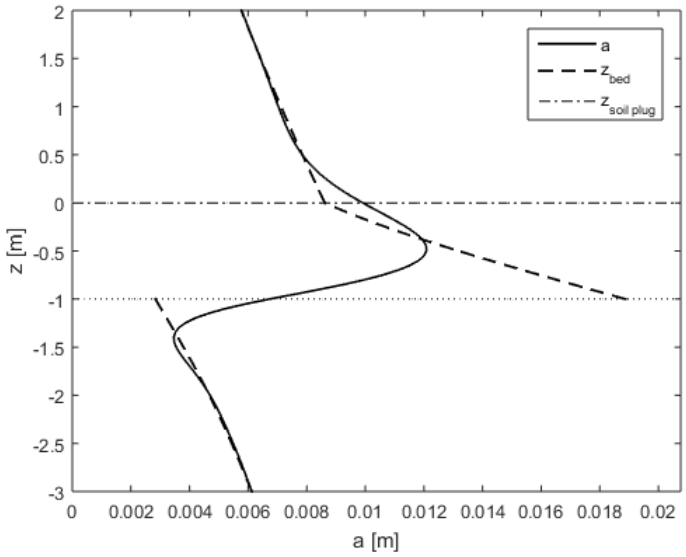

Figure 3.8: Continuous wall deformation.

3.4. Local Buckling

To find out whether local buckling might occur, the strain is compared with the critical strain. For the elastic deformation as found in the SLS, the occurring strain is directly related to the bending moment through the curvature. Therefore the highest strain occurs at the place with the biggest bending moment. In case of the pile from the example in paragraph 3.2 this is between $z = -2.5$ and $z = -3$ m. The critical curvature depends on the constant pile characteristics R_m and t and the varying ovalisation a. The biggest ovalisation results in the lowest critical strain. Both the occurring strain and critical strain (according to Gresnigt [1]) from the example in the transition area are illustrated in figure 3.9. To compare the strain with its critical value, their ratio, which should be below 1, is presented in figure 3.10. It should be noted that the the critical strain are dependent on the ovalisation, but do not include other effects of the soil on the local buckling. Assuming the critical strain is not affected, figure 3.10 shows that in this case local buckling is expected to occur close to the location of the highest strain. However, it does not exclude that in another case local buckling could occur higher in the pile where large ovalisations and hence low values for the critical strain arise.

The level of the maximum bending moment indicates the location of the maximum compressive strain in the dolphin wall. The location of the minimum critical strain is indicated by the level of the maximum ovalisation. When the maximum bending moment and the maximum ovalisation are at the same level, it is clear that local buckling will occur at this level. This is presented as situation 1 in figure 3.11a. If the ovalisation is reduced by the plug, the level of the maximum ovalisation can be at a higher level. Hence, the critical strain

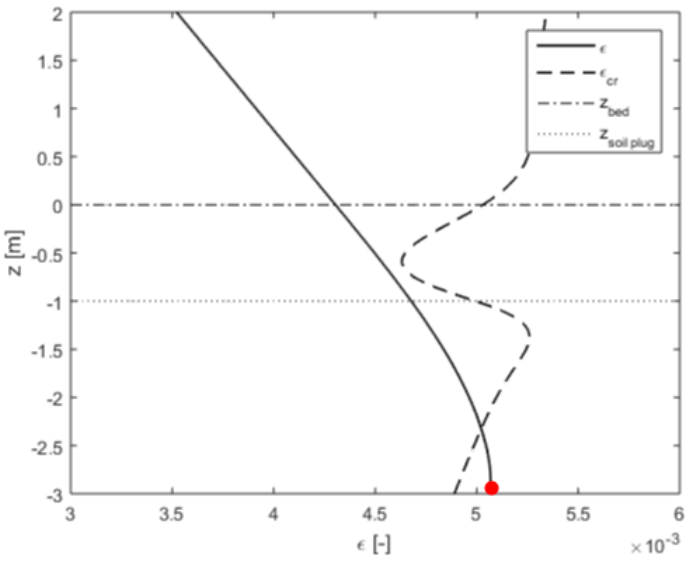

Figure 3.9: Occurring strain and critical strain in the transition area, with the local buckling level at -3m.

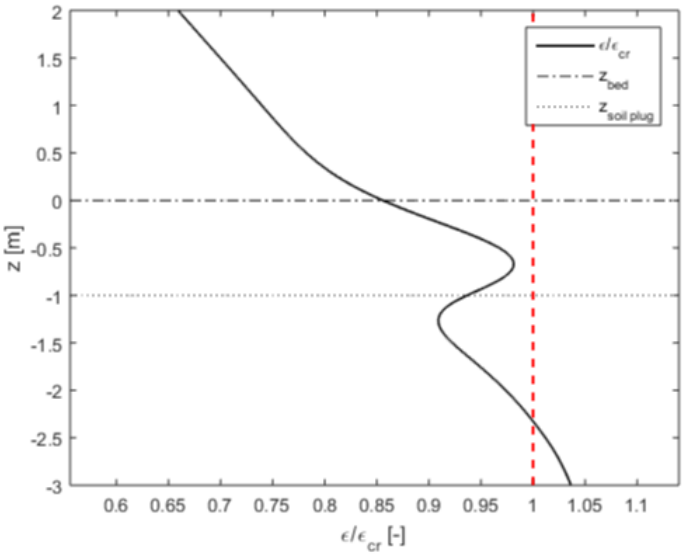

Figure 3.10: Ratio $\frac{\varepsilon}{\varepsilon_{cr}}$.

is at a higher level. This can lead to three more situations with different buckling locations. In the second possible situation there is a gradual reduction of the ovalisation. The critical location remains at the level of the maximum compressive strain. However, the compressive strain can be larger, before local buckling occurs. This is shown in figure 3.11b. If the ovalisation reduction is sharper the level of the minimum critical strain can become critical. Local buckling will occur at a higher level (figure 3.11c). In a fourth situation (figure 3.11d), it is possible that the buckling level is not at the level of the maximum compressive strain, neither is it at the level of the minimum critical strain. In this situation, local buckling will occur in between these levels.

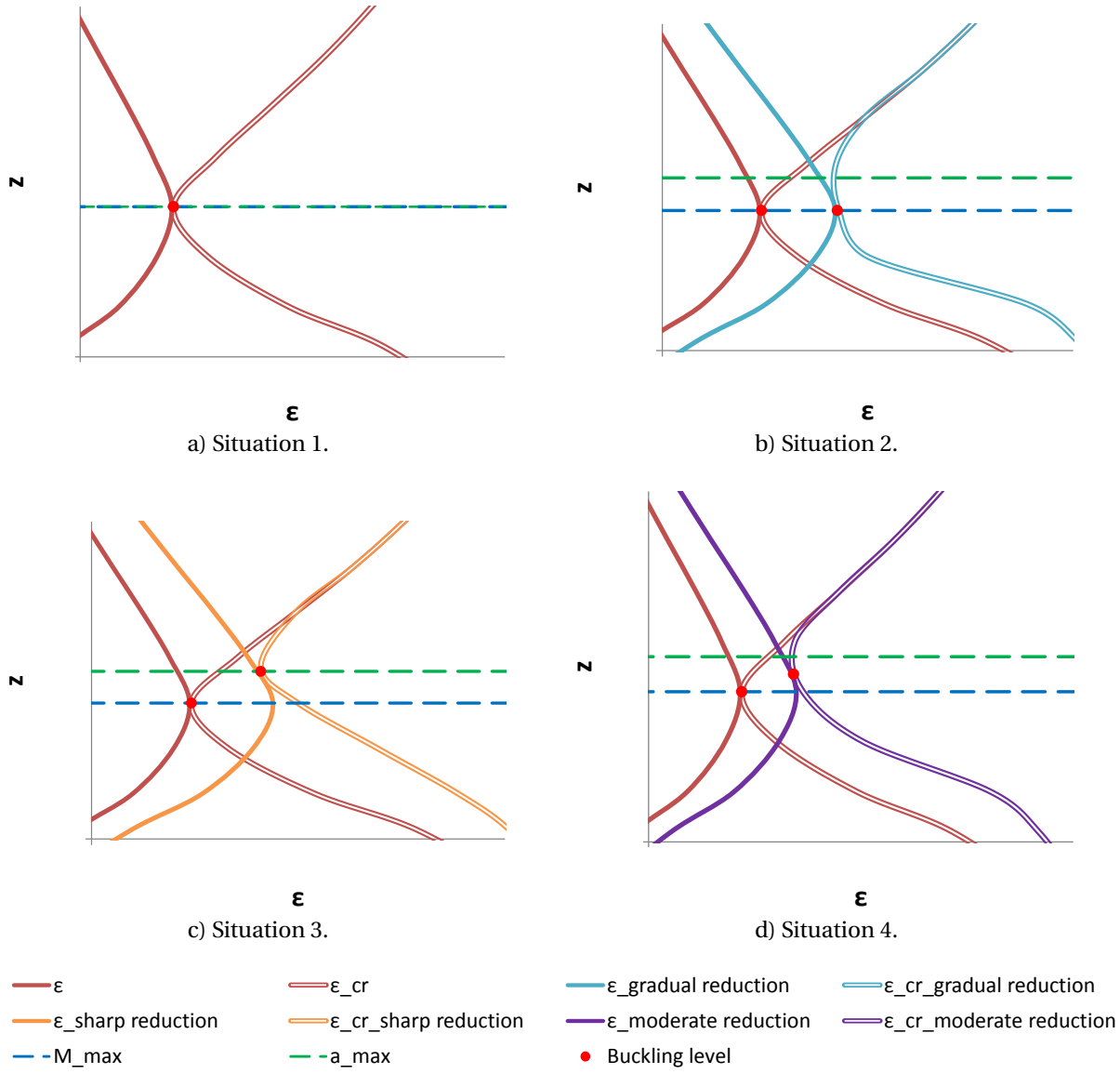

Figure 3.11: Adaptation critical strain and buckling level due to reduced ovalisation.

3.5. Spring stiffness

The spring stiffness of the steel wall as given in equation 3.12 is based on the symmetrical ovalisation assumed by Gresnigt [1]. Ovalisation based on the formulas in ROARK [25] would be more realistic.

The correctness of the spring stiffness of the sand k_{plug} can be discussed. It is meant for piles fully filled with sand under symmetrical ovalisation conditions. First of all, for dolphins the ovalisation is not likely to be symmetrical. Second, the vertical sand strut may collapse when the ovalisation increases above a certain critical value. The sand can move sideways (see figure 2.16). Also, in the transition zone the sand is able to move upwards, influencing the backpressure as equivalent in the p-y curve method. The plug does not provide resistance at the transition level.

To check whether the value for k_{plug} may be determined accordingly to the method described in CUR 211E [3] the values are compared to values found with the geotechnical finite element software Plaxis. In Plaxis, an embedded pile is modelled with surrounding soil and a plug in the pile. The pile has a length of 15 m and an embedded length L_s of 10 m. The diameter is 1 m and the thickness is 20 mm. It is loaded with pressure from two sides according to the symmetric load scheme presented in figure 3.12. The applied material

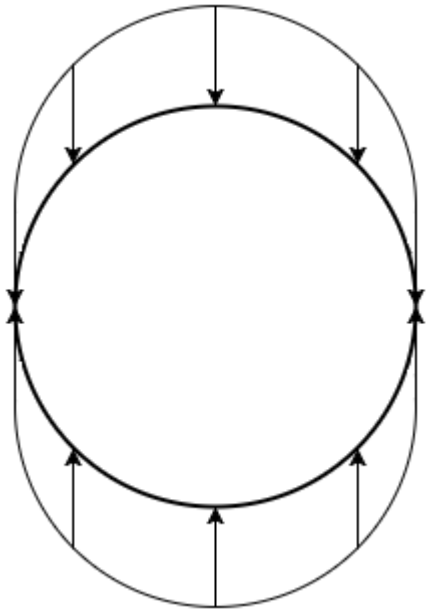

Figure 3.12: Case with soil pressure from two opposite sides.

model is a Mohr-Coulomb model, with linear elastic perfectly-plastic behaviour. This model represents a 'first-order' approximation of soil behaviour [48]. It is a simple model, to investigate if the value for k_{plug} can be predicted analytically from the inputted parameters. The properties of the soil and plug are the same and are tabled in table 3.1. The steel pile is modelled as a linear elastic plate, with E_s=210,000 MPa and ν=0.3. Plasticity behaviour is not included. The focus is on the horizontal soil pressures when a circular plug is ovalised. Therefore the correct material property for the steel is not of big importance. The strength of the soil is related to the strength of the interface by means of the parameter R_{inter}, according to the equation:

$$\tan\varphi'_{\text{interface}} = R_{\text{inter}} \cdot \tan\varphi'_{\text{soil}} \tag{3.13}$$

Hence, using the entered R_{inter} value gives a reduced interface friction. This is the wall friction. Using $\delta = \frac{2\varphi'}{3}$, the value of R_{inter} is approximated as 0.6667.

Table 3.1: Parameters used in Plaxis for the soil material.

γ [kN/m3]	E_g [MPa]	ν [-]	φ' [°]	ψ [°]	c' [kPa]
20	30	0.3333	30	0	0

The pressure applied is adapted to find a reasonable ovalisation. A loaded pile shows ovalisation values in the order of centimetres. Therefore on the modelled pile in Plaxis a pressure is applied to find an ovalisation of approximately five centimetres. A pressure of 1500 kPa is found appropriate.

The result of the analysis shows a symmetrically ovalised pile, as shown in figure 3.14. The outward ovalisation is approximately equal to the inward ovalisation (figure 3.15). It shows that with an equal pressure, the ovalisation deeper in the soil is less. This is due to the higher soil pressures deeper in the soil which have a bigger rerounding effect (illustrated in figure 1.13). Close to the top of the plug (at the bed level), the plug also has the freedom to move upwards. This reduces the rerounding effect, causing the ovalisation to be even larger compared to values found deeper in the soil. The latter effect seems to be effective up to a depth of -3m ($3D_m$).

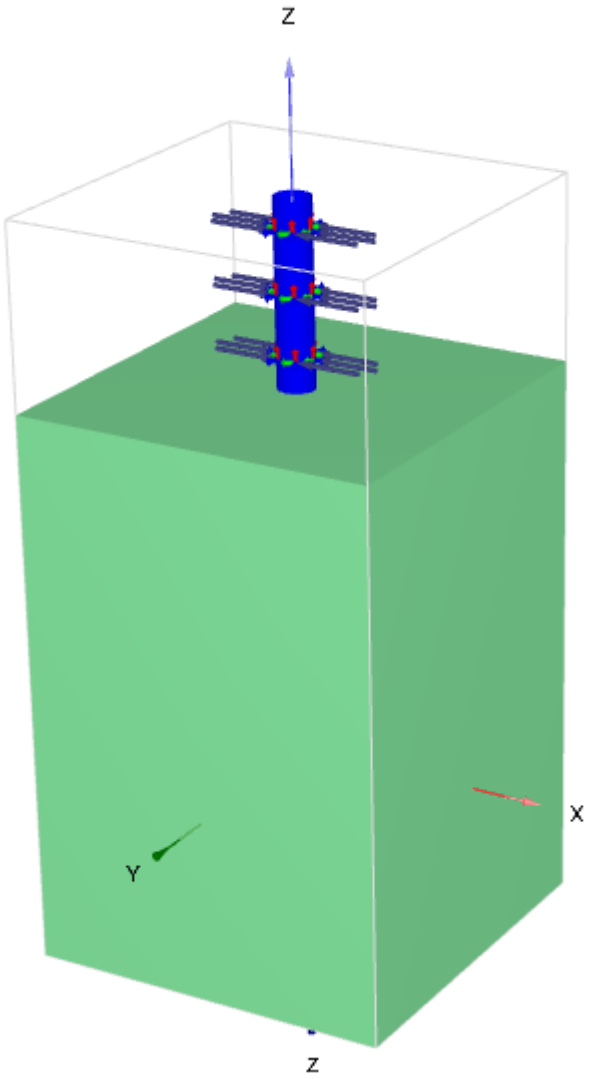

Figure 3.13: Plaxis model of embedded pile, symmetrically loaded.

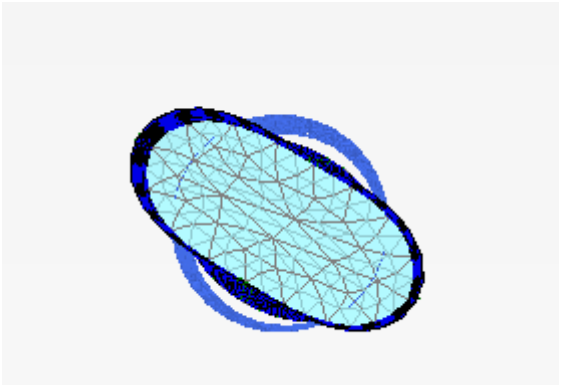

Figure 3.14: Symmetrically ovalised pile in Plaxis.

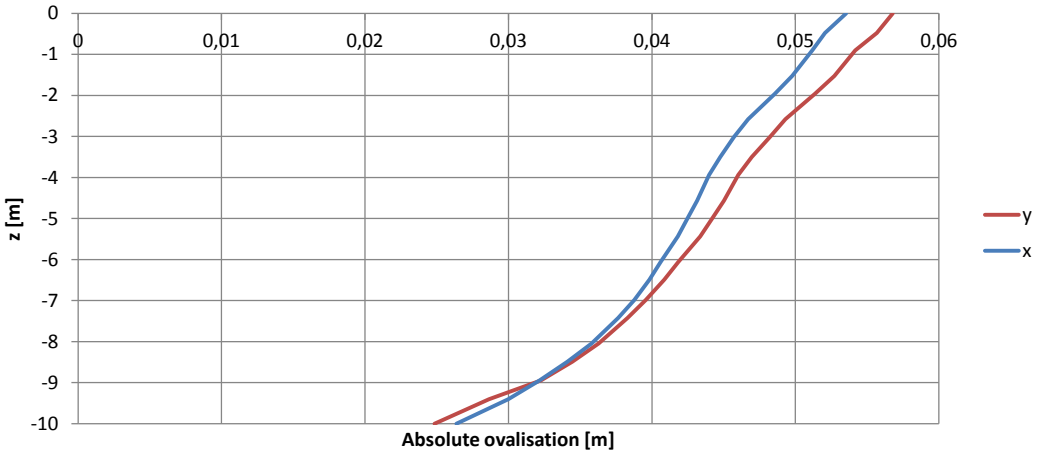

Figure 3.15: Absolute outward (y) and inward (x) ovalisation.

According to CUR 211E [3] the stiffness of the sand can be derived with equation 2.44. This equation was obtained from the relation between the load and the displacement. The load in this case is the horizontal pressure from the plug σ'_h and the displacement is the ovalisation a. The horizontal soil pressure here is determined with:

$$\sigma'_h = \varepsilon_h E_{\text{plug}} \tag{3.14}$$

Without any pressure due to ovalisation, there is already horizontal soil stress related to the vertical soil stress σ'_v with the neutral earth stress coefficient K_0. Therefore the total horizontal soil pressure is a summation of both:

$$\sigma'_h = K_0 \gamma z + \varepsilon_h E_{\text{plug}} \tag{3.15}$$

The Young's modulus E_{plug} is stress dependent. For a similar soil, a higher modulus is obtained when the stresses are higher. Hence, deeper in the soil, the soil is stiffer than in the shallow area. The Young's modulus E_{ref} as used in Plaxis is standardized for an effective horizontal soil stress of 100 kPa. The Young's modulus is converted with equation 3.16. The amount of stress dependency is given by the power m.

$$E_{\text{plug}} = E_{\text{ref}} \left(\frac{\sigma'_h}{100} \right)^m \tag{3.16}$$

From the results of the calculations in Plaxis, the relation in equation 3.15 is checked (figure 3.16). The strain in this equation is the strain obtained in Plaxis. Different stress dependencies are tried. For soft clays the power m should be taken equal to 1 [49]. For sands a value of 0.5 can be used. In this case a value of 0.2 showed good comparison with the stress obtained in Plaxis.

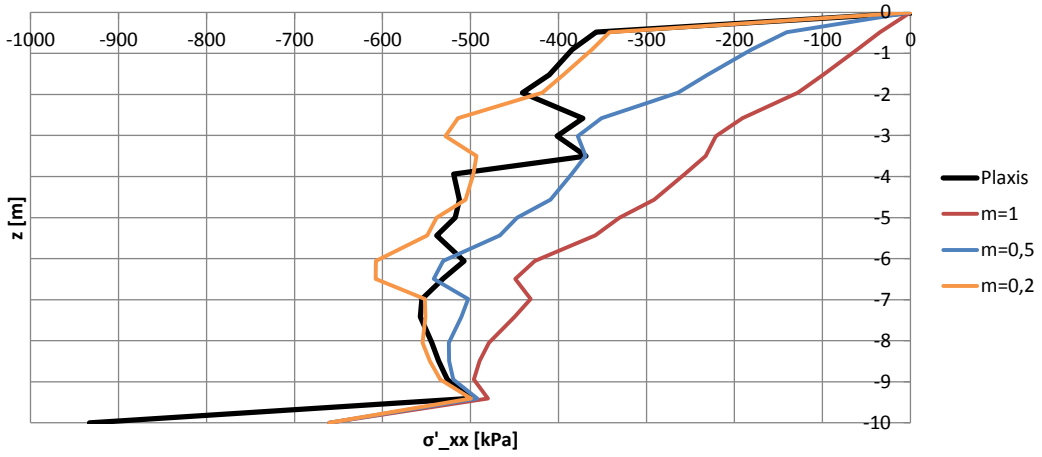

Figure 3.16: Comparison of horizontal earth stress found in Plaxis with the pressures according to equation 3.15 for different values of m.

Using equations 3.15 and 3.16, the stiffness of the sand can be derived if the horizontal strain in the plug is known. According to the derivation in CUR 211E [3] this strain is a/r. This is the strain from a 1D assumption. Another way to find the horizontal strain in the plug is by means of the volumetric strain ε_V. The ovalisation causes the area of a cross-section to decrease. The mass of the plug cannot be lost. Either the soil has to move up without loosing volume, or the soil has to be compressed, increasing the density. Soil is characterized with a high porosity. Therefore it is likely that the grains will be compacted. From Plaxis this seems to occur, as there is as good as no vertical displacement of the plug. The decrease in volume in the cross-section causes a volumetric strain ε_V:

$$\varepsilon_V = \frac{\Delta V}{V} = \frac{\Delta A}{A} = \frac{\pi r^2 - \pi (r+a)(r-a)}{\pi r^2} \tag{3.17}$$

Both strains are compared with the horizontal strains from Plaxis in figure 3.17. The strain as proposed in the CUR 211E [3] results in much higher strains than the strains from Plaxis. This means the horizontal stresses will be too high and therefore the plug is assumed too stiff. The real ovalisation will be larger and the risk

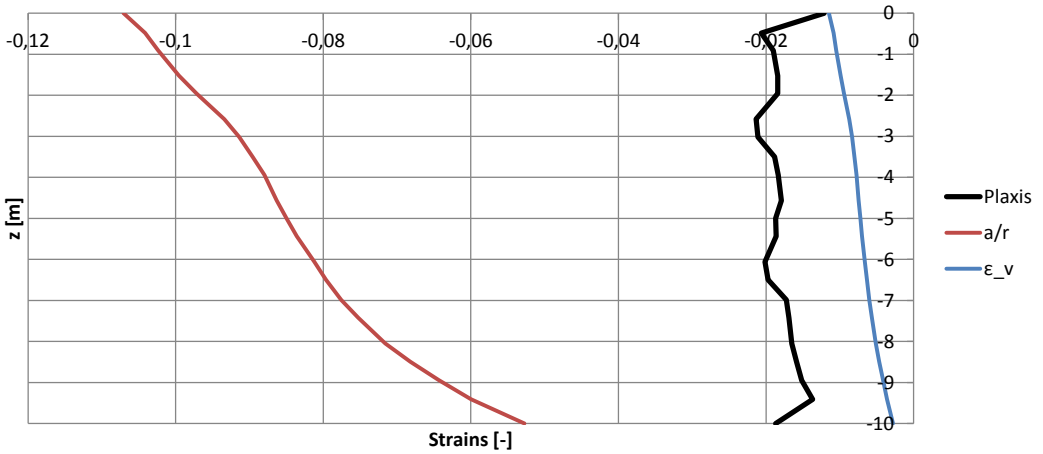

Figure 3.17: Comparison of strains found in Plaxis with the theoretical strains.

of local buckling higher. The volumetric strain on the other hand is lower than the strains from Plaxis. The reasoning is the other way around, resulting in an overestimated ovalisation and a conservative estimation of the local buckling resistance. Both methods seem to represent boundaries in between which the real strain is found.

3.6. Discussion

In chapter 2, present codes and general theoretical background was studied. In this chapter the knowledge is put together in an analytical model to discover whether local buckling can analytically be predicted. Beam theory is used to determine the dolphin pile deformation and loads on the pile. Literature provides equations to calculate the ovalisation that can be applied in three distinct parts: above the bed level, between the bed level and plug level and below the plug level. The provided equations however, show inconsistencies at the transitions. It is proposed to apply beam theory on the pile wall, modelled as a linear beam with springs providing resistance against ovalisation. Above the plug level the resistance is provided by the ring behaviour of the shell. Below the plug level the stiffness is increased with the stiffness of the soil plug. The model overcomes the inconsistencies in ovalisation.

The method assumes the stiffness of the plug in the pile k_{plug} can be approximated. However, from Plaxis calculations it is plain that the theoretical horizontal stress is not equal to the occurring horizontal soil stress within the pile. Therefore, the ovalisation is not properly estimated. The lack of knowledge of the ovalisation results in an unknown critical strain. Hence it cannot analytically be determined whether a semi-filled pile might buckle locally.

The theoretical critical strain from Gresnigt [1] was proposed for buried pipelines. Kostis showed that the critical strain can be higher for sand-filled piles and also the CUR 211E proposes a higher critical strain for sand-filled piles. It remains unclear whether these values are proper values for the transitional areas in semi-filled piles, like large diameter dolphins.

3.7. Key parameters

Even though with the available literature and the proposed analytical model the local buckling behaviour cannot be predicted, insight is gained in the parameters that affect local buckling in semi-filled piles.

Whether local buckling will occur depends on the compressive strain in the wall of the flexible dolphin and the the critical buckling strain. These are influenced by parameters that are either starting points for a design or can be chosen by the engineer.

The compressive strain is highest at the location of the maximum bending moment. The relation between the bending moment and the strain is influenced by the bending stiffness of the dolphin which again is determined by the diameter and thickness of the dolphin. The bending moment itself differs for soils with different stiffness.

The critical strain by Gresnigt [1] is influenced by the slenderness ratio ($D_e/t\varepsilon^2$) and the ovalisation. The latter depends on the stiffness of the plug and the plug level.

Key parameters are therefore the packings of the plug and the soil, the plug level and the slenderness ratio.

In the succeeding part of the research, the influence of these key parameters are studied with the finite element method. Furthermore, with the finite element calculations, design values for the plug stiffness are derived.

4

Finite Element Model

The finite element method (FEM) is used to approximate the real local buckling behaviour. In this chapter, the description of the finite element model is presented. The influence of the key parameters will be studied with this model (chapter 5). The model is validated with full scale tests (chapter 6).

First, a general description of the FEM is provided. Next, a representative pile from the field test is depicted that will be modelled. Then, it is explained which programme is used in this thesis. After that, the model that is used in the research analyses is described. Last, the post-processing is clarified.

4.1. General

The finite element method (FEM) is a numerical method for solving partial differential equations. The method cuts a structure into several elements and connects these elements at nodes. This leads to systems (often very large [50]) of linear equations which can be solved using a computer. In reality a structure is not subdivided in elements and there are infinite degrees of freedom. The finite element method approximates the reality by introducing boundaries and dividing the geometry in finite number of elements and finite degrees of freedom. Hence, the name of the method.

The fundamental concept of the method is that forces and displacements are coupled via the material properties which determine the stiffness of the geometry. For each element equations are obtained, minimizing the potential energy. Put all together and solving the equations results in the previously unknown variables at the nodes.

The FEM has the advantage that it can handle very complex geometries, restraints and loadings [51]. However, solutions can differ with different parameters. The system response to changes of the parameters has to be checked to find that the approximate solutions are realistic.

4.2. Representative Pile

The tests performed in the Port of Rotterdam with eight full scale piles (chapter 6) can be used to validate the finite element model. A representative pile is modelled. Piles that failed due to local buckling in the embedded part are piles 2, 3, 6 and 8. Piles 2 and 3 were located in a slope. They did not fail within the predicted deformation range and were pulled out the slope. In order to be able to load them beyond their capacity, piles 2 and 3 had to be elongated with extra tube sections. Pile 8 was filled with sand. Even though the density was negligible, possible effects are rather excluded. Pile 6 was not located in a slope, neither was it filled with sand. Yet it also buckled. Therefore, pile 6 is chosen to model in Abaqus.

Pile 6 has a total length of 22 m, of which the embedded part L_s is 11.5 m ($L_s/D_m = 12.6$). The bed level is at -8 m Ref. The plug reaches up to -8.78 m Ref. Therefore the PLR is $10.72/11.5 \approx 0.93$. The programme was subject to constraints in time and budget and available locations. For that reason the steel piles were procured from stock. Pile 6 is an assembly of three parts, all with a diameter D_e of 914 mm, but of different steel grades and different thickness. The bottom part is 3 metres long, the steel grade is X70 and it has a

thickness of 17.2 mm. The mid-section is the longest, 13.5 m, also has a grade of X70 and the thickness is 17.5 mm. The top part has a length of 5.5 m, the steel grade is X52 and the thickness is 16.0 mm. This information is visualized in figure 4.1. The critical locations with the maximum bending moment, the transition between a filled-part and an empty part and the transition between the embedded part and the free part of the pile are all in the mid-section. Stress strain data of this section was measured and is provided in table 4.1. For the Young's modulus of steel E_s 210,000 MPa is assumed, as prescribed by EN 1993-1-1 [21].

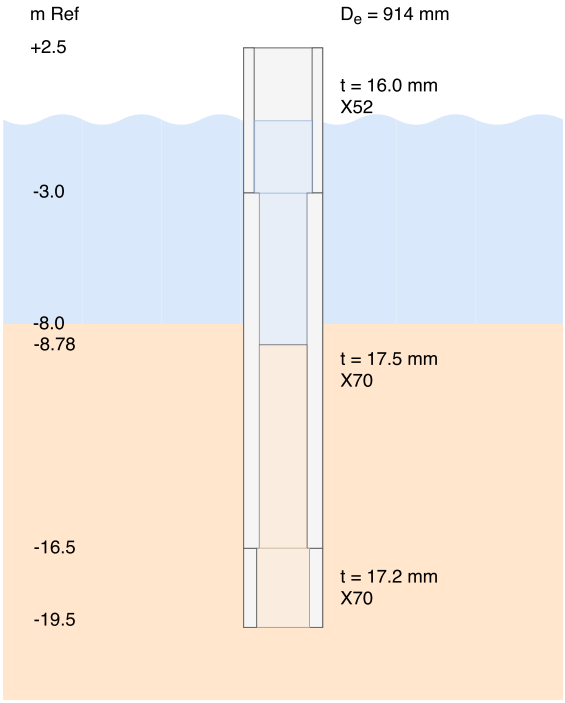

Figure 4.1: Assembly of pile 6.

Table 4.1: Measured stress strain data of the mid-section of pile 6.

Pile	Section	Grade	$R_{t0.5}$	$R_{p1\%}$ [MPa]	R_m	Hardening Modulus
6	mid	X70	582	596	662	875

4.3. Program

There are many FEM programs. At Royal HaskoningDHV, TNO Diana is generally used for modelling buildings. For soil structure interaction problems, Plaxis is used at Royal HaskoningDHV. This program is also well known at the Geoscience and Engineering department of the Delft University of Technology. At the Structural Engineering department of the Delft University of Technology, Abaqus is generally used.

The finite element model has to solve soil structure interaction problems and be able to model the geometrical local instability observed in local buckling problems. In this research static non-linear analyses are run. The non-linearities origin among others from the material behaviour with a non-linear stress-strain relation. The geometry also causes non linearities. Because of large deformations the shape of the elements changes. Furthermore there are boundary condition and loading condition non-linearities. The boundary condition non-linearities include the interaction between the components which cause non-linear deformations. The loading condition non-linearity comes from the change of the load during an analysis.

Abaqus has been used in research on the investigation of the local buckling behaviour of pipes in general, as well as the effect of imperfections, initial residual stresses and weldings on the local buckling behaviour [52]. Furthermore Abaqus was used to study the influence of a sand-fill on the local buckling behaviour [10].

Plaxis is intended to be used by geotechnical engineers. It is developed for the anlysis of deformation, stability and groundwater flow in geotechical engineering [53]. However, it is unable to model local buckling of steel piles.

TNO Diana has been used within Royal HaskoningDHV to model local buckling on an empty pile without surrounding soil [18].

To verify the ability of Abaqus and TNO Diana to solve soil structure interaction problems, a model of the physical test performed by Holeyman, Hübner, Saal & Tomboy [54], was set up to validate against the test results. A similar model was made in Plaxis to compare the results. This model uses a volume pile, a solid pile of which the Young's Modulus was adapted so the bending stiffness of the pile is equal to the pile used in the test.

The results are presented in figure 4.2. The physical test was performed in a special Brusalian sand. An advanced hypo-plastic material model in Plaxis approaches the test results. Abaqus and TNO Diana used a simplified Mohr Coulomb model that deviate from the results. A Plaxis analysis with the Mohr Coulomb material model shows comparable results as Abaqus and TNO Diana. Therefore, it is thought that Abaqus and TNO Diana are able to solve soil structure interaction problems.

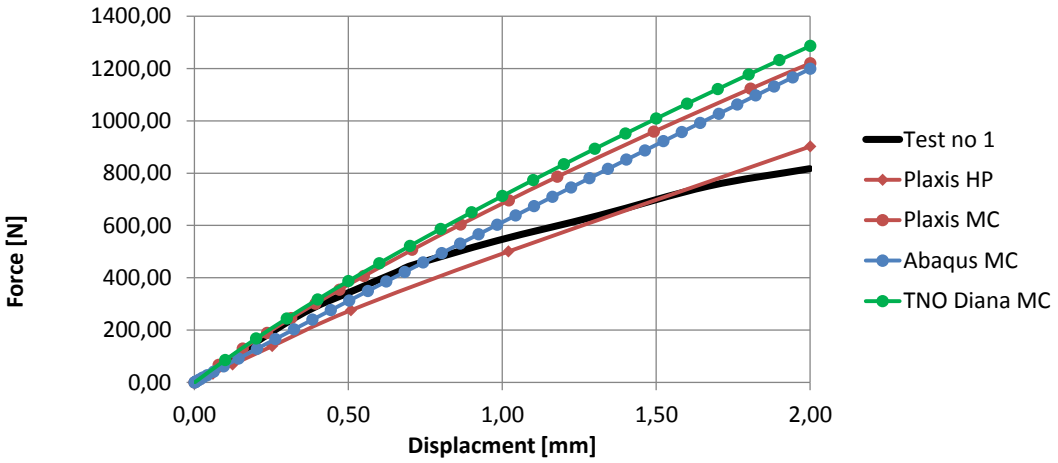

Figure 4.2: Force-displacement results of Abaqus, TNO Diana and Plaxis compared to the physical test results.

The multi criteria analysis is presented in table 4.2. Even though Plaxis remains more advanced in the geotechnical possibilities, only Abaqus and TNO Diana fulfil the requirements for this research. Due to the fact that Kostis' research with Abaqus [10] also included soil-structure interaction in a local buckling problem, Abaqus is used for this research.

Table 4.2: Multi criteria analysis FEM program.

Program	**Local buckling**	**Soil structure interaction**
Abaqus	++	+
Plaxis	- -	++
TNO Diana	+	+

4.4. Model

In Abaqus, pile 6 from the field tests in the Port of Rotterdam is modelled and loaded. From the analysis the diagrams of the displacement and bending moment are derived. Also force-displacement and moment-curvature diagrams are obtained.

Pile 6 has a total length of 22 m and an embedded length of 11.5 m. In the deeper part the earth pressures are high, offering high resistance against horizontal deformation. From the tests it is known that at this level there indeed is hardly any horizontal deformation of the pile (figure 6.9). There has to be a small displacement at the foot of the pile, triggering the high passive earth stress, required for equilibrium of the forces [55]. In the model, the pile and the soil are considered as clamped. The bending moment and shear forces in the pile will be modelled in consistence with the ones found in the field tests. The soil stresses will not be in consistence deeper in the soil. For this research with the focus on the area close to the bed level, that is accepted. As there is a transition between grades of steel at -16.5 m Ref, this level is taken as the bottom level of the model. There is another transition of steel grade at -3 m Ref. In the model the top part is modelled as a beam, constrained to the pile surface. The side boundaries of the model suppress horizontal deformation of the soil. These boundaries have to be set far enough from the pile as to not influence the soil deformation. The vertical and horizontal cross-sections of the model with the applied boundary conditions are shown in figures 4.3 and 4.4.

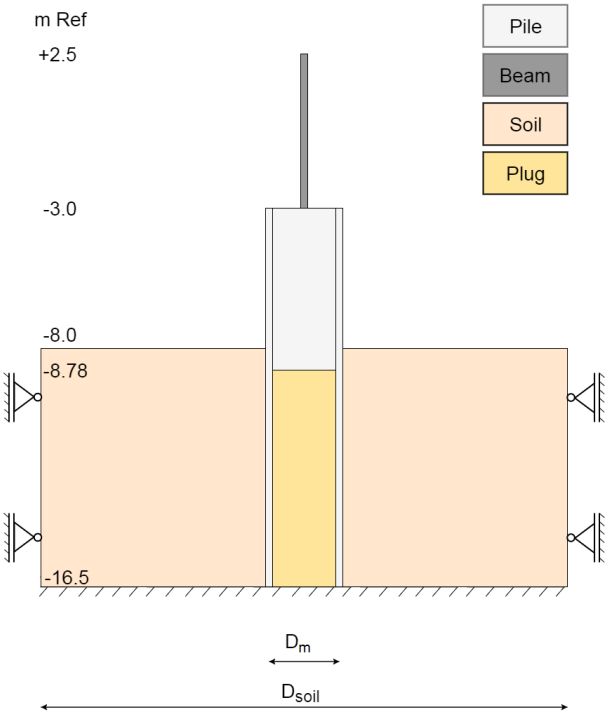

Figure 4.3: Vertical cross-sections of the model with applied boundary conditions.

The initial imperfections that are essential for the failure mode of local buckling are implemented with the aid of a buckling analysis. Through this analysis a buckling mode is obtained, which provides translational and rotational deformations of the elements' nodes. These deformations are used as initial imperfections.

The soil pressures are realized in a Geostatic step with gravitational load. Next, the pile can be laterally loaded. This is done by applying a displacement at the top of the model. Abaqus provides a reaction force corresponding to the applied displacement which can be implied as the lateral load F_v.

In the next sections it is presented how the model is built up.

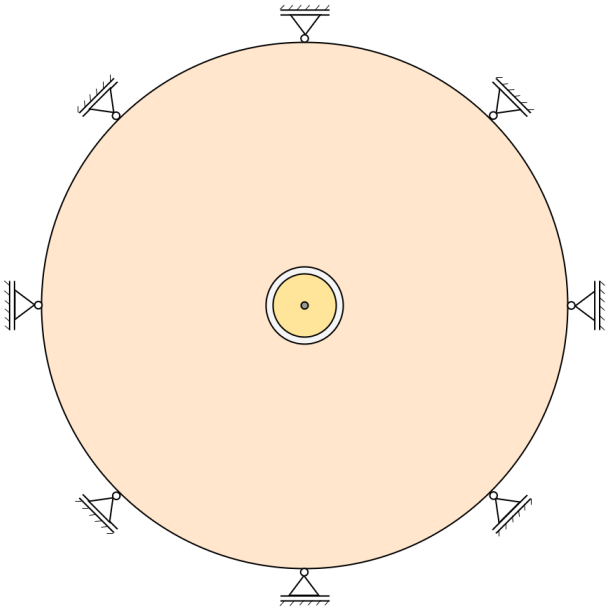

Figure 4.4: Horizontal cross-sections of the model with applied boundary conditions.

4.4.1. Part

In the model are four parts: the mid-section of the pile, the top-section of the pile, the surrounding soil and the soil plug.

The mid-section of the pile is an extruded shell shape. The radius is the radius to the mid-surface of the pile wall, equal to R_m or $\frac{D_e - t}{2}$. For pile 6 this radius is 448.25 mm. It has a length of 13.5 m. The top-section of the pile is a beam with a length of 5.5 m. The plug is a solid with the radius equal to the inner radius of the pile. With the pile being 17.5 mm thick, the radius of the plug is 439.5 mm. The length of the plug is 7.72 m to set the top of the plug at -8.78 m Ref.

The outer soil is also a solid. To determine the radius of the outer soil it should be tested if the boundary conditions do not effect the analysis. To test this, analyses with different soil diameters D_{soil} are run. In each analysis the top of the mid-section of the pile is displaced for 1 m in the x-direction. In Abaqus, this is resembled by the displacement of $U1$ (directions x, y and z correspond to directions 1, 2 and 3 respectively). It is checked whether the displacements of the soil at the boundaries are naturally 0, or if the displacements were forced by the boundary conditions. Generally $D_{\text{soil}} = 15D_m$ or $D_{\text{soil}} = 16D_m$ is used. Analyses are done for factors of 5, 10, 15, 16 and 20. Figures 4.5-4.8 show that there are still deformations at the boundaries. Only for $D_{\text{soil}} = 20D_m$ the horizontal deformations at the boundary are naturally close to 0. In figure 4.9, the horizontal displacements during the analysis are shown for the nodes at the top of the soil highlighted in figure 4.10. They remain below 1 mm. Therefore $D_{\text{soil}} = 20D_m$ is used. In the centre of the soil part, a hole has to be left for the pile and plug. This hole has a radius equal to the outer radius of the pile, 457 mm. (Note that this is equal to half the outer diameter of the pile, which is 914 mm.) To reach up to -8 m Ref, the length of the outer soil is 8.5 m.

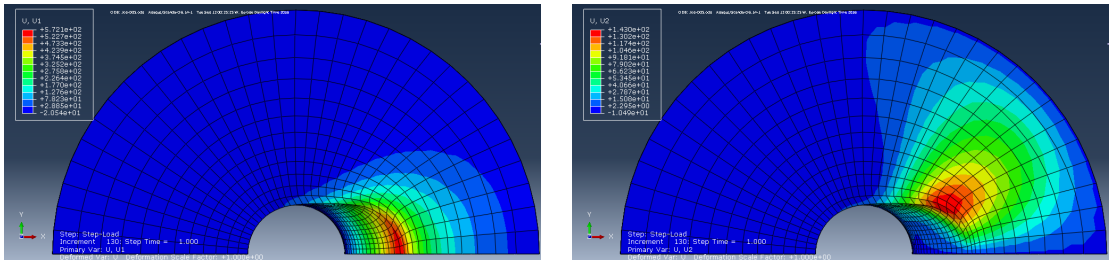

Figure 4.5: $U1$ and $U2$ for $D_{\text{soil}} = 5D_m$

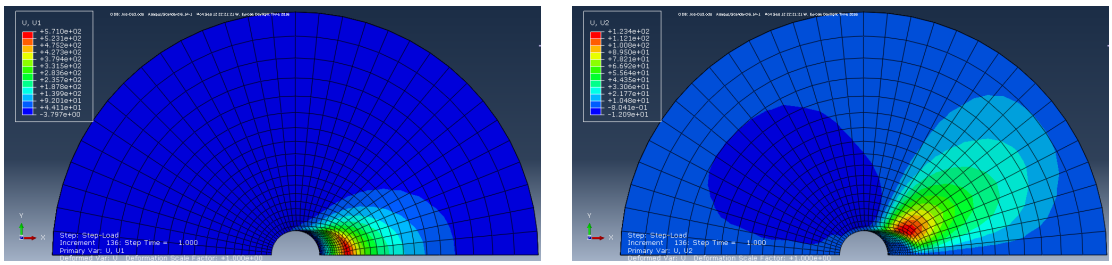

Figure 4.6: $U1$ and $U2$ for $D_{\text{soil}} = 10D_m$

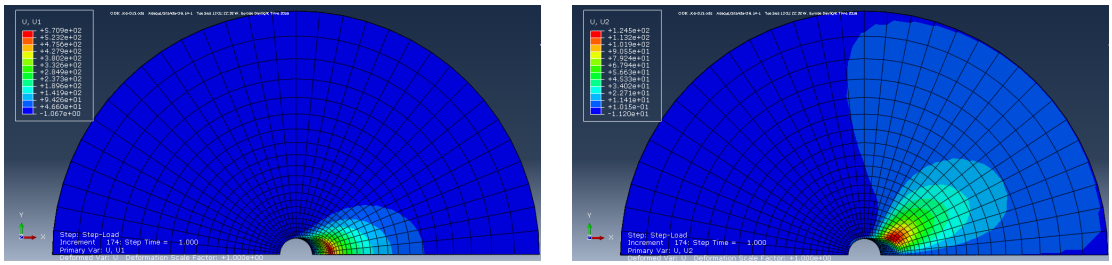

Figure 4.7: $U1$ and $U2$ for $D_{\text{soil}} = 15D_m$

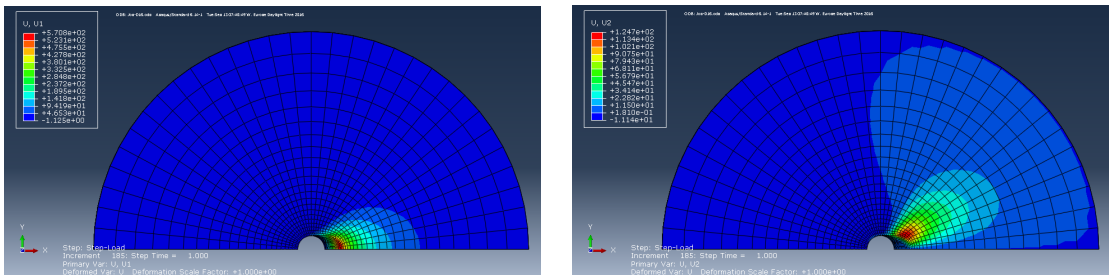

Figure 4.8: $U1$ and $U2$ for $D_{\text{soil}} = 16D_m$

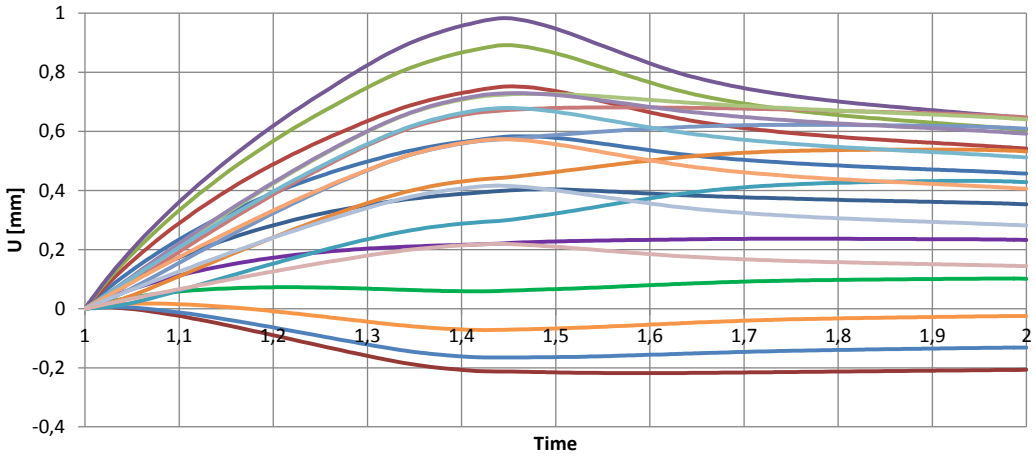

Figure 4.9: $U1$ and $U2$ for nodes close to the boundary during the analysis with $D_{\text{soil}} = 20D_m$.

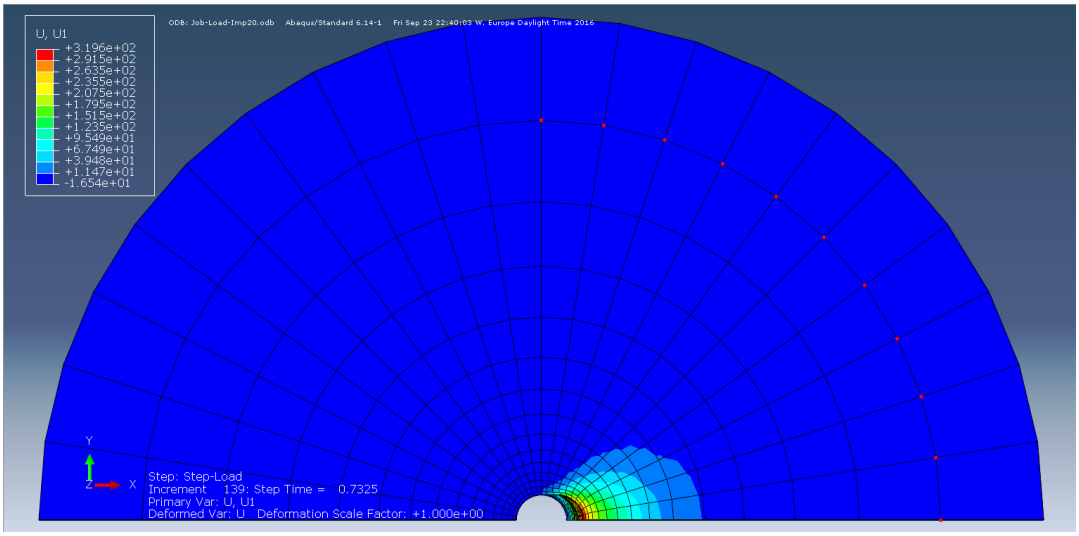

Figure 4.10: Nodes close to the boundary in the model with $D_{\text{soil}} = 20D_m$.

4.4.2. Property

Each of the parts has its own density, elasticity and plasticity properties. The steel pile is given a density of 78 kN/m^3. A Young's modulus E_s of 210,000 MPa is used. The Poisson's ratio ν is set as 0.3. Plasticity values are obtained from the measured stress strain data and are presented in table 4.3. For the maximum measured stress, no strain was provided. It is derived using the hardening modulus as the gradient of the line between the $R_{p1\%}$ and R_m values in the stress-strain diagram.

Table 4.3: Plastic stress strain values for the mid-section of pile 6.

True Stress [MPa]	True Strain
582	0
596	0.01
662	0.084576

The material properties have to be assigned to the parts. As the steel pile wall is modelled as a homogeneous shell, the thickness has to be given its correct value and it has to be defined that the shell is the middle-surface of the pile. Furthermore the number of thickness integration points has to be set. From Kostis' research [10] it is known that this number can influence the results. Therefore, for this pile it was tested how many integration points are sufficient. The same buckling and loading analysis as described by Kostis [10] are performed with different numbers of integration points. Standard 5 points are used, Kostis used 15 points for the implementation of residual stresses, even though it was concluded that 9 points were sufficient. In this thesis therefore, a comparison is made for 5, 7, 9, 11 and 15 thickness integration points. In figure 4.11 the error compared to the analysis with 15 integration points is presented for the critical curvature and the bending moment. From these results, it is concluded that the number of thickness integration points hardly influences the critical curvature or the maximum bending moment (less than 1.0%). Hence, 5 thickness integration points are used.

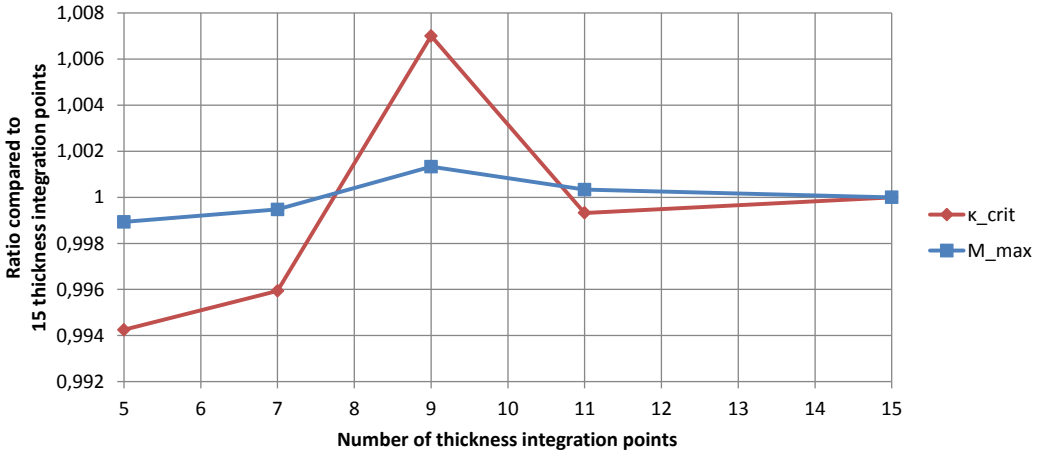

Figure 4.11: Effect of the number of thickness integration points on the maximum bending moment and critical curvature.

For the beam, the same material properties as the pile are used. The required cross-sectional profile that has to be assigned, matches the dimensions of the pile. This part is only used to apply the loading of the pile with a correct corresponding bending moment to the lateral force. Furthermore, no buckling or plasticity is expected in this part.

For the soil in this study, the Mohr-Coulomb material model of Abaqus is chosen, which was also used in Kostis' research with Abaqus [10]. The Mohr-Coulomb material is considered as linearly elastic-perfectly plastic idealized material. This material model allows plastic deformation when the material element yields, but it does not take into consideration the effect of stress history.

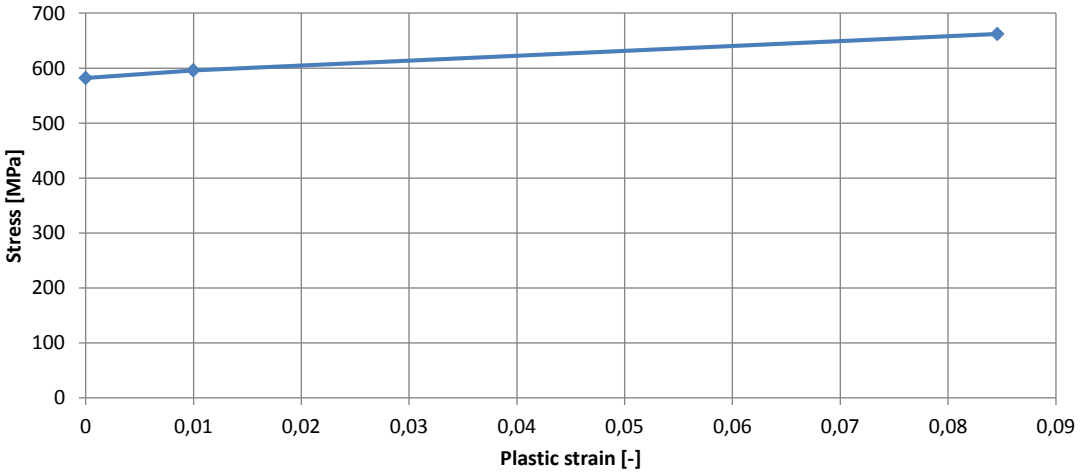

Figure 4.12: Plastic stress strain diagram for the mid-section of pile 6.

Witteveen+Bos made a report for the full scale tests that covers the predictions of the anticipated geotechnical behaviour during the testing of the piles. They compared D-Pile Group, D-sheet Piling, Blum and Plaxis models. The D-Pile Group and Plaxis models are judged reliable. The parameters they used are in table 4.4. The dilitation angle ψ is $\varphi' - 30°$.

Table 4.4: Plaxis soil parameters used by Witteveen+Bos.

Description	γ [kN/m^3]	φ' [°]	c' [kPa]	ψ [°]	E_g [MPa]
Sand, loose to medium dense	19	31	2.5	1	25

From this information, the parameters for the model are obtained. For the elasticity also the Poisson's ratio ν is required. This value defines the ratio between the horizontal and vertical effective stresses by means of equation 4.1. For one-dimensional compression it is the same ratio of the neutral earth pressure coefficient K_0, which was calculated with equation 2.12. Hence, ν is evaluated by matching K_0 (equation 4.2). The Plaxis manual [48] states that in many cases, values in the range between 0.3 and 0.4 will be obtained and that in general, such values also can be used for loading conditions other than one-dimensional compression.

$$\frac{\sigma'_h}{\sigma'_v} = \frac{\nu}{1-\nu} \tag{4.1}$$

$$1 - \sin\varphi' = \frac{\nu}{1-\nu} \tag{4.2}$$

Due to vibrations during the installation of the pile, the plug will be compacted and can be expected to be stiffer than the surrounding soil. Kostis [10] also showed that a higher stiffness of the soil resulted in a better agreement of his model with the test results. The stiffness in this thesis is assumed to be four times the stiffness of the surrounding soil. The properties are similar to dense sand in table 2.b of the NEN-EN 9997-1 [38]. The cohesion is not adapted, as Abaqus requires a small value to run [10]. The soil packing is one of the key parameters, analysed in paragraph 5.1. The used parameters for the soil in the Abaqus model are in table 4.5. They are assigned to the parts as homogeneous solids.

Table 4.5: Soil parameters used in the model.

Part	γ [kN/m^3]	φ' [°]	c' [kPa]	ψ [°]	E [MPa]	ν [-]
Soil	19	31	2.5	1	25	0.33
Plug	19	39	2.5	9	100	0.27

4.4.3. Interaction

The contact between the soil and the pile has to be defined. As they cannot intersect each other, for the normal behaviour "Hard" Contact is used. In reality, a gap can arise behind the pile, when it is deflected. Therefore, in the model, separation after contact is allowed. Also friction exists between the soil and the pile. This can be implemented by defining tangential behaviour with a penalty formulation. The value of the friction coefficient is the tangent of the soil-wall friction angle of δ. In this thesis $\delta = 2/3\ \varphi'$ is assumed. The surface-to-surface contact is defined between the outer surface of the pile and the attached inner surface of the hole in the soil part. Equivalently, the contact interaction between the inner surface of the pile and the outer surface of the plug is defined. For both interactions, the stiffer pile wall is set as master-surface.

The top-section (modelled as a beam) has to interact with the mid-section (modelled as a circular extruded shell). This is done with a kinematic constraint between the bottom node of the beam (master) and the top surface of the pile (slave). They are constrained to all degrees of freedom.

For the buckling analysis, two reference points are required to apply a rotation to the pile as explained in paragraph 4.4.4. One is at the top of the pile and the other is created lower in the pile. Here the pile part has to be partitioned in order to create the cross-sectional surface. The constraints are again kinematic coupling constraints, constrained to all degrees of freedom. In the loading step, they are suppressed.

4.4.4. Step

The complete analysis is split up in two. First a buckling analysis is performed to obtain nodal displacements. These are used as initial imperfections in the second analysis, the loading analysis.

Buckling Analysis

Generally the buckling analysis is used to estimate the critical (bifurcation) load of 'stiff' structures (classical eigenvalue buckling) [56]. However, for this thesis a general eigenvalue buckling analysis provides useful estimates of collapse mode shapes. When the pile is subjected to a constant bending moment, by applying two evenly sized, oppositely directed rotations at two cross-sections, the first two buckling modes will be half of a sine wave between these cross-sections (figure 4.13). The soil and plug and their interactions have to be suppressed. The modes are on the opposite sides of the pile (figure 4.14). In the loading analysis, these deformations can be implemented as initial imperfections. In the imperfection, local buckling can be initiated [24]. The maximum displacement in the buckling analysis is 1 mm. For the initial imperfections, this can be scaled to the preferred size. To be able to use the buckling mode for initial deformations, the keywords of the buckling model have to be edited. This is presented in appendix D. The size of the initial imperfections that should be used is studied in paragraph 4.6.

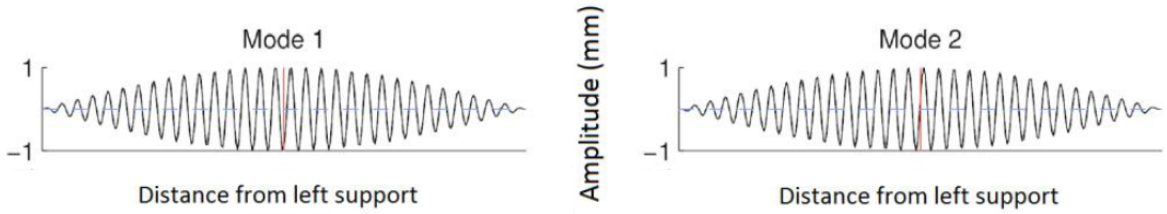

Figure 4.13: First two buckle modes for a pile under pure bending. [10]

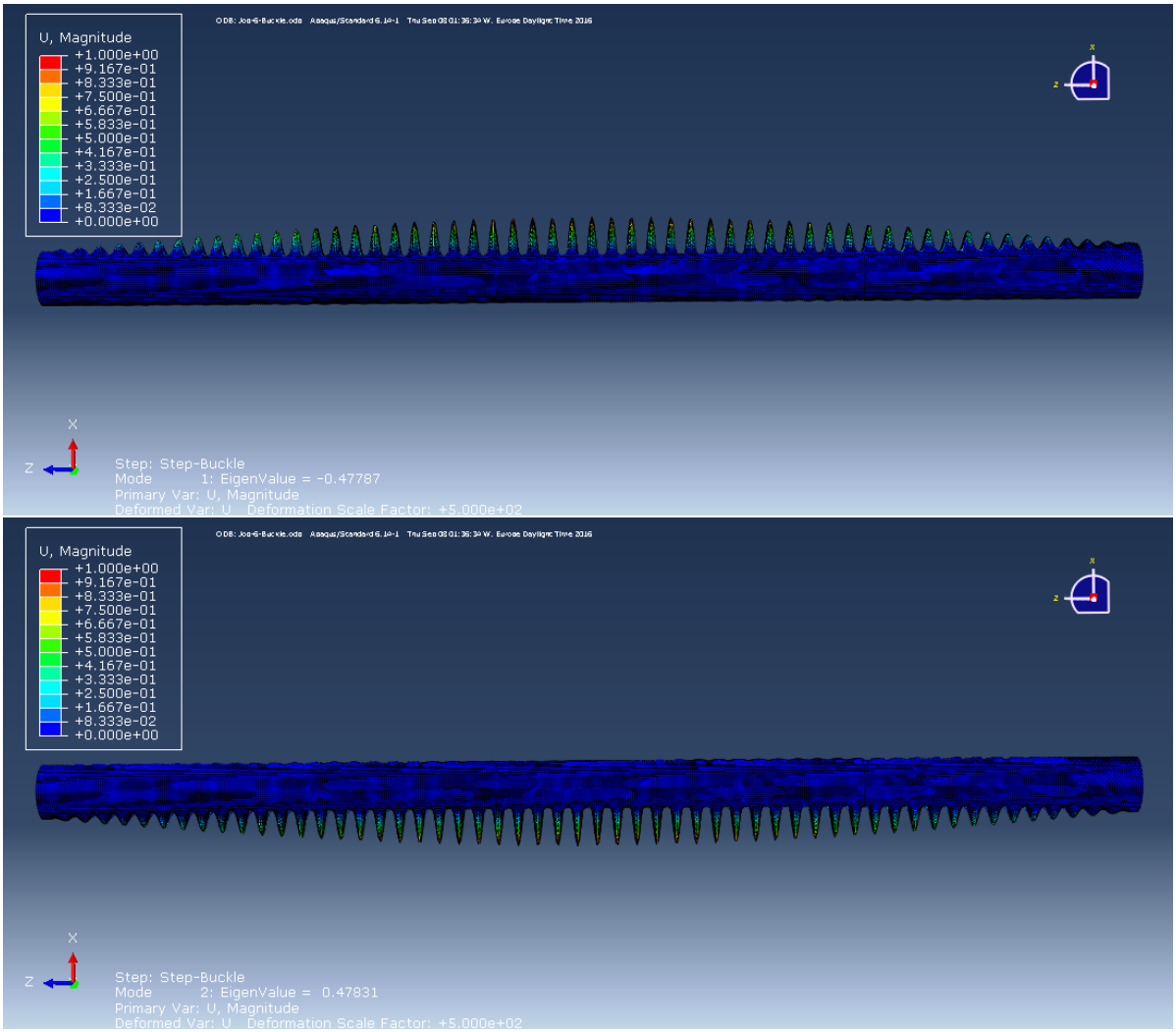

Figure 4.14: First two buckle modes for a pile under pure bending.

Loading Analysis

Before the model can be laterally loaded, the initial soil pressures have to be realised in a Geostatic step. Next the top of the beam is given a lateral displacement in a Static General step.

First, however, the initial dimples from the Buckling analysis have to be implemented (see appendix D).

In the Geostatic step, gravity is applied on the soil and plug. Besides setting the gravitational load, the keywords have to be edited. How this is done, is reported in the appendix.

After the soil stresses are set, the pile can be deformed. Geometrically nonlinear static problems involve buckling or collapse behaviour, where the load-displacement response shows a negative stiffness and the structure must release strain energy to remain in equilibrium. Several approaches are described in the Abaqus user's guide [56] for modeling such behaviour. One is to treat the buckling response dynamically, thus actually modeling the response with inertia effects included as the structure snaps. In some cases displacement control can provide a solution, even when the reaction force is decreasing as the displacement increases (figure 4.15). Another approach would be to use dashpots to stabilize the structure during a static analysis. Alternatively, static equilibrium states during the unstable phase of the response can be found by using the "modified Riks method".

The latter was used by Kostis [10], but as also stated in the Abaqus user's guide [56] "for postbuckling problems involving loss of contact, the Riks method will usually not work; inertia or viscous damping forces (such as those provided by dashpots) must be introduced in a dynamic or static analysis to stabilize the solution". As contact with the soil and the plug is lost this method does not work. Alternatively the displacement controlled static general step is used, which finds equilibrium. No stabilization is required.

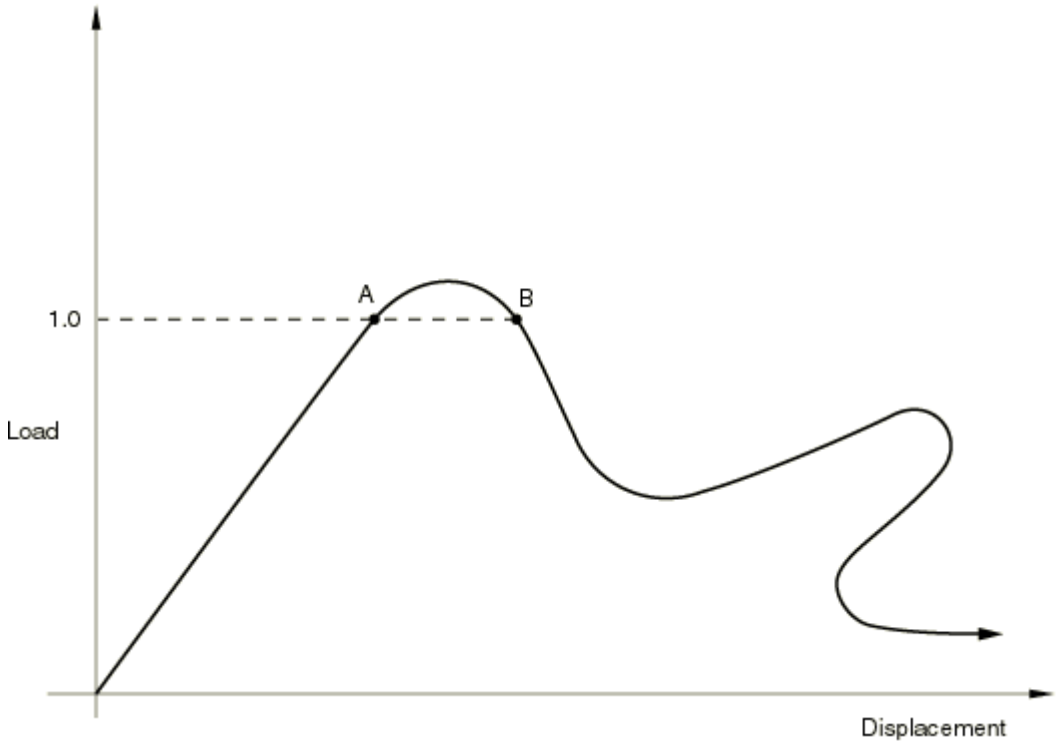

Figure 4.15: Unstable response: increasing displacement and decreasing reaction force. [56]

4.4.5. Boundary conditions

Buckling Analysis

In the buckling analysis the boundary conditions are applied on two cross-sections, between which a constant moment is introduced by applying a rotation on these cross-sections. One cross-section should be constrained in the directions U1, U2, UR1 and UR3. The other cross-section should be constrained in U1, U2, U3, UR1 and UR3. These conditions prevent the pile from rotating or moving, but allow one side to slide along the pile axis.

Local buckling will be initiated easier in the largest imperfections. To exclude this effect, the sine wave of the buckling mode has to be long enough. Then, in the area where local buckling is expected, the imperfections are approximately of the same size. As local buckling could occur at the transition at the bed level, at the transition at the plug level and at the position of the maximum bending moment, this area is between the bed level and approximately $2D_e$ below the bed level. The dimples are assumed to be the same size, when the amplitude is between 0.95 and 1, with 1 being the maximum amplitude. A buckling mode with a length of $12D_e$ fulfils these requirements (figure 4.16). This means the cross-sections on which the rotations are set, are located $5D_e$ away from the area where local buckling is expected.

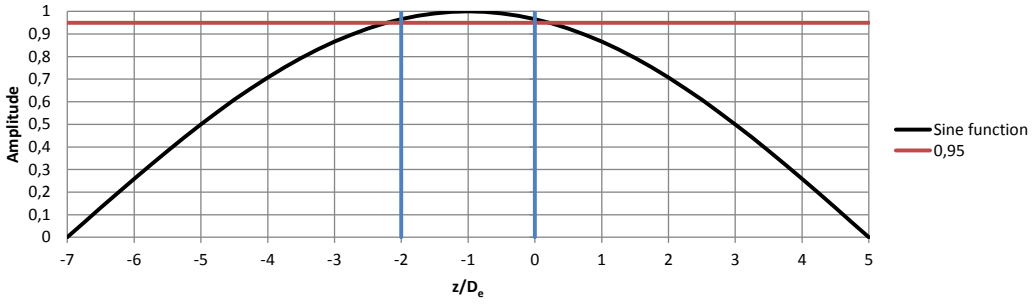

Figure 4.16: The dimples in the area of $2D_e$ where local buckling is expected have an amplitude of more than 0.95 for a buckling mode with a length of $12D_e$.

Loading Analysis

The bottom of the model is clamped, as explained before. This is done with an encastre boundary condition. Also as mentioned before, the side boundaries at the soil are prevented to move in the $U1$ and $U2$ direction.

To simplify and speed up the calculation in the Geostatic step, boundary conditions are applied on the surfaces of the hole in the soil and on the side surfaces of the plug. They too are constrained in the U1 and U2 direction. These boundary conditions are suppressed in the Static General step.

4.4.6. Load

Buckling Analysis

The pile is subjected to a constant bending moment, by applying two equal, oppositely directed rotations at the two cross-sections $5D_e$ away from the area where local buckling is expected. In the buckling analysis, the maximum rotation component is normalized to 1.0, because all displacement components are zero [56]. The size of the rotation therefore does not matter. It is chosen to set them to 1.0 radian.

Loading Analysis

In the Geostatic step, gravity is applied. As the density was inserted with the units of N/mm^2, the gravity is set to -1 in the U3 direction on the soil. On the plug, the gravitational force is adjusted. The stress at the top of the soil and plug is 0 kN/m^2. As the soil is 8.5 m deep in the model and has a density of 19 kN/m^3, the stress at the bottom will be 161.5 kN/m^2. For the plug, the stress at the bottom will be the same, as originally there was also 8.5 m of sand on top. However the plug is only 7.78 m deep. To compensate for this, the gravitational force will be set bigger. The value is equal to the ratio of the depth of the soil over the depth of the plug. In this case $\frac{8.5}{7.78}$.

The lateral displacement is applied at the top of the beam. In the field test a maximum displacement of 1.5 m was observed. To be sure the pile will buckle, a displacement of 2.5 m is applied.

4.4.7. Mesh

Element types

The pile is modelled by shell elements, because it is a thin walled structure. The soil and plug are modelled by 3D solid elements. The pile could also be modelled by 3D solid elements, but the shell elements are preferred because of their computational efficiency.

The shell elements of the pile are S4R elements. Kostis compared the S4 element that uses full integration with the S4R element that uses reduced integration with hourglass control. Also a comparison with the 2^{nd} order accuracy was made. The results are equal. Due to its computational efficiency the S4R element is used.

The S4R element is a 4-node general-purpose shell element that uses reduced integration with hourglass control and has finite membrane strains. It has 6 active degrees of freedom. The numbering of the integration points are presented in figure 4.17.

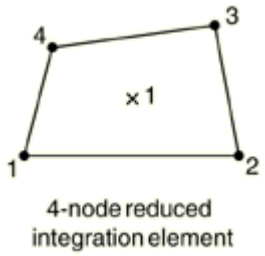

Figure 4.17: Numbering of the integration points for the S4R element. [56]

The Abaqus manual [56] provides recommendations for the selection of the solid elements. Taking these recommendations into account the C3D8 element is chosen. This element can again be compared to the variant with reduced integration (C3D8R) and it can be checked if 2^{nd} order element should be used. This was also done by Kostis [10]. The results show same results in a moment-curvature diagram and only minor differences in the ovalisation-curvature diagram. Kostis [10] points out that there could be mesh size issues with the C3D8R element in fine meshes. Also in bending this element tends to be not stiff enough in bending. Furthermore, no computational efficiency was experienced [10]. Therefore the C3D8 element is used.

The C3D8 element is an 8-node linear brick. It has 3 active degrees of freedom. The node ordering and face numbering on the element are presented in figure 4.18.

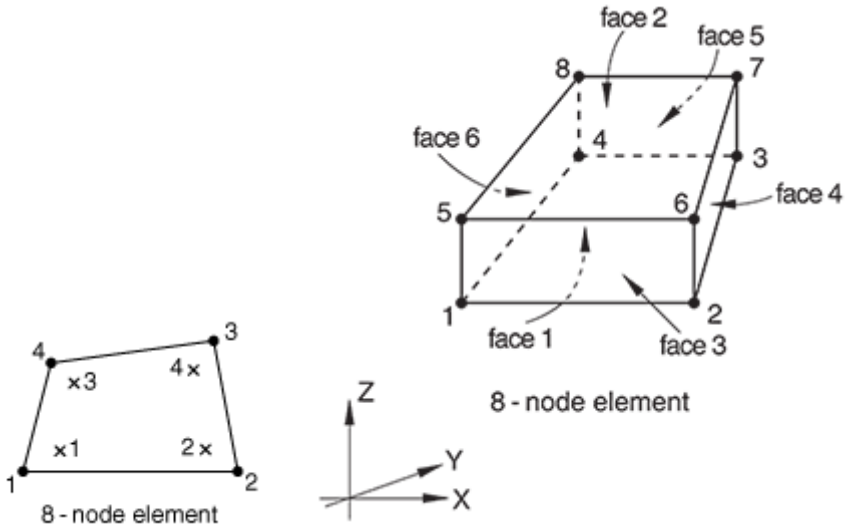

Figure 4.18: Node ordering and face numbering on the C3D8 element. [56]

The top part is modelled as a thin-walled pipe with B31 elements. These are 2-node linear beam elements. It has 6 active degrees of freedom and one additional variable relating to the hoop strain. The node ordering on the element and the integration point for output is presented in figure 4.19.

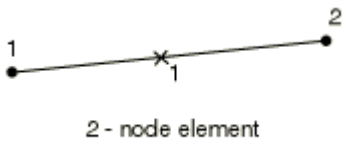

Figure 4.19: Node ordering and integration point for output on the B31 element. [56]

Mesh size pile

To be able to analyse local buckling behaviour properly, in the buckling analysis, the buckling mode has to be captured. A fine mesh of the pile is required in order not to skip a dimple and catch its maxima. Preferably several elements define the dimple. Kostis [10] used a mesh size of approximately $0.04D_m$. A comparison in the range of $0.02D_m$ to $0.10D_m$ is made for a pile under pure bending, without soil or plug. With D_m = 896.5mm, the maximum moment and critical curvatures of mesh sizes of 20, 30, 45, 60 and 90 mm are compared (4.20). It is clear that the maximum moment does not differ much for the different mesh sizes. However, there is a significant change in the critical curvature. That is because the bending moments reached are beyond the elastic moment, when the bending moment only increases slightly compared to an increasing curvature. Fewer degrees of freedom result in a faster analysis, yet can give inaccurate results. The optimum of both is achieved with a mesh size of 35 mm (approximately $0.04D_m$). The results only slightly differ from the finer mesh, yet they are obtained much faster.

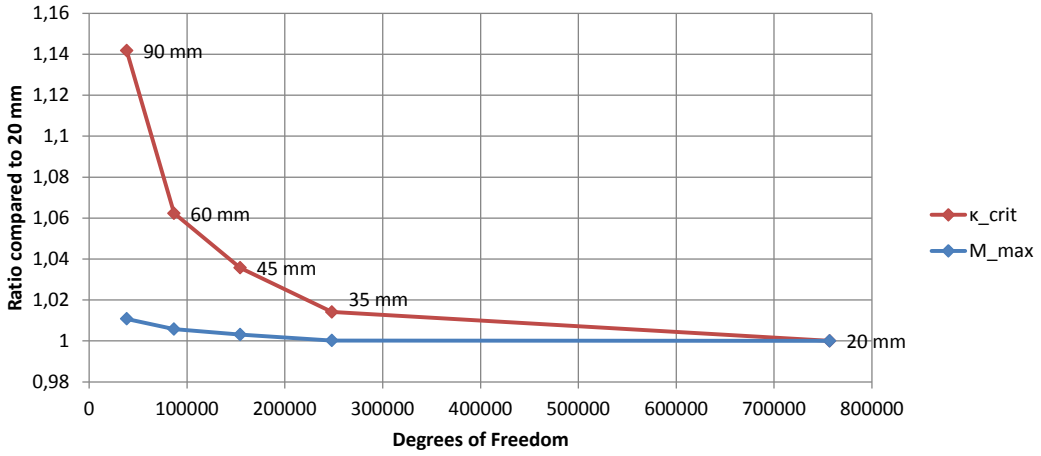

Figure 4.20: Pile mesh size effect on the critical curvature and maximum moment.

To decrease the number of degrees of freedom, outside the area that is loaded in the buckling analysis, the vertical mesh size can be increased. The mesh size in the circumferential direction remains the same. Analyses have been performed for a factor 2, 4 and 8 (mesh sizes of 70, 140 and 280 mm respectively). In these analyses the pile was loaded at the ends, and the transition in mesh size is $5D_m$ from the middle of the pile, where buckling is expected. The results are visualized in figure 4.21. Even though the pile in the model will not be loaded in the same way, from these analyses, it can be concluded that elements with a difference in size of a factor 8 do not exchange stresses accurately, causing deviating results. Therefore, a factor of 4 is applied in the model.

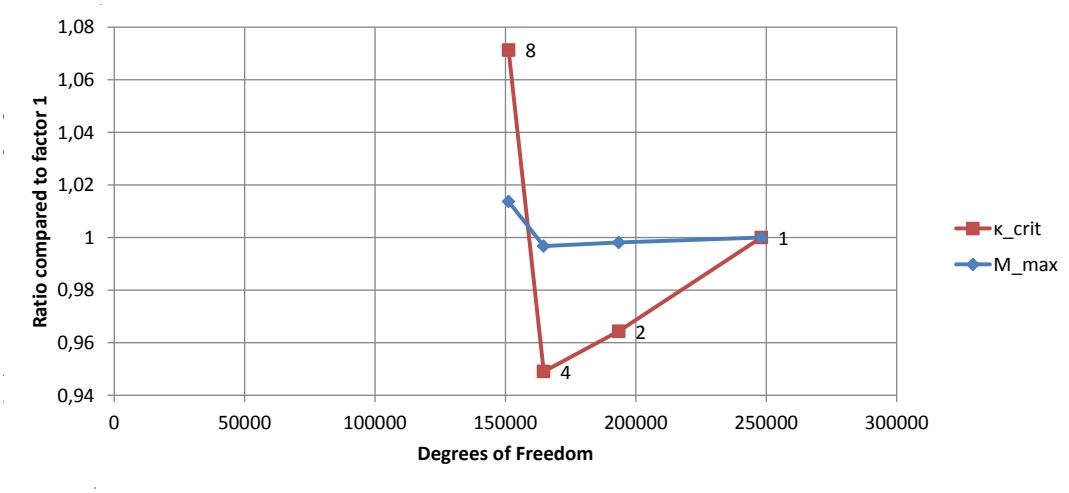

Figure 4.21: Effect of mesh size factor.

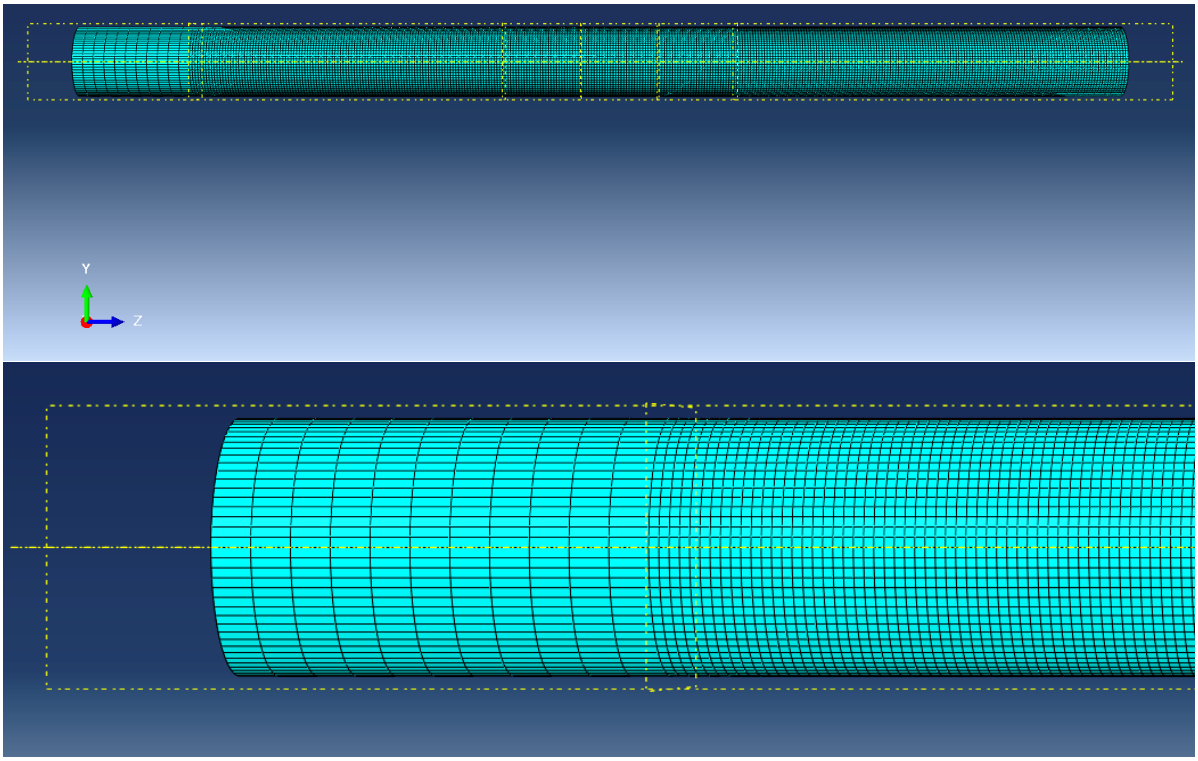

Figure 4.22: Meshed pile.

Mesh size beam

The factor 4 is also applied on the factor between the element sizes between the pile and the beam. The elements of the beam are therefore 140 mm.

Mesh size plug

The mesh size of the plug is related to the mesh size of the pile. The elements should be small enough to move in the dimple and provide correct contact stresses to the pile wall. Kostis [10] checked the effect of the mesh size of the solid elements and concluded that the mesh size is not playing an important role. A factor 2 can be applied. The elements are therefore approximately $0.08D_m$, or 70 mm, in meridional direction and in circumferential direction. In the lower part, where the pile has a coarser mesh, the mesh of the soil is also a

factor 2 larger: 280 mm.

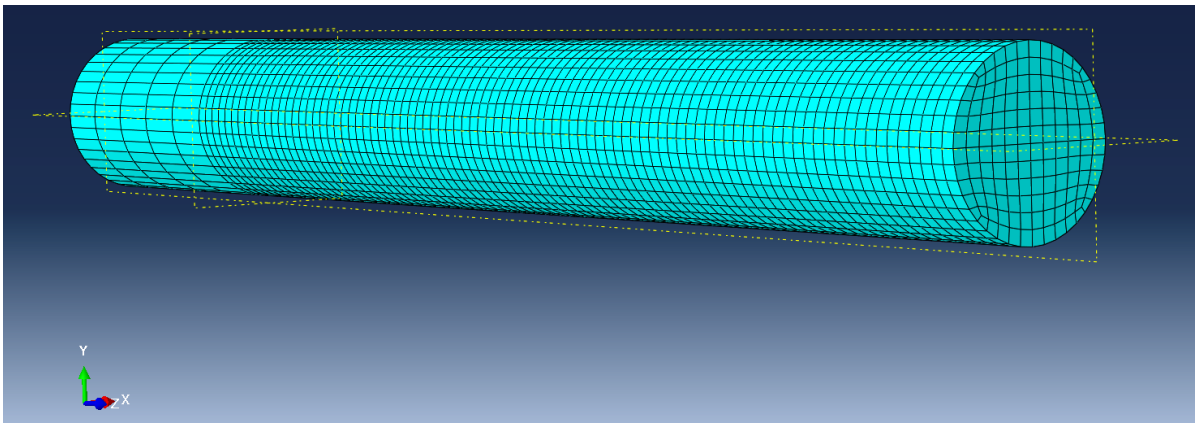

Figure 4.23: Meshed plug.

Mesh size soil

The mesh size of the soil at the interaction with the pile is the same as the plug approximately $0.08D_m$, in meridional and circumferential direction. Towards the outside of the model, away from the pile, the mesh size can be increased. This is done by seeding local edges biased by size, from the outer circumference of the soil towards the pile. The minimum and maximum size is preferably as big as possible, minimizing the number of elements. However, the size may not influence the results. Analyses with a minimum size of $0.04D_m$ and maximum sizes of $0.5D_m$, $1.0D_m$, $2.0D_m$ and $4.0D_m$ are compared in figure 4.24. In these analyses, the pile was loaded at the top cross-section with 10 kN, and the U1 deformation results at the top of the pile are compared to the deformation with a maximum mesh size of $0.5D_m$.

It can be seen that a maximum size larger than $2.0D_m$ rapidly deviates. A maximum size of $3.0D_m$ still results in 0.990 times the deformation of the finer mesh. For the coarsest mesh this ratio is already 0.982, without significantly reducing the number of elements (and hence the number of degrees of freedom). Next the same comparison is made for meshes with a minimum size of $0.08D_m$, and maximum sizes of $0.5D_m$, $1.0D_m$ and $2.0D_m$. Approximately the same number of degrees of freedom are used for a maximum mesh size of $2.0D_m$ as for a mesh with a maximum mesh size of $3.0D_m$ and a minimum mesh size of $0.04D_m$. The prior ends with better results compared to the finest mesh. Therefore, the biased seeding is done with a minimum mesh size of $0.08D_m$ (70 mm) and a maximum of $2.0D_m$ (1882 mm).

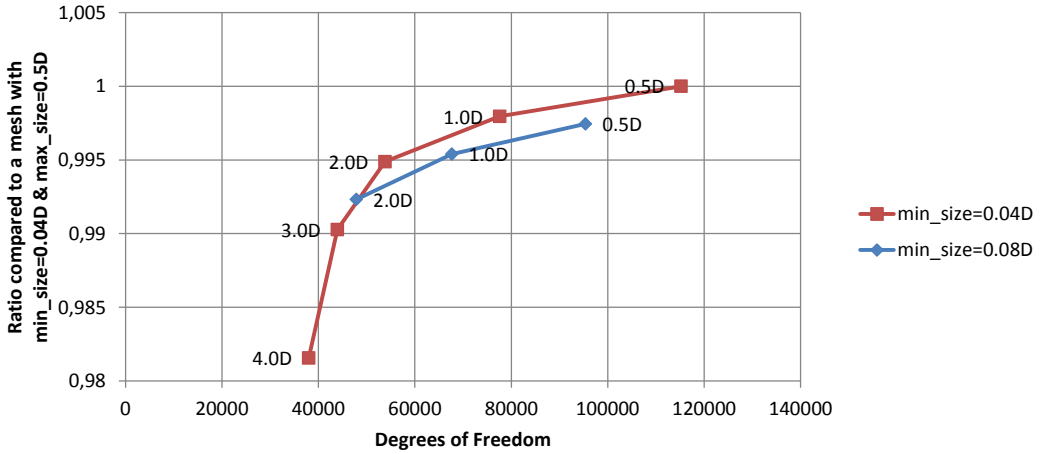

Figure 4.24: Effect of the minimum and maximum mesh size on the biased seeded edges.

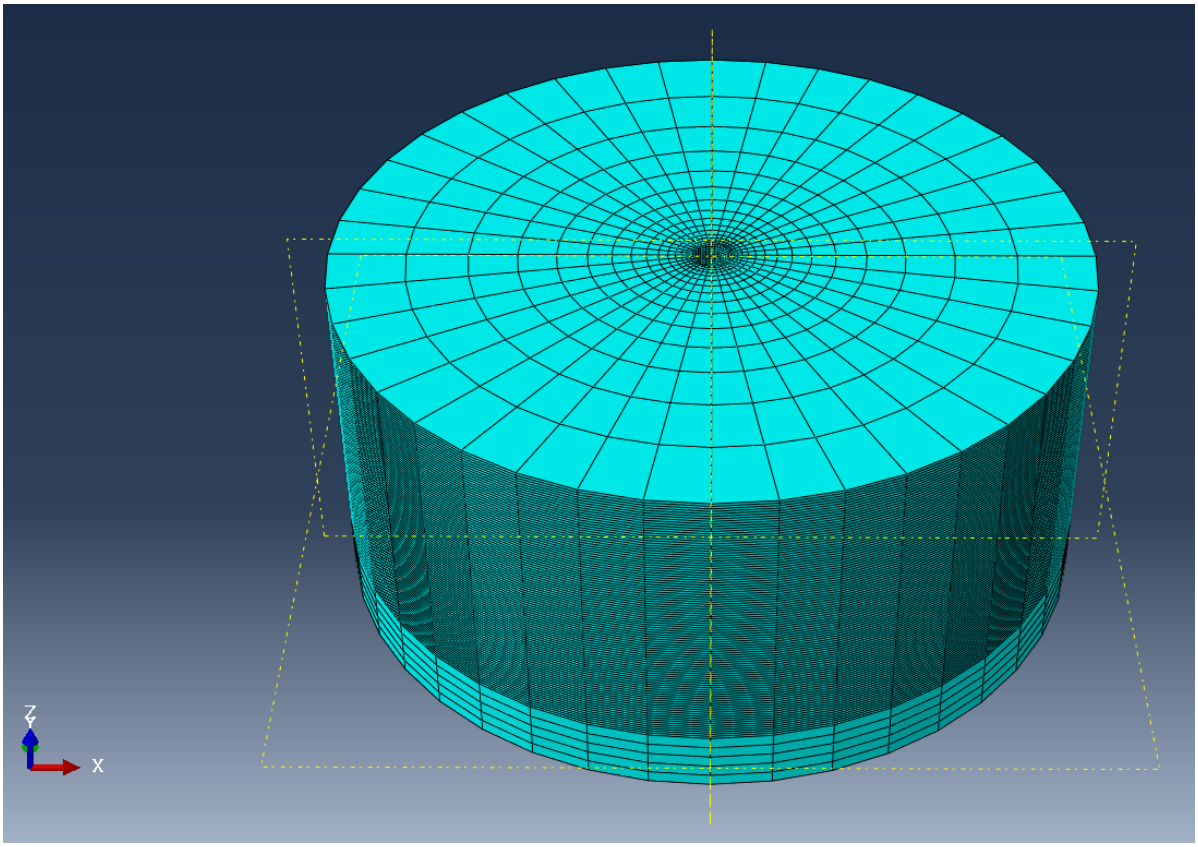

Figure 4.25: Meshed soil.

4.5. Post-processing

Once the analysis is completed the results can be obtained. Diagrams required to study the effect of the parameters are the force-displacement, moment-curvature and bending moment diagrams.

The force-displacement diagram illustrates the relation between the applied force and the displacement at the top of the dolphin at z_f. These are obtained by extracting the ODB field output U1 and RF1 of the top node of the beam.

The curvature is determined from the displacements. With a second order central difference formula (equation 4.3), the second derivative is estimated.

$$\frac{\partial^2 y}{\partial z^2} \approx \frac{y(z-h) - 2y(z) + y(z+h)}{h^2} \tag{4.3}$$

This estimate is $O(h^2)$ accurate. In general a small step size h gives more accurate results. However, the step size is too small when a local disturbance results in a local curvature in stead of the global curvature. A buckle can be such a disturbance. In a NASA Technical Memorandum [57] a formula for the optimal step size is presented:

$$h_{\text{opt}} = 2\sqrt{\frac{e}{\kappa}} \tag{4.4}$$

Here κ is the curvature derived with the second order central difference formula and e is a bound on the absolute error in the computed value. For small curvatures a higher step size is required. The other way around, for larger curvatures a smaller step size is required. The error in equation 4.4 should not be excessive. On the other hand, when the condition error is very small, there is a risk of high truncation errors. According to the NASA Technical Memorandum [57] the error should not be below 0.001. Here, an error of 0.003 is assumed acceptable. The range of κ where local buckling occurs is approximately between κ_e and $3\kappa_e$. The

optimal step size h ranges between 0.80 and 1.39. Hence, a step size of 1.00 m is chosen to calculate the curvature.

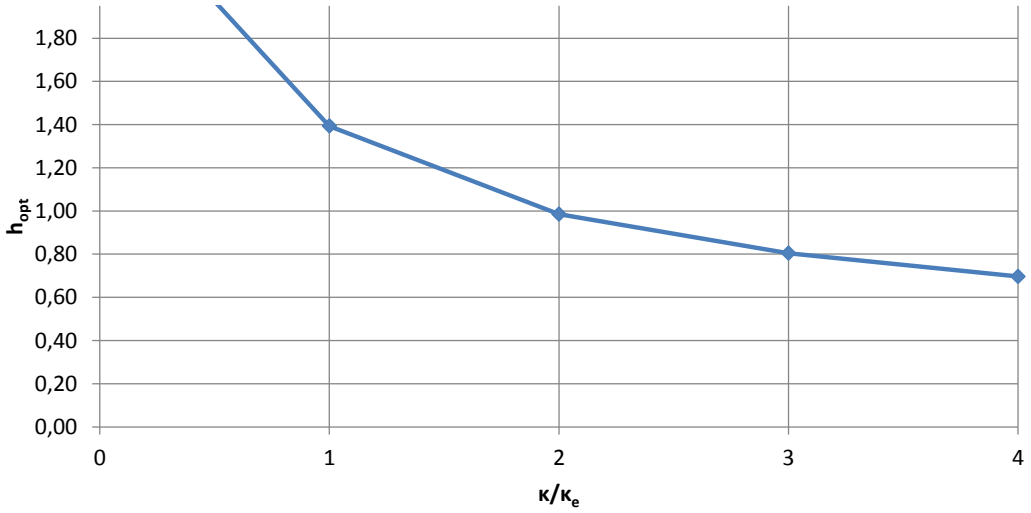

Figure 4.26: Optimal stepsize h.

The curvature is calculated at the depth where the maximum bending moment is observed. Often the higher point at $z+h$ in equation 4.3 is above the depth where a local buckle is formed. After buckling the pile deforms here faster than below the buckle. Hence, the calculated curvatures after local buckling are not reliable.

The pile is partitioned in such a way that every meter, results can be obtained (figure 4.27). To exclude ovalisation in the displacement of the pile, the displacement U1 is gathered on the Y-axis of the pile at the partitioned cross-sections.

At the partitioned levels, 'free body cuts' are created. Such a free body cut sums all the nodal forces at the cross-section, through which the shear force of the cross-section is obtained. Also all the contributions of the nodes to the cross-sectional bending moment around its neutral axis are summed. This tool is especially handy when a cross-section is in the elastic-plastic range. For the shear force, the force component 1 is required. Moment component 2 is used to obtain the bending moment of the cross-section. The bending moment diagram is produced assuming no bending moment at both ends of the dolphin pile.

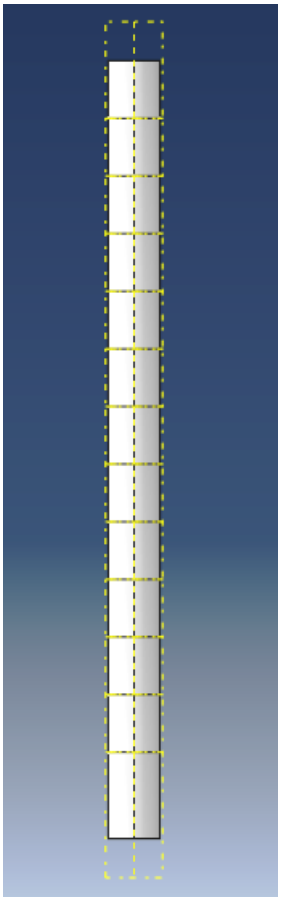

Figure 4.27: The pile is partitioned every meter.

4.6. Imperfection

The initial imperfections are produced by scaling the deformations obtained in the buckling analysis. The scale factor that has to be used is studied in this paragraph.

The size of the initial imperfections influence the bending moment capacity [10][52]. Kostis [10] studied the imperfection over thickness ratio in a range from 0.04 to 0.20. The results showed that for a ratio of 0.20 his model got closest to the test results, but even a higher percentage is needed. An extensive study is done on the use of the scale factor. Analyses are run for imperfection thickness ratios of 0.05, 0.10, 0.20, 0.30, 0.40, 0.60 and 0.80. Ratios of 0.05 and 0.10 would be classed in fabrication tolerance quality class A. 0.20 and 0.30 are class B and class C ratios respectively. The higher ratios would not be accepted if imperfections of these sizes are measured. These are tested to study their impact on the finite element analysis and its comparison with capacities obtained in the field test. Here the focus is on the impact of the imperfection ratio. A more thorough validation of the model is presented in chapter 6. In theory, if there are no imperfections, a dolphin pile will not show failure due to local buckling. It is expected that for smaller imperfections, buckling occurs with a higher load. The energy capacity as well as the bending moment capacity are expected to be higher for smaller imperfections.

All analysis showed local buckling to occur approximately 1.2 meters ($1.3D_e$) below the bed level. This only differs for the very large imperfections. Notable is that there are two buckling shapes occurring. For large imperfections the dolphin buckles inward. This is a typical buckling shape, also seen with empty tubes (figure 4.28). The smaller imperfections show an outward buckle. Filled piles, where the filling provides a radial support, typically have this buckling shape as can be seen in figure 4.29. Both shapes are experienced for piles in the field (figure 4.30). An inward buckle was encountered in the field test for pile 6 (6.5). A buckle moves inward or outward depending on the resistance of the soil and the plug. The initial imperfection in

Table 4.6: Scale factors for tested imperfection thickness ratios.

Imperfection/Thickness	Imperfection [mm]	Scale factor
0.05	0.875	0.4375
0.10	1.750	0.8750
0.20	3.500	1.7500
0.30	5.250	2.6250
0.40	7.000	3.5000
0.60	10.500	5.2500
0.80	14.000	7.0000

the pile also causes an initial imperfection in the plug. This decreases the resistance of the plug. Hence, a bigger imperfection paves the way for an inward buckle. Furthermore, the resistance is influenced by the soil pressure and the passive earth pressure coefficient. Therefore, the depth and the packing density of the soils might also influence the buckle shape.

Table 4.7: Buckle location and shape for tested imperfection thickness ratios.

Imperfection/Thickness	z_{buckle}	$\lvert z_{\text{buckle}}/D_e \rvert$	Buckle shape
0.05	-1.2	1.3	Outward
0.10	-1.2	1.3	Outward
0.20	-1.2	1.3	Outward
0.30	-1.2	1.3	Outward
0.40	-1.2	1.3	Inward
0.60	-1.1	1.2	Inward
0.80	-0.8	0.9	Inward

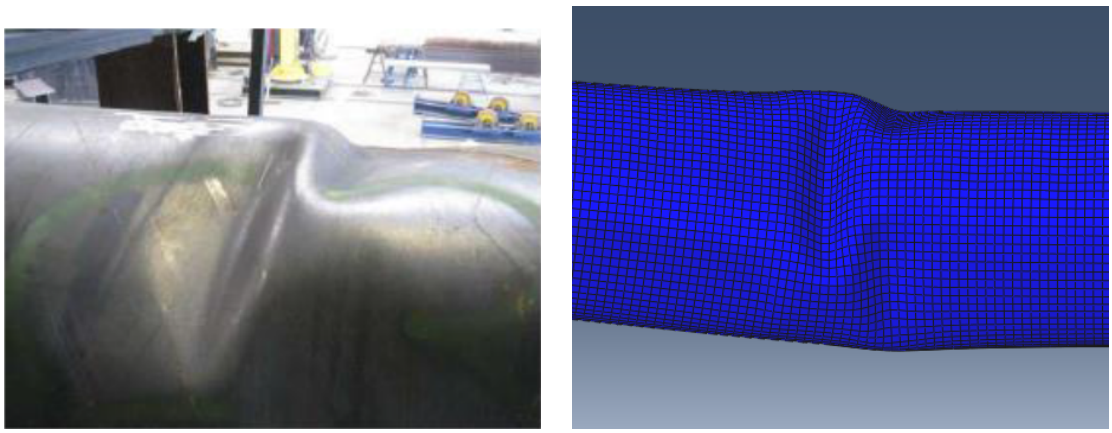

Figure 4.28: Typical inward buckle from lab test (left) [10] and in Abaqus (right).

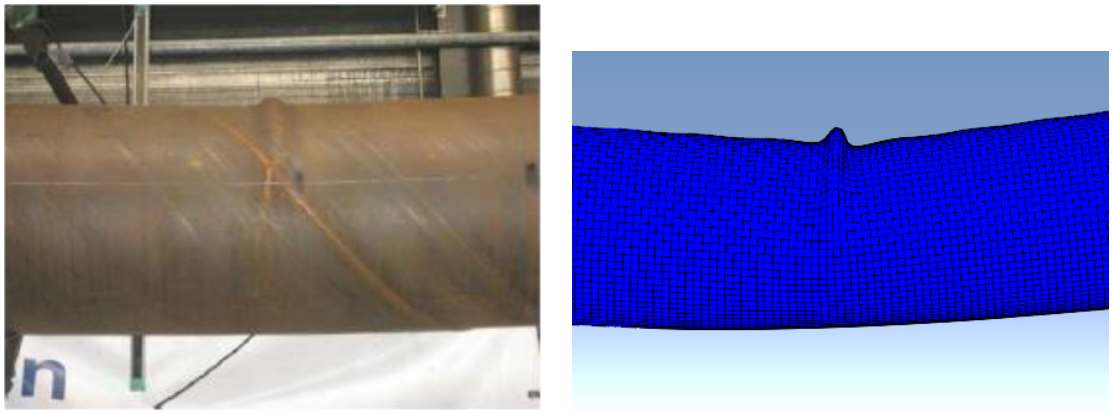

Figure 4.29: Typical outward buckle from lab test (left) [10] and in Abaqus (right).

Figure 4.30: Buckle shape of empty (left) and sand-filled pile (right) experienced in the field. [18]

In all tests, the maximum bending moment occurred at the same level (figure 4.31). From the moment-curvature diagram in figure 4.32, it becomes clear that the critical curvatures (related to the maximum bending moment) for the smaller imperfections indeed have higher values for the critical curvature κ_{cr}, as well as for the maximum bending moment M_{max}. Except for the imperfection thickness ratios of 0.05 and 0.10, the critical curvatures are quite similar (0.0136-0.0141). The maximum bending moments however, have a wide range. An imperfection thickness ratio of 0.40 shows best comparison to the measured maximum bending moment of pile 6 (7611 kNm).

A closer look to the moment-curvature diagram comparing the results from Abaqus with the analytical method used to evaluate the results from the field measurements shows that, before local buckling occurs, the results in Abaqus deviate. For the same curvature, a lower bending moment is obtained. This can be explained by the absence of the ovalisation effect in the used analytical method. EN 1993-4-3 [2] prescribes how ovalisation can be taken into account. Assuming pure bending (neglecting the soil pressures), the analytical moment-curvature diagram for an imperfection ratio of 0.40 would be as illustrated in figure 4.33.

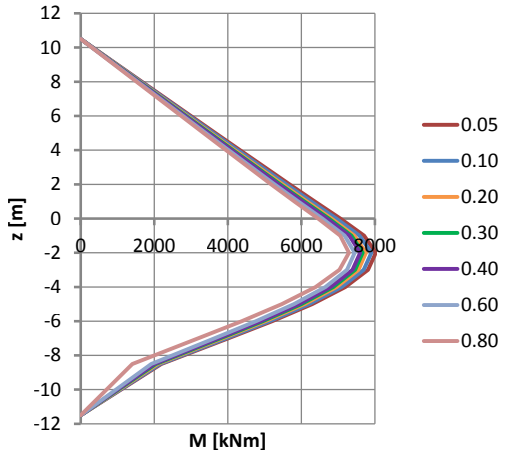

Figure 4.31: Bending moment diagram for different imperfection thickness ratios.

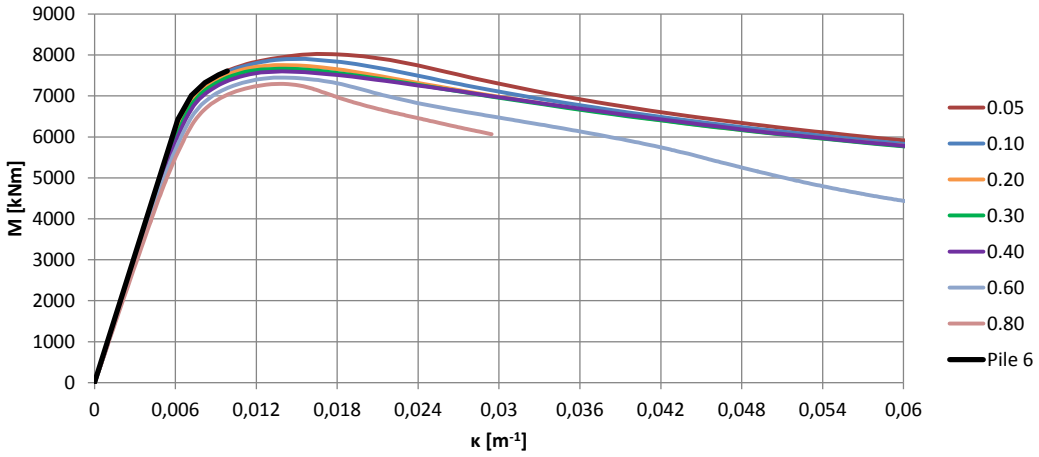

Figure 4.32: Moment-curvature diagram for different imperfection thickness ratios.

Table 4.8: Maximum bending moment for tested imperfection thickness ratios.

Imperfection/Thickness	$M_{\mathbf{max}}$ **[kNm]**	$M_{\mathbf{max}}/M_y$	$z_{\mathbf{Mmax}}$	$\lvert z_{\mathbf{Mmax}}/D_e \rvert$	$\kappa_{\mathbf{cr}}$	$\kappa_{\mathbf{cr}}/\kappa_e$
0.05	8026	1.25	-2	2.2	0.0165	2.67
0.10	7903	1.23	-2	2.2	0.0156	2.53
0.20	7755	1.21	-2	2.2	0.0140	2.26
0.30	7666	1.19	-2	2.2	0.0136	2.21
0.40	7599	1.18	-2	2.2	0.0139	2.25
0.60	7450	1.16	-2	2.2	0.0141	2.28
0.80	7293	1.13	-2	2.2	0.0138	2.22

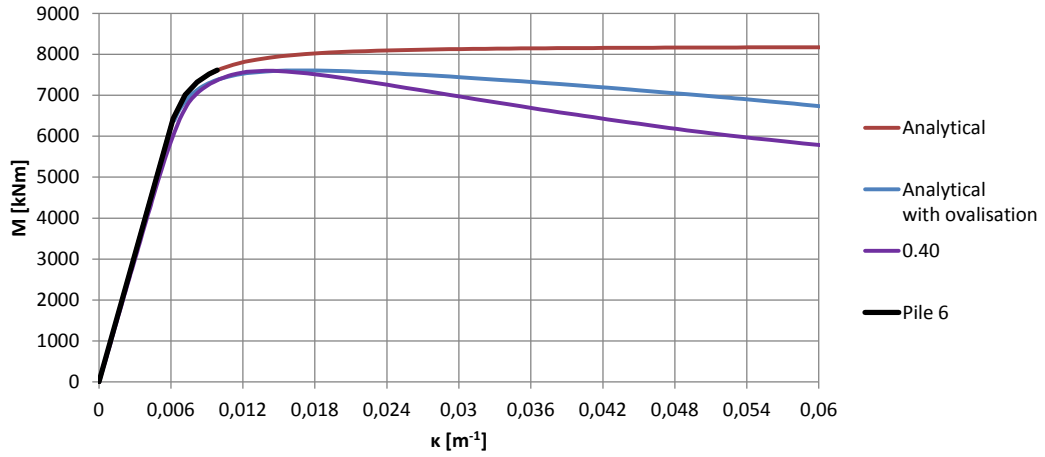

Figure 4.33: Moment-curvature diagram for an imperfection thickness ratio of 0.40 compared to the analytical moment-curvature diagram with and without the ovalisation taken into account.

The SLS is reached when the loading regime moves from the elastic to the elastic-plastic range. All tests exceed this limit before local buckling occurs. When buckling occurs and the ULS is reached, the typical drop in the force-displacement diagram is seen (figure 4.34). A higher load is needed when the imperfections are smaller to reach the ULS. Also there is more displacement at this point. Hence, there is more energy capacity. Compared to pile 6, the analyses in Abaqus show less displacement. Hence, the energy capacities are too low compared to the energy capacity of the dolphin, which is estimated to be 639 kNm. The properties of the surrounding soil can have impact on this (paragraph 5.4).

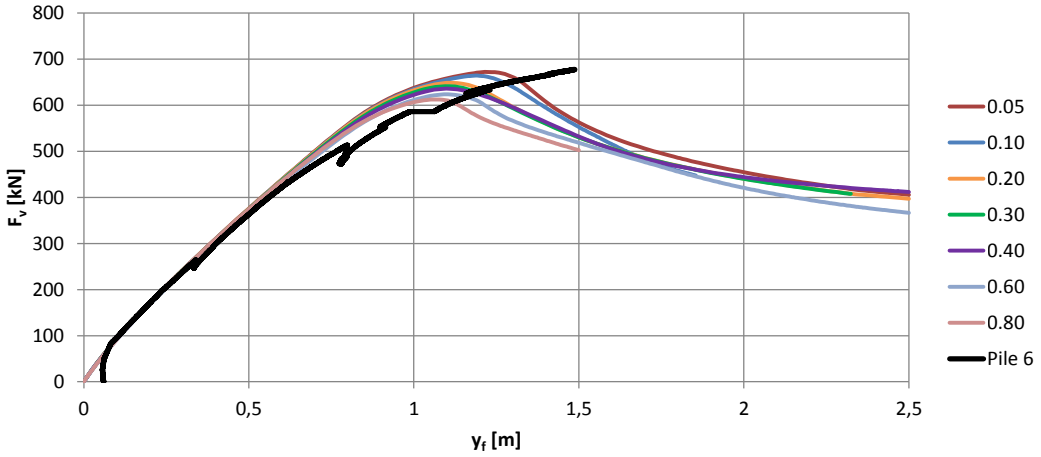

Figure 4.34: Force-displacement diagram for different imperfection thickness ratios.

Table 4.9: Maximum lateral load and energy capacity in the SLS and ULS for tested imperfection thickness ratios.

Imperfection/Thickness	**SLS**		**ULS**	
	$F_{v,max}$ **[kN]**	$E_{v,max}$ **[kNm]**	$F_{v,max}$ **[kN]**	$E_{v,max}$ **[kNm]**
0.05	531	215	672	504
0.10	525	210	662	473
0.20	531	217	649	433
0.30	536	223	641	420
0.40	539	229	636	419
0.60	535	230	624	417
0.80	537	231	631	398

The higher imperfection ratios of 0.60 and 0.80 show differing buckle locations. Also their capacities seem too low compared to the field test. Imperfection thickness ratios of 0.05 and 0.10 tend to overestimate the bending moment capacity. Furthermore, their critical curvatures are incomparable higher than the other ratios. 0.20, 0.30 and 0.40 are imperfection ratios that show similar results comparing their bending moment capacity as well as the lateral force and energy capacity. An imperfection thickness ratio of 0.40 compares best with pile 6 of the field tests. Other than the lower ratios, it has an inward buckle shape which was also encountered in the field. The parametric study in the next chapter will be performed with a scale factor of 3.5, corresponding to an imperfection thickness ratio of 0.40. This factor is most likely to obtain results matching the ones of the field test.

5

Parametric Study

The effect of the key parameters on the local buckling behaviour as identified in chapter 3.7 is studied in this chapter. First the influence of the imperfection parameter of the model on the buckling location and shape is examined as well as its influence on the bending moment capacity and the capacity of the lateral load and energy. After that the capacities of different plug packings, plug levels, slenderness ratios and soil packings are compared with those measured in the full scale field test. For these latter parameters also their effect on the ovalisation is studied which can be related to the plug stiffness applied in the analytical model.

5.1. Plug packing

The stiffness of the plug material is expected to influence the local buckling behaviour. From theory on sand-filled piles a higher stiffness decreases the ovalisation of the pile, allowing higher compressive strains before local buckling occurs [3]. Kostis' study [10] confirms this theory.

The packing of the plug depends on the type of soil that is present in the bedding. Furthermore, the installation method influences the plug packing. During installation the soil is trembled, resulting in a denser packing. Driving a pile compacts the soil within the pile more than when a vibrating installation method is used.

Here, it is checked whether a denser packing also increases the capacity of semi-filled piles. In the basic model a compacted plug is assumed with a Young's modulus E_{plug} of 100 MPa. The properties of the plug are adapted in order to have a loosely packed plug and a densely packed plug according to the classification introduced by Meyerhof [58]. Corresponding plug properties are obtained from table 2.b of the NEN-EN 9997-1 [38]. Also an analyses is done in which the plug is suppressed. For the plug with a loose packing the Young's modulus is halved to 50 MPa with a friction angle of 32.5°. The dense packing of the plug is modelled with a Young's modulus of 200 MPa. This value does not appear in the table 2.b of the NEN-EN 9997-1 [38]. Nevertheless well graded dense sand exists with this property and it is coupled to a friction angle φ' of 45° [59]. With these properties, the parameters are derived as explained in paragraph 4.4.2. These parameters are presented in table 5.1.

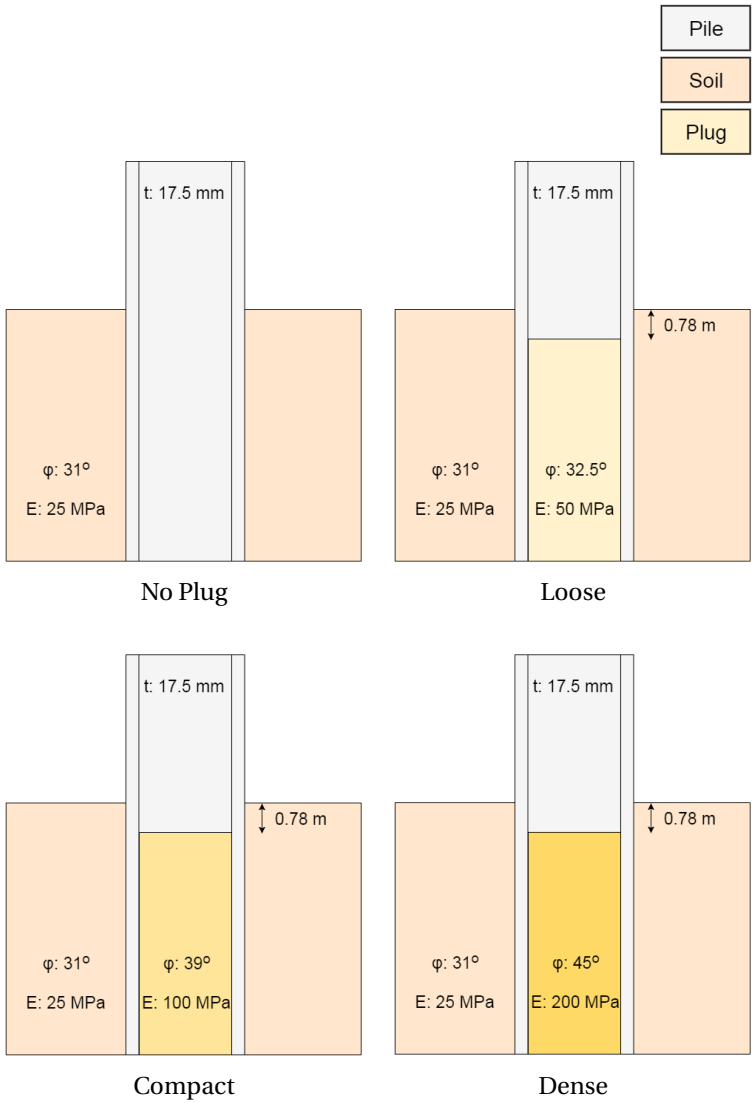

Figure 5.1: Plug parameters applied.

Table 5.1: Plug parameters applied.

Plug Packing	φ' [°]	ψ [°]	$E_{\mathbf{plug}}$ **[MPa]**	ν [-]	K_0 [-]	**Friction coefficient** [-]
Loose	32.5	2.5	50	0.32	0.463	0.40
Compact	39	9	100	0.27	0.371	0.49
Dense	45	15	200	0.23	0.293	0.58

A denser packing significantly reduces the ovalisation (figure 5.2). Also the maximum ovalisation for denser packings is observed at a higher level. As can be seen in figure 5.3, the bending moment line does not differ. Therefore, the maximum ovalisation does not necessarily occur at the depth of the maximum bending moment. This was illustrated in figure 3.11.

In figure 5.4, it can be seen that there is more potential for the compressive strain if the reduction of the ovalisation is sharper. In this case however, the improvement is not in proportion with the reduction of the critical strain at the level of the maximum compressive strain. It is limited at a higher level.

In all analyses an inward buckle appears. However, the depth at which local buckling occurs differs. This is presented in figure 5.5. The dolphin pile with a loose packing buckles at the same location where local

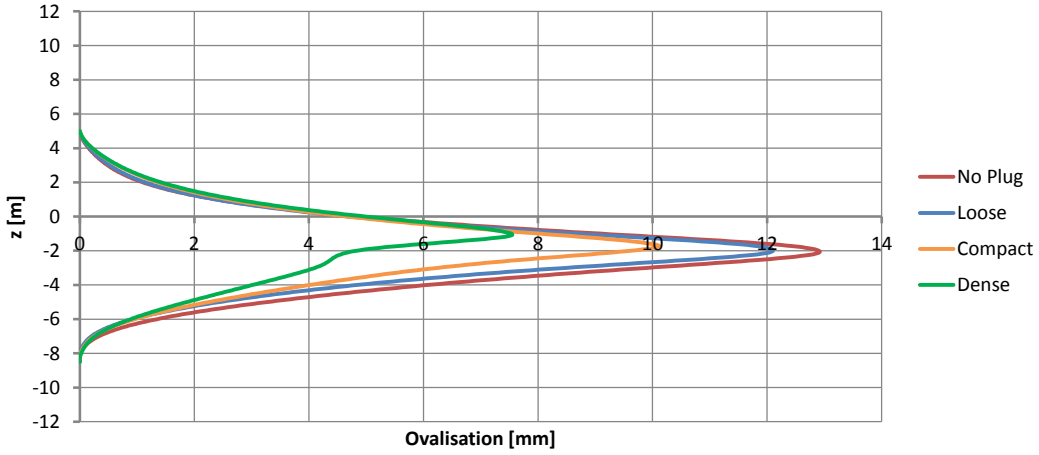

Figure 5.2: Ovalisation for tested plug packings.

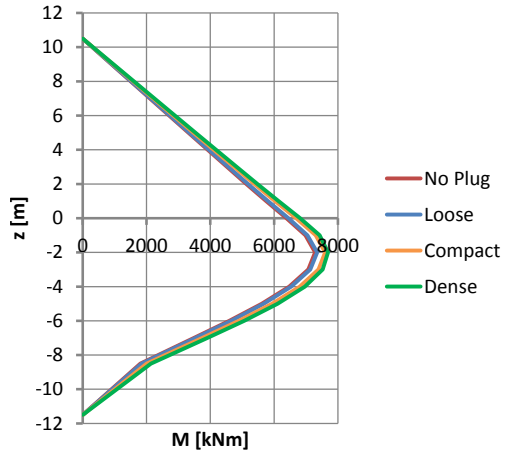

Figure 5.3: Bending moment diagram for tested plug packings.

buckling would occur if no plug would be present. This is at the depth of the maximum bending moment, where also the ovalisation has its maximum (buckling situation 1). The dense packed plug buckles higher, just under the plug level. This is due to the sharp reduction of the ovalisation. Also the pile with a compact packed plug buckles at the location of the maximum ovalisation. However, this level is deeper in the plug. Yet it is at a higher level than at which buckling occurred with a loosely packed plug.

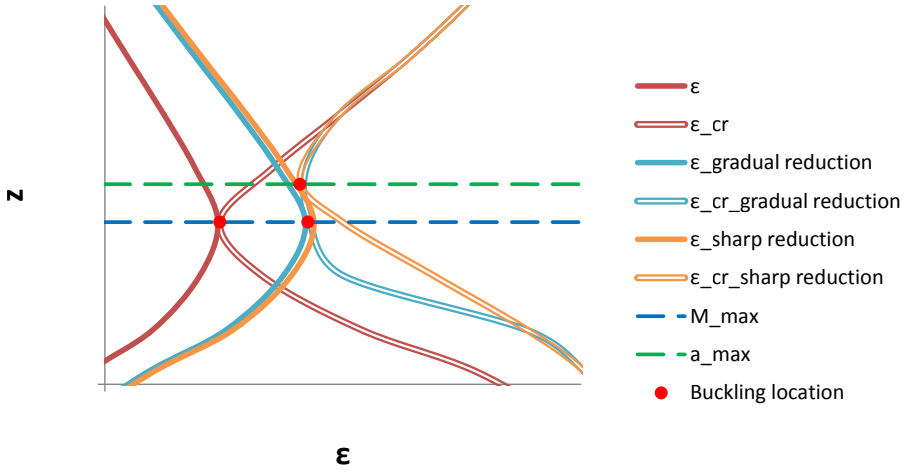

Figure 5.4: The improvement of the maximum compressive strain is not in proportion with the reduction of the critical strain at the level of the maximum compressive strain.

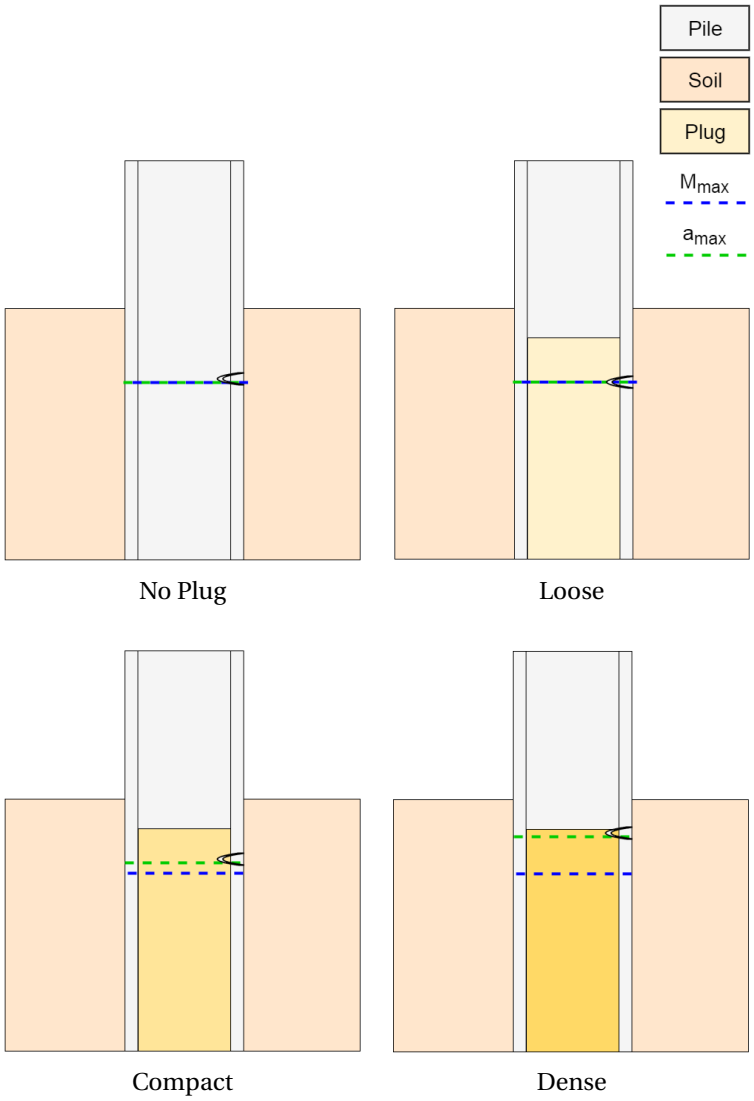

Figure 5.5: Buckling location for tested plug packings (not to scale).

Table 5.2: Buckle location and shape for tested plug packings.

Plug Packing	$z_{\textbf{buckle}}$	$\lvert z_{\textbf{buckle}}/D_e \rvert$	**Buckle shape**
No Plug	-1.9	2.1	Inward
Loose	-1.9	2.1	Inward
Compact	-1.6	1.8	Inward
Dense	-0.9	1.0	Inward

Besides the buckling depth, the bending moment capacity is also influenced by the plug packing. The dense packing has the highest bending moment capacity (7691 kNm). The looser the packing of the plug the lower the capacity. However, the differences are not linear. The loose packing shows a slightly increased capacity of 0.8% compared to a dolphin without a plug. The bending moment capacity with a compact plug is higher (4.3%). A denser plug does not increase the capacity with the same proportion, due to the effect that was presented in figure 3.11. Its capacity is 5.6% higher than if no plug would be present.

The critical curvature is higher for the denser packed plugs. Remarkable is that the calculated critical curvature of the compact packed plug is higher than for the dense packed plug. In designing a dolphin, the critical curvature is not directly a relevant characteristic. The bending moment capacity is more important.

The moment-curvature diagram for the dense packing shows a steeper decline after local buckling occurred than the other packings. This is due to the calculation method of the curvature (see paragraph 4.5).

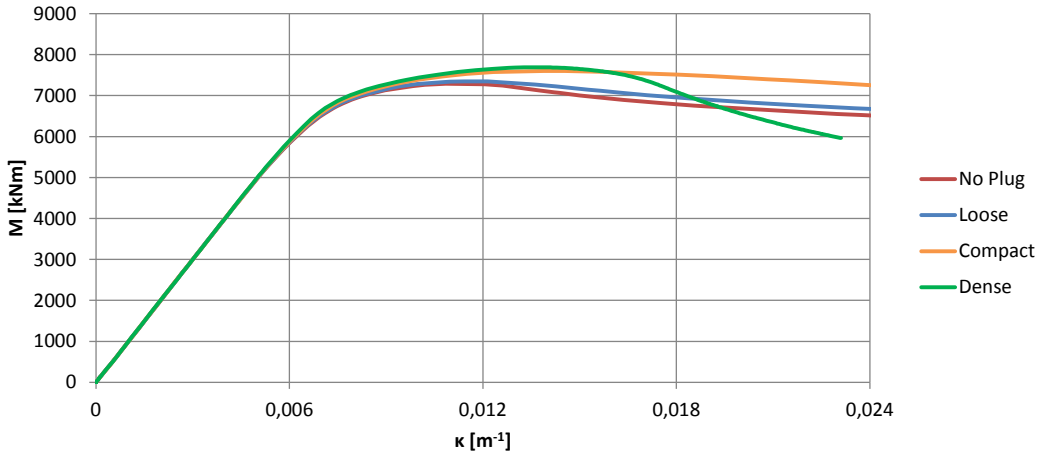

Figure 5.6: Moment-curvature diagram for tested plug packings.

Table 5.3: Maximum bending moment for tested plug packings.

Plug Packing	$M_{\mathbf{max}}$ **[kNm]**	$M_{\mathbf{max}}/M_y$	$M_{\mathbf{max}}/M_p$	$\kappa_{\mathbf{cr}}$	$\kappa_{\mathbf{cr}}/\kappa_e$
No Plug	7286	1.13	0.89	0.0108	1.75
Loose	7349	1.14	0.90	0.0114	1.85
Compact	7599	1.18	0.93	0.0139	2.25
Dense	7691	1.20	0.94	0.0136	2.19

The load capacity and energy capacity improve if the packing of the plug is denser. The improvement for the load capacity is comparable to that of the bending moment capacity. Compared to the situation without a plug the packings show improvements of 0.9% (loose), 5.0% (compact) and 6.9% (dense). As the deformation also increases before local buckling occurs, the energy capacity is improved more significantly. The loose packing has an energy capacity of 4.0% more and the compact and dense packings show improvements of 21.8% and 30.2% respectively.

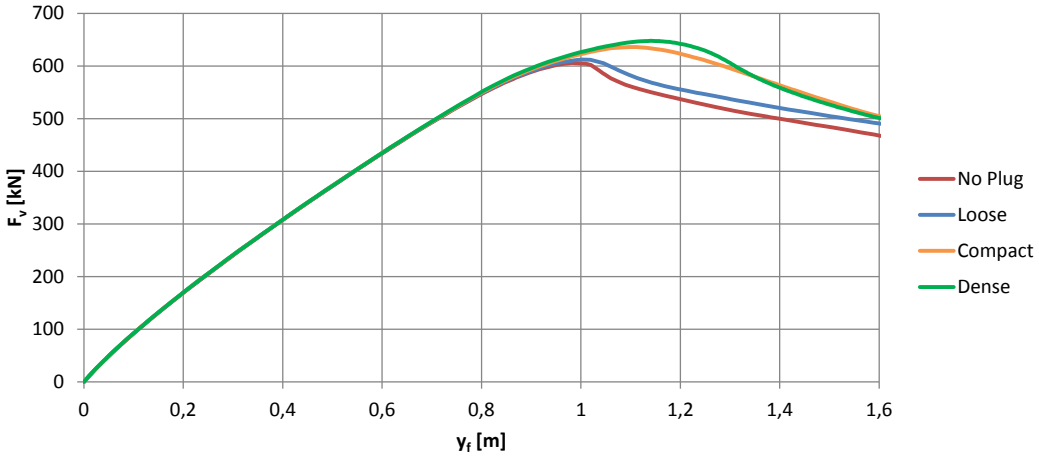

Figure 5.7: Force-displacement diagram for tested plug packings.

Table 5.4: Maximum lateral load and energy capacity in the SLS and ULS for tested plug packings.

Plug Packing	**SLS**		**ULS**	
	$F_{v,max}$ **[kN]**	$E_{v,max}$ **[kNm]**	$F_{v,max}$ **[kN]**	$E_{v,max}$ **[kNm]**
No Plug	538	229	606	344
Loose	536	226	612	358
Compact	539	229	636	419
Dense	541	229	648	448

The depth at which the maximum bending moment occurs is not changed because of the plug packing. Neither is a change in the path of the force-displacement diagram observed. This indicates that the plug packing does not significantly contribute to the stiffness of the dolphin.

In conclusion a denser packing of the plug reduces the ovalisation, improving the capacities of the bending moment and lateral load. Most of all, the dolphin can dissipate more energy. This could influence the installation method to apply. Yet, the improvement is limited as local buckling will occur higher where the critical strain is lower.

5.2. Plug level

In the previous paragraph, it is concluded that a soil plug has an effect on the ovalisation. Therefore, besides the plug packing, the plug level is expected to influence the local buckling resistance as well. A higher plug is thought to move the maximum ovalisation to a higher level. Then different buckling locations could occur.

The length of the soil plug depends on the friction between the pile's inner shaft and the soil. Hence, the packing of the soil is of importance. Furthermore, different installation methods result in different friction loads. Moreover, the inner diameter of the dolphin pile influences the plug level [17, 45, 46]. These conditions cause different plug levels to arise in the field.

The influence of the plug level on the buckling location and shape, as well as on the capacities of the dolphin pile, are studied with four different plug levels. In the basic model, the plug level is 0.72 m, or approximately 0.8 D_e, below the bed level. This situation is compared to a situation with a small PLR, with the plug level even below the level of the maximum bending moment, at 3 D_e below the bed level. Also, an analysis is run in which there is no plugging at all. The plug level is at the bed level, here indicated as 0 D_e below the bed level. In the other extreme situation, the pile is fully plugged from the start of the installation. In this case, there is no soil present in the pile.

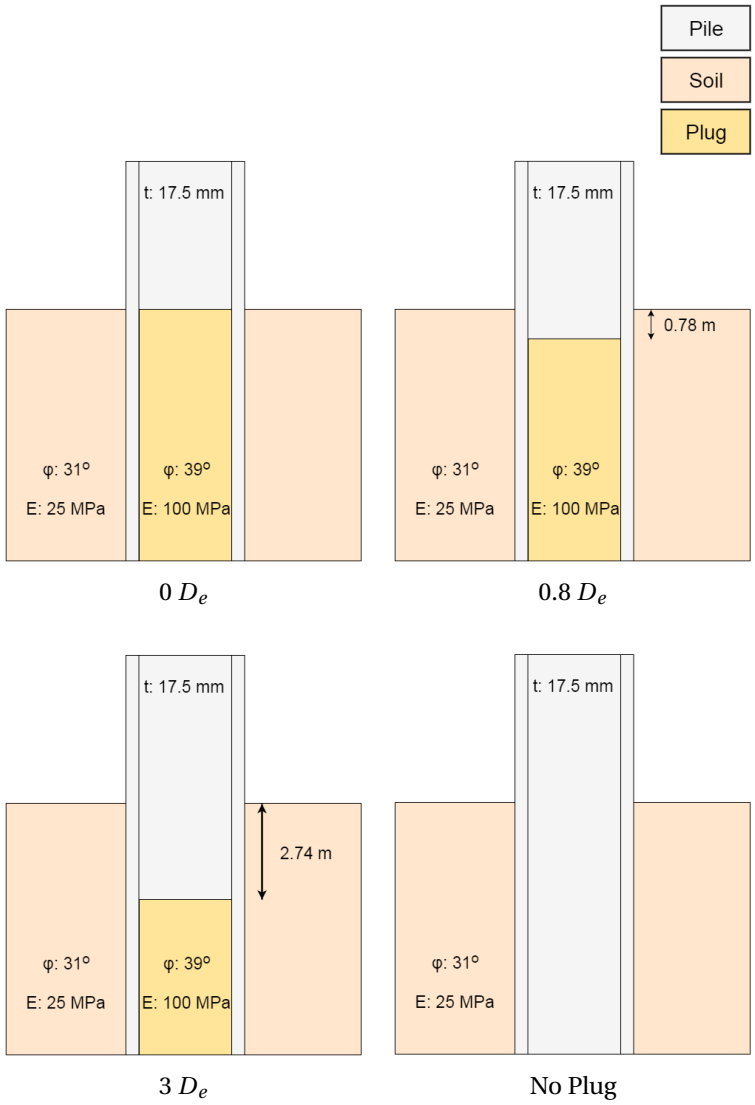

Figure 5.8: Plug levels tested.

Table 5.5: Plug levels tested.

Plug Level z [m]	**Plug Level $\lvert z/D_e \rvert$**
0.000	0.0
-0.780	0.8
-2.742	3.0

Figure 5.9 shows again that the presence of a plug influences the ovalisation. The higher the plug level, the higher the ovalisation is influenced. The deep plug, 3 D_e below the bed level, is located below the level of the maximum ovalisation when no plug is present. It does not significantly reduce the ovalisation. The plug reaching up to the bed level produces higher horizontal soil pressures and provides more resistance against the ovalisation. The levels of the maximum ovalisation are at the same level of the maximum bending moment, except for the situation with a plug level at 0.8 D_e below the bed level. In that situation the level of the maximum ovalisation is slightly higher. Hence, except for the situation with a plug level at 0.8 D_e below the bed level, all situations are as situation 1 in figure 3.11.

Figure 5.11 shows that the pile with the plug level at 0.8 D_e below the bed level local buckling occurs at the level of the maximum ovalisation. In the other situations, local buckling is indeed initiated at the level of the

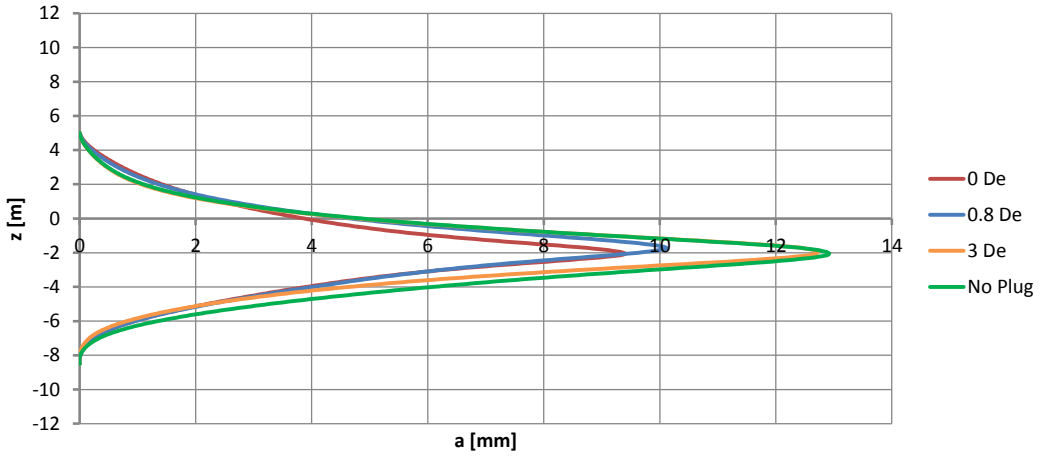

Figure 5.9: Ovalisation for tested plug levels.

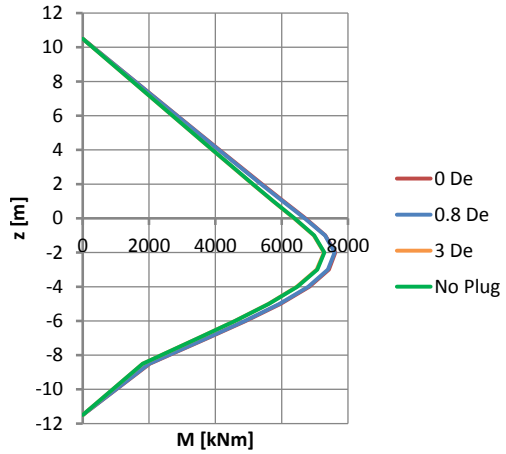

Figure 5.10: Bending moment diagram for tested plug levels, just before buckling.

maximum bending moment and the maximum ovalisation. Furthermore, an inward buckle is observed in the cases where there is no plug present at the buckling level. Also the situation with the plug at 0.8 D_e below the bed level shows an inward buckle. With the plug level on the bed level on the other hand, an outward buckle is observed. In this situation the denser packed plug provides more resistance than the outer soil.

In case the plug reaches above the level of the maximum bending moment and above the level of the maximum ovalisation, the moment capacity is improved. 4.5% and 4.3% for plug levels 0 and 0.8 D_e respectively, compared to the situation without a plug. Also the capacities of the lateral load (5.0-5.5%) and the energy (22-25 %) are improved. Due to the change in buckling level, the improvement is not in proportion with the reduction in ovalisation. Their improvements are approximately the same, with a plug reaching up to the bed level showing slightly more favorable results. The situation with a deeper plug level, at 3 D_e below the bed level, performs equally as a situation without a plug. Therefore, if the plug level is below the risk area, the pile can be assumed empty.

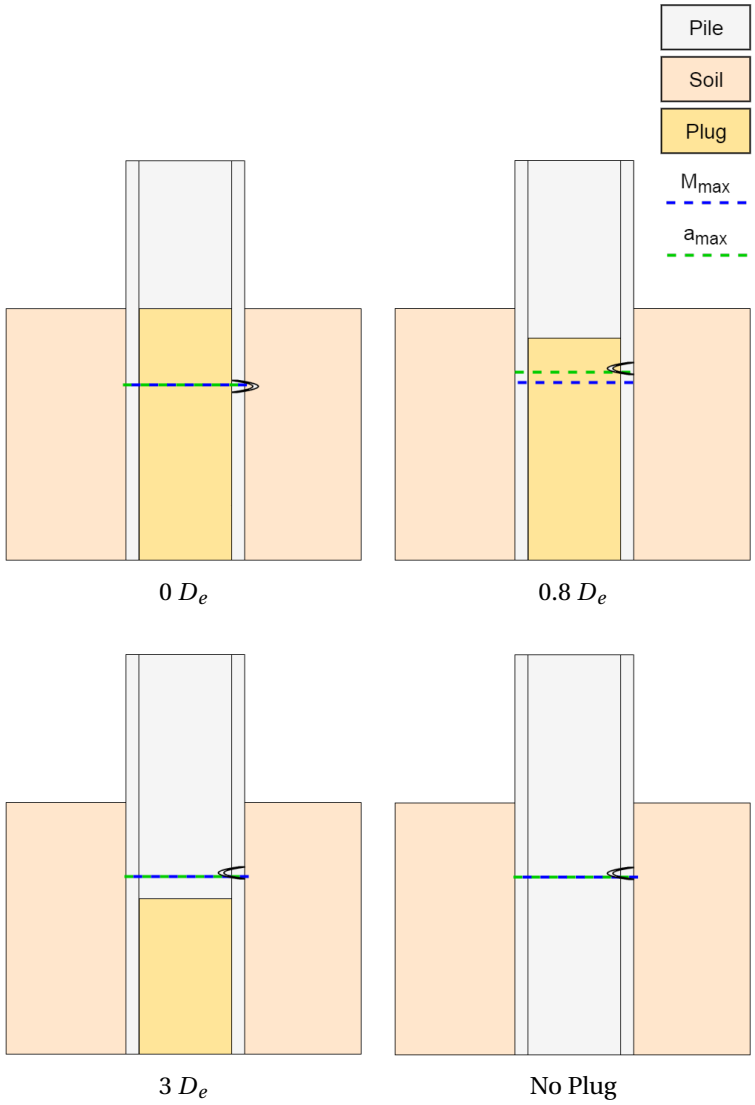

Figure 5.11: Buckling location for tested plug levels (not to scale).

Table 5.6: Buckle location and shape for tested plug levels.

Plug Level	$z_{\textbf{buckle}}$	$\lvert z_{\textbf{buckle}}/D_e \rvert$	**Buckle shape**
0 D_e	-2.1	2.3	Outward
0.8 D_e	-1.6	1.8	Inward
3 D_e	-1.9	2.1	Inward
No Plug	-1.9	2.1	Inward

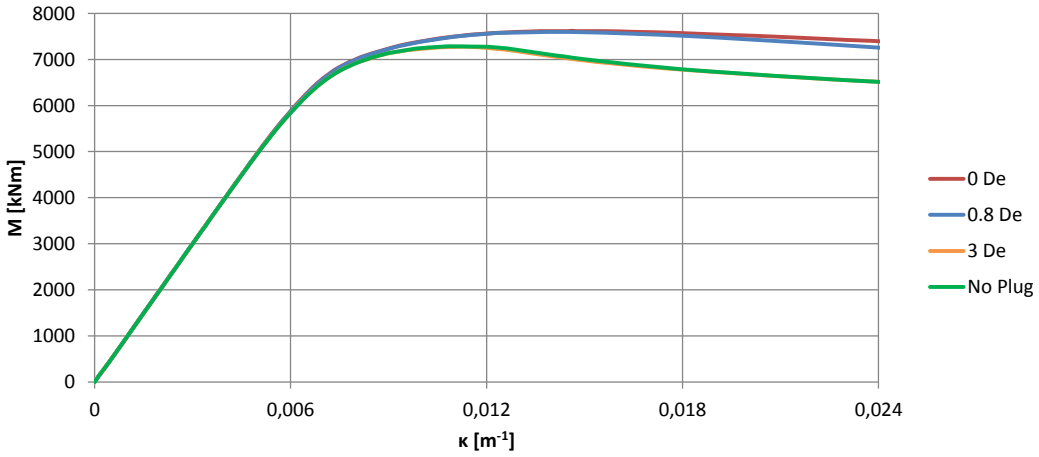

Figure 5.12: Moment-curvature diagram for tested plug packings

Table 5.7: Maximum bending moment for tested plug levels.

Plug Level	$M_{\mathbf{max}}$ **[kNm]**	$M_{\mathbf{max}}/M_y$	$M_{\mathbf{max}}/M_p$	$\kappa_{\mathbf{cr}}$	$\kappa_{\mathbf{cr}}/\kappa_e$
0 D_e	7617	1.18	0.93	0.0146	2.36
0.8 D_e	7599	1.18	0.93	0.0139	2.25
3 D_e	7273	1.13	0.89	0.0111	1.80
No Plug	7286	1.13	0.89	0.0108	1.75

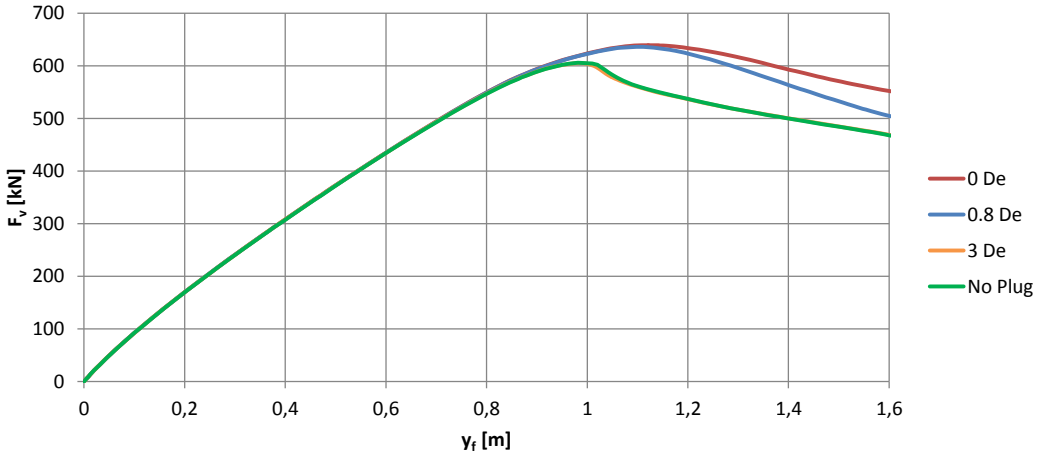

Figure 5.13: Force-displacement diagram for tested plug levels.

Table 5.8: Maximum lateral load and energy capacity in the SLS and ULS for tested plug levels.

Plug Level	**SLS**		**ULS**	
	$F_{\mathbf{v,max}}$ **[kN]**	$E_{\mathbf{v,max}}$ **[kNm]**	$F_{\mathbf{v,max}}$ **[kN]**	$E_{\mathbf{v,max}}$ **[kNm]**
0 D_e	536	226	639	429
0.8 D_e	539	229	636	419
3 D_e	536	227	605	347
No Plug	538	229	606	344

Even though the buckling level and buckling shape differ for the situation with a plug up to the bed level and when the plug level is 0.8 D_e below the bed level, there is no significant difference in their capacities. In case of a deep plug, below the level of the maximum bending moment there is no significant difference compared to an empty pile. In designing dolphin piles the buckling location and shape are irrelevant. Therefore if the plug level is approximated outside a reach of 1 D_e of the maximum bending moment, a rough indication of the plug level will satisfy. A pile with a plug below this reach can be assumed to be empty, whereas a pile with the plug level above this reach has improved capacities.

5.3. Slenderness ratio

With a positive effect of the soil plug, a cross section with a higher slenderness ratio, $D_e/(t\varepsilon^2)$, can be used. The parameters of the slenderness ratio are design parameters and are determined by the engineer. A more economical design is obtained with a higher slenderness ratio. Yet a higher ratio makes the the dolphin pile more susceptible to local buckling.

According to Gresnigt [1], the slenderness ratio has a direct impact on the critical strain (equation 2.26). Cross- sections with a higher ratio are more susceptible to local buckling. The slenderness of the cross-section influences the bending stiffness of the pile, EI_p, and therewith the deflection and curvature of the pile. The ovalisation due to the curvature will therefore differ for different slenderness ratios, which is explicated with equation 2.36. The slenderness ratio more directly influences this ovalisation via the thickness, t, and the radius R_m that are included in this equation. Furthermore, a different deflection of the pile results in different soil pressures, p_e. Also, the slenderness influences the bending stiffness of the pile wall, EI_w. These two parameters determine the ovalisation due to the soil pressure, a_q (equation 2.38). Moreover, the bending stiffness of the pile wall affects the impact of a soil plug on the ovalisation. This is implicated in equation 2.45.

In many ways the slenderness ratio influences the local buckling behaviour of the dolphin pile. To gain insight on this influence, the results of three analyses with different slenderness ratios are studied (5.9). In these analyses, the diameter and steel grade are the same, only the thickness is adjusted. The slenderness ratios tested are 90, 129 and 250. The ratio of 129 is the ratio in the basic model. EN 1993-1-1 [13] prescribes that the slenderness limit for first yield has a value of 90. The characteristic behaviour of a class 4 cross-section should be shown by a cross-section with a very high slenderness ratio. Hence, the slenderness ratio of 250 is analysed.

With a thinner wall thickness, increased ovalisation and less capacity can be expected. Also, it is thought that the soil plug will have more influence on the ovalisation.

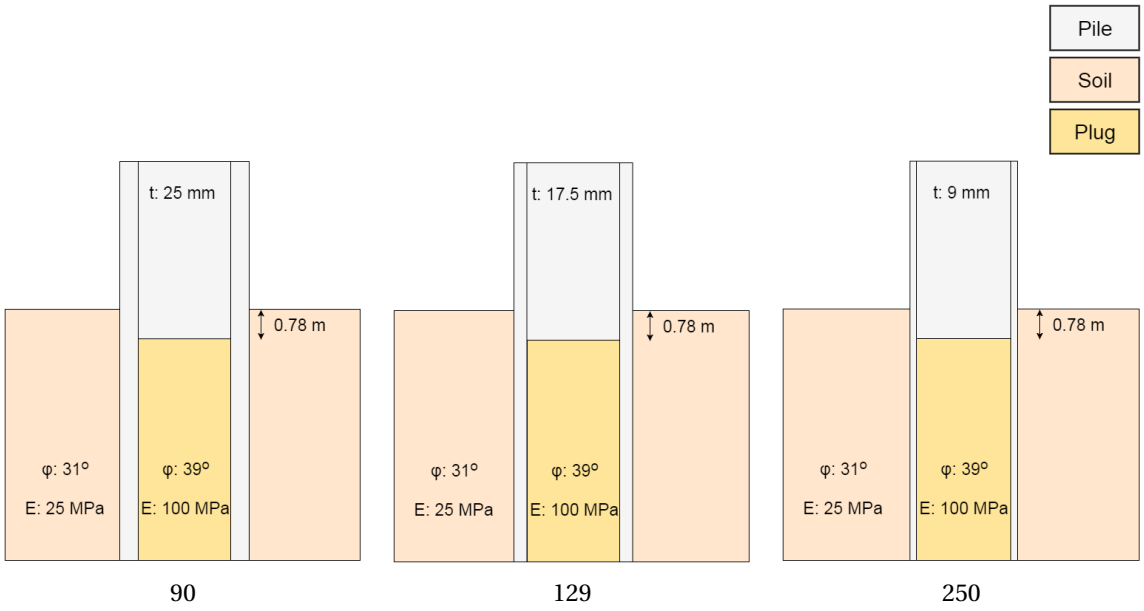

Figure 5.14: Slenderness ratios applied.

Table 5.9: Slenderness ratios applied.

Slenderness Ratio	D_e **[mm]**	t **[mm]**	f_y **[MPa]**
90	914	25.0	582
129	914	17.5	582
250	914	9.0	582

The bending moment just before buckling is lower for a more slender cross-section. In figure 5.15 it can also be seen that, for a more slender cross-section, the level of the maximum bending moment is higher. This is explained by the lower bending stiffness of the pile that relates to larger curvatures and larger deflections. The larger deflection triggers higher soil pressures, reducing the bending moment at a higher level.

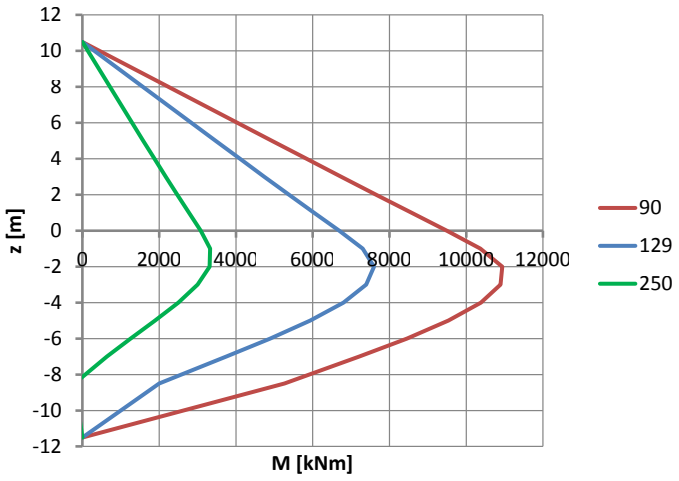

Figure 5.15: Bending moment diagram for tested slenderness ratios.

Figure 5.16 presents the ovalisation of the piles, just before buckling. Even though for the more slender piles the bending moment is lowest, the ovalisation is largest. A more slender cross-section ovalises easier. The figure also shows that the maximum ovalisation occurs at a higher level for a more slender cross-section.

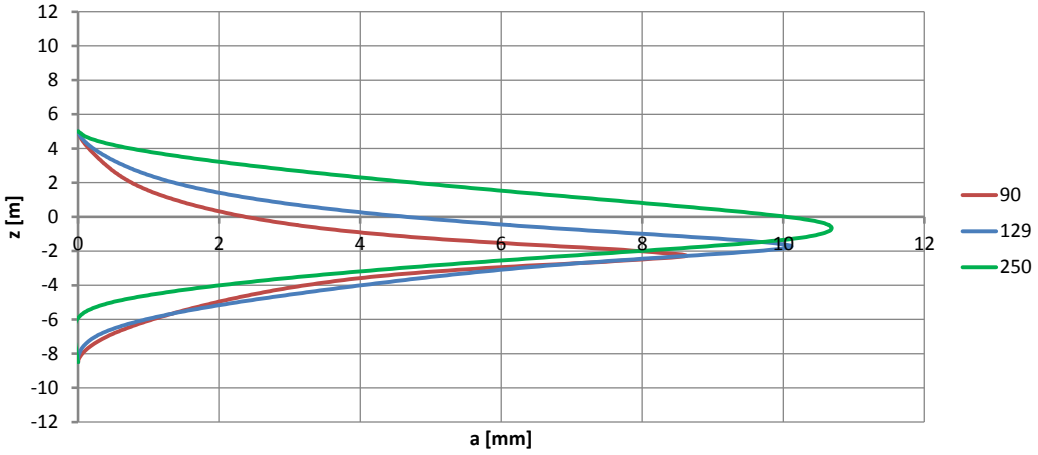

Figure 5.16: Ovalisation for tested slenderness ratios.

As a consequence of the different levels of the maximum bending moment and maximum ovalisation, the buckling levels differ. The pile with a slenderness ratio of 90 buckles at the level of the maximum bending moment, which is the same level as the maximum ovalisation. This level is deep enough under the plug level that the plug provides more resistance against an inward buckle than the outer soil against an outward buckle. The pile buckles outward. Local buckling occurs at a higher level for the pile with a slenderness ratio of 129. An inward buckle is observed at the level of the maximum ovalisation. For the pile with a slenderness ratio of 250, the level of the maximum bending moment is just below the plug level. The maximum ovalisation occurs just above the plug level. In this case an inward buckle is observed at the plug level.

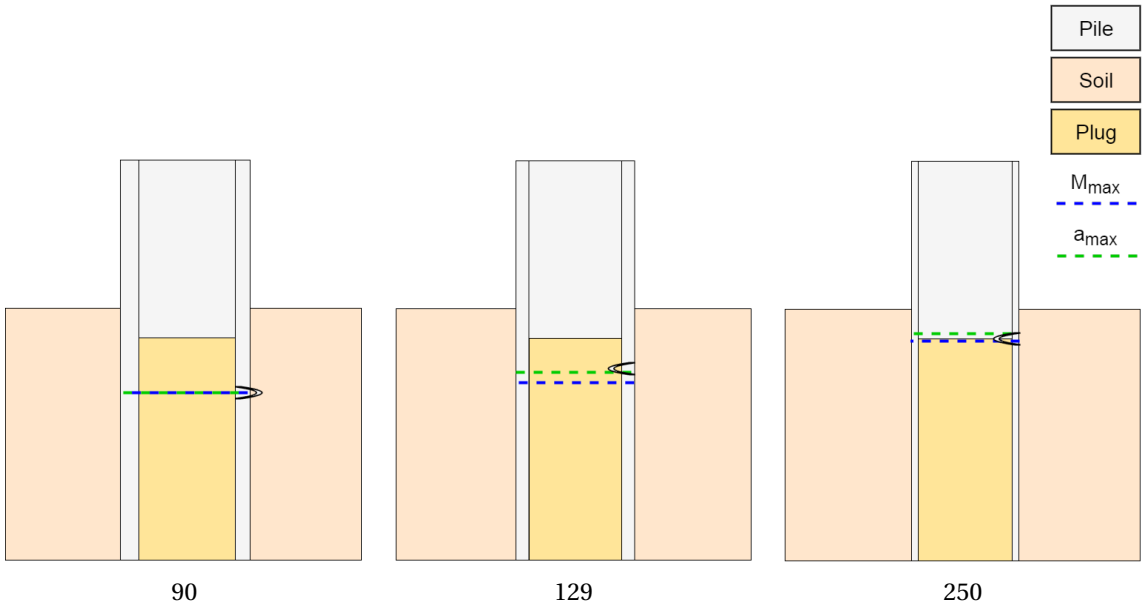

Figure 5.17: Buckle location for tested slenderness ratios (not to scale).

Table 5.10: Buckle location and shape for tested slenderness ratios.

Slenderness Ratio	$z_{\textbf{buckle}}$	$\lvert z_{\textbf{buckle}}/D_e \rvert$	**Buckle shape**
90	-2.3	2.5	Outward
129	-1.6	1.8	Inward
250	-0.8	0.9	Inward

Compared to the pile with slenderness ratio of 90, the bending moment capacity of the pile with slenderness ratio of 129 is reduced with 30.5% (see figure 5.18). The pile with slenderness ratio of 250 has a reduced bending moment capacity of 69.5%. In figure 5.19 the bending moment is divided by the plastic bending moment of the pile, M_p. The behaviour as described for a class 4 slender cross-section, is shown by the pile with slenderness ratio of 250. It buckles before the bending moment capacity reaches the yield moment capacity. The other piles exceed this capacity.

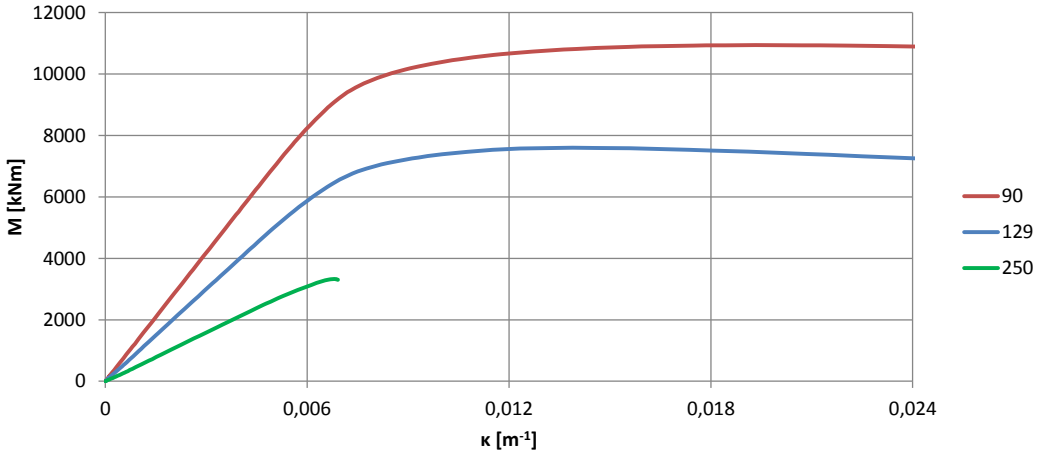

Figure 5.18: Moment-curvature diagram for tested slenderness ratios.

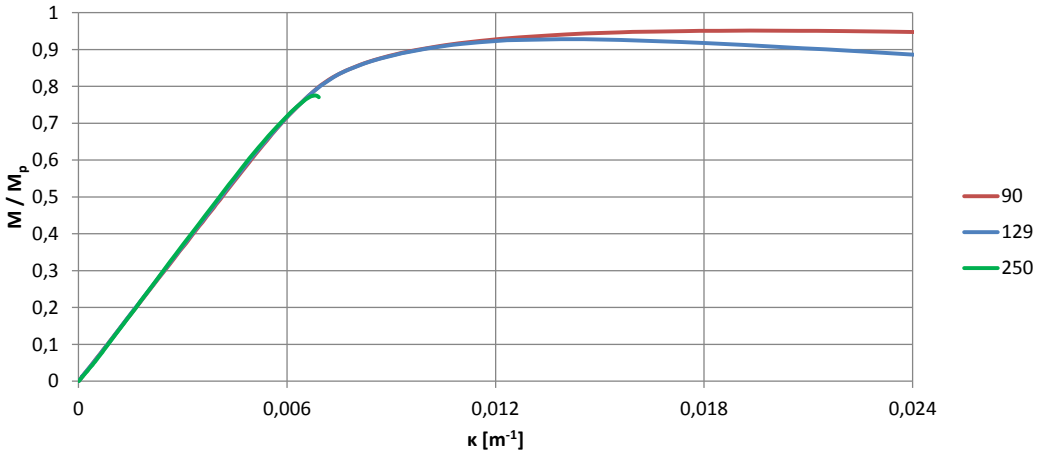

Figure 5.19: Plastic moment ratio plotted against the curvature for tested slenderness ratios.

Table 5.11: Maximum bending moment for tested slenderness ratios.

Plug Level	M_{max} **[kNm]**	M_{max}/M_y	M_{max}/M_p	κ_{cr}	κ_{cr}/κ_e
90	10939	1.21	0.95	0.0193	3.10
129	7599	1.18	0.93	0.0139	2.25
250	3326	0.99	0.78	0.0068	1.11

The force-displacement diagram in figure 5.20 indicates that also the lateral load capacity is lower for a more slender cross-section. The ultimate load capacity for the piles with slenderness ratios of 129 and 250 are respectively 30.0 and 68.2% lower compared to the pile with slenderness ratio of 90. Due to the fact that a more slender pile has a lower bending stiffness, less force is required to displace the pile. Hence, the energy capacities are even lower: 47.6% (slenderness ratio of 129) and 86.6% (slenderness ratio of 250).

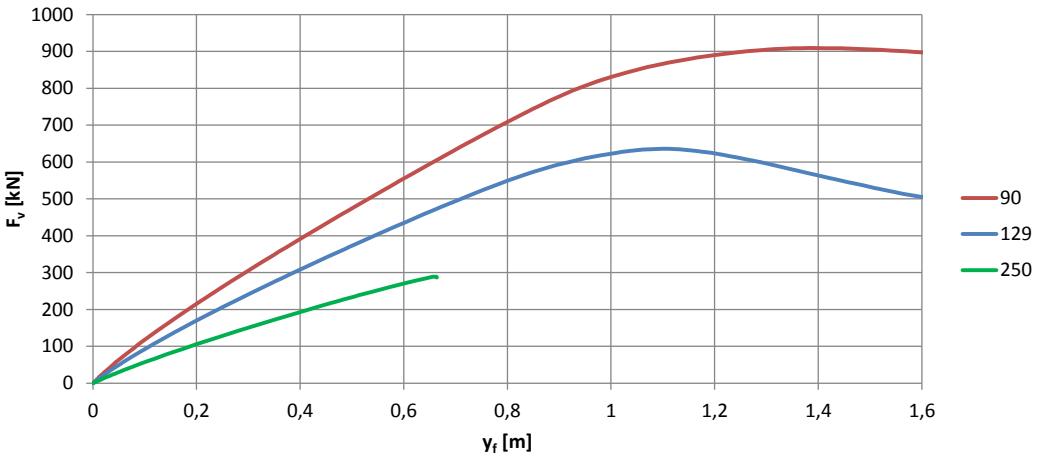

Figure 5.20: Force-displacement diagram for tested slenderness ratios.

Table 5.12: Maximum lateral load and energy capacity in the SLS and ULS for tested slenderness ratios.

Slenderness ratio	**SLS**		**ULS**	
	$F_{v,max}$ **[kN]**	$E_{v,max}$ **[kNm]**	$F_{v,max}$ **[kN]**	$E_{v,max}$ **[kNm]**
90	748	346	909	800
129	539	229	636	419
250	289	105	289	105

From this paragraph it can be concluded that designing the pile more slender, reduces its capacities. The energy capacity is reduced even more than the bending moment and lateral load capacities. The improvement on the capacities due to the presence of a plug as presented in paragraphs 5.1 and 5.2 can be compromised by designing the pile more slender.

Furthermore, only a very slender pile, with slenderness ratio of 250 showed typical cross-sectional class 4 behaviour as described in EN 1993-1-1 [13]. It can be presumed that the limit value of 90 in this code can be increased.

5.4. Soil packing

A denser packing stiffens the berthing and mooring system. Smaller displacements for an equal energy dissipation are then expected. Also larger ovalisations are expected, because the soil pressure in the risk area is higher. The higher soil pressure causes the maximum bending moment to occur at a higher level. Therefore, it is thought that local buckling occurs at a higher level.

The packing of the soil can be obtained with CPTs. CPTs are performed on specimen taken out of their environment with the natural soil pressures. These specimen are transported and in a laboratory put under stress again. During the hole procedure many inaccuracies can appear, resulting in significant deviation from the original specimen. The test results can therefore be argued. Furthermore, the loading type can influence the saturated soil reaction. In a short term loading, a densely packed sand will have a tendency to expand (dilatancy). This increases the effective stress. The reverse effect (contractancy) can occur in loosely packed sands. The volume decrease means that there is less space available for the pore water. This has to flow out of the soil, but that takes some time, and in the case of very rapid loading the tendency for volume decrease will lead to an increasing pore pressure in the water. The effective stresses will decrease, and the soil will become weaker and softer.

Because of these uncertainties, it is valuable to know what the influence of a looser or denser soil packing can be on the local buckling resistance of the dolphin pile. For the looser sand packing (compared to the basic model) the properties of a very silty sand in table 2.b of the NEN-EN 9997-1 [38] is assumed. For the denser packed soil the Young's modulus E_g is doubled to 50 MPa with a friction angle of 32.5°. Other soil parameters are derived from these properties as explained in paragraph 4.4.2. The applied parameters are presented in table 5.13.

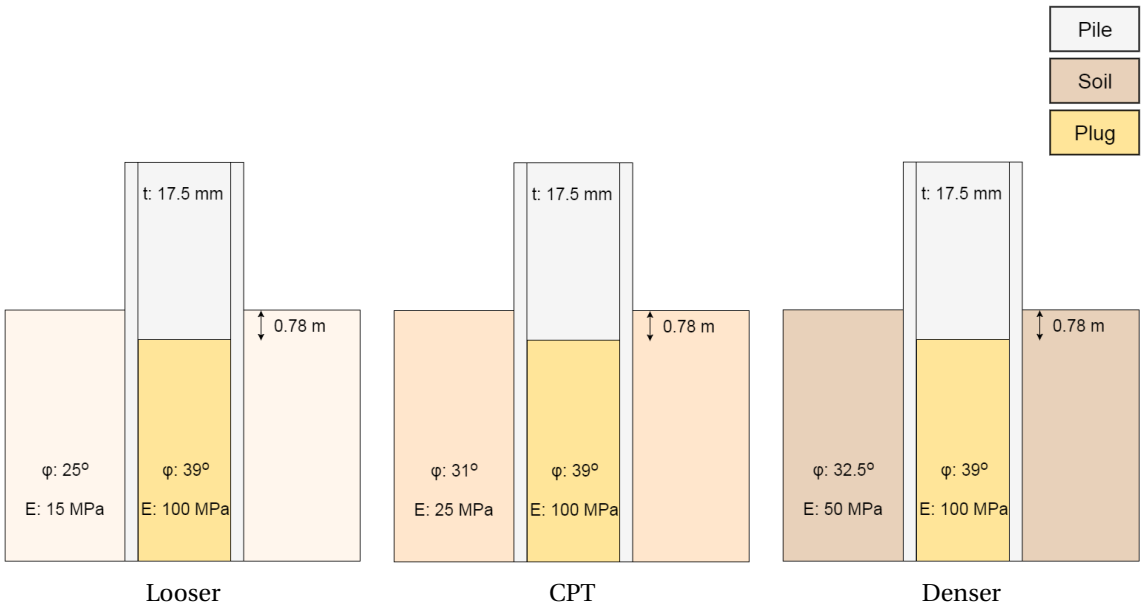

Figure 5.21: Slenderness ratios applied.

Table 5.13: Plug levels applied.

Soil Packing	φ' [°]	ψ [°]	E_g **[MPa]**	ν [-]	K_0 [-]	**Friction coefficient** [-]
Looser	25	0	15	0.37	0.577	0.30
CPT	31	1	25	0.33	0.485	0.38
Denser	32.5	2.5	50	0.32	0.463	0.40

Due to the higher soil pressures, in figure 5.23 it is seen that the bending moment under the bed level declines faster for a denser soil packing. The maximum bending moment is also obtained at a higher level. Furthermore, the ovalisation is larger for a denser soil packing (figure 5.22). Also, the level of the maximum ovalisation is higher.

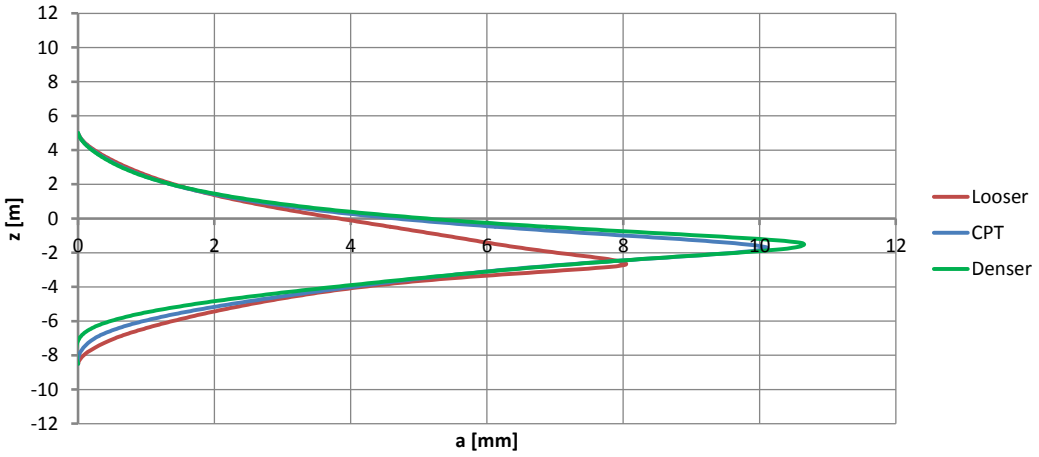

Figure 5.22: Ovalisation for tested soil packings.

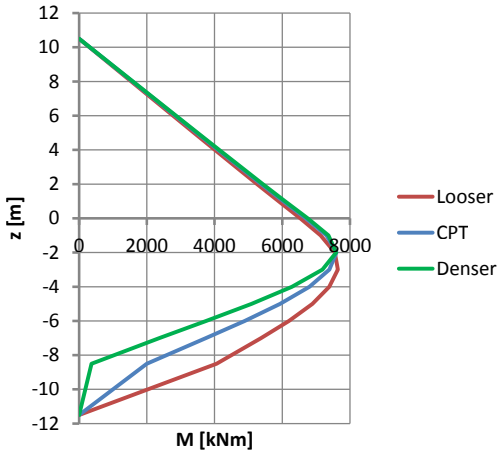

Figure 5.23: Bending moment diagram for tested soil packings.

In the situation with a looser soil packing, buckling is observed deeper under the bed level than in the situation with soil parameters from the CPT. This is due to the fact that the levels of the maximum bending moment and maximum ovalisation are lower. The looser soil has less resistance against an outward buckle, than the plug has against an inner buckle, at this level. Hence, an outward buckle is observed. In case of a denser soil packing, the level of the maximum ovalisation is higher compared to the situation with soil parameters from the CPT. However, buckling is observed at the same level. The situation with a denser soil packing can be compared to situation 4 in figure 3.11, whereas the situation with the CPT parameters can be compared to situation 3 in the same figure.

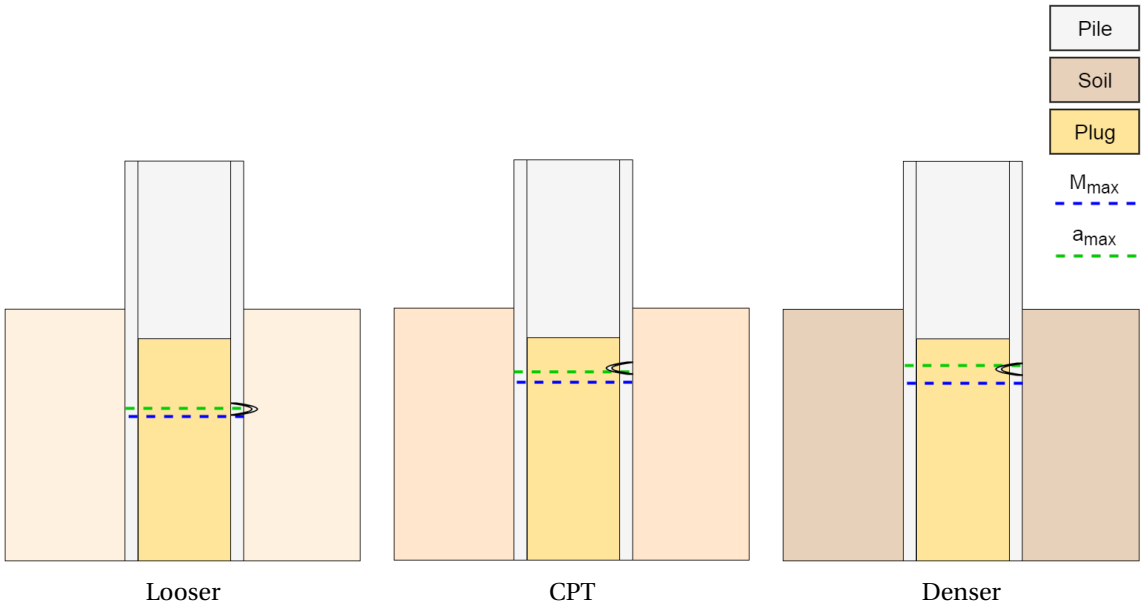

Figure 5.24: Buckle location for tested soil packings (not to scale).

Table 5.14: Buckle location and shape for tested soil packings.

Soil packings	$z_{\textbf{buckle}}$	$\lvert z_{\textbf{buckle}}/D_e \rvert$	**Buckle shape**
Looser	-2.7	3.0	Outward
CPT	-1.6	1.8	Inward
Denser	-1.6	1.8	Inward

There is no significant difference in bending moment capacity for the different soil packings. This is presented in figure 5.25 and table 5.15. The difference is no more than 0.5% for a looser or denser soil packing compared to the situation with the parameters from the CPT.

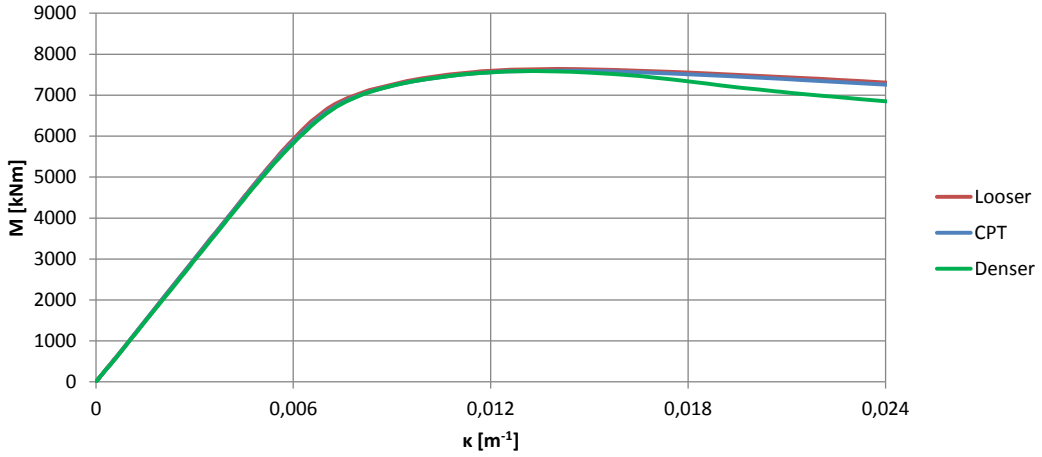

Figure 5.25: Moment-curvature diagram for tested soil packings.

Table 5.15: Maximum bending moment for tested soil packings.

Soil Packing	$M_{\mathbf{max}}$ **[kNm]**	$M_{\mathbf{max}}/M_y$	$M_{\mathbf{max}}/M_p$	$\kappa_{\mathbf{cr}}$	$\kappa_{\mathbf{cr}}/\kappa_e$
Looser	7639	1.19	0.93	0.0140	2.27
CPT	7599	1.18	0.93	0.0139	2.25
Denser	7590	1.18	0.93	0.0133	2.15

Table 5.16 suggests there is little difference in lateral load capacity. A denser soil packing has 0.7% more capacity and the looser soil packing has 2.2% less capacity than the soil packing according to the CPT. Yet figure 5.26 illustrates that the displacement is increased with a looser soil packing. This results in a higher energy capacity (11.6 %). The denser soil packing has a lower energy capacity (8.8 %).

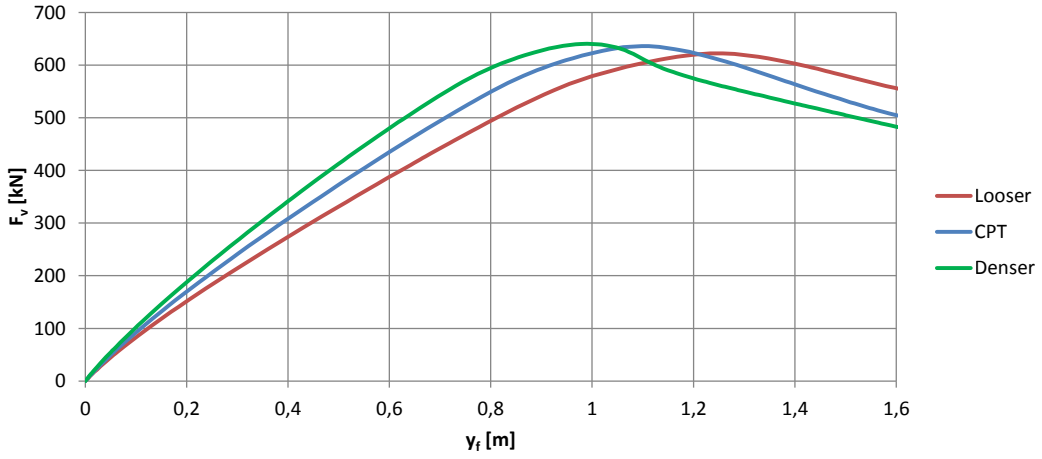

Figure 5.26: Force-displacement diagram for tested soil packings.

Table 5.16: Maximum lateral load and energy capacity in the SLS and ULS for tested soil packings.

Soil Packing	**SLS**		**ULS**	
	$F_{\mathbf{v,max}}$ **[kN]**	$E_{\mathbf{v,max}}$ **[kNm]**	$F_{\mathbf{v,max}}$ **[kN]**	$E_{\mathbf{v,max}}$ **[kNm]**
Looser	622	240	622	468
CPT	539	229	636	419
Denser	540	204	641	382

The bending moment capacity is not significantly influenced by the soil packing. The lateral load capacity is improved by a denser soil packing, yet the improvement is little. The influence on the energy capacity however, is substantial. A looser soil packing improves the energy capacity. Therefore, to maintain a significant energy capacity an installation method should be chosen that does not compact the soil packing.

This advice is contradicting with paragraph 5.1. For the soil plug, the effect is the other way around. A looser soil plug reduces the energy capacity. Hence, the solution to use best of both would be to use an installation method that does not compact the soil and plug packing and after installation, the plug packing is compacted.

5.5. Plug stiffness

In chapter 3 an analytical method is introduced to test a pile against local buckling. The advantage of the analytical method over the finite element method is that it saves time, because no finite element model has to be set up. It was concluded however, that the analytical method lacks knowledge about the stiffness of the sand plug, k_{plug}. In the CUR 211E [3] the value of E_{plug}/r is suggested (equation 2.44) for piles fully-filled with sand. From the Abaqus analyses the plug stiffness in piles partly filled with sand can be studied. Design values for k_{plug} are proposed. These are compared to the value of the CUR 211E [3].

Rewriting equation 2.45 the value of k_{plug} is calculated with:

$$k_{\text{plug}} = k_{\text{wall}} \left(\frac{a_{\text{empty}}}{a_{\text{sand-filled}}} - 1 \right) \tag{5.1}$$

First, a pile under pure bending is modelled to verify the value of k_{wall}. This is done for an empty pile, using the same method Kostis [10] analysed piles under pure bending in Abaqus, by applying a rotation on both ends of the pile. The pile has a radius of 500 mm, thickness of 10 mm and the modulus of elasticity is 210,000 MPa. The analytical stiffness of the pile wall is calculated with equation 2.46. In this equation a_{empty} is equal to $a_c = q_c \frac{R_m^4}{12EI_w}$ (equation 2.32). Hence, the analytical wall stiffness $k_{\text{wall,analytical}}$ is $\frac{12EI_w}{R_m^4} = 3692\ \text{kN/m}^2$. As flexible dolphins are to provide their service in the elastic range, the stiffness is only valuable for elastic loadings. Therefore, the pile is loaded below the elastic curvature. The calculated stiffness from the Abaqus results for different curvatures is compared to the analytical stiffness in table 5.17. It shows that the value of the wall stiffness obtained by Abaqus, $k_{\text{wall,FEM}}$ has a constant deviation factor from the analytical value of approximately 1.23. Therefore, the stiffness value in the FEM $k_{\text{wall,FEM}}$ can well be calculated by multiplying the analytical stiffness $k_{\text{wall,analytical}}$ by this factor. The ovalisation in Abaqus is smaller than analytically predicted. Therefore the pipe wall in Abaqus acts stiffer.

Table 5.17: Comparison of the analytical stiffness of the pile wall with the stiffness in Abaqus.

κ [1/**m**]	q_c [**kN/m**]	a [**mm**]	$k_{\mathbf{wall,FEM}}$ [**kN/m**^{3}]	$k_{\mathbf{wall,FEM}}/k_{\mathbf{wall,analytical}}$ [−]
0.001	1.1	0.23	4536	1.23
0.002	4.2	0.92	4547	1.23
0.003	9.5	2.08	4554	1.23
0.004	16.8	3.7	4518	1.22

With $k_{\text{wall,FEM}}$ known, for a given distributed load q the ovalisation for an empty pile a_{empty} can be calculated. The distributed load q is the summation of the load due to bending q_c ($R_m t E_s \kappa^2$, equation 2.33) and the load due to soil pressure Q_i. The latter is derived by differentiating the shear force V, that is obtained from the Abaqus analysis. Last, to determine the value of k_{plug} the ovalisation for the sand-filled pile $a_{\text{sand-filled}}$ is required. It is equal to the ovalisation in the Abaqus analysis, a_{FEM}, calculated as the difference in the displacement $U1$ at position A and C as defined in figure 5.27.

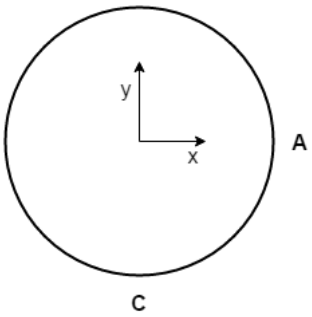

Figure 5.27: Position A and C to determine the ovalisation at A.

Dolphin piles that are semi-filled with sand have a transition from an empty part to a part where sand is present. At the top of the plug, the sand has the freedom to move upwards. Deeper in the pile, this freedom is limited due to the presence of the sand column above it. Due to this contrast in freedom, less resistance against ovalisation is expected at higher levels. Therefore, the plug stiffness is studied at -1m, -2m, -3m and -4m, i.e. $1.1D_e$, $2.2D_e$, $3.3D_e$ and $4.4D_e$ below the bed level. The plug level is at -0.78m ($0.8D_e$). This is illustrated in figure 5.28.

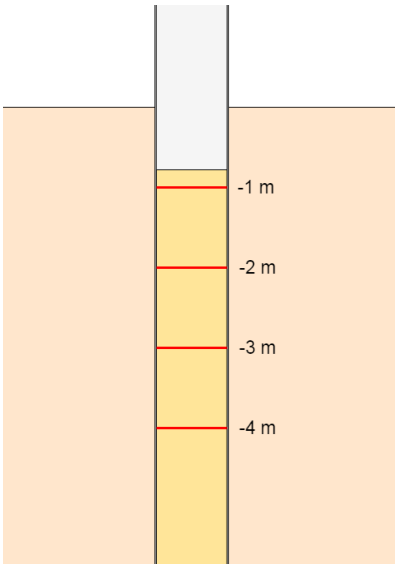

Figure 5.28: Levels at which the plug stiffness is studied.

Figure 5.29 shows that a compact packed plug (as described in paragraph 5.1) reduces the ovalisation, since the ovalisation obtained in Abaqus, a_{FEM}, is smaller than the ovalisation for an empty pile a_{empty}. The reducing effect is stronger at deeper levels. The relation between a_{empty} and a_{FEM} is non-linear. This is different than the relation that is suggested by the CUR 211E [3]. Furthermore, at higher values for a_{empty}, larger ovalisations are observed than obtained with the relation of the CUR 211E [3].

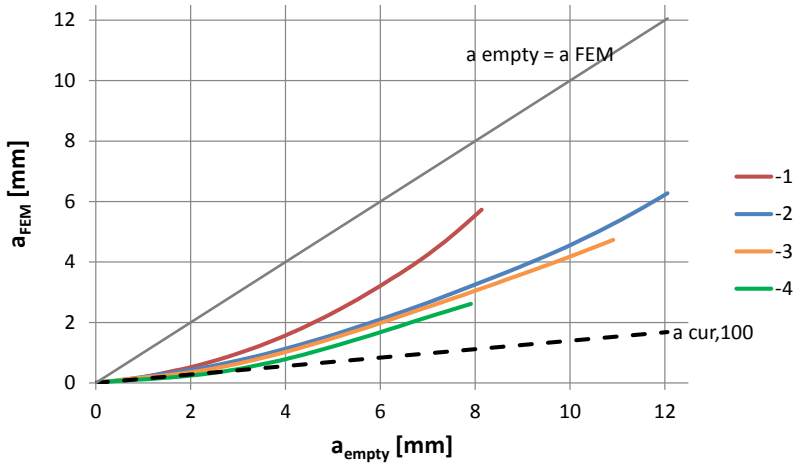

Figure 5.29: a_{FEM} obtained at different levels for E_{plug} = 100 MPa.

With the obtained ovalisation, the stiffness $k_{\text{plug,FEM}}$ is derived (figure 5.30). Again, it is observed that the plug is stiffer at deeper levels. At deeper levels, when the pile starts to ovalise, the stiffness of the plug increases. This indicates that the sand-strut has a non-linear stiffness. A maximum is reached when a_{empty} is approximately 1.5 mm. At this point the sand-strut fails. The sand moves sideways, as was illustrated in figure 2.16. Increasing the ovalisation even further, reduces the stiffness. At -1m and -2m the sand strut seems not to exist. This can be due to the fact that at these levels the sand is able to move upwards. For higher values of a_{empty}, the stiffness $k_{\text{plug,FEM}}$ is considerably lower than the suggested stiffness in CUR 211E [3].

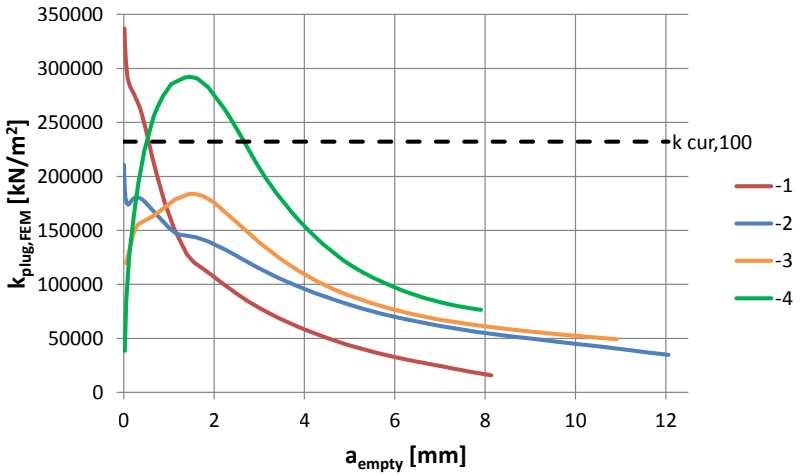

Figure 5.30: $k_{\text{plug,FEM}}$ derived at different levels for E_{plug} = 100 MPa.

Local buckling occurs when the ovalisation is significant. Using the analytical method from chapter 3, a stiffness k_{plug} should be used that corresponds to a larger ovalisation. For a larger a_{empty}, the value of $k_{\text{plug,FEM}}$ closer to the top of the plug are considerably lower than the values obtained at the deeper depths. Only at the top of the plug, the sand is able to move upwards, which leads to a lower stiffness. As an example, when ovalisations in the order of 8 mm are to be expected, the stiffness along the depth is presented in figure 5.31. It shows that there is a kink in the relation along the depth. This indicates up to what level the extra degree of freedom (being able to move upwards) can be accounted for.

The local buckling resistance of the studied situation in this paragraph can be predicted with the analytical

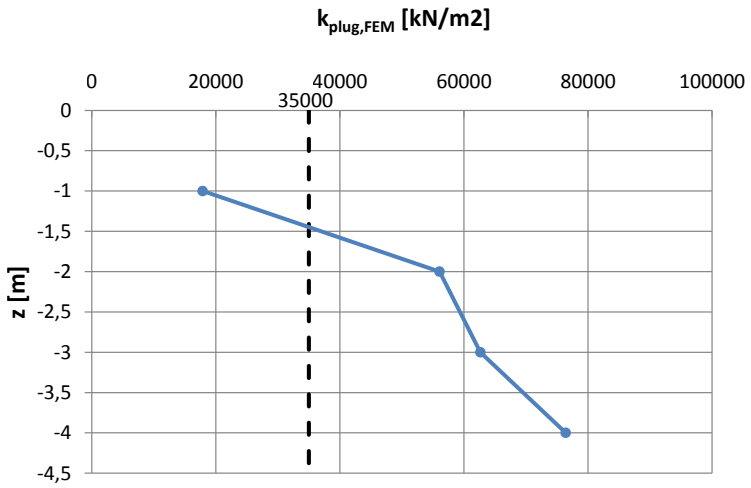

Figure 5.31: Relation between $k_{\text{plug,FEM}}$ and z for E_{plug} = 100 MPa and a_{empty} = 8 mm.

method from chapter 3. Local buckling is expected between the level of the maximum bending moment and the level of the maximum ovalisation. The latter is in all Abaqus analyses observed at the same level or above the level of the maximum bending moment, which analytically can be computed around -2m. Therefore, it can be assumed that local buckling would occur between -1.5m and -2m. To be safe, the improvement of the plug on the resistance is rather underestimated than overestimated. Therefore, a value of 35,000 kN/m^2 is a proper estimation for the plug stiffness.

5.5.1. Plug packing

It is thought that the packing influences the stiffness of the plug. Hence, the situations with a loose and dense plug packing as described in paragraph 5.1 are also studied. CUR 211E [3] insinuates that a looser packing of the plug, with a lower modulus of elasticity, is less stiff (equation 2.44).

The reducing effect of a plug on the ovalisation is also observed in the situations with a loose plug packing and a dense plug packing (figures 5.32 and 5.33). Both figures show that at deeper levels the reduction is larger, indicating a larger stiffness $k_{\text{plug,FEM}}$.

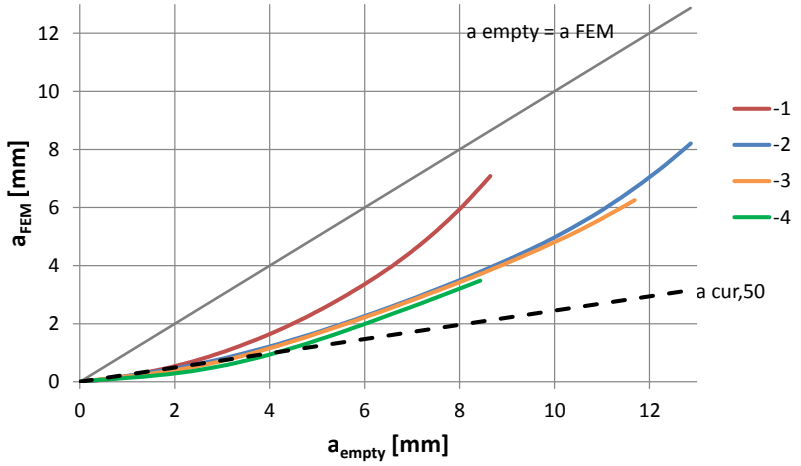

Figure 5.32: a_{FEM} obtained at different levels for E_{plug} = 50 MPa.

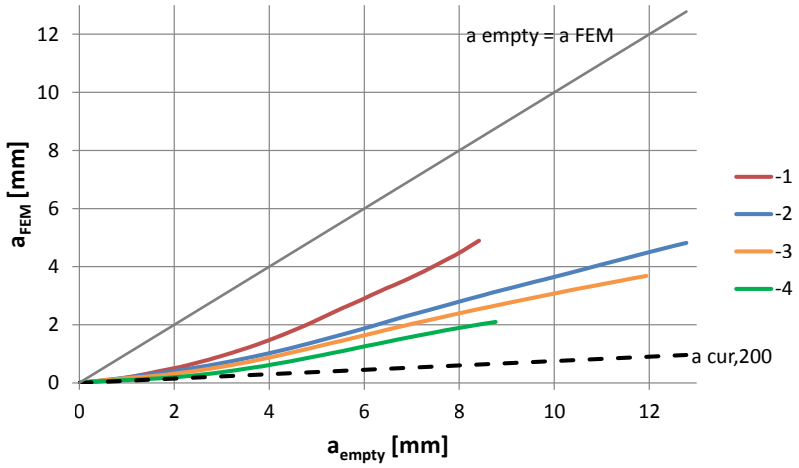

Figure 5.33: a_{FEM} obtained at different levels for $E_{\mathrm{plug}} = 200$ MPa.

More clearly it is noticed that the stiffness is larger at deeper depths in figures 5.34 and 5.35. Again, the sand-strut behaviour at deeper depths and the lacking of this behaviour close to the plug level is observed. A difference can be denoted comparing the values of $k_{\mathrm{plug,FEM}}$ with the values of $k_{\mathrm{plug,CUR}}$. With $E_{\mathrm{plug}} = 200$ MPa, the value of k_{plug} is highly overestimated, even at the deep levels. With the compact plug packing, the suggestion of the CUR 211E [3] can be an estimation of k_{plug} at deep levels for small ovalisations. In the situation where $E_{\mathrm{plug}} = 50$ MPa, this suggestion can also be used at a higher levels for small ovalisations, yet it underestimates $k_{\mathrm{plug,FEM}}$. Local buckling occurs for the larger ovalisations. At these values, the CUR 211E [3] overestimates the stiffnesses for all studied plug packings at all studied levels. Therefore, it can be concluded that this suggestion is not able to determine the plug stiffness for semi-filled piles. The overestimation of the stiffness will lead to an underestimated ovalisation and hence to an overestimated local buckling resistance. The same conclusion was drawn in paragraph 3.5.

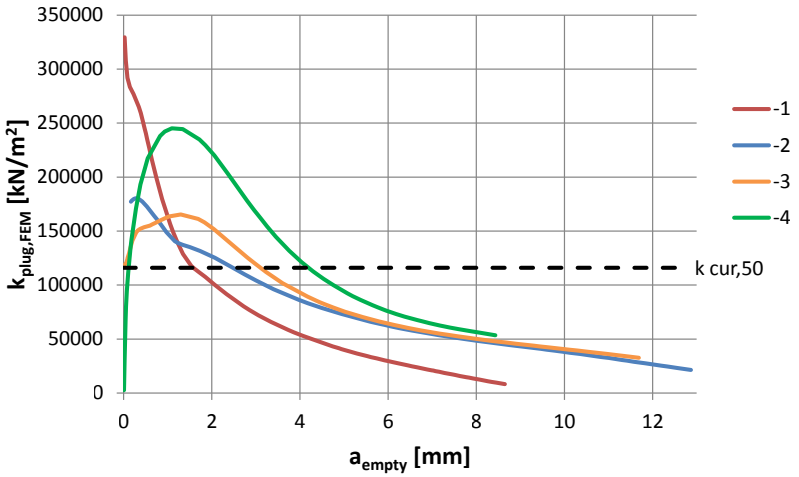

Figure 5.34: $k_{\mathrm{plug,FEM}}$ derived at different levels for $E_{\mathrm{plug}} = 50$ MPa.

The influence of the soil packings on -2m is compared in figures 5.36 and 5.37. A denser packing reduces the ovalisation more. This was also concluded in paragraph 5.1. The difference in stiffness $k_{\mathrm{plug,FEM}}$ however, is much smaller than suggested in CUR 211E [3].

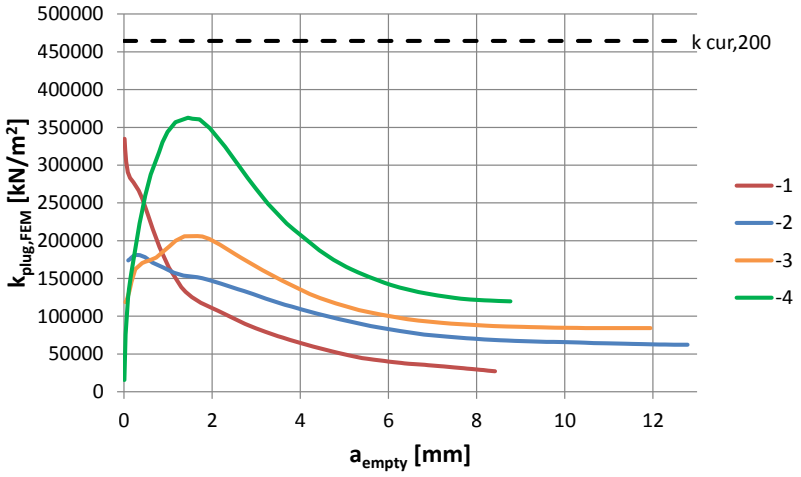

Figure 5.35: $k_{\text{plug,FEM}}$ derived at different levels for $E_{\text{plug}} = 200$ MPa.

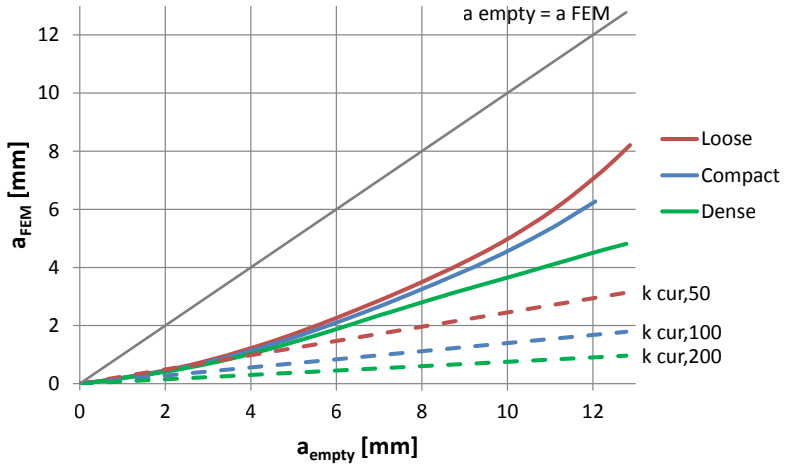

Figure 5.36: a_{FEM} obtained with different plug packings at $z = -2$ m.

The comparison is also made at the other levels. The results are presented in appendix E. From these results, the same conclusions can be drawn.

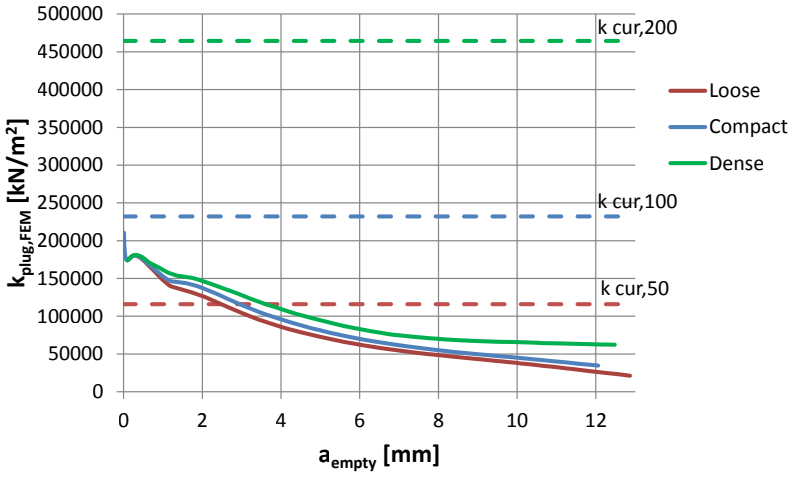

Figure 5.37: $k_{\text{plug,FEM}}$ derived with different plug packings at $z = -2$ m.

The relation between the stiffness and the depth for different plug packings is presented in figure 5.38. The influence of the packing increases at deeper levels. Close to the plug level however, the stiffnesses $k_{\text{plug,FEM}}$ are in the same range for different packings. Hence, if values of a_{empty} less than 8 mm are expected, a value of 30,000 kN/m^2 can be assumed, regardless of the plug packing. In case, it can be assumed that local buckling will occur at deeper levels, or it is known that the plug is densely packed, higher values for k_{plug} may be used.

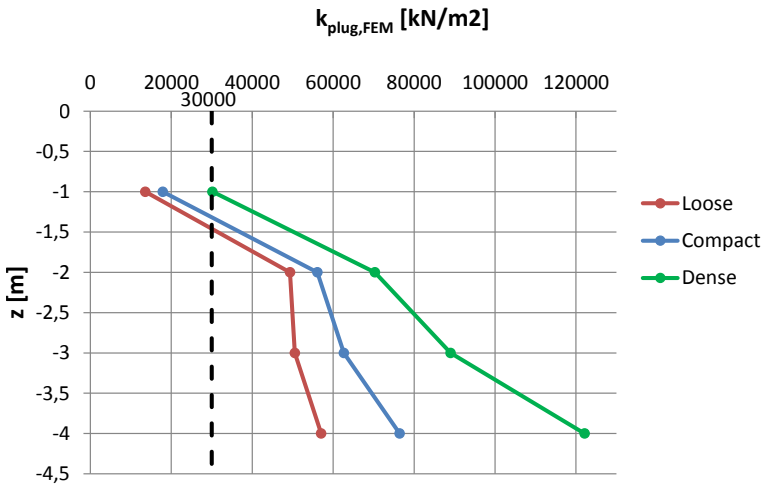

Figure 5.38: Relation between $k_{\text{plug,FEM}}$ and z for different plug packings with $a_{\text{empty}} = 8$ mm.

5.5.2. Slenderness Ratio

So far, the stiffness is studied with the same pile properties. To check whether the plug stiffness $k_{\text{plug,FEM}}$ is independent of the stiffness of the pile wall k_{wall}, situations with different thicknesses, as described in paragraph 5.3, are studied.

The difference with these geometries is taken into account in the stiffness of the pile wall $k_{\text{wall}}\left(\frac{12EI_w}{R_m^4}\right)$. k_{wall} is smaller for more slender cross-sections, i.e. for similar ovalisation loads, the cross-section will ovalise more. Hence, larger values for the a_{empty} will be obtained.

Table 5.18: Pile wall stiffness $k_{\text{wall,FEM}}$ for different slenderness ratios.

Slenderness Ratio	D_e [**mm**]	t [**mm**]	R_m [**mm**]	EI_w [$\mathbf{kNm^2/m}$]	$k_{\mathbf{wall,FEM}}$ [$\mathbf{kN/m^3}$]
90	914	25	444.5	300	113,610
129	914	17.5	448.25	103	37,680
250	914	9	452.5	14	4,936

It is expected that $k_{\text{plug,FEM}}$ is only influenced by the size of the ovalisation. Regardless of the slenderness, at the same value for a_{FEM} the same reaction of the plug and therefore a similar value for $k_{\text{plug,FEM}}$ is expected.

Equation 5.1 prescribes that with an equal value for k_{plug} and a smaller value for k_{wall}, the ratio $a_{\text{empty}}/a_{\text{sand-filled}}$ should increase. Figure 5.39 shows that this ratio indeed is larger for a more slender cross-section, as for the same value of a_{empty}, larger values of a_{FEM} are observed.

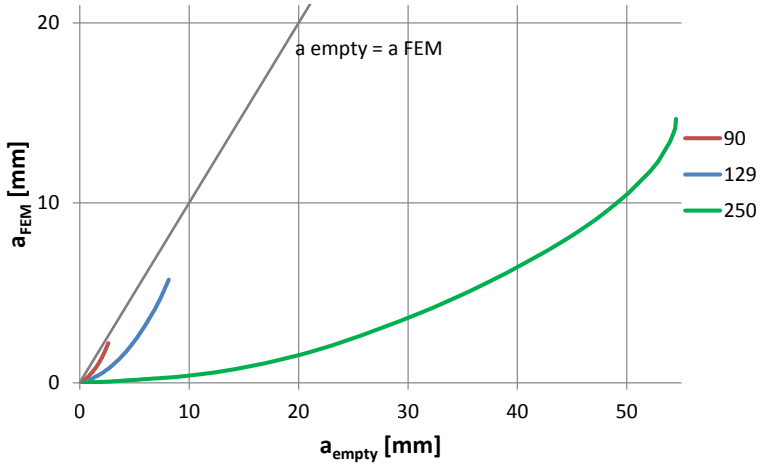

Figure 5.39: a_{FEM} obtained with different slenderness ratios at $z = -2$ m.

The plug stiffness $k_{\text{plug,FEM}}$ is plotted against a_{FEM} in figures 5.40-5.43. For similar values of a_{FEM}, the same $k_{\text{plug,FEM}}$ is derived. Therefore, it can be concluded that the plug stiffness is independent of the slenderness ratio.

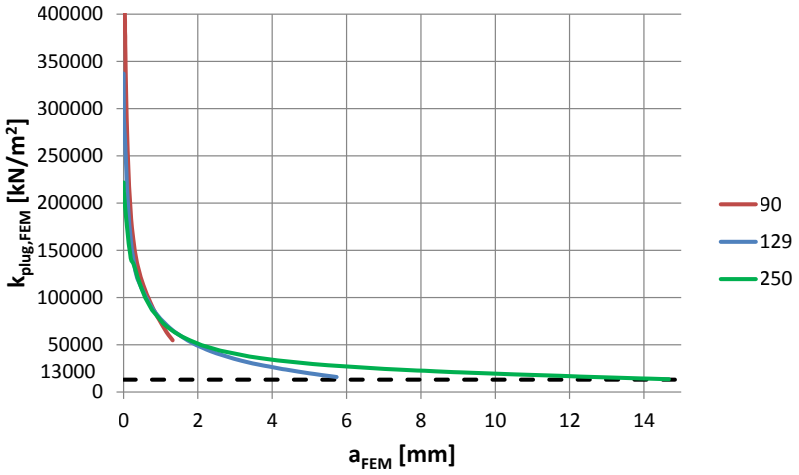

Figure 5.40: Relation between $k_{\text{plug,FEM}}$ and a_{FEM} obtained with different slenderness ratios at $z = -1$ m.

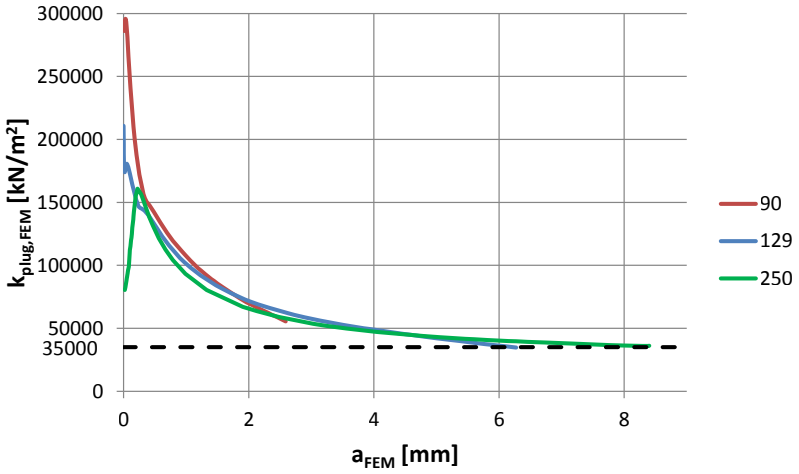

Figure 5.41: Relation between $k_{\text{plug,FEM}}$ and a_{FEM} obtained with different slenderness ratios at $z = -2$ m.

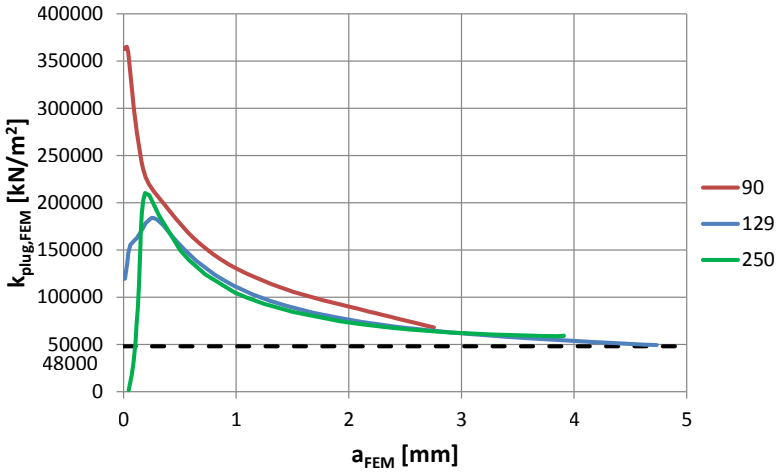

Figure 5.42: Relation between $k_{\text{plug,FEM}}$ and a_{FEM} obtained with different slenderness ratios at $z = -3$ m.

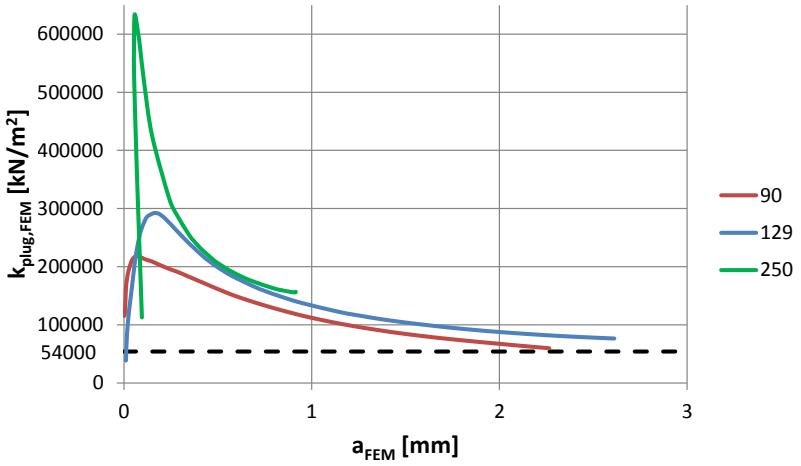

Figure 5.43: Relation between $k_{\text{plug,FEM}}$ and a_{FEM} obtained with different slenderness ratios at $z = -4$ m.

The figures indicate that the stiffness is not significantly reduced when the ovalisation a_{FEM} is further increased. This value of $k_{\text{plug,FEM}}$ can be used in the analytical method to calculate the ovalisation. In figure 5.44, these values are plotted at their corresponding depth. This plot can be used to estimate the stiffness of the plug. It should be noted that this figure is obtained with a compact plug. A loosely packed plug will be less stiff, especially at deeper depths (see 5.5.1).

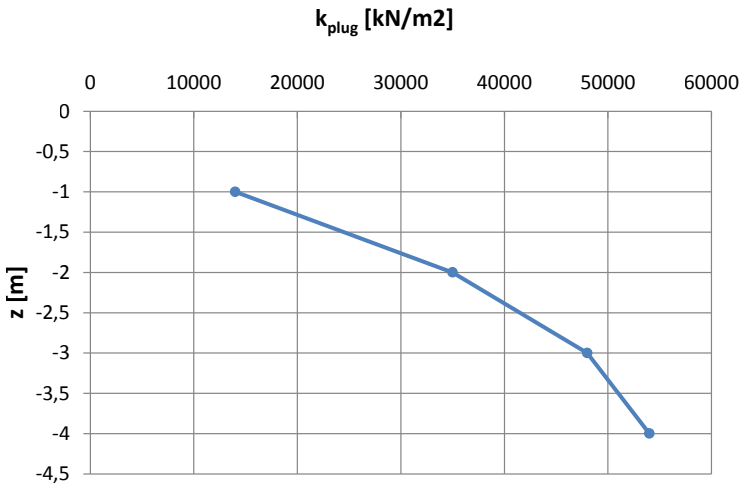

Figure 5.44: k_{plug} for a compact packed plug.

Studying the plug stiffness derived from the Abaqus analyses, $k_{\text{plug,FEM}}$, also showed that the plug is stiffer deeper below the plug level. At deeper levels, for small ovalisations, a sand-strut improves the plug stiffness. However, this sand strut fails before the ovalisation has reached values that are observed just before local buckling.

Comparing the behaviour of the plug for different plug packings with the suggested value for k_{plug} in CUR 211E [3], again revealed that it is not able to determine the plug stiffness for semi-filled piles. The comparison also confirmed that a denser packing reduces the ovalisation more. Close to the plug level however, the stiffnesses $k_{\text{plug,FEM}}$ are in the same range for different packings. Hence, if values of a_{empty} less than 8 mm are expected, a value of 30,000 kN/m^2 can be assumed, regardless of the plug packing.

From the analyses with different slenderness ratios it can be concluded that the plug stiffness is independent of this ratio. Moreover, for large ovalisations, a further increase in ovalisation does not significantly reduce the plug stiffness. Hence, a plot could be created that can be used to estimate the stiffness of the plug with a compacted packing.

It should be noted that the stiffness is studied only for a diameter of 914 mm. Soil plugs with a significant different diameter could respond differently.

6

Validation with full scale tests

To study the failure modes of dolphins, the Port of Rotterdam facilitated a full scale field test with eight piles. One of these piles, pile 6, was modelled in Abaqus. The results obtained with the Abaqus analyses are validated using the observations in the field test. First, this chapter discusses the test set-up, the evaluation methodology and general results of the field test. Next, the comparison with the Abaqus model is made. Finally, the buckling behaviour of three other piles is clarified with the knowledge gained from the parametric study in chapter 5.

6.1. Test set-up

The test programme was defined around the main parameters listed below. Levels are relative to a reference hight (Ref).

- Water depth: Ref –8 m
- Water level variation: Ref -1.0 and +1.5 m
- Top of pile: minimum Ref +2.5 m
- Pile diameter D_e: 914 mm
- Embedded length L_s: 9 to 11 m
- Pile wall thickness t: 12 to 21 mm
- Measured yield strength f_y: 340 to 580 MPa

The geotechnical characterization of the site and the corresponding derivation of model parameters are based on six CPTs. The test site mainly consists of loose to medium dense sand layers, inter-layered with thin layers of silt and clay. The general geotechnical profile is presented in table 6.1.

Table 6.1: General geotechnical profile from 6 cone penetration tests.

Description	γ [kN/m^3]	φ' [°]	c' [kPa]
Sand, loose to medium dense	19	31	2.5

The eight piles were devided in three types with a typical steel design as indicated in figure 6.1. Type 1 is a full-length class 4 pile of which the target wall thickness ratio $D_e/t\varepsilon^2$ is 120-130 in the soil. Type 2 has a slenderness ratio of 90-100 in the embedded section and is assumed to show significant yielding. On top is a part with a reduced wall thickness. Therefore, there also is a wall thickness transition. The target slenderness of type 3 is 140-160 over the full length. These piles were filled with sand. However, the process of filling the part above the bed level did not result in an adequate soil density. Hence, the effect of the sand-fill could not be studied from these tests.

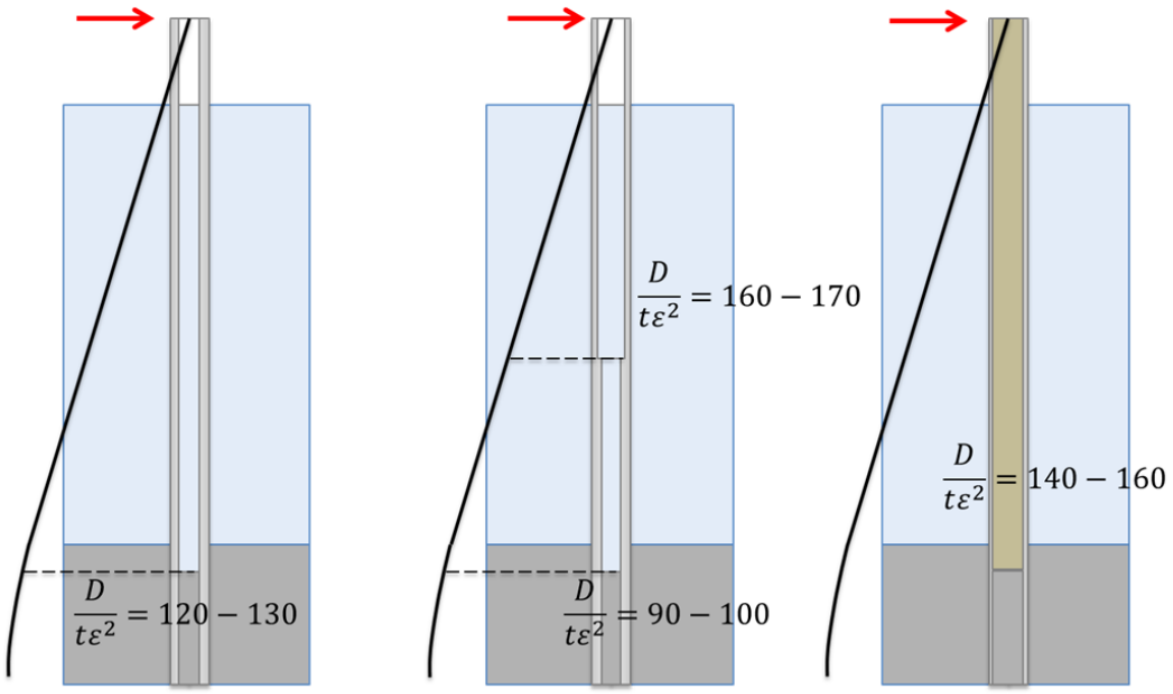

Figure 6.1: Three pile types with indicated target wall thickness.

All piles were subjected to a series of load tests. The first tests were all meant to stay within the range of elastic response. The load tests were divided into dynamic tests and static tests. The dynamic tests were executed with a system of cables and pulleys and a crane on a floating pontoon. The crane was modified in such a way that it could suddenly impose a line pull of 150 kN. The pulley system multiplied the load to 300 and 450 kN lateral force acting on the pile. Given the inertia of the pontoon and the system stiffness this resulted in an almost idealised load-time diagram with a 1 second rise time. The load was typically maintained at a constant level during 3, 6, 10 and 15 seconds over the various tests.

The static tests were carried out using two hydraulic jacks (figure 6.2) with a stroke of 2.5 m and push/pull capacities of 2 × 1,000 and 2 × 400 kN. The deformation rate of the hydraulic jacks was typically at 2 cm/sec. The jacks were mounted in a purpose made frame (figure 6.3) that rested on three piles, while loading a fourth pile. All piles were installed on a grid of uniform triangles, spacing 7.5 m. Three piles with 1420 mm diameter were used as anchor piles.

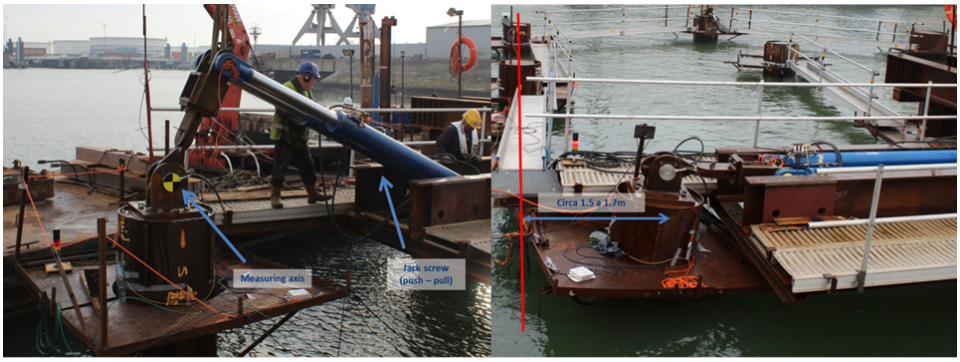

Figure 6.2: Rearranging the loading set-up between static push and pull tests. [18]

Figure 6.3: Top view of test set-up with static loading frame. [18]

Steel stresses and bending moments can be calculated from measured strains (paragraph 6.2). The strains are measured by fibre optic strain sensors (figure 6.4). They are installed on all test piles on both sides at the outer fibre line on eight vertical positions.

To measure circumferential strains, fibre optic strain sensors were also installed at four quarter positions in selected cross-sections. The piles of type 1 were equipped with circumferential sensors in one cross-section 0.5 m above the bed level. On the piles of type 2 sensors were installed in two additional cross-sections 0.5 m under and above the wall thickness transition.

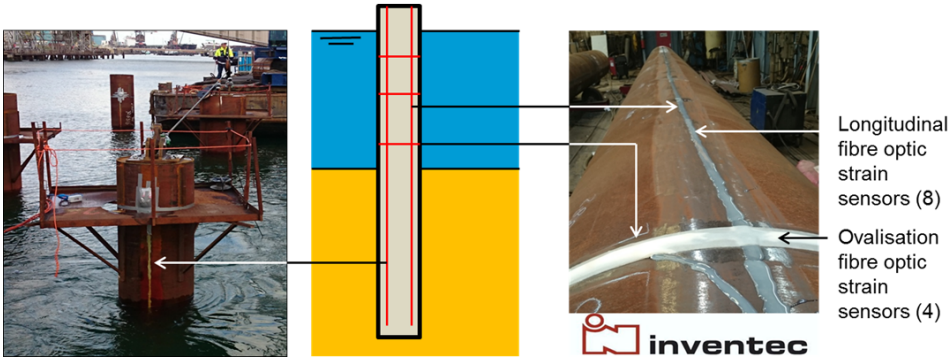

Figure 6.4: Fibre optic strain sensors. [18]

The exerted force was measured using an electronic shear beam. The shear beam was mounted as an axle in a stool that was bolted on top of the piles. Also the jack stroke was measured. Furthermore, at critical time steps the displacements of the piles were measured by surveying the xyz coordinates using station keeping equipment.

6.2. Evaluation methodology

From the strain measurements, curvatures are calculated according to equation 6.1. The strains at both sides are averaged, thereby excluding strains caused by normal forces.

$$\kappa = \frac{\varepsilon_t - \varepsilon_c}{D_e} \tag{6.1}$$

Where:

ε_t	Measured longitudinal strain at the tension side	[-]
ε_c	Measured longitudinal strain at the compression side	[-]

From the curvatures, the deflection of the pile can be calculated with the relation in equation 2.4. Before yielding, when $\kappa < \kappa_e$, also the bending moment can be calculated (equation 2.34). Here the elastic curvature κ_e is found with:

$$\kappa_e = 2\frac{f_y}{E_s}\frac{1}{D_e} \tag{6.2}$$

When the curvature is bigger than the elastic curvature $\kappa > \kappa_e$, the cross-section will be elastic-plastic. The idealized moment-curvature relation is used to find the bending moment:

$$M = M_p \cdot \frac{1}{2}\left(\frac{\theta}{\sin\theta} + \cos\theta\right) \tag{6.3}$$

In which:

$$M_p = 4R_m^2 t f_y \tag{6.4}$$

$$\theta = \arcsin\frac{\kappa_e}{\kappa} \tag{6.5}$$

The shear force V is derived by differentiating the bending moment. It was checked to match the applied lateral load F.

From the circumferential strains it was attempted to find the ovalisation a. From the nominal measured strain, a difference in wall curvature is found with:

$$\varepsilon_{\text{nom}} = \Delta\kappa_{\text{nom}}\frac{t}{2} \tag{6.6}$$

Where:

ε_{nom}	Measured circumferential strain	[-]
κ_{nom}	Circumferential curvature of the pile wall	[m^{-1}]

Gresnigt [1] derives the ovalisation a from the circumferential curvature κ_{nom}:

$$\Delta\kappa_{\text{nom}} = \frac{3a}{R_m^2} \tag{6.7}$$

Here symmetrical ovalisation is assumed. However, besides the ovalisation due to bending a_c, the ovalisation is also influenced by the earth pressure a_q. Hence, the assumption is not valid.

6.3. Test Results

For all piles, the predicted failure mode was failure of the steel tube due to local buckling or excessive yielding. All piles of type 1 failed due to local buckling in the embedded part, at the location of the maximum bending moment at approximately 2 m below the bed level.

During the failure tests the piles developed large deformations caused by elastic and plastic pile deformation supplemented with rotation of the pile in the soil. Some of the piles did not fail within the available jack stroke but showed typical softening. Other piles failed and showed a typical force-displacement-curve related to buckling.

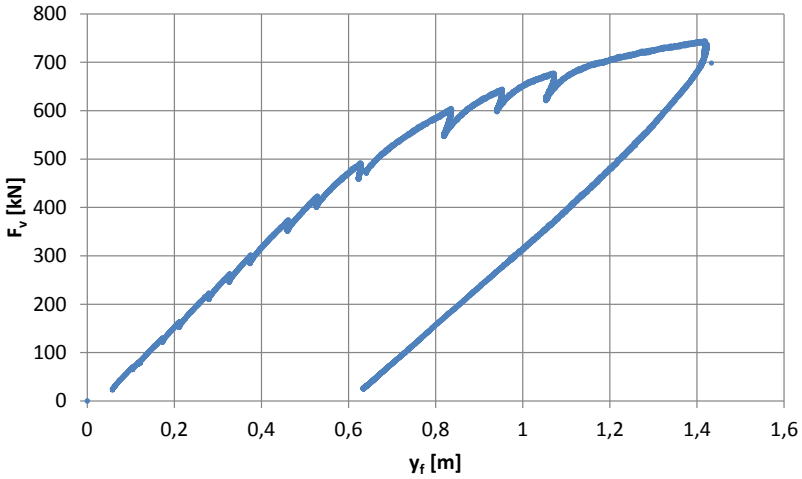

Figure 6.5: Force-displacement diagram pile 2 with softening, plasticity and unloading.

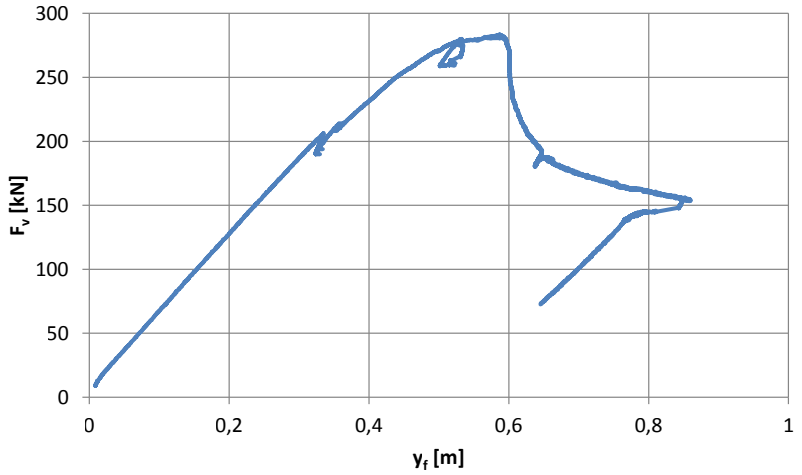

Figure 6.6: Force-displacement diagram pile 8 with local buckling in the embedded part of the pile.

6.4. Pile 6

First, the pile was dynamically loaded in two tests with applied loads of 16.5 and 32.5 ton. The next day static tests were performed. The pile was first pushed (42 ton) and then pulled (42.7 ton). In a third test the pile was pushed with 47 ton. Next, the pile was loaded until failure. In a first attempt, the pile was pulled with 60 ton, but the pile did not fail yet. In a second attempt, the pile was loaded up to 71 ton when local buckling occurred.

The moment-curvature diagram evaluated from the measurements is presented in figure 6.8. Here, the maximum calculated curvature is the critical curvature corresponding to the maximum bending moment. A drop in the moment-curvature diagram indicating local buckling cannot be found using this method. This is because the curvature is coupled to the analytical corresponding bending moment.

A force-displacement diagram from the measurements of the last test, in which pile 6 was loaded to failure, has to be adapted to find the true force-displacement diagram of the pile. In the previous test the pile was loaded beyond the elastic capacity. Therefore, the pile has an initial plastic deformation. Hence, the diagrams of the last two tests have to be combined (6.7). When buckling occurs there is a drop in the force-displacement diagram. This indicates that less force is required to displace the top of the dolphin. The local buckle causes

the resistance to decrease. This drop was not accurately measured for pile 6. Pile 8 that also buckled did show this typical descent (figure 6.6). The other diagrams obtained from the measurements are presented in figure 6.9.

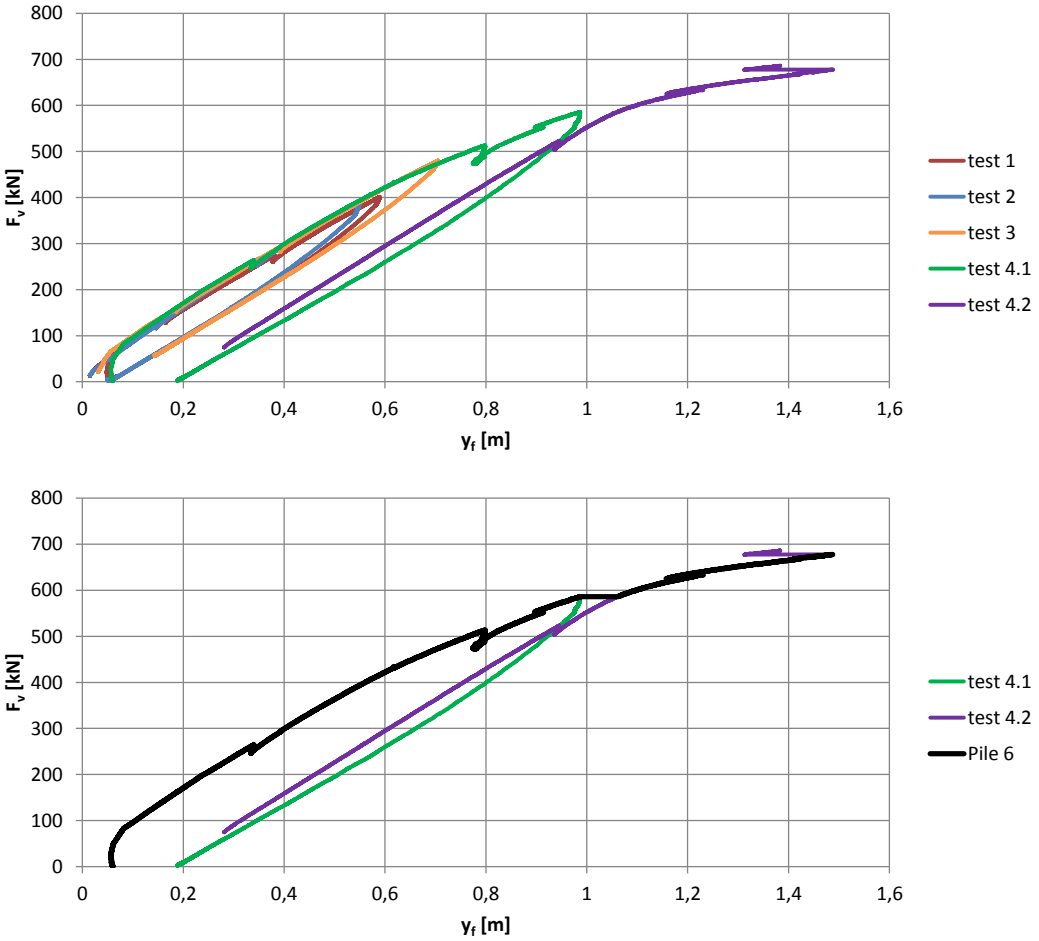

Figure 6.7: Force-displacement diagram of pile 6.

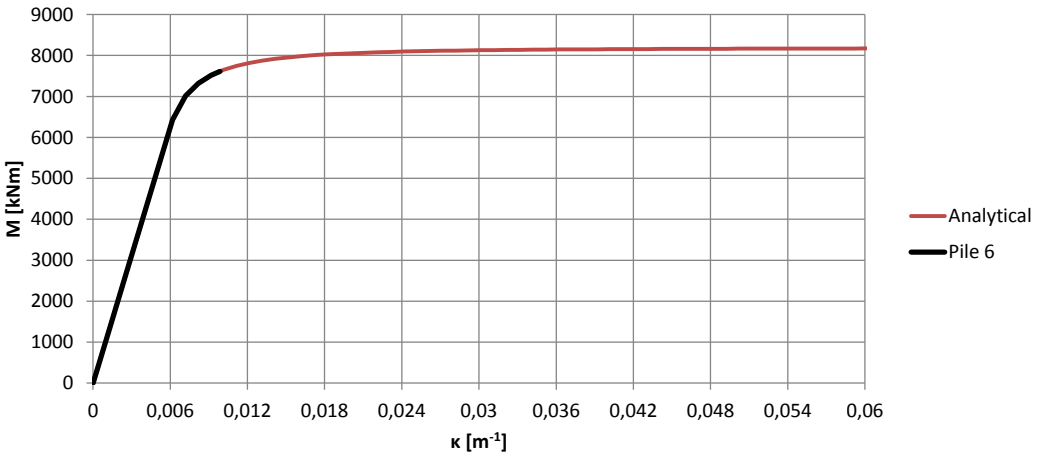

Figure 6.8: Moment-curvature diagram of pile 6.

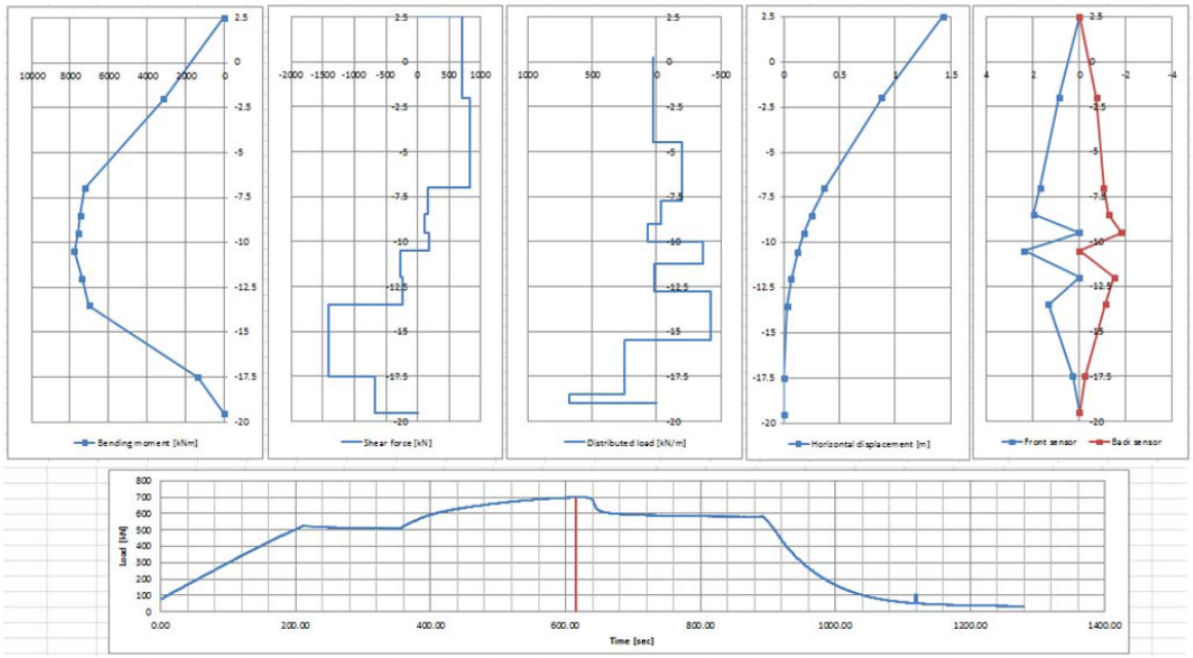

Figure 6.9: Results of pile 6 just before failure.

6.5. Validation - Pile 6

The model in Abaqus is based on pile 6 and hence it is validated with the test results of this pile. The location of the buckle in Abaqus and its shape are compared to the buckle observed in the field test. Also, it is analysed how the pile capacities of the modelled pile relate to the capacities experienced in reality.

The bending moment lines are compared for the same applied lateral load in figure 6.10. The bending moment produced by Abaqus that is presented, is obtained just before buckling occurred. The applied lateral load was 636 kN. The bending moment diagram of pile 6 that is presented, was retrieved when a similar later load was applied on the pile. The bending moment line produced by Abaqus shows good comparison with the results obtained in the field test. Both locate the maximum bending moment at -2m.

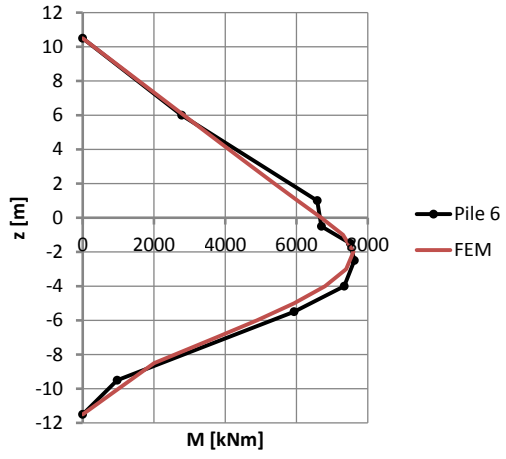

Figure 6.10: Bending moment diagram of pile 6 and FEM.

The level of local buckling in the field tests is determined with measurements of the permanent deflections. These are measured every meter. The permanent deformations are a consequence of loading the pile beyond its yield capacity. In general, the measured permanent deformation is positive and increases towards higher levels, revealing the permanent curved shape of the pile. An example of a permanently curved dolphin pile is shown in figure 6.12. For pile 6, the buckle is observed around 2m below the bed level (figure 6.11). At the buckling level, a negative permanent deformation is measured. This indicates that the buckle is an inward buckle. In Abaqus also an inward buckle was observed. However, the buckle was observed at -1.6m. The difference could be due to the low accuracy of the measurement in the field test. It could also be that the plug packing in the field test is less compact than was assumed in Abaqus. The Abaqus analysis with a looser plug packing resulted in local buckling at the same level the maximum bending moment occurred (figure 5.5).

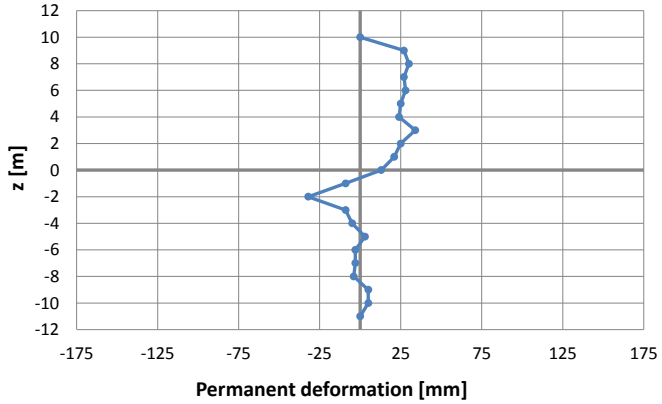

Figure 6.11: Measured permanent out of roundness of pile 6.

Figure 6.12: Permanently curved dolphin pile. [18]

Figure 6.13 presents the moment-curvature diagram of pile 6 and the pile modelled in Abaqus. In the elastic range, the moment-curvature diagram obtained with the finite element analysis corresponds to a pile with the dimensions and steel grade of pile 6. For larger curvatures, the pile ovalises. Yet, the ovalisation effect is not taken into account for determining the bending moment of pile 6 from the derived curvature (paragraph 4.6). Therefore, the bending moment capacities can not accurately be compared. The bending moment capacity in reality is probably lower than assumed for pile 6. The critical curvatures deviate. The curvature itself is not a parameter that is generally used in designing a dolphin pile. The bending moment that corresponds to the critical curvature derived for pile 6 (0.0099 $m^{-}1$), according to the relation obtained in Abaqus, is 7388 kNm rather than 7611 kNm. The bending moment capacity of pile 6 and the modelled pile are therefore in the same range.

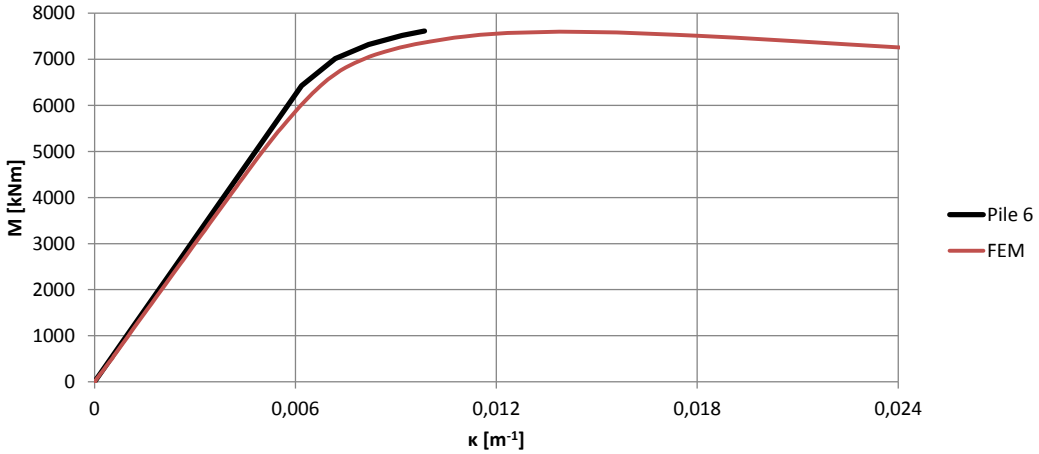

Figure 6.13: Moment-curvature diagram pile 6 and the pile modelled in Abaqus.

Table 6.2: Maximum bending moment of pile 6 and the pile modelled in Abaqus.

	M_{max} [kNm]	M_{max}/M_y	M_{max}/M_p	κ_{cr}	κ_{cr}/κ_e
Pile 6	7611	1.18	0.93	0.0099	1.59
FEM	7599	1.18	0.93	0.0139	2.25

The force and displacement are more reliable. For lateral loads up to approximately 400 kN, the diagrams presented in figure 6.14 demonstrate the same relation. For larger displacements, higher loads are required in Abaqus compared to the reality. The soil packing may influence this behaviour. The lateral load capacity observed in Abaqus (636 kN) is 6.0% less than the real capacity (677 kN). Moreover, as the displacement is larger the energy capacity is significantly higher in reality than observed in Abaqus.

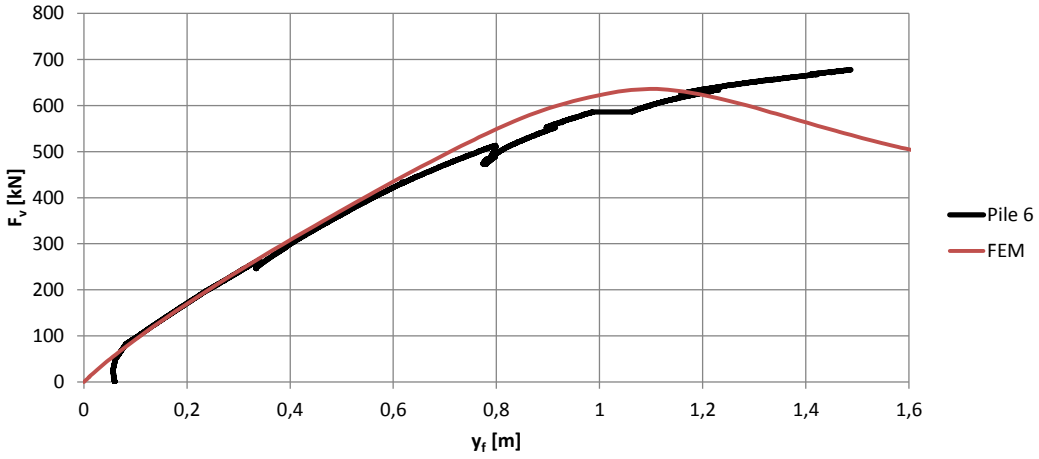

Figure 6.14: Force-displacement diagram of pile 6 and the pile modelled in Abaqus.

Table 6.3: Maximum lateral load and energy capacity in the SLS and ULS of pile 6 and the pile modelled in Abaqus.

	SLS		**ULS**	
	$F_{v,max}$ [kN]	$E_{v,max}$ [kNm]	$F_{v,max}$ [kN]	$E_{v,max}$ [kNm]
Pile 6	636	468	677	639
FEM	539	229	636	419

Figure 6.15 compares the force-displacement diagrams of pile 6 with the soil packing as assumed from the CPT's and a looser soil packing, as described in paragraph 5.4. It shows that for larger displacements the force-displacement relation is better predicted with a looser soil packing. The lateral load capacity is still underestimated. That Abaqus provides deviating results for larger deformations could be because of the material model used for the soil. A more advanced soil model than the Mohr-Coulomb model, might produce more realistic results.

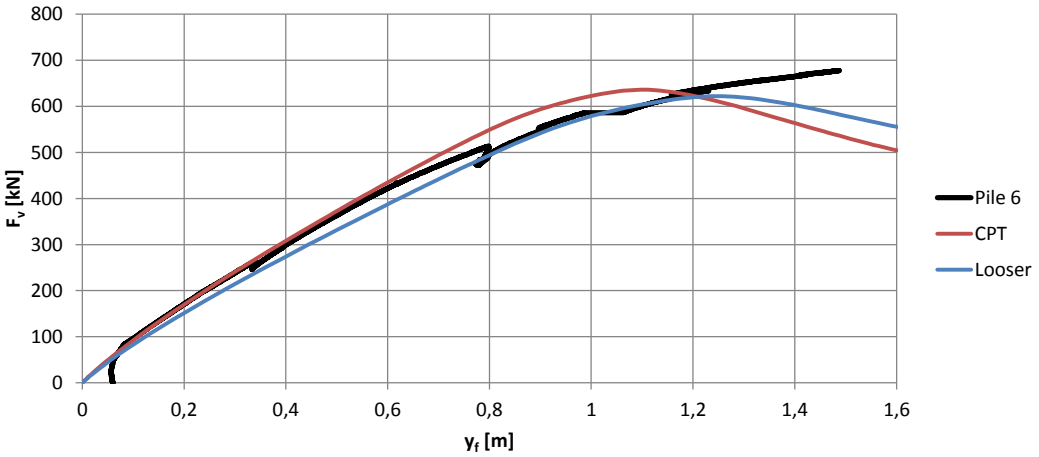

Figure 6.15: Force-displacement diagram of pile 6 and the pile modelled in Abaqus with different soil packings.

Due to the difference in buckling level, previously it was stated that perhaps in reality the plug was packed looser. This could also be an explanation for the overestimated critical curvature. The effect of a looser plug packing on the capacities is illustrated in figures 6.16 and 6.17. Even though the critical curvature is more comparable with a looser plug packing, the lateral load capacity is further reduced.

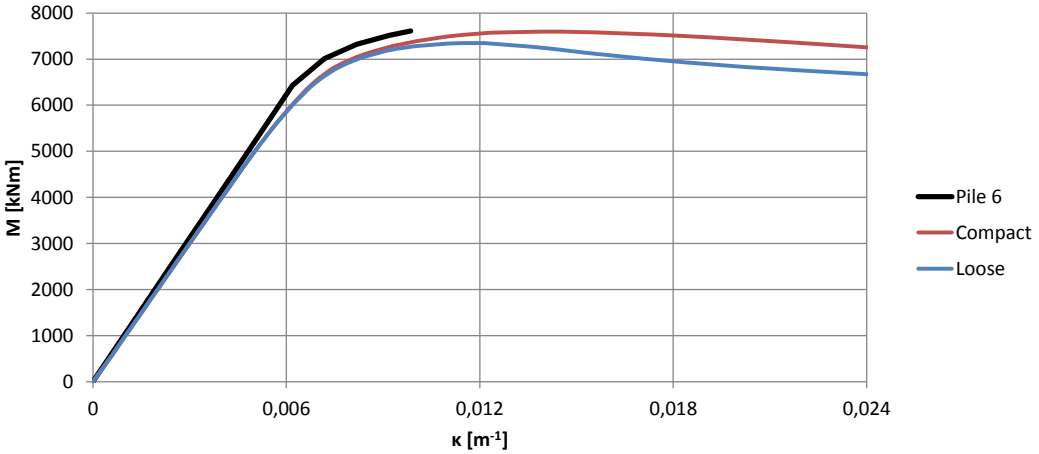

Figure 6.16: Moment-curvature diagram of pile 6 and the pile modelled in Abaqus with different plug packings.

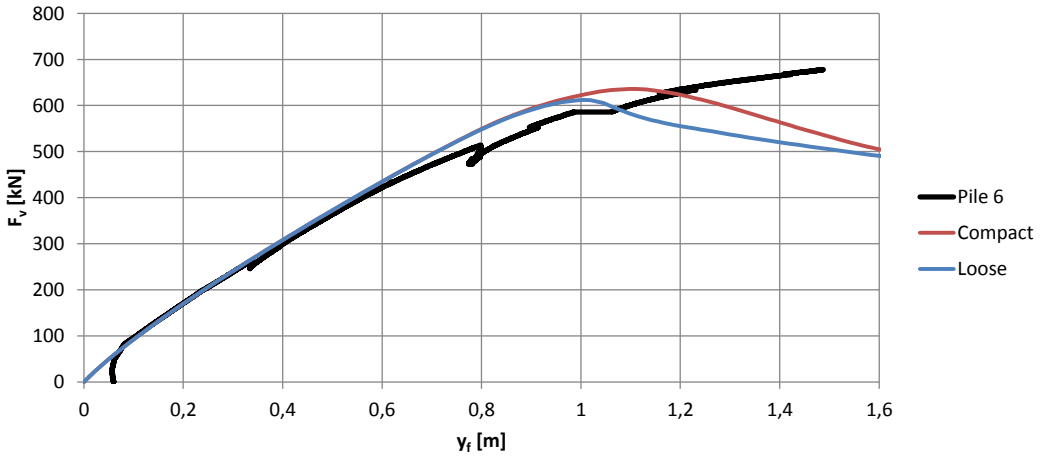

Figure 6.17: Force-displacement diagram of pile 6 and the pile modelled in Abaqus with different plug packings.

In general, the Abaqus model is comparable with the results obtained from the full scale test. Probably the plug is more loosely packed than assumed in the Abaqus model. The deviating force-displacement diagram and hence the energy capacity is allocated to the material model used.

6.6. Piles 2, 3 and 8

With the gained knowledge of chapter 5 the local buckling behaviour of piles 2, 3 and 8 is clarified.

6.6.1. Pile 2

Pile 2 is also a pile of type 1. Compared to pile 6, pile 2 has a different assembly. The assembly of pile 2 is illustrated in figure 6.18. The main differences are the thickness of the mid-section of the pile (17.2 mm compared to 17.5 mm of pile 6) and the yield strength of 540 MPa, whereas pile 6 has a yield strength of 582 MPa. Hence, the slenderness ratio of pile 2 is 122, compared to 129 of pile 6. For a pile with a lower slenderness ratio the pile is expected to have more capacity. Due to the fact that the piles are installed in the same bedding and the plug level is at 1.55 m below the bed level, lower than in the setting of pile 6, the same buckling location and shape are expected.

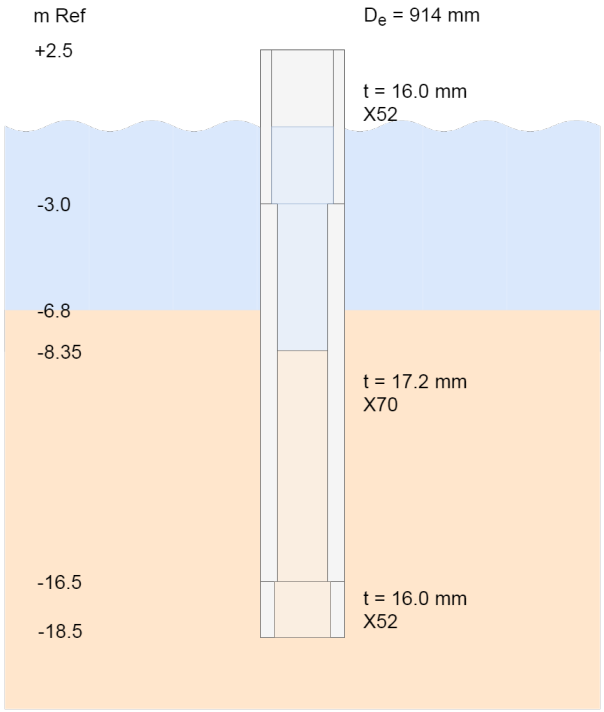

Figure 6.18: Assembly of pile 2.

Local buckling is observed around -1.7m, 1.15m below the plug level. Whether the buckle is an inward or outward buckle is not clear from figure 6.19. That is because there is no clear general curve of the pile. If the permanent curve observed above the bed level is assumed as the general curve, it would indicate that the buckle is towards the midpoint of the circle of curvature and hence an outward buckle would be present. The maximum bending level is obtained at a lower level, at -3.2m. That local buckling occurs above the maximum bending moment, closer to the plug level, can be explained by a larger ovalisation at a this level. The plug has a larger reducing effect on the ovalisation at deeper levels (paragraph 5.5). The situation can be described as a situation 3 or 4 as clarified in paragraph 5.1. Local buckling occurring above the level of the maximum bending moment was also observed in the Abaqus analysis for a compact and dense plug packing. The buckling location differs from the expected level. Probably the plug packing in pile 2 is more compact than in pile 6.

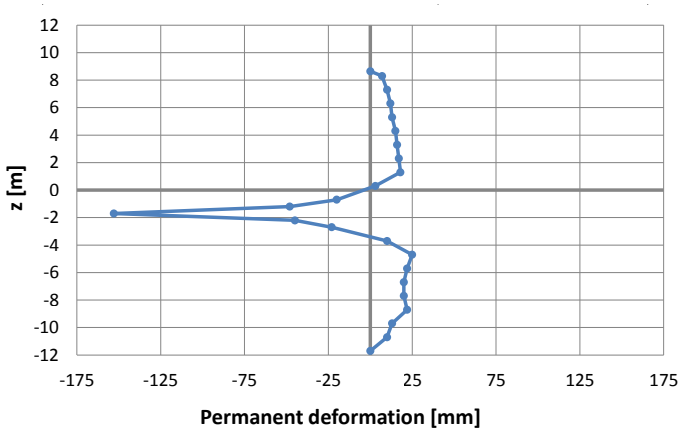

Figure 6.19: Measured permanent out of roundness of pile 2.

Due to the lower slenderness ratio, a higher capacity $M_{\max}/M_p$ is obtained. The maximum bending moment

Table 6.4: Bending moment capacity of pile 2 and 6.

	$z_{\mathbf{Mmax}}$ [m]	$M_{\mathbf{max}}$ [kNm]	$M_{\mathbf{max}}/M_y$	$M_{\mathbf{max}}/M_p$
Pile 2	-3.2	7185	1.22	0.96
Pile 6	-1.5	7611	1.18	0.93

itself is lower, because of the smaller thickness and yield strength.

6.6.2. Pile 3

Pile 3 has just another assembly, illustrated in figure 6.20. The mid-section of the pile has a thickness of 17.2 mm, like pile 2. The yield strength is 528 MPa. The slenderness ratio of pile 3 is therefore 119. A little more capacity than pile 2 is therefore expected. Again the expectation is that buckling will be observed at the same location with an inward shape.

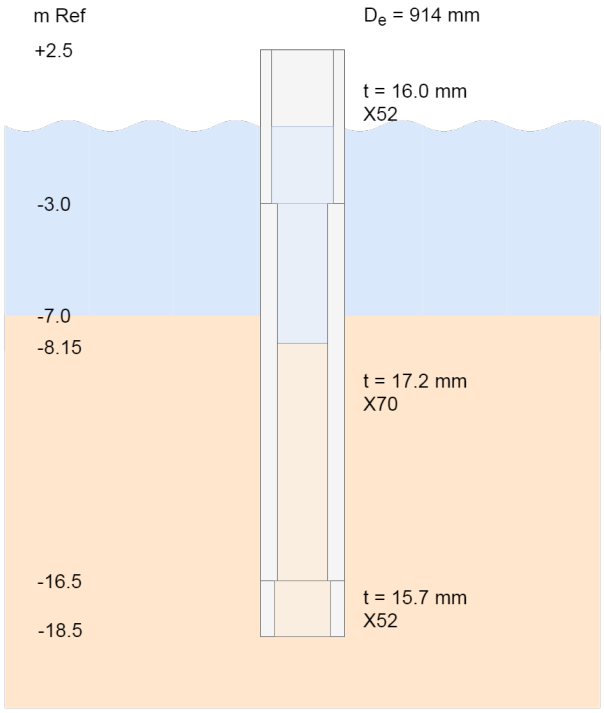

Figure 6.20: Assembly of pile 3.

Like with pile 6, at the buckling level the deformation is opposite of the general deformation, therefore pile 3 buckles inward (figure 6.21). Local buckling occurs at -1.5m, 0.35m below the plug level. The maximum bending level is obtained at -3.0m, again at a lower level than the buckling level. This makes the situation similar to the situation of pile 2.

The slight difference in slenderness ratio compared to pile 2, does not influence the capacity. Due to the fact that the yield strenght is lower, the maximum bending moment is lower.

Table 6.5: Maximum bending moment of pile 3.

	$z_{\mathbf{Mmax}}$ [m]	$M_{\mathbf{max}}$ [kNm]	$M_{\mathbf{max}}/M_y$	$M_{\mathbf{max}}/M_p$
Pile 2	-3.2	7185	1.22	0.96
Pile 3	-3	6977	1.22	0.96
Pile 6	-1.5	7611	1.18	0.93

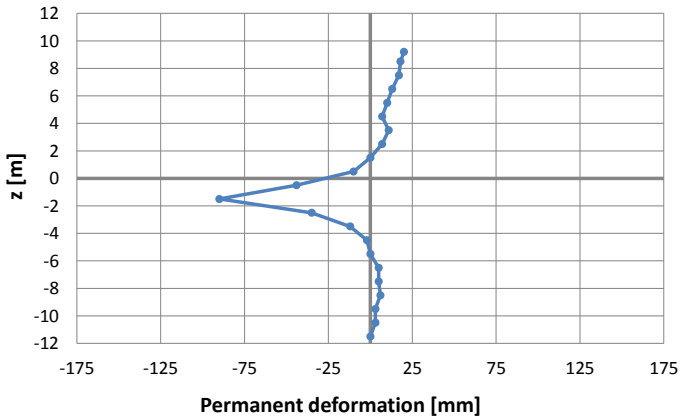

Figure 6.21: Measured permanent out of roundness of pile 3.

6.6.3. Pile 8

Pile 8 is thinner than the other piles (figure 6.22). Yet, the yield strength is also lower. With a thickness of 12 mm and yield strength of 380 MPa, the slenderness ratio is 123. A similar capacity as pile 2 is expected (slenderness ratio of 122). Pile 8 was filled with sand. However, the process of filling the top part after pile installation did not result in an adequate soil density. Even though the sand-fill is not expected to contribute to a reduction of the ovalisation above the soil plug, it increases the soil pressure in the plug, enhancing the plug stiffness. Therefore an outward buckle is expected at the level of the maximum bending moment, as was observed in the analysis with a plug level at the bed level (paragraph 5.2).

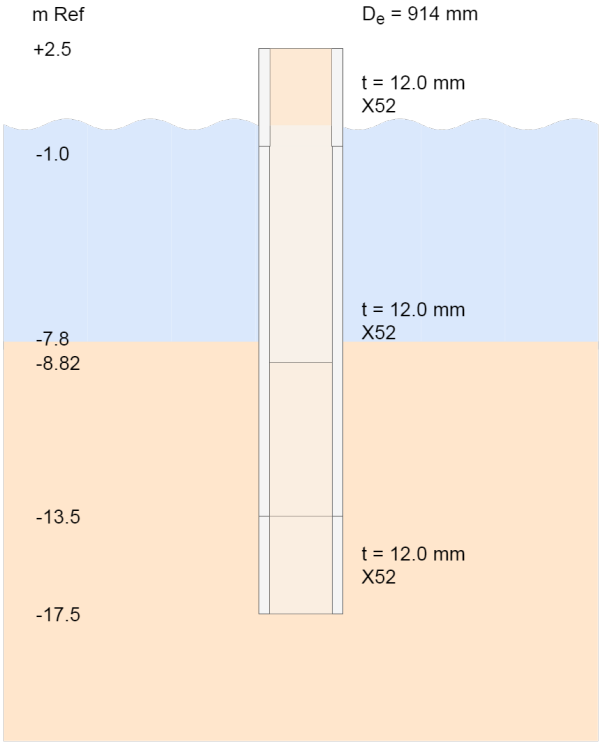

Figure 6.22: Assembly of pile 8.

In figure 6.23 it appears that the buckle is towards the midpoint of the circle of curvature, indicating an outward buckle. The buckle is located at -1.7m. This is around the same level at which the maximum bending moment is observed. This is conform the expectation.

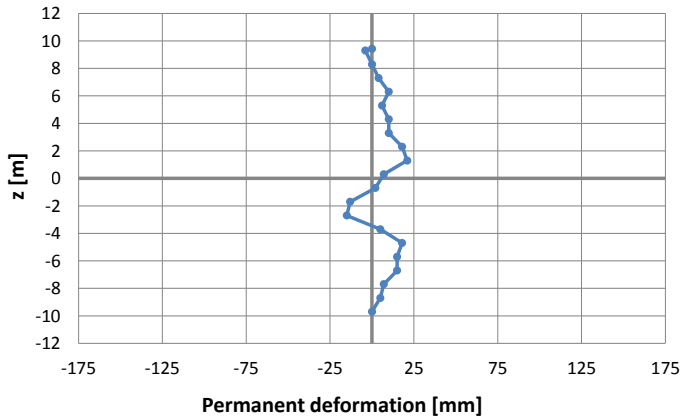

Figure 6.23: Measured permanent out of roundness of pile 8.

Table 6.6: Maximum bending moment of piles 2, 3, 6 and 8.

	$z_{\mathbf{Mmax}}$ **[m]**	$M_{\mathbf{max}}$ **[kNm]**	$M_{\mathbf{max}}/M_y$	$M_{\mathbf{max}}/M_p$
Pile 2	-3.2	7185	1.22	0.96
Pile 3	-3	6977	1.22	0.96
Pile 6	-1.5	7611	1.18	0.93
Pile 8	-1.5	3511	1.20	0.95

As expected the capacity is a little lower, yet comparable to the capacities of piles 2 and 3. Due to the reduced thickness and yield strength, a lower maximum bending moment is obtained.
The observed local buckling levels and shapes in the field tests can well be explained with the results of the finite element analyses presented in chapter 5. Just the buckling location of pile 6 deviates from the expected results. A looser plug packing might be the cause. Furthermore, it can well be predicted what pile has a higher capacity.

7

Conclusions and recommendations

7.1. Conclusions

Does the soil in dolphin piles contribute to the local buckling resistance and can this be used in the design of these piles?

To be able to answer this main question, the available codes and general background is studied. Gresnigt [1] prescribes a strain based method to check a pile on local buckling. This method is incorporated in EN 1993-4-3 [2]. The resistance against local buckling depends on the slenderness ratio $D_e/t\varepsilon^2$. Also, ovalisation influences the resistance. The presence of a soil plug reduces the ovalisation. Hence, the soil in dolphin piles contributes to the local buckling resistance.

An analytical method, based on beam theory, is proposed that overcomes the issue of different theoretical ovalisation values at transition areas. The method was verified with Plaxis calculations.

Key parameters that affect the local buckling resistance are identified. These are the plug packing, plug level, slenderness ratio and the soil packing. The influence of these key parameters are studied with finite element analyses. The finite element programme has to be able to compute local buckling as well as the soil-structure interaction.

The Port of Rotterdam facilitated a full scale field test. These tests are used to validate the finite element model.

How the existence of a soil plug can be used in the design of dolphin piles is deliberated more extensively in the succeeding conclusions.

7.1.1. Analytical method

Based on the knowledge from studied literature an analytical model is introduced to discover whether local buckling can analytically be predicted. The resulting analytical model provides a quantitative insight in the local buckling behaviour of flexible dolphins. Herewith key parameters that influence the local buckling behaviour are identified.

Analytical model

Beam theory is used to determine the dolphin pile deformation and loads on the pile. Literature provides equations to calculate the ovalisation that can be applied in three distinct parts: above the bed level, between the bed level and plug level and below the plug level. The provided equations however, show inconsistencies at the transitions. It is proposed to apply beam theory on the pile wall, modelled as a linear beam with springs providing resistance against ovalisation. Above the plug level the resistance is provided by the ring behaviour of the shell. Below the plug level the stiffness is increased with the stiffness of the soil plug. The model overcomes the inconsistencies in ovalisation.

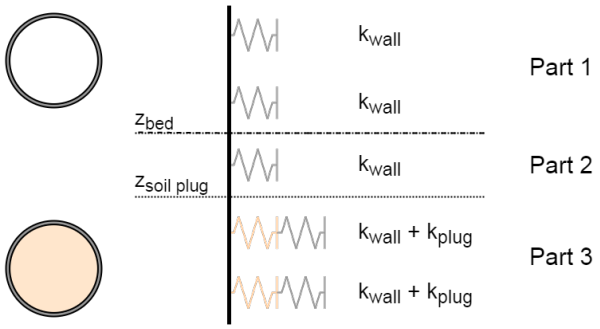

Figure 7.1: Model of pile wall.

The method assumes the stiffness of the plug in the pile k_{plug} can be approximated. In CUR 211E [3] a simple 1D model of the support of a sand plug to a steel ring was introduced. This sand-strut model can be improved using analytical expressions for the initial soil stress state and the soil stiffness in the plug:

$$\sigma'_h = K_0 \gamma z + \varepsilon_h E_{\text{plug}}$$

With:

$$E_{\text{plug}} = E_{\text{rep}} \left(\frac{\sigma'_h}{100} \right)^m$$

From Plaxis calculations a value of 0.2 is obtained for stresss dependency power m.

Following this improved formulation, the plug is less stiff and the ovalisation will be larger than assumed with the 1D model. This 1D model might underestimate the risk of local buckling.

Another method, the volumetric method, is introduced to estimate the plug stiffness. This method is a 2D method, based on the compression due to a reduced area of the cross-section when it ovalises. The decrease in area in the cross-section causes a volumetric strain ε_V:

$$\varepsilon_V = \frac{\Delta V}{V} = \frac{\Delta A}{A} = \frac{\pi r^2 - \pi (r+a)(r-a)}{\pi r^2}$$

The volumetric strain method introduced results in a stiffness of the plug that is too low, compared to the Plaxis calculations. It might predict a larger ovalisation than the ovalisation that will occur in practice. Therefore, the volumetric strain method results in a too conservative estimation of the local buckling resistance.

As the sand-strut model is overestimating the stiffness of the plug and the volumetric strain method underestimates this stiffness, they form boundaries in between which the real stiffness is found.

Key parameters

Insight is gained in the parameters that affect local buckling in semi-filled piles.

The compressive strain is highest at the location of the maximum bending moment. The relation between the bending moment and the strain is influenced by the bending stiffness of the flexible dolphin, which again is determined by the diameter and thickness of the dolphin pile. The bending moment itself differs for soils with different stiffness.

The critical strain by Gresnigt [1] is influenced by the slenderness ratio ($D_e/t\varepsilon^2$) and the ovalisation. The latter depends on the stiffness of the plug and the plug level.

Key parameters are therefore the packings of the plug and the soil, the plug level and the slenderness ratio.

7.1.2. FEM

The FEM is used to approximate the real local buckling behaviour. A model is set up with which the influence of the key parameters is studied. The model is validated with full scale tests.

Of the eight piles that were tested in the field, pile 6 is considered a representative pile to model. The pile has a length of 22 m of which 11.5 m is embedded. It has a diameter D_e of 914 mm. The mid-section, where local buckling occurred, has a thickness of 17.5 mm and yield strength of 582 MPa. Hence, the slenderness ratio is 129. The plug level is 0.78 m (approximately $0.8D_e$) below the bed level.

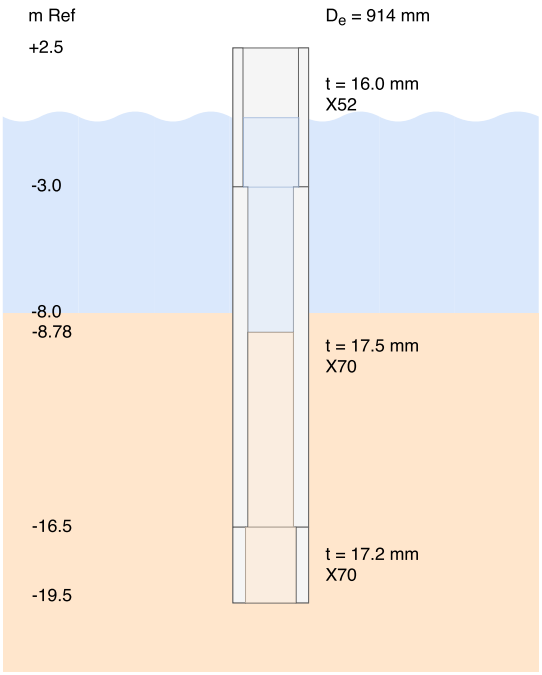

Figure 7.2: Assembly of pile 6.

Program

To decide which FEM program is used, a multi criteria analysis is performed on three available programs: Abaqus, Plaxis and TNO Diana. The programs are assessed on their ability to model local buckling and to solve soil structure problems. The latter is tested by comparing the results of an analysis with the measured physical results of the test [54]. Plaxis is more advanced in the geotechnical possibilities, yet it is not able to model local buckling. Abaqus and TNO Diana can model local buckling. It is thought that both programs are able to solve soil structure interaction problems. Therefore Abaqus and TNO Diana fulfil the requirements for this research. Due to the fact that Abaqus was used in previous local buckling research in which soil-structure interaction was concluded [10], Abaqus is used for this research.

Table 7.1: Multi criteria analysis FEM program.

Program	Local buckling	Soil structure interaction
Abaqus	++	+
Plaxis	- -	++
TNO Diana	+	+

Model

The mid-section of pile 6 is modelled in Abaqus. At the bottom of the model, the pile and the soil are considered as clamped. The pile is loaded by a horizontal displacement transferred to the mid-section by the top part that is modelled as a beam, constrained to the pile surface. The side boundaries of the model are at $20D_m$ from the center of the model. They suppress horizontal deformation of the soil. The vertical and horizontal cross-sections of the model with the applied boundary conditions are shown in the figure below.

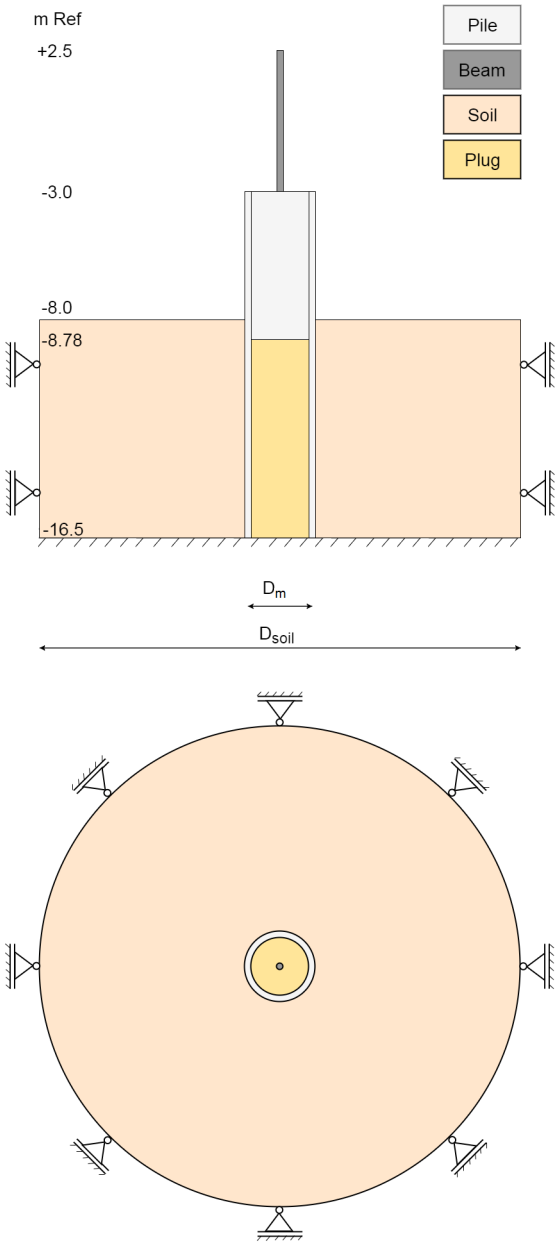

Figure 7.3: Vertical and horizontal cross-sections of the model with applied boundary conditions.

Imperfection

The initial imperfections that are essential for the failure mode of local buckling are implemented with the aid of a buckling analysis. Through this analysis a buckling mode is obtained, which provides translational and rotational deformations of the elements' nodes. These deformations are used as initial imperfections. The deformations from the buckling mode can be scaled. The size of the initial imperfections that should be used is studied for imperfection over thickness ratios of 0.05, 0.10, 0.20, 0.30, 0.40, 0.60 and 0.80.

The higher imperfection ratios of 0.60 and 0.80 show differing buckle locations. Also, their capacities seem too low compared to the field test. Imperfection thickness ratios of 0.05 and 0.10 tend to overestimate the bending moment capacity. Furthermore, their critical curvatures are incomparable higher than the other ratios. 0.20, 0.30 and 0.40 are imperfection ratios that show similar results comparing their bending moment capacity as well as the lateral force and energy capacity. An imperfection thickness ratio of 0.40 compares best with pile 6 of the field tests. Other than the lower ratios, it has an inward buckle shape which was also encountered in the field. The parametric study is performed with an imperfection thickness ratio of 0.40.

Plug packing

The influence of the plug packing is studied by comparing the results of the basic model with models with a looser and denser plug packing and a model without a plug. In the basic model a compacted plug is assumed with a Young's modulus E_{plug} of 100 MPa. The properties of the plug are adapted in order to have a loosely packed plug and a densely packed plug (see the figure below).

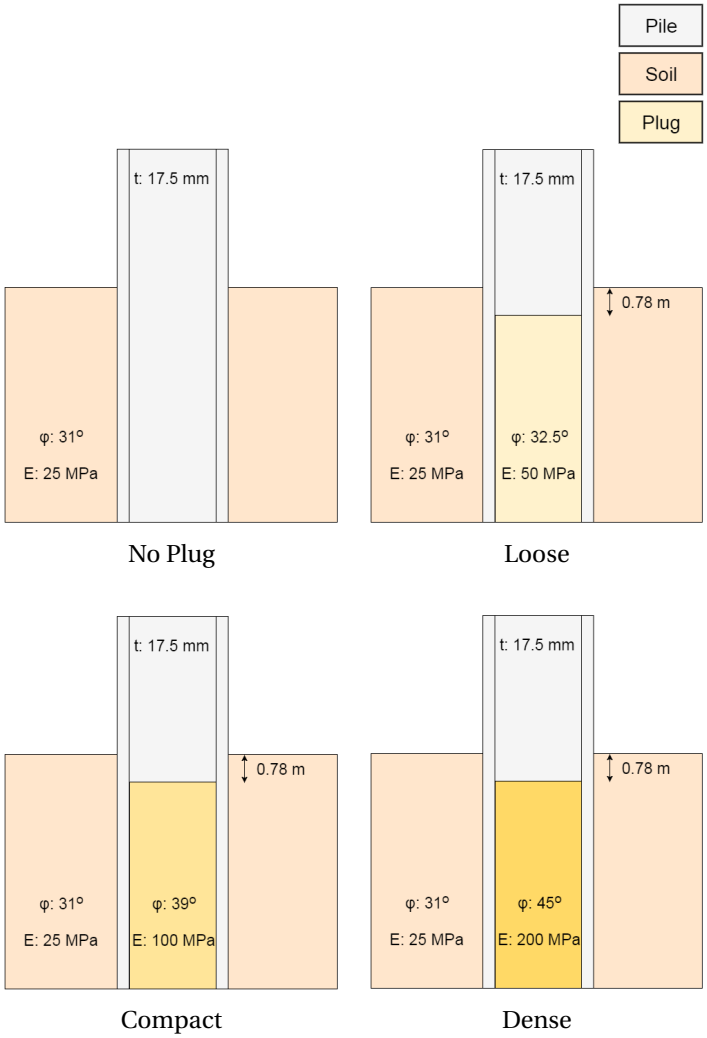

Figure 7.4: Plug parameters applied.

Table 7.2: Plug parameters applied.

Plug Packing	φ' [°]	ψ [°]	$E_{\mathbf{plug}}$ **[MPa]**	ν [-]	K_0 [-]	**Friction coefficient** [-]
Loose	32.5	2.5	50	0.32	0.463	0.40
Compact	39	9	100	0.27	0.371	0.49
Dense	45	15	200	0.23	0.293	0.58

The depth at which the maximum bending moment occurs is not changed because of the plug packing. Neither is a change in the path of the force-displacement diagram observed. This indicates that the plug packing does not significantly contribute to the stiffness of the dolphin.

A denser packing of the plug reduces the ovalisation, improving the capacities of the bending moment and lateral load. Most of all, the dolphin can dissipate more energy. This could influence the installation method to apply. Yet, the improvement is limited as local buckling will occur higher where the critical strain is lower. This is illustrated in the theoretical diagram below.

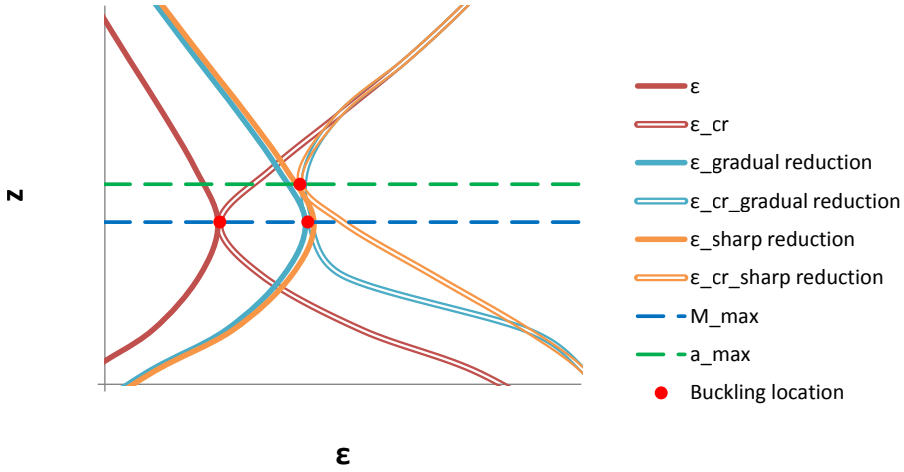

Figure 7.5: The improvement of the maximum compressive strain might not be in proportion with the reduction of the critical strain at the level of the maximum compressive strain, due to a higher critical point.

Plug level

The influence of the plug level on the buckling location and shape, as well as on the capacities of the dolphin pile, are studied with four different plug levels. In the basic model, the plug level is 0.72 m, or approximately 0.8 D_e, below the bed level. This situation is compared to a situation with the plug level even below the level of the maximum bending moment, at 3 D_e below the bed level. Also, analyses are run in which the plug level is at the bed level (0D_e below the bed level) and with no soil present in the pile.

Even though the buckling level and buckling shape differ for the situation with a plug up to the bed level and when the plug level is 0.8 D_e below the bed level, there is no significant difference in their capacities. In case of a deep plug, below the level of the maximum bending moment there is no significant difference compared to an empty pile. In designing dolphin piles the buckling location and shape are irrelevant. Therefore, if the plug level is approximated outside a reach of 1 D_e of the maximum bending moment, a rough indication of the plug level will satisfy. A pile with a plug below this reach can be assumed to be empty, whereas a pile with the plug level above this reach has improved capacities.

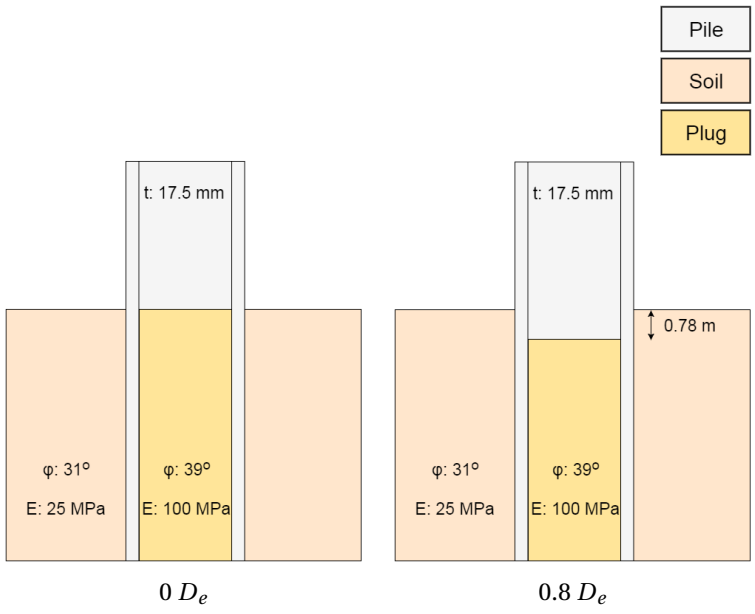

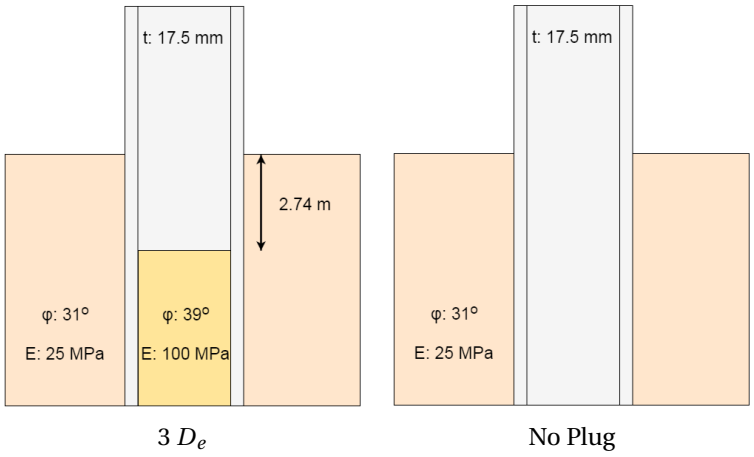

Figure 7.6: Plug levels tested.

Slenderness ratio

The slenderness ratios tested are 90, 129 and 250. The ratio of 129 is the ratio in the basic model. In these analyses, the diameter and steel grade are the same, only the thickness is adjusted. EN 1993-1-1 [13] prescribes that the slenderness limit for first yield has a value of 90. The characteristic behaviour of a class 4 cross-section should be shown by a cross-section with a very high slenderness ratio. Hence, the slenderness ratio of 250 is analysed.

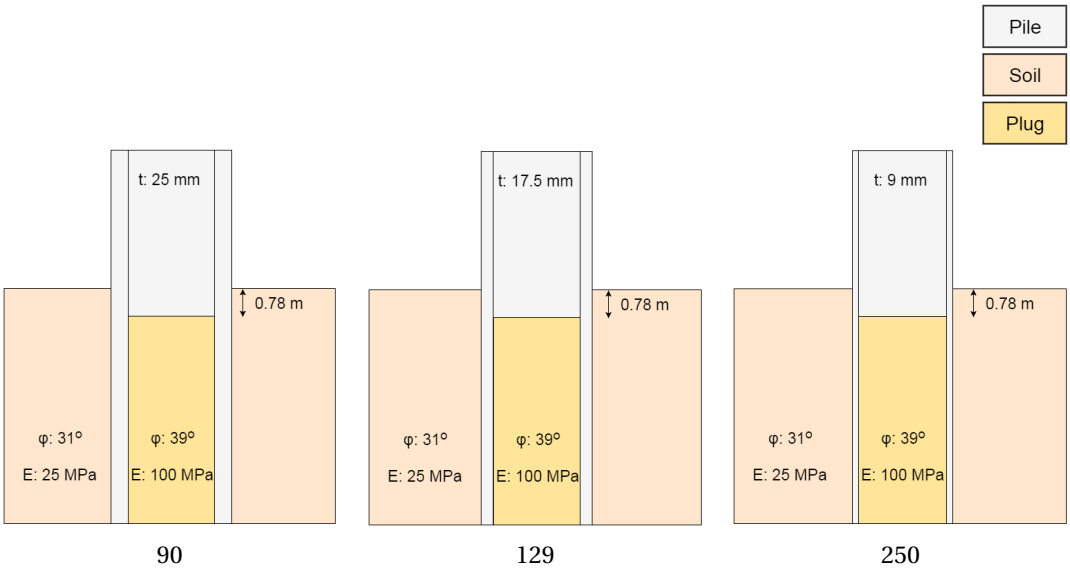

Figure 7.7: Slenderness ratios applied.

Table 7.3: Slenderness ratios applied.

Slenderness Ratio	D_e **[mm]**	t **[mm]**	f_y **[MPa]**
90	914	25.0	582
129	914	17.5	582
250	914	9.0	582

Designing the pile more slender, reduces its capacities. The energy capacity is reduced even more than the bending moment and lateral load capacities. The improvement on the capacities due to the presence of a plug can be compromised by designing the pile more slender.

Furthermore, only a very slender pile, with slenderness ratio of 250 showed typical cross-sectional class 4 behaviour as described in EN 1993-1-1 [13]. It can be presumed that the limit value of 90 in this code can be increased.

Soil packing

Models with a looser and denser soil packing are compared to the basic model. For the looser sand packing the properties of a very silty sand in table 2.b of the NEN-EN 9997-1 [38] is assumed. For the denser packed soil the Young's modulus E_g is doubled to 50 MPa with a friction angle of 32.5°. The applied parameters are presented in table below.

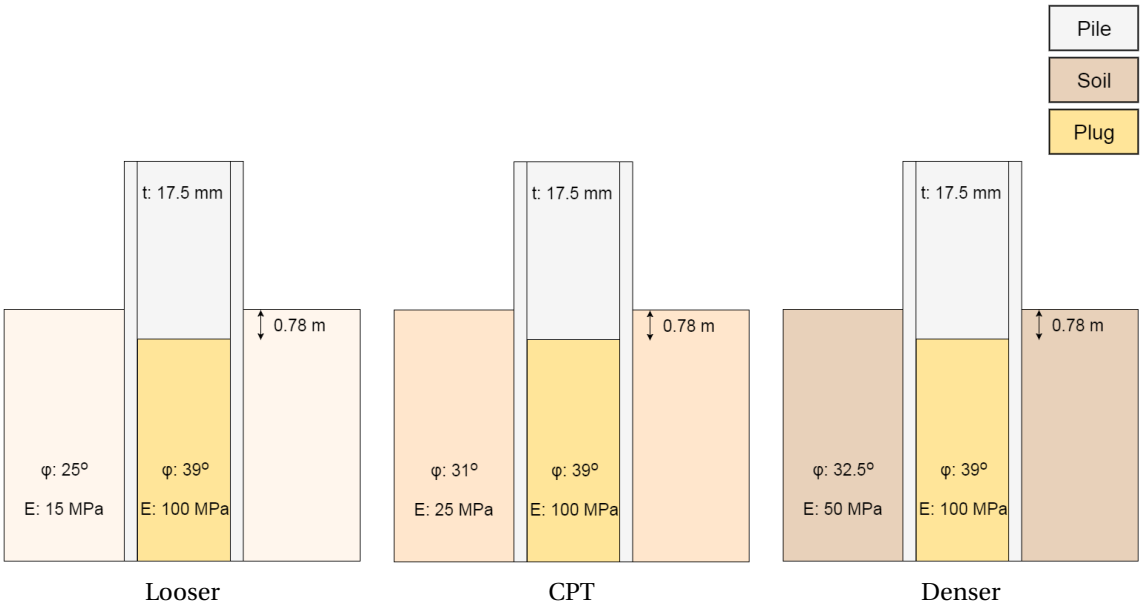

Figure 7.8: Slenderness ratios applied.

Table 7.4: Plug levels applied.

Soil Packing	φ' [°]	ψ [°]	E_g **[MPa]**	ν [-]	K_0 [-]	**Friction coefficient** [-]
Looser	25	0	15	0.37	0.577	0.30
CPT	31	1	25	0.33	0.485	0.38
Denser	32.5	2.5	50	0.32	0.463	0.40

The soil packing does not significantly influence the bending moment capacity. The lateral load capacity is improved by a denser soil packing, yet the improvement is little. The influence on the energy capacity however, is substantial. A looser soil packing improves the energy capacity. Therefore, to maintain a significant energy capacity an installation method should be chosen that does not compact the soil packing.

For the soil plug, the effect is the other way around. A looser soil plug reduces the energy capacity. Hence, the solution to use best of both would be to use an installation method that does not compact the soil and plug packing and after installation, the plug packing is compacted.

Plug stiffness

From the Abaqus analyses the plug stiffness in piles partly filled with sand is studied. Design values for k_{plug} are proposed. These are compared to the value of the CUR 211E [3].

Dolphin piles that are semi-filled with sand have a transition from an empty part to a part where sand is present. At the top of the plug, the sand has the freedom to move upwards. Deeper in the pile, this freedom is limited due to the presence of the sand column above it. Due to this contrast in freedom the plug stiffness is studied at -1m, -2m, -3m and -4m, i.e. $1.1D_e$, $2.2D_e$, $3.3D_e$ and $4.4D_e$ below the bed level. The plug level is at -0.78m ($0.8D_e$). This is illustrated in the figure below.

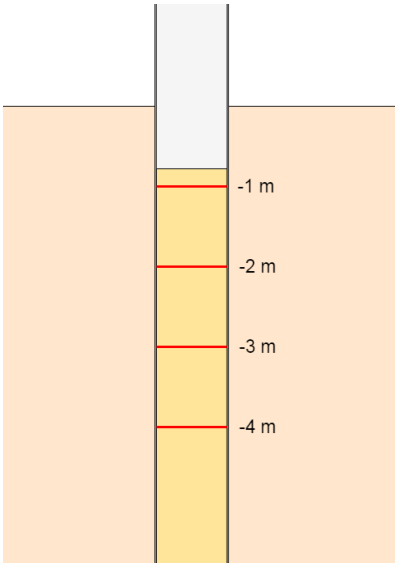

Figure 7.9: Levels at which the plug stiffness is studied.

Studying the plug stiffness derived from the Abaqus analyses, $k_{\text{plug,FEM}}$, also showed that the plug is stiffer deeper below the plug level. At deeper levels, for small ovalisations, a sand-strut improves the plug stiffness. However, this sand strut fails before the ovalisation has reached values that are observed just before local buckling, as can be seen in the figure below.

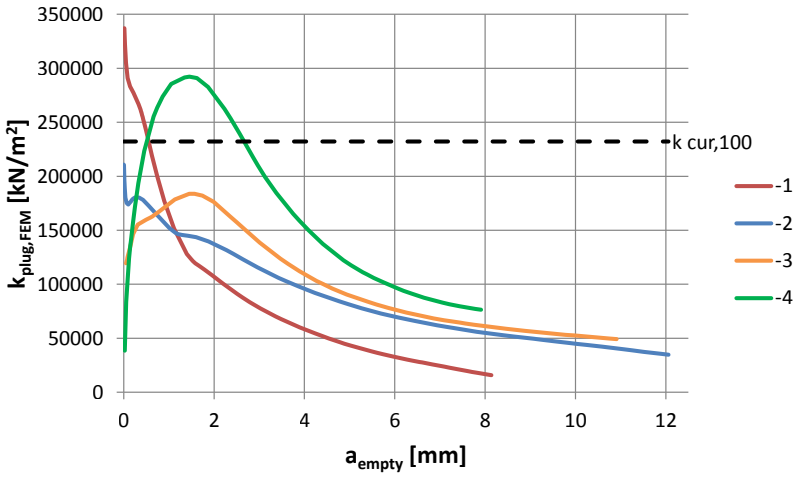

Figure 7.10: $k_{\text{plug,FEM}}$ derived at different levels for E_{plug} = 100 MPa.

The behaviour of the plug in the basic situation is studied, as well as in the situations with a loose and dense plug packing. Comparing the behaviour of the plug with the suggested value for k_{plug} in CUR 211E [3], again revealed that it is not able to determine the plug stiffness for semi-filled piles. The comparison also confirmed that a denser packing reduces the ovalisation more. Close to the plug level however, the stiffnesses $k_{\text{plug,FEM}}$ are in the same range for different packings. Hence, if values of a_{empty} less than 8 mm are expected, a value of 30,000 kN/m^2 can be assumed, regardless of the plug packing. The relation between $k_{\text{plug,FEM}}$ and z for different plug packings with $a_{\text{empty}} = 8$ mm is presented in the figure below.
To check whether the plug stiffness $k_{\text{plug,FEM}}$ is independent of the stiffness of the pile wall k_{wall}, situations with different thicknesses are studied. The difference with these geometries is taken into account in the stiffness of the pile wall $k_{\text{wall}}\left(\frac{12EI_w}{R_m^4}\right)$.

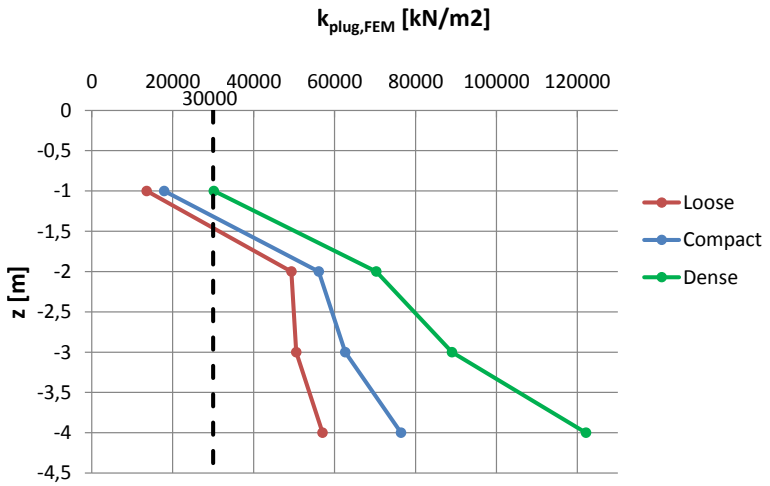

Figure 7.11: Relation between $k_{\text{plug,FEM}}$ and z for different plug packings with $a_{\text{empty}} = 8$ mm.

From the analyses with different slenderness ratios it can be concluded that the plug stiffness is independent of this ratio. Moreover, for large ovalisations, a further increase in ovalisation does not significantly reduce the plug stiffness. Hence, the plot below could be created that can be used to estimate the stiffness of the plug with a compacted packing.

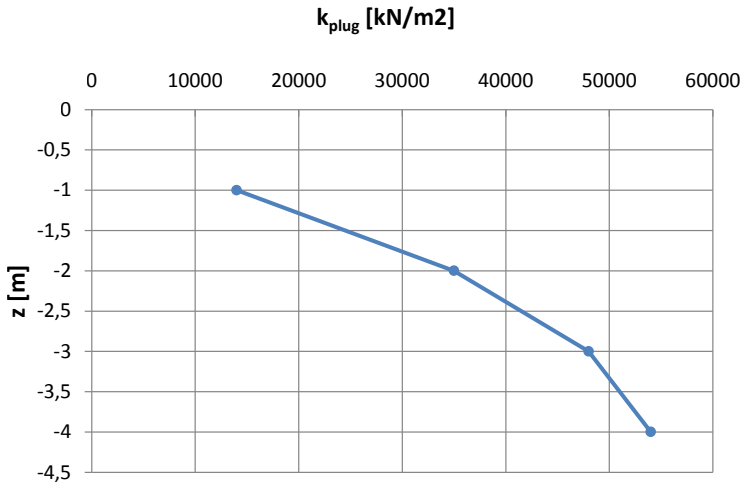

Figure 7.12: k_{plug} for a compact packed plug.

7.1.3. Full scale field tests

To study the failure modes of dolphins, the Port of Rotterdam facilitated a full scale field test with eight piles. Pile 6, was modelled in Abaqus. The results obtained with the Abaqus analyses are validated using the observations in the field test.

The bending moment line produced by Abaqus shows good comparison with the results obtained in the field test. The maximum bending level is located at the same level.

For pile 6, an inward buckle is observed at the level of the maximum bending moment. In Abaqus also an inward buckle was observed. However, the buckle was observed higher.

In the elastic range, the moment-curvature diagram obtained with the finite element analysis corresponds to a pile with the dimensions and steel grade of pile 6. Due to an inaccurate evaluation methodology the

bending moment capacities can not accurately be compared. However, it is concluded that the bending moment capacity of pile 6 and the modelled pile are in the same range.

For lateral loads up to approximately 400 kN, the diagrams presented in the force-displacement diagram demonstrate the same relation. For larger displacements, higher loads are required in Abaqus compared to the reality. The figure below shows that for larger displacements the force-displacement relation is better predicted with a looser soil packing. The lateral load capacity is still underestimated. That Abaqus provides deviating results for larger deformations is prescribed to the Mohr-Coulomb material material model used for the soil.

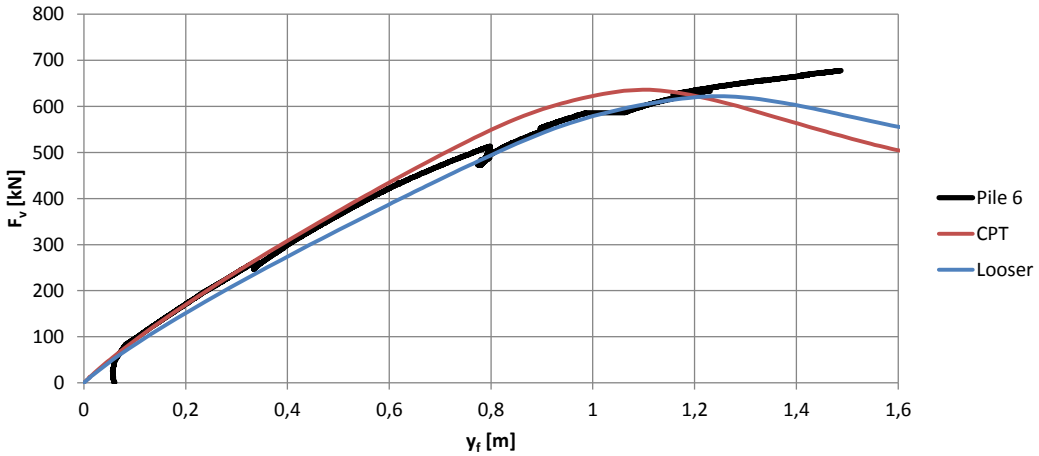

Figure 7.13: Force-displacement diagram of pile 6 and the pile modelled in Abaqus with different soil packings.

The local buckling behaviour of piles 2, 3 and 8 is clarified with the knowledge gained from the parametric study. The effects of the design differences on the observed local buckling levels and shapes can well be explained with insights gained from the results of the finite element analyses. Furthermore, it can well be predicted what pile has a higher capacity.

7.2. Recommendations

For further study on the local buckling resistance of semi-filled piles, recommendations are provided. These are divided in recommendations for research on the analytical model, recommendations to improve the finite element model and recommendations for tests performed in the field.

7.2.1. Analytical model

Before the analytical model can be used it has to be validated. For the approach to find the displacement of the dolphin, the effect of the number of segments should be checked as well as the number of iterations or stop criteria. The ovalisation calculated can be compared to the ovalisation measured in field tests. It would be best to validate it for a full scale test in which the deformation and ovalisation is neatly measured. A semi-filled pile loaded in a lab would also give a good indication for the ovalisation.

The stiffness of the sand in the pile k_{plug} is studied only for a diameter of 914 mm. Soil plugs with a significant different diameter could respond differently. To find this stiffness more knowledge about the horizontal soil pressure by soils in a pile is required, especially when the cross-sectional area is reduced due to ovalisation. The Plaxis model used in this thesis can be improved to get better insight in the horizontal earth pressure of soils in a pile that is ovalised. Different material models can be used.

7.2.2. FEM

With the Abaqus model, for larger displacements, higher loads are required compared to the reality. For larger displacements the force-displacement relation is better predicted with a looser soil packing. The material model can be studied to determine whether this is the cause of the deviating force-displacement relation for larger displacements.

An imperfection over thickness ratio of 0.40 is assumed. Improved capacities are expected with smaller ratios. A parametric study with different imperfection ratios can be performed.

The FEM model is clamped at the bottom. Even for the small horizontal displacements occurring in practice, the soil stresses in the deeper soil in the model differ from the real stresses. The effect of the clamping boundary condition on the found capacities of the modelled pile can be investigated.

Local buckling is responsive for initial imperfections. Therefore other imperfections than geometry imperfections can also be implemented. For example, this can be the initial stresses caused by the fabrication of the pile.

Once the model is improved to a level that it accurately represents the reality, the critical strain can be studied.

7.2.3. Field tests

The installation of the pile changes the original packing. This effects the local buckling resistance of the dolphin and therefore it is valuable to know the effect of the installation method on the packings. Soil tests can be performed before and after the installation of the pile to investigate this. This should be done for the surrounding soil as well as for the plug. The installation method also introduces stresses in the soil and plug. These can be added to the finite element model, to study its effect.

The soil properties influence the local buckling behaviour of large diameter dolphins. To gain more knowledge on their effect, more full scale field tests in different soils should be performed.

The critical strain according to Gresnigt [1] was proposed for buried empty pipelines. More full scale field tests are required to propose an appropriate critical strain valid in the transitional areas.

A

Emperical equations for determination of K_0

K_0 is determined by field or laboratory tests. Some of the most widely used relationships for nonconsolidated soils are provided in table A.1.

Table A.1: Empirical equations for determination of K_0^{NC}.

Reference	**Equation**
Jaky (1944)	$K_0^{NC} = 1 - \sin\varphi'$
Brooker and Ireland (1965)	$K_0^{NC} = 0.95 - \sin\varphi'$
Alpan (1967)	$K_0^{NC} = 0.15 + 0.233\lg(I_P)$ - clay, where I_p = plasticity index
Mayne and Kulhawy (1982)	$K_0^{NC} = 1 - 0.987\sin\varphi'$ - clay, $K_0^{NC} = 1 - 0.998\sin\varphi'$ - sand
Bolton (1991)	$K_0^{NC} = \frac{1-\sin(\varphi'_{crit}-11.5^o)}{1+\sin(\varphi'_{crit}-11.5^o\varphi'_{crit}-11.5^o)}$
Simpson (1981, 1992)	$K_0^{NC} = \frac{1-\sin(\varphi'_{crit}-11.5^o)}{1+\sin(\varphi'_{crit}-11.5^o\varphi'_{crit}-11.5^o)}$

Widely accepted formulas to determine K_0^{OC} for over consolidated soils are given in table A.2. They can be found for known values of K_0^{NC} and overconsolodation ratio (OCR).

Table A.2: Empirical equations for determination of K_0^{OC}.

Reference	**Equation**
Wroth (1975)	$K_0^{OC} = \mathrm{OCR}\cdot K_0^{NC} - \frac{\nu}{1-\nu}(\mathrm{OCR}-1)$
Brooker and Ireland (1965)	$K_0^{OC} = K_0^{NC}(\mathrm{OCR})^n, n = f\left(\frac{1}{I_P}\right), n \approx 0.4 \pm 0.05$
Schmidt (1966)	$K_0^{OC} = (1-\sin(1.2\varphi'))\cdot(\mathrm{OCR})^{\sin(1.2\varphi')}$
Pruska (1973)	$K_0^{OC} = \frac{\sqrt{K_a}\mathrm{OCR}}{1-K_a(1-\mathrm{OCR})}, K_a = \frac{1-\sin\varphi'}{1+\sin\varphi'}$
Meyerhof (1976)	$K_0^{OC} = K_0^{NC}(\mathrm{OCR})^\alpha, \alpha = 0.5$
Mayne and Kulhawy (1982)	$K_0^{OC} = (1-\sin\varphi')\cdot(\mathrm{OCR})^{\sin\varphi'}$

B

Influence of boundary conditions in a stress based calculation

In EN 1993-1-6 [21] the check against local buckling differs for different boundary conditions. The influence of these boundary conditions are studied in this appendix.

The key value of the combined membrane stress state is checked with the unity check. The situation assumed is for a pile with an outer diameter of 0.914 m and wall thickness of 22.6 mm. The pile is of steel with Young's modulus of 210,000 MPa, yield stress of 495 MPa and Poisson's ratio of 0.3. The quality class is class B and the material factor used is 1.1. The pile is exposed to a bending moment of 5,000 kNm and shear force of 500 kN. The earth pressure is 500 kN/m^2. The pile length is varied between 3, 4, 10, 15 and 20 times the length of the diameter.

Checks are performed for the three cases with different boundary conditions. The first case is clamped on both boundaries. The second case is clamped on one end and pined on the other end. In the third case both ends are pined. Furthermore the checks are carried out on three locations in the cross-section. At the 'front', with a circumferential rotation of 0 rad, where the bending moment causes the largest compressive stress in the longitudinal direction. At the 'side', with a circumferential rotation of $\pi/2$ rad, where the shear force causes the largest compressive stress in the cross-section. And in between both locations.

The results are presented in the tables B.1, B.2, B.3. A visual comparison can be made from graphs B.4, B.5, B.6. The highest values, indicating the highest risk of local buckling, are at the front of the pile. Furthermore, case three with pined boundary conditions, results in the highest values. Piles with a length of ten times its diameter show a deviation of 5% between the three cases. When the pile length is 15 times the diameter of the pile or more, the cases do not show any difference. This indicates the boundary conditions have no influence on the risk to local buckling.

		circumferential	**0**	quality class	B	Middle diameter [m]	0,8914	bending moment [kNm]	5000	Young's Modulus [Mpa]	210000
bc1	**1**	**degree [rad]**				wall thickness [m]	22,6	earth pressure [kPa]	500	yielding stress [Mpa]	495
bc2	**1**							shear force [kN]	500	material factor	1,1
										Poisson's ratio	0,3
										radius [m]	0,4457
length of pile	3	unity check	0,651653615	size_x	long	size_theta	short	size_tau	medium		
segment	5		0,651653615		long		medium		medium		
[x Dm]	10		0,675543542		long		long		medium		
	15		0,711585846		long		long		medium		
	20		0,711585846		long		long		long		
		circumferential	**0**	quality class	B	Middle diameter [m]	0,8914	bending moment [kNm]	5000	Young's Modulus [Mpa]	210000
bc1	**1**	**degree [rad]**				wall thickness [m]	22,6	earth pressure [kPa]	500	yielding stress [Mpa]	495
bc2	**2**							shear force [kN]	500	material factor	1,1
										radius [m]	0,4457
length of pile	3	unity check	0,651653615	size_x	long	size_theta	medium	size_tau	medium		
segment	5		0,668281219		long		long		medium		
[x Dm]	10		0,711585846		long		long		medium		
	15		0,711585846		long		long		medium		
	20		0,711585846		long		long		long		
		circumferential	**0**	quality class	B	Middle diameter [m]	0,8914	bending moment [kNm]	5000	Young's Modulus [Mpa]	210000
bc1	**2**	**degree [rad]**				wall thickness [m]	22,6	earth pressure [kPa]	500	yielding stress [Mpa]	495
bc2	**2**							shear force [kN]	500	material factor	1,1
										radius [m]	0,4457
length of pile	3	unity check	0,693846282	size_x	long	size_theta	medium	size_tau	medium		
segment	5		0,711585846		long		long		medium		
[x Dm]	10		0,711585846		long		long		medium		
	15		0,711585846		long		long		medium		
	20		0,711585846		long		long		long		

Figure B.1: Checks at a radial rotation of 0 rad.

		circumferential	**Pi/2**	quality class	B	Middle diameter [m]	0,8914	bending moment [kNm]	5000	Young's Modulus [Mpa]	210000
bc1	**1**	**degree [rad]**				wall thickness [m]	22,6	earth pressure [kPa]	500	yielding stress [Mpa]	495
bc2	**1**							shear force [kN]	500	material factor	1,1
										Poisson's ratio	0,3
										radius [m]	0,4457
length of pile	3	unity check	0,00530574	size_x	long	size_theta	short	size_tau	medium		
segment	5		0,006789281		long		medium		medium		
[x Dm]	10		0,009927583		long		long		medium		
	15		0,010994097		long		long		medium		
	20		0,011650721		long		long		long		
		circumferential	**Pi/2**	quality class	B	Middle diameter [m]	0,8914	bending moment [kNm]	5000	Young's Modulus [Mpa]	210000
bc1	**1**	**degree [rad]**				wall thickness [m]	22,6	earth pressure [kPa]	500	yielding stress [Mpa]	495
bc2	**2**							shear force [kN]	500	material factor	1,1
										radius [m]	0,4457
length of pile	3	unity check	0,005591561	size_x	long	size_theta	medium	size_tau	medium		
segment	5		0,007685581		long		long		medium		
[x Dm]	10		0,010221066		long		long		medium		
	15		0,011020135		long		long		medium		
	20		0,011659001		long		long		long		
		circumferential	**Pi/2**	quality class	B	Middle diameter [m]	0,8914	bending moment [kNm]	5000	Young's Modulus [Mpa]	210000
bc1	**2**	**degree [rad]**				wall thickness [m]	22,6	earth pressure [kPa]	500	yielding stress [Mpa]	495
bc2	**2**							shear force [kN]	500	material factor	1,1
										radius [m]	0,4457
length of pile	3	unity check	0,006152955	size_x	long	size_theta	medium	size_tau	medium		
segment	5		0,008727483		long		long		medium		
[x Dm]	10		0,010292855		long		long		medium		
	15		0,011034511		long		long		medium		
	20		0,011663561		long		long		long		

Figure B.2: Checks at a radial rotation of $\pi/2$ rad.

		circumferential	**Pi/4**	quality class	B	Middle diameter [m]	0,8914	bending moment [kNm]	5000	Young's Modulus [Mpa]	210000
bc1	**1**	**degree [rad]**				wall thickness [m]	22,6	earth pressure [kPa]	500	yielding stress [Mpa]	495
bc2	**1**							shear force [kN]	500	material factor	1,1
										Poisson's ratio	0,3
										radius [m]	0,4457
length of pile	3	unity check	0,322500006	size_x	long	size_theta	short	size_tau	medium		
segment	5		0,322737486		long		medium		medium		
[x Dm]	10		0,336412247		long		long		medium		
	15		0,356827072		long		long		medium		
	20		0,357152161		long		long		long		
		circumferential	**Pi/4**	quality class	B	Middle diameter [m]	0,8914	bending moment [kNm]	5000	Young's Modulus [Mpa]	210000
bc1	**1**	**degree [rad]**				wall thickness [m]	22,6	earth pressure [kPa]	500	yielding stress [Mpa]	495
bc2	**2**							shear force [kN]	500	material factor	1,1
										radius [m]	0,4457
length of pile	3	unity check	0,322500006	size_x	long	size_theta	medium	size_tau	medium		
segment	5		0,331936548		long		long		medium		
[x Dm]	10		0,356461598		long		long		medium		
	15		0,356827072		long		long		medium		
	20		0,357152161		long		long		long		
		circumferential	**Pi/4**	quality class	B	Middle diameter [m]	0,8914	bending moment [kNm]	5000	Young's Modulus [Mpa]	210000
bc1	**2**	**degree [rad]**				wall thickness [m]	22,6	earth pressure [kPa]	500	yielding stress [Mpa]	495
bc2	**2**							shear force [kN]	500	material factor	1,1
										radius [m]	0,4457
length of pile	3	unity check	0,345891932	size_x	long	size_theta	medium	size_tau	medium		
segment	5		0,356011713		long		long		medium		
[x Dm]	10		0,356461598		long		long		medium		
	15		0,356827072		long		long		medium		
	20		0,357152161		long		long		long		

Figure B.3: Checks at a radial rotation of $\pi/4$ rad.

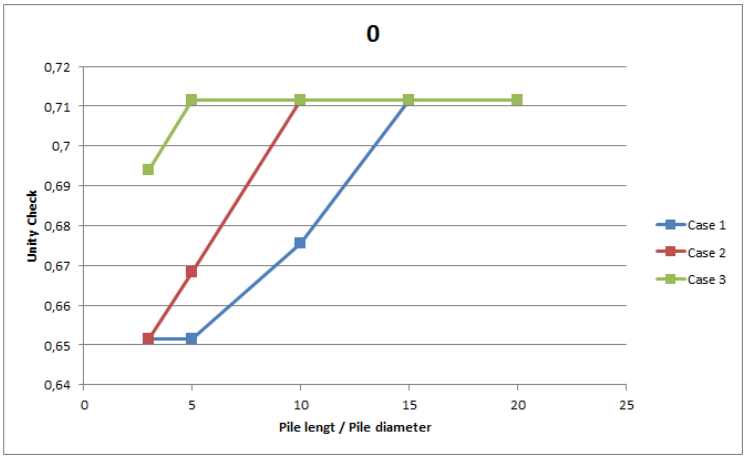

Figure B.4: Comparison of values at a radial rotation of 0 rad.

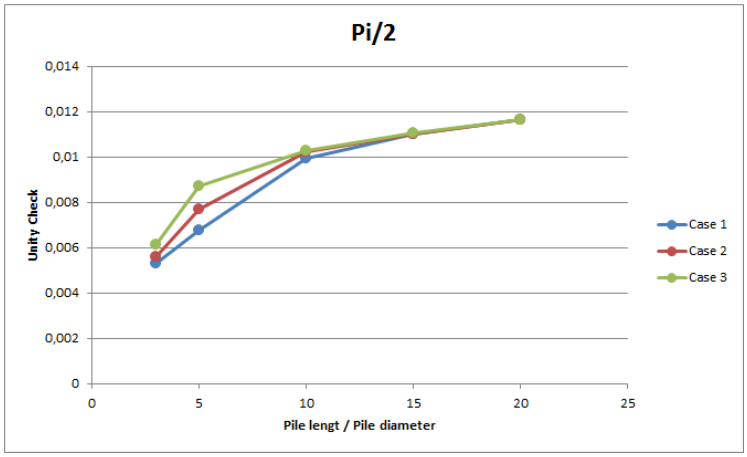

Figure B.5: Comparison of values at a radial rotation of $\pi/2$ rad.

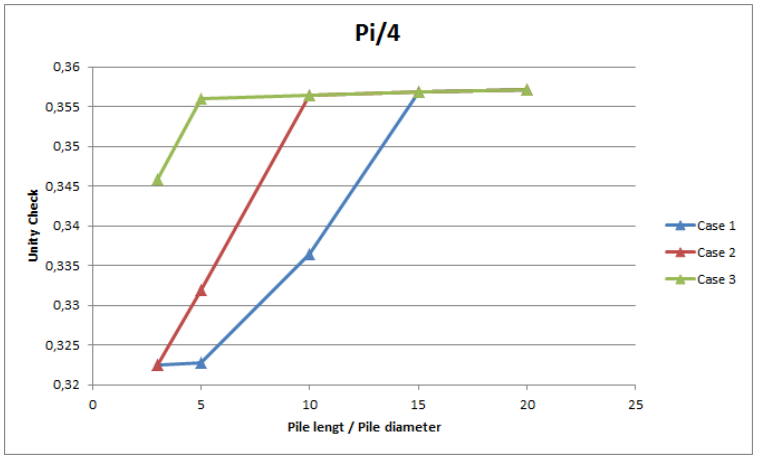

Figure B.6: Comparison of values at a radial rotation of $\pi/4$ rad.

C

Comparison stress based and strain based local buckling check

To compare the stress based method with the strain based method, it is checked for what wall thickness the same pile would be safe for local buckling according to each method. A pile with the same material properties as described in appendix B is used, exposed to the same loadings. It has a diameter of 0.914 m and a length of twenty times the diameter. The wall thickness is varied with steps of 0.5 mm and the unity checks are compared. For the stress based method the cross-section is compared at the 'front', with a circumferential rotation of 0 rad.

Table C.1: Unity checks stress and strain based methods.

Wall thickness [mm]	**Unity check stress based**	**Unity check strain based**
12.5	2.54	1.04
13	2.33	0.87
19	1.03	0.27
19.5	0.98	0.25

According to the stress based method, a wall thickness of 19.5 or bigger should be chosen, whereas the strain based method considers piles with a wall thickness of 13 mm or bigger safe. 1.5 times less steel is required according to the strain based method in this case. It shows that the strain based method results in more economical designs.

D

Finite Element Model Keywords Editing

To be able to use the buckling mode for initial deformations, the keywords of the buckling model have to be edited. At the end, right before the keyword "*End Step" should be added:
"*NODE FILE
U"
The initial dimples from the Buckling analysis have to be implemented. This is done adding the keyword '*IMPERFECTION, FILE=[name of Buckle Analysis], STEP=1'. In the next data line, first the correct mode (1 or 2) has to be given. The correct mode has to be chosen, in order to set the imperfections on the compressive side of the pile wall. Next in line, is the scale factor. The amplitude of the wave in the buckling mode is 1 mm. The depth of the dimple Δw_0 is therefore 2 mm. This can be scaled to the preferred size.

In the Geostatic step gravity is applied on the soil and plug. Beside the gravitational load in the keywords the keyword "*INITIAL CONDITIONS,TYPE=STRESS,GEOSTATIC" and a data line have to be added. The data line indicates what the initial stress should be. In this way there are barely displacements, yet the geostatic stress field, that varies with elevation only is set. The lines are added between the '*Imperfection line' and the '**Step line'. In the data line seven parts are required:

1. Element number or element set label.
2. First value of vertical component of (effective) stress.
3. Vertical coordinate corresponding to the above value.
4. Second value of vertical component of (effective) stress.
5. Vertical coordinate corresponding to the above value.
6. First coefficient of lateral stress. This coefficient defines the x-direction stress components.
7. Second coefficient of lateral stress. This coefficient defines the y-direction stress component in three-dimensional cases and the thickness or hoop direction component in plane or axisymmetric cases. If this value is omitted, it is assumed to be the same as the first lateral stress coefficient given in the previous field.

The stress at the top of the soil and plug is 0 kN/m^2. As the soil is 8.5 m deep in the model and has a density of 19 kN/m^3, the stress at the bottom will be 161.5 kN/m^2. For the plug, the stress at the bottom will be the same, as originally there was also 8.5 m of sand on top. However the plug is only 7.78 m deep. To compensate for this, the gravitational force will be set bigger (see 4.4.6). The coefficient of lateral stress is the K_0 factor. These are calculated with equation 2.12. The edited keywords are presented in figure D.1. Note that the units used in Abaqus are Newtons and millimetres. The vertical stresses S33 and the vertical displacement U3 of the soil after the Geostatic step are presented in figures D.2 and D.3.

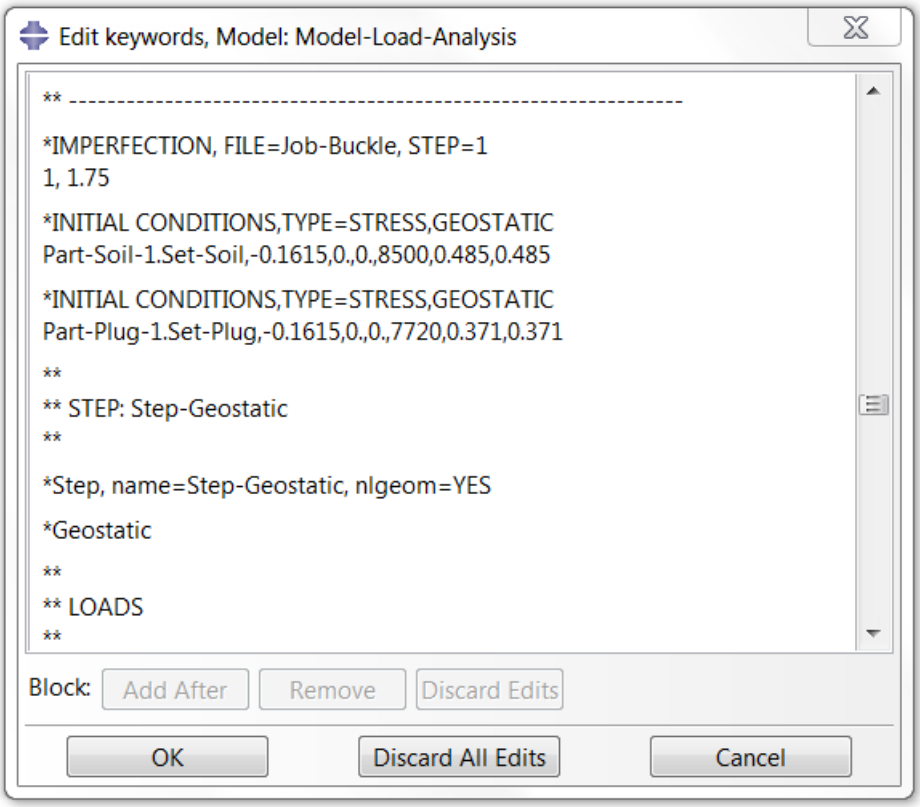

Figure D.1: The edited keywords for the loading analysis, showing the lines for the initial imperfection and initial stress.

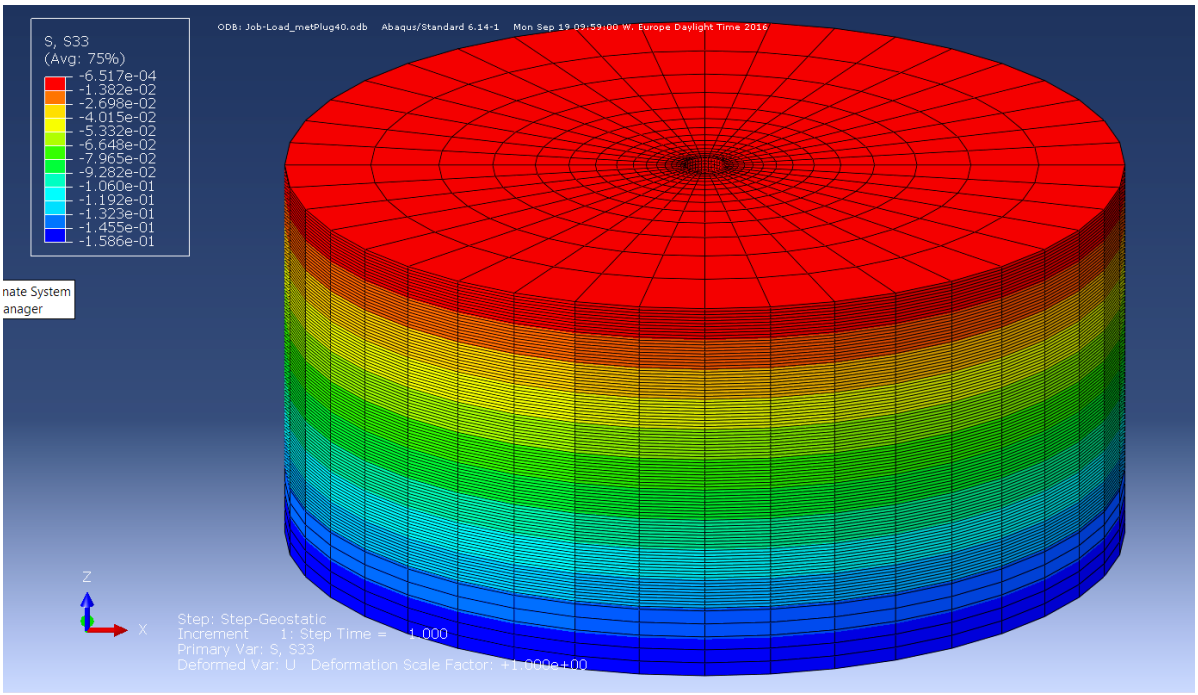

Figure D.2: SS3 of the soil after the Geostatic step.

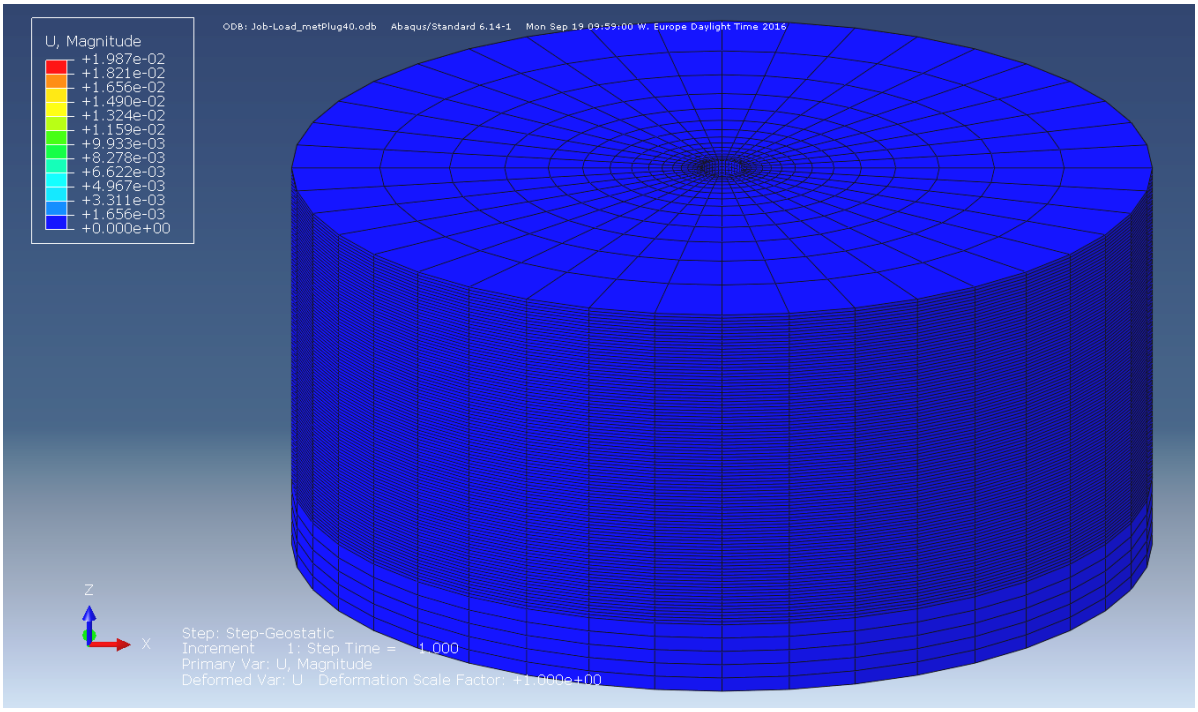

Figure D.3: U3 of the soil after the Geostatic step.

E

Effect of plug packing on the ovalisation and plug stiffness

Plug packing

z = -1 m

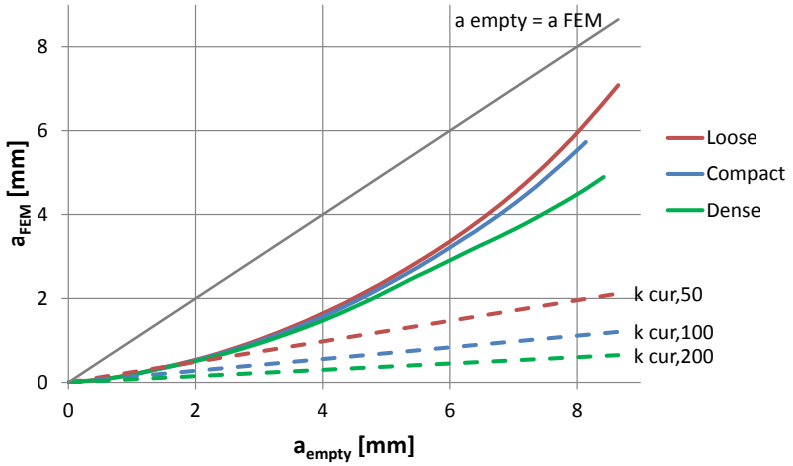

Figure E.1: a_{FEM} obtained with different plug packings at $z = -1$ m.

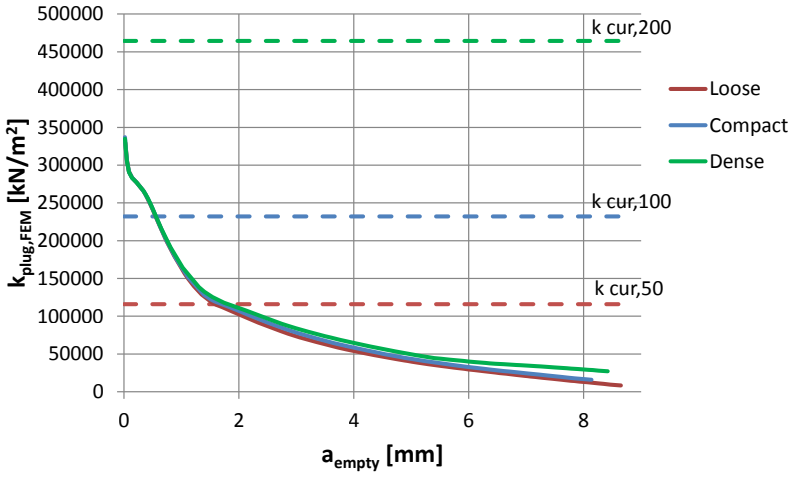

Figure E.2: $k_{\text{plug,FEM}}$ derived with different plug packings at $z = -1$ m.

z = -3 m

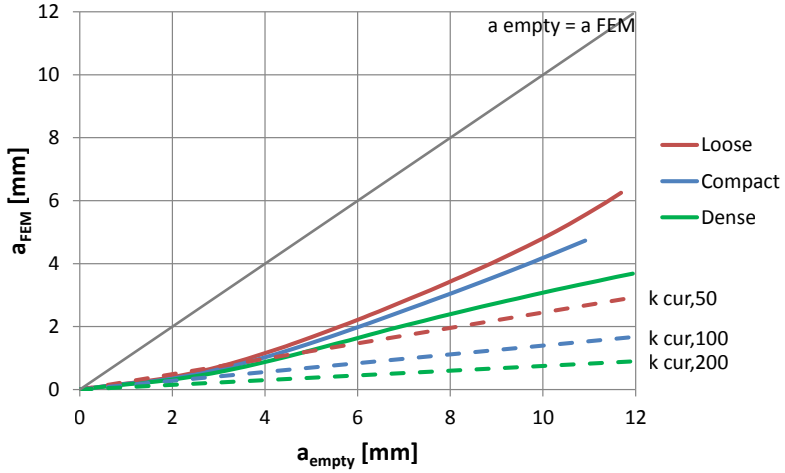

Figure E.3: a_{FEM} obtained with different plug packings at $z = -3$ m.

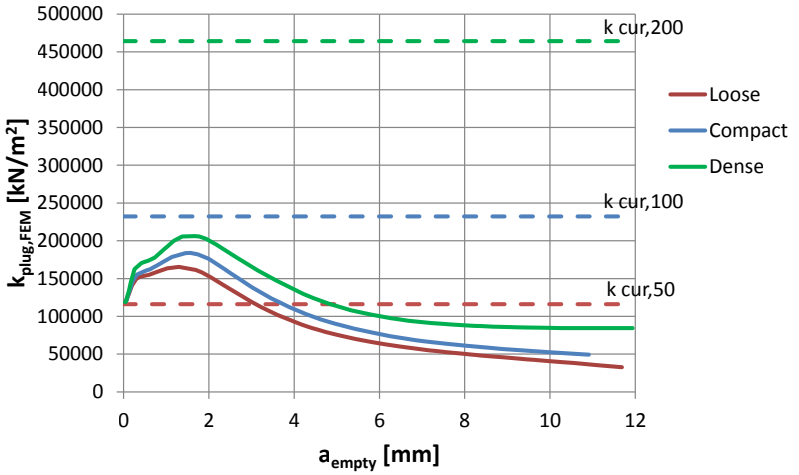

Figure E.4: $k_{\text{plug,FEM}}$ derived with different plug packings at $z = -3$ m.

z = -4 m

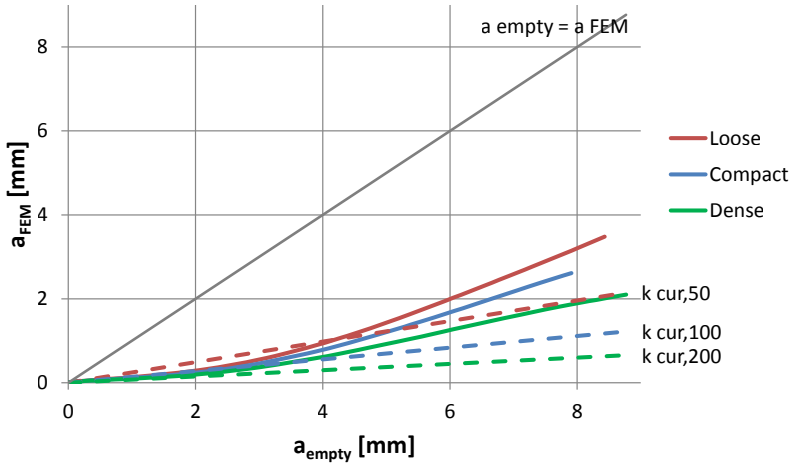

Figure E.5: a_{FEM} obtained with different plug packings at $z = -4$ m.

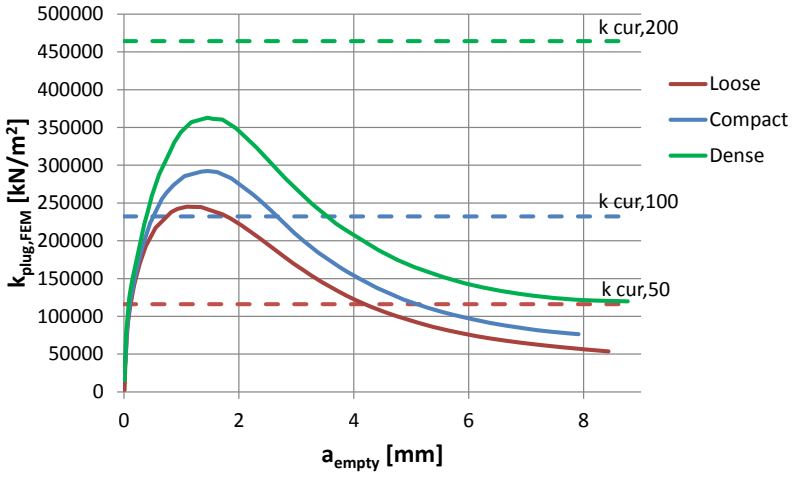

Figure E.6: $k_{\text{plug,FEM}}$ derived with different plug packings at $z = -4$ m.

Bibliography

[1] A. M. Gresnigt. Plastic design of bureid steel pipelines in settlement areas. *HERON*, 31(4):113, 1986.

[2] EN 1993-4-3. *Eurocode 3: Design of steel structures, Part 4-3: Pipelines*, Brussels, 2009. CEN.

[3] SBRCURnet, Municipality of Rotterdam, and Port of Rotterdam. *SBRCURnet Publication 211E Quay Walls Second edition.* CRC Press, 2013.

[4] Port of Rotterdam. *Port of Rotterdam Authority invests €32 million in buoys and dolphins.* August 2015.

[5] J. M. van der Meer A. A. Roubos and D. J. Jaspers Focks. Praktijkproef "Flexible Dolphins", 2015. Presentation.

[6] J. A. T. Ruigrok. Laterally loaded piles, models and measurements. Master's thesis, Delft University of Technology, 2010.

[7] E Winkler. Die lehrevon elastizitat und festigkeit (on elasticity and fixity). 1867.

[8] IHS Maritime and Trade. Historical vessel and orderbook data, 2015.

[9] Hiroyuki Shima. Buckling of carbon nanotubes: a state of the art review. *Materials*, 5(1):47–84, 2011.

[10] N. Kostis. Local buckling of sand-filled steel tubes for combined walls. Master's thesis, Delft University of Technology, 2016.

[11] EL Axelrad. Flexible shells. In *Proceedings of the XV International Congress of Theoretical and Applied Mechanics*, pages 45–50. Springer, 1980.

[12] M Esslinger and B Geier. Postbuckling behaviour of structures. cism courses and lectures no. 236. *International Center for Mechanical Sciences, Springer-Verlag, Berlin*, 1975.

[13] EN 1993-1-1. *Eurocode 3: Design of steel structures, Part 1-1: General rules and rules for buildings*, Brussels, 2011. CEN.

[14] S. R. Satish Kumar and A. R. Santha Kumar. Design of steel structures, 2016. Webcourse: `http://nptel.ac.in/courses/105106112/6_beams/3_behaviour_of_steel_beams.pdf`.

[15] Armin Patsch, Carlos F Gerbaudo, and Carlos A Prato. Analysis and testing of piles for ship impact defenses. *Journal of Bridge Engineering*, 7(4):236–244, 2002.

[16] Dirk Jan Peters, EJ Broos, AM Gresnigt, SHJ van Es, et al. Local buckling resistance of sand-filled spirally welded tubes. In *The Twenty-fifth International Offshore and Polar Engineering Conference*. International Society of Offshore and Polar Engineers, 2015.

[17] Feng Yu and Jun Yang. Base capacity of open-ended steel pipe piles in sand. *Journal of Geotechnical and Geoenvironmental Engineering*, 138(9):1116–1128, 2012.

[18] Alfred Roubos, Dirk Jan Jaspers Focks, and Dirk Jan Peters. Innovation flexible dolphins by full scale field test laterally loaded tubular piles. (to appear), 2015.

[19] D. J. Peters. Static and dynamic lateral load tests on flexible dolphins: Factual and interpretation report. Technical report, Witteveen+Bos and Royal HaskoningDHV, 01 2015.

[20] American Institute of Steel Construction. *Specification for Structural Steel Buildings*, Chicago, 2010. AISC.

[21] EN 1993-1-6. *Eurocode 3: Design of steel structures, Part 1-6: General - Strength and Stability of Shell Structures*, Brussels, 2007. CEN.

[22] R. J. van Foeken and A. M. Gresnigt. Buckling and collapse of uoe manufactured steel pipes. *TNO-report*, 96-CON-R0500:160, 1998.

[23] A. M. Gresnigt. Kritieke stuik en kritieke rotatie in verband met plooien van stalen transportleidingen. *IBBC-TNO Raport*, 85(343):40, 1985.

[24] EL Axelrad. On local buckling of thin shells. *International journal of non-linear mechanics*, 20(4):249–259, 1985.

[25] Warren Clarence Young and Richard Gordon Budynas. *ROARK'S Formulas for Stress and Strain*, volume 6. McGraw-Hill New York, 1989.

[26] LC Reese and V Impe. Piles under lateral loading. *AA Balkema: Rotterdam, Netherlands*, 2001.

[27] J Jaky. The coefficient of earth pressure at rest. *Journal of the Society of Hungarian Architects and Engineers*, 78(22):355–358, 1944.

[28] W. J. Macquorn Rankine. On the stability of loose earth. *Philosophical Transactions of the Royal Society of London*, 147:9–27, 1857.

[29] C. A. Coulomb. Essai sur une application des regles de maximis et minimis a quelques problemes de statique, relatifs a l'architecture. *Memoires de l'Academie Royale pres Divers Savants*, 7, 1776.

[30] Bramlette McClelland and John A Focht. Soil modulus for laterally loaded piles. *Transactions of the American Society of Civil Engineers*, 123(1):1049–1063, 1958.

[31] Lymon C Reese and Hudson Matlock. *Non-dimensional solutions for laterally-loaded piles with soil modulus assumed proportional to depth*. Association of Drilled Shaft Contractors, 1956.

[32] William R Cox, Lyman C Reese, Berry R Grubbs, et al. Field testing of laterally loaded piles in sand. In *Offshore Technology Conference*. Offshore Technology Conference, 1974.

[33] Lymon C Reese, William R Cox, and Francis D Koop. Analysis of laterally loaded piles in sand. *Offshore Technology in Civil Engineering Hall of Fame Papers from the Early Years*, pages 95–105, 1974.

[34] American Petroleum Institute. *Recommended practice for planning, designing, and constructing fixed offshore platforms*, Washington, 2002. API.

[35] JM Gere and SP Timoshenko. Mechanics of materials, wadsworth. *Inc., Belmont, California*, pages 351–355, 1984.

[36] D. J. Peters. Local buckling tests on tubular piles evaluation report. Technical report, Royal Haskoning DHV, 2013.

[37] Samuel G Paikowsky, Robert V Whitman, and Mohsen M Baligh. A new look at the phenomenon of offshore pile plugging. *Marine Georesources & Geotechnology*, 8(3):213–230, 1989.

[38] EN 1997-1. *Eurocode 7: Geotechnical design - Part 1: General rules*, Brussels, 2012. CEN.

[39] CUR 2001-8. *Bearing Capacity Of Steel Pipe Piles*, Gouda, The Netherlands, 2001. Centre for Civil Engineering Research and Codes (CUR).

[40] HM Zuidberg, P Vergobbi, et al. Euripides, load tests on large driven piles in dense silica sands. In *Offshore Technology Conference*. Offshore Technology Conference, 1996.

[41] K. Paik and R. Salgado. Determination of bearing capacity of open-ended piles in sand. *Journal of Geotechnical and Geoenvironmental Engineering*, 129(1):46–57, 2003.

[42] A De Nicola and MF Randolph. The plugging behaviour of driven and jacked piles in sand. *Geotechnique*, 47(4):841–856, 1997.

[43] Junhwan Lee, Rodrigo Salgado, and Kyuho Paik. Estimation of load capacity of pipe piles in sand based on cone penetration test results. *Journal of Geotechnical and Geoenvironmental Engineering*, 129(5):391–403, 2003.

[44] Samuel G Paikowsky and Robert V Whitman. The effects of plugging on pile performance and design. *Canadian Geotechnical Journal*, 27(4):429–440, 1990.

[45] BM Lehane, JA Schneider, and X Xu. A review of design methods for offshore driven piles in siliceous sand. *UWA Report GEO 05358*, 2005.

[46] SR Gudavalli, O Safaqah, and H Seo. Effect of soil plugging on axial capacity of open-ended pipe piles in sands. In *Proceedings of the 18th International Conference on Soil Mechanics and Geotechnical Engineering*, pages 1487–1490, 2013.

[47] Miklos Hetényi. *Beams on Elastic Foundation*. University of Michigan press, 8th edition, 1967.

[48] Plaxis bv. *PLAXIS 3D. Material Models Manual 2015*, 2015.

[49] Chanaton Surarak, Suched Likitlersuang, Dariusz Wanatowski, Arumugam Balasubramaniam, Erwin Oh, and Hong Guan. Stiffness and strength parameters for hardening soil model of soft and stiff bangkok clays. *Soils and Foundations*, 52(4):682–697, 2012.

[50] G. N. Wells. The finite element method: An introduction. Master's thesis, University of Cambridge & Delft University of Technology, 2009.

[51] Glaucio H Paulino. Introduction to fem (history, advantages and disadvantages).

[52] Sjors HJ van Es, Arnold M Gresnigt, Daniel Vasilikis, and Spyros A Karamanos. Ultimate bending capacity of spiral-welded steel tubes–part i: Experiments. *Thin-Walled Structures*, 102:286–304, 2016.

[53] Plaxis bv. *PLAXIS 2016*, 2016.

[54] Alain Holeyman, Anton Hübner, Helmut Saal, Olivier Tomboy, et al. Laterally loaded tubular piles–experiments and numerical analyses. In *The Seventeenth International Offshore and Polar Engineering Conference*. International Society of Offshore and Polar Engineers, 2007.

[55] Dirk Jan Peters. New analytical plasticity model for lateral loaded mono-piles. (to appear), 2015.

[56] Dassault Systèmes. *Abaqus 6.14 Online Documentation*, 2014.

[57] RT Haftka, J Iott, and HM Adelman. Selecting step sizes in sensitivity analysis by finite differences. *Aug., NASA TM-86382*, 1985.

[58] GG Meyerhof. Penetration tests and bearing capacity of cohesionless soils. *Journal of the Soil Mechanics and Foundations Division*, 82(1):1–19, 1956.

[59] Michael Carter, Stephen P Bentley, et al. *Correlations of soil properties*. Pentech press publishers, 1991.